AD-A033 497 ADVISORY GROUP FOR AEROSPACE RESEARCH AND DEVELOPMENT--ETC F/G 21/8.2
SMALL SOLID PROPELLANT ROCKETS FOR FIELD USE.(U)
1976

UNCLASSIFIED AGARD-CP-194 NL

1 OF 2
AD
A033497

AGARD-CP-194

AGARD-CP-194

AGARD

ADVISORY GROUP FOR AEROSPACE RESEARCH & DEVELOPMENT

7 RUE ANCELLE 92200 NEUILLY SUR SEINE FRANCE

AGARD CONFERENCE PROCEEDINGS No. 194

on

Small Solid Propellant Rockets for Field Use

NORTH ATLANTIC TREATY ORGANIZATION

DISTRIBUTION AND AVAILABILITY
ON BACK COVER

AGARD-CP-194

NORTH ATLANTIC TREATY ORGANIZATION

ADVISORY GROUP FOR AEROSPACE RESEARCH AND DEVELOPMENT

ORGANISATION DU TRAITE DE L'ATLANTIQUE NORD

GROUP CONSULTATIF POUR LA RECHERCHE ET LE DEVELOPPEMENT AEROSPATIAL

AGARD Conference Proceedings No.194

SMALL SOLID PROPELLANT ROCKETS FOR FIELD USE.

NOTE: Additional papers are published in AGARD Conference Proceedings No.194 (Supplement) classified NATO CONFIDENTIAL

1976

154p.

Papers presented at the 47th Meeting of the AGARD Propulsion and Energetics Panel held at DFVLR Porz-Wahn, 5 Köln 90, Linder Höhe, Germany, 17–19 May 1976.

THE MISSION OF AGARD

The mission of AGARD is to bring together the leading personalities of the NATO nations in the fields of science and technology relating to aerospace for the following purposes:

- Exchanging of scientific and technical information;
- Continuously stimulating advances in the aerospace sciences relevant to strengthening the common defence posture;
- Improving the co-operation among member nations in aerospace research and development;
- Providing scientific and technical advice and assistance to the North Atlantic Military Committee in the field of aerospace research and development;
- Rendering scientific and technical assistance, as requested, to other NATO bodies and to member nations in connection with research and development problems in the aerospace field;
- Providing assistance to member nations for the purpose of increasing their scientific and technical potential;
- Recommending effective ways for the member nations to use their research and development capabilities for the common benefit of the NATO community.

The highest authority within AGARD is the National Delegates Board consisting of officially appointed senior representatives from each member nation. The mission of AGARD is carried out through the Panels which are composed of experts appointed by the National Delegates, the Consultant and Exchange Program and the Aerospace Applications Studies Program. The results of AGARD work are reported to the member nations and the NATO Authorities through the AGARD series of publications of which this is one.

Participation in AGARD activities is by invitation only and is normally limited to citizens of the NATO nations.

Published September 1976

ISBN 92-835-0174-8

Printed by Technical Editing and Reproduction Ltd
Harford House, 7–9 Charlotte St, London, W1P 1HD

AGARD PROPULSION AND ENERGETICS PANEL OFFICERS

CHAIRMAN: M. l'Ing. en Chef Marc Pianko
ONERA, Châtillon-sous-Bagneux, France

DEPUTY CHAIRMAN: Dr Ing. G.Winterfeld
DFVLR, Porz-Wahn, 5 Köln 90, Germany

PROGRAM COMMITTEE

Dr Ing. G.Winterfeld (Chairman) DFVLR Porz-Wahn, 5 Köln 90, Germany
Mr M.Barrère, ONERA, Châtillon-sous-Bagneux, France
Professor J.Chauvin, VKI, Rhode-St-Genèse, Belgium
Professor D.Dini, Università di Pisa, Italy
Professor I.Glassman, Princeton University, Princeton, New Jersey, USA
Mr G.Kristofersen, NDRE, Kjeller, Norway
Professor A.H.Lefebvre, CIT, Cranfield, Bedford, UK
Mr D.Weidhuner, Transportation Energy Conservation, ERDA, Washington, DC, USA
Professor H.Wittenberg, Delft Technical University, Delft, The Netherlands

HOST COORDINATOR

Dr Ing. G.Winterfeld, DFVLR, Porz-Wahn, 5 Köln 90, Germany

PANEL EXECUTIVE

Lt. Colonel J.B.Catiller, USAF

The Propulsion and Energetics Panel wishes to express its thanks to the hosts, the German National Delegates to AGARD, for the invitation to hold the meeting in the DFVLR Porz-Wahn Research Centre, near Cologne, Germany, and for the provision of the necessary facilities and personnel.

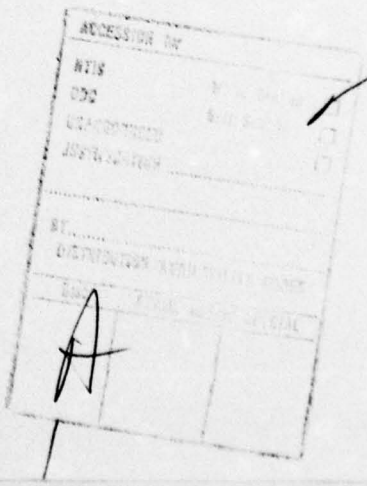

PREFACE

SMALL SOLID PROPELLANT ROCKETS FOR FIELD USE

The specialists' meeting is devoted to technological problems associated with propulsion systems of advanced small rocket motors for anti-tank, anti-aircraft, and light artillery rockets. After specification of the requirements for the three types of weapon systems, problems of systems development will be discussed including the optimization and matching of propulsion systems as well as new methods for control and thrust vectoring. High energy solid propellants and ignition problems will be reviewed. A discussion of important problems of application, such as noise and shock effects on the gunner, will terminate the sessions.

PETITS MOTEURS FUSEES A POUDRE L'EMPLOI SUR LE CHAMP DE BATAILLE

Cette réunion de spécialistes sera consacrée aux problèmes technologiques que posent les systèmes propulsifs des petits moteurs de conception avancée destinés aux roquettes antichars, anti-aériennes et d'artillerie légère. Les conditions requises pour ces trois types de systèmes d'armes seront tout d'abord définis; puis seront présentés les problèmes liés à la phase de développement, en particulier l'optimisation et l'adaptation des systèmes propulsifs, ainsi que les nouvelles méthodes de commande et de déviation de jet. Il sera procédé ensuite à un tour d'horizon des propergols solides hautement energétiques et des problèmes d'allumage. Enfin, un examen de certains problèmes majeurs d'application tels que l'impact du bruit et de la secousse sur le tireur, cloturera la réunion.

CONTENTS

* These papers are published in AGARD Conference Proceedings No.194 (Supplement), classified NATO CONFIDENTIAL

* These papers are published in AGARD Conference Proceedings No.194 (Supplement), classified NATO CONFIDENTIAL

LES ROQUETTES D'AVIATION - CONTRAINTES INHERENTES A LEUR UTILISATION

Claude SENGEISSEN
Ingénieur en Chef des Etudes et Techniques d'Armement
Section Armements Missiles
Service Technique Aéronautique
4, avenue de la Porte d'Issy
75996 PARIS ARMEES
France

SOMMAIRE

Cet exposé concerne l'utilisation des roquettes non guidées en aviation. Il comporte deux parties:

La première partie est une présentation sommaire des roquettes et de leurs conditions d'utilisation: Les roquettes d'aviation sont des projectiles autopropulsés, empennés, non guidés, tirés à partir d'avion, Le tir s'effectue en léger piqué à des distances variant de 800m à 3000m selon le type de roquettes.

La deuxième partie est une analyse des contraintes inhérentes à l'emploi à partir d'avion. Elle comporte: des considérations générales sur les avantages et inconvénients de ce type de munition (coût modéré, puissance de frappe appréciable, mais l'avion doit s'exposer pendant le tir),une discussion sur les contraintes d'emploi qui conditionnent le choix des caractéristiques, et des précisions sur les conditions d'environnement et de fonctionnement à partir d'avion: sécurité de fonctionnement, température en vol etc...

1. - SITUATION DE L'EXPOSE

Cet exposé a pour but de présenter les roquettes non guidées utilisées en aviation, de préciser les conditions dans lesquelles elles sont utilisées et d'émettre certaines considérations qui conditionnent leur définition et celle de leur propulseur. Ces considérations ne relèvent pas de la technique des propulseurs mais des conditions particulières d'emploi à partir d'avion.

2. - PRECISIONS SUR LES ROQUETTES D'AVIATION ET LEUR UTILISATION

2.1. - Présentation de la roquette

La roquette est un projectile autopropulsé, empenné, non guidé. Elle se compose:
- d'un propulseur,
- d'une tête militaire de forme ogivale fixée sur le fond avant du propulseur,
- d'un empennage à l'arrière.

L'ensemble forme un projectile aérodynamique stable.

Il existe une grande diversité de roquettes d'aviation dont les caractéristiques sont très variables des plus petites aux plus grosses: (voir exemples fig. 1).
les calibres vont de 37mm à 135mm,
les masses varient de 1kg à 50Kg pour les projectiles complets
et de 0,5 Kg à 25Kg pour les propulseurs,
les impulsions spécifiques vont de 45 daN.s, à 3000daN.s,
les temps de combustion vont de 0,25 s et 2 s.
Les roquettes de moyen calibre (70mm environ) sont les plus répandues.

2.2. - Conditions d'emport sur avion

Les roquettes sont généralement emportées dans des lanceurs accrochés sous les points d'emport dont son munies les voilures d'avion pour l'accrochage de charges extérieures diverses telles que les bombes, les réservoirs supplémentaires,etc... (voir exemple fig.2).

Les lanceurs sont généralement constitués de plusieurs tubes parallèles rassemblés en un seul corps fuselé pour offrir une moindre trainée.

Chaque tube contient une roquette. La roquette est munie d'un empennage repliable pour pouvoir être logée dans le tube. A la mise à feu, le tube sert de rampe de guidage. A la sortie du tube, l'empennage se déploie, la roquette a alors sa configuration de vol.

Il existe de nombreux types de lance-roquettes de capacités très variées pour convenir aux diverses possibilités des points d'emport de voilure. (Voir exemples fig.3).

Les lanceurs de gros calibres contiennent en général de 4 à 6 roquettes.

Les lanceurs de petits calibres ont des capacités plus variées:
les lanceurs de 18 roquettes de 68mm ou 19 roquettes de 2,75" sont les plus répandus mais il existe aussi un lanceur français de 36 roquettes de 68mm.

2.3. - Conditions de tir à partir d'avion

Les roquettes sont aujourd'hui réservées à un usage AIR-SOL.

Le tir s'effectue en léger piqué, l'avion se dirigeant vers l'objectif. Les conditions de vol au tir sont généralement les suivantes:
- vitesse avion : comprise entre 400 Kt et 600 Kt
- angle de piqué : 20° environ
- distance de tir : entre 800m et 1500m pour les roquettes de petit et moyen calibre
  : entre 1500m et 3000m pour les roquettes de gros calibres.

Le pilote effectue la mise en direction de l'avion en pointant, sur l'objectif, un réticule de son viseur de tir.

Les roquettes de moyen ou petit calibre sont tirées en salve pour que la probabilité d'atteinte de l'objectif ou la couverture de la zone traitée soit convenable.

2.4. - Les objectifs et les têtes militaires

Les objectifs peuvent être soit pontuels (véhicules isolés) soit une zone comprenant plusieurs véhicules ou des personnels.

Les objectifs de plus grandes dimensions comme les vedettes marines, les bateaux, les abris d'avion, les hangars, les écluses, les radars etc..... nécessitent l'emploi de grosses roquettes.

Les têtes militaires utilisées sont de plusieurs types:

- têtes à charge creuse pour l'attaque de blindage (chars ou autres véhicules, blindés),
- têtes à effet d'éclats ou à fléchettes pour l'attaque de véhicules non blindés ou faiblement blindés ainsi que de personnels,
- têtes de démolition à pouvoir perforant pour l'attaque d'objectifs "durs" avec des roquettes de gros calibre.

Il existe aussi d'autres têtes pour des usages moins répandus:

- têtes fumigènes pour le marquage d'objectifs,
- têtes éclairantes pour l'éclairage d'objectifs de nuit,
- têtes à "chaffs" pour le leurrage de radars.

3. - CONSIDERATIONS SUR L'EMPLOI - REPERCUSSION SUR LA DEFINITION

3.1. - Considérations générales

Les conditions d'emploi de la roquette, tir en piqué à faible distance, oblige l'avion à s'exposer aux défenses adverses. C'est là l'inconvénient majeur de ce type d'arment qui présente par contre l'avantage d'offrir une force de frappe appréciable pour un coût relativement faible. La recherche du moindre coût et l'augmentation des distances de tir pour limiter la vulnérabilité de l'avion, sont deux soucis constants qui pèsent sur la définition de la roquette au moment de sa conception.

3.2. - Considérations sur le choix des principales caractéristiques

Les caractéristiques principales de la roquette et du propulseur, masse, dimensions, loi de poussée résultent d'un compromis à établir pour satisfaire au mieux plusieurs contraintes contradictoires, à savoir:

- une efficacité terminale unitaire suffisante,
- une capacité d'emport sur avion optimale,
- une probabilité d'atteinte convenable à la plus grande distance de tir possible,
- un coût modéré.

Considérations sur l'efficacité terminale

Ce sont les caractéristiques de la charge utile à transporter, la tête militaire, qui déterminent le type de roquette, petite, moyenne ou grosse, et donc le type de propulseur.

C'est l'efficacité terminale qui doit posséder la tête militaire qui fixe ses caractéristiques. On cherche notamment, en tir ponctuel, à ce que le coup au but d'une seule roquette soit décisif. La masse minimale de la tête est ainsi fixée, mais aussi le calibre pour les têtes à charge creuse ou la vitesse terminale pour les têtes de pénétration. Le propulseur est optimisé autour de la tête correspondant à la mission principale, cepndant, le même propulseur doit être aussi capable de recevoir d'autres types de têtes correspondant à des missions secondaires,

Optimisation de la capacité d'emport de l'avion

Pour optimiser la capacité d'emport de l'avion ou minimiser les pénalisations de ses performances, il y a intérêt à ce que la masse unitaire de la roquette soit la plus faible possible dans la mesure où son efficacité terminale unitaire est assurée.

A la masse totale disponible donnée, le maximum de roquettes peuvent être ainsi emportées à capacité donnée, la masse et le volume des lanceurs peuvent être minimisés.

Recherche de la plus grande distance de tir

Afin de limiter la vulnérabilité de l'avion tireur, on s'efforce de tirer du plus loin possible. Cependant, la probabilité d'atteinte de l'objectif décroissant rapidement lorsque la distance augmente, une limite est vite atteinte pour que le tir reste efficace. Deux caractéristiques de la roquette peuvent être optimisées pour améliorer cette probabilité d'atteinte: il s'agit du temps de parcours et de la dispersion propre de la roquette.

Toutes choses égales par ailleurs, on recherche les temps de parcours les plus courts possibles. Les erreurs de tir dues au vent sont ainsi réduites. De plus les erreurs de tir résultant d'une mauvaise appréciation de la distance de tir par le pilote sont d'autant plus faibles que la trajectoire est tendue. Tous les avions, en effet, ne sont pas munis d'une conduite de tir sophistiquée or pour des raisons économiques, la roquette doit être une munition banalisée. Elle doit donc pouvoir être tirée à partir d'avion ne possédant qu'une conduite de tir rudimentaire : un simple collimateur réglé pour des conditions moyennes de tir.

La recherche d'une dispersion propre acceptable impose aussi des contraintes particulières pour la roquette et son propulseur. La dispersion propre de la roquette dépend en grande partie de la stabilité aérodynamique. En effet les oscillations de l'axe longitudinal de la roquette, donc de l'axe de poussée du propulseur, introduisent des composants transversales de la poussée qui sont des causes de pertubations importantes de la trajectoire. Ces oscillations doivent donc être amorties rapidement. Pour cela, certaines relations entre les caractéristiques aérodynamiques, donc dimensionnelles, et massiques (centrage, inertie) doivent être respectées.

3.3. - Contraintes relatives aux conditions de fonctionnement à partir d'avion

Contraintes électriques

La mise à feu du propulseur doit être effectuée à partir de l'énergie électrique continue de l'avion fournie par la génération de bord. Ses caractéristiques sont: valeur nominale de la tension : 28 volts,
valeur minimale : 22 volts.

La durée d'application du courant, commandée par les intervallomètres de tir des lanceurs, ne dépasse pas 15 millisecondes dans certains cas de tir à cadence élevée.

Conditions ambiantes au tir

Conditions de pression

Les tirs sont effectués à faible altitude au-dessus du sol, cependant pour permettre de traiter tous les objectifs, y compris ceux qui pourraient se trouver en altitude, le propulseur doit pouvoir fonctionner normalement pour des pressions extérieures comprises entre la pression à l'altitude de 8000 m et la pression au niveau de la mer.

Conditions de températures

La température au tir dépend des conditions d'emport qui précédent le tir. De l'examen de ces conditions (voir paragraphe 3.4.) il ressort que le propulseur doit fonctionner normalement entre les températures de - 40°C et + 100°C.

La température haute correspond à des conditions extrêmes qui pourraient être rencontrées par temps chaud par des avions à hautes performances et grande autonomie. Elle concerne plus spécialement les avions futurs. Actuellement, la température maximale pour laquelle le fonctionnement normal des matériels existant est assuré est de 70°C environ.

Les variations de performances du propulseur en fonction de la température doivent être pratiquement insensibles au niveau de la balistique extérieure de la roquette pour ne pas remettre en cause le réglage du viseur de tir dans tout le domaine d'emploi en température.

Compatibilité avec l'avion tireur

Sécurité de l'avion.

La sécurité de l'avion tireur est un impératif absolu. Des précautions particulières doivent être prises pour éviter tout fonctionnement intempestif du propulseur ou toute explosion à la mise à feu:

- l'allumeur doit être insensible aux effets des rayonnements électromagnétiques ou à tout autres parasites électriques pouvant apparaitre par décharge d'électricité statique
- le propulseur doit présenter un grand coefficient de sécurité vis à vis des surpressions internes. Il doit pouvoir supporter sans exploser, dans tout le domaine d'emploi en température, des surpressions consécutives à des dégradations du chargement de propergol ou à toute autre cause.

Projections arrières au tir

Les projections, à l'allumage, de corps solides susceptibles de déteriorer les éléments de l'avion, voilure, empennage, fuselage, situés en arrière du lance roquettes doivent être évitées.

Compatibilité avec les moteurs de l'avion

Les gaz éjectés par le propulseur peuvent être absorbés par les moteurs de l'avion. Des décrochages du compresseur voire l'extinction du moteur peuvent alors se produire. Fort heureusement les condition de tir des roquettes ne sont pas des conditions de vol où les moteurs sont sensibles à ces phénomènes. Des problèmes peuvent cependant exister au tir de grosses roquettes.

Effets corrosifs des gaz éjectés.

Dans la mesure du possible, on doit s'efforcer de limiter les effets corrosifs des gaz d'éjection. Ceux-ci provoquent en effet la détérioration rapide des éléments de l'avion placés dans leur sillage, tels que les carénages des pylônes, les prises électriques de liaison du pylône au lanceur, etc...

3.4. - Contraintes d'environnement pendant la phase d'emport qui précéde le tir

La roquette et le propulseur doivent pouvoir supporter sans dommage les conditions d'environnement propre à la phase d'emport qui précéde le tir.

Plus précisément, ils devront supporter:

- les vibrations de vol,
- les températures en vol,
- les pressions,
- la traversée de nuagesou de zones de pluie.

En ce qui concerne les températures, les précisions suivantes doivent être apportées:

Les températures sont liées au profil du vol. Les profils de vol des missions "d'attaque roquettes" sont déterminés par les critères suivants:

- au-dessus du territoire ami, l'avion pourra voler à haute altitude, à la tropopause, au régime économique. Ces conditions de vol lui assureront un plus grand rayon d'action et une navigation plus aisée.
- au-dessus du territoire ennemi, l'avion volera à la plus basse altitude et à la plus grande vitesse possibles, compatibles avec ses moyens de navigation et son autonomie.

Selon la position de la base de départ et de l'objectif, le vol s'effectuera en partie à haute altitude et en partie ou en totalité à basse altitude.

Le tableau ci-dessous donne pour différentes conditions de vol, les températures de paroi d'un corps placé dans un écoulement d'air.

	M / Øs	0,8	0,9	1	1.1	1.2
haute altitude	- 65°C	- 41°C	- 35°C	- 28°C	- 20°C	- 11°C
	- 56,5°C	- 32°C	- 25°C	- 17°C	- 9°C	0°C
basse altitude	+ 15°C	+ 48°C	+ 57°C	+ 67°C	+ 78°C	+ 90°C
	+ 20°C	+ 54°C	+ 63°C	+ 73°C	+ 84°C	+ 96°C
	+ 30°C	+ 65°C	+ 74°C	+ 84°C	+ 96°C	+108°C
	+ 40°C	+ 76°C	+ 86°C	+ 96°C	+108°C	+120°C

Øs est la température statique à l'altitude du vol M: est le nombre de Mach de l'écoulement.

Dans les lanceurs à tubes, les roquettes ne sont pas directement placées dans l'écoulement aérodynamique. Elles n'atteindront donc les températures indiquées ci-dessus qu'après un retard plus ou moins long, fonction de leur propre inertie thermique et de celle du lanceur. Compte tenu de ces considérations, la plage de température à considérer, dans laquelle les propulseurs doivent présenter un fonctionnement normal est:-40°C + 100°C.

La limite haute qui suppose un vol prolongé à basse altitude et grande vitesse, n'est pas atteinte avec les avions actuels mais elle comporte une marge pour l'avenir.

Un autre type d'échauffement particulier à l'emport en tube est aussi à signaler: il est provoqué par des mouvements de convection de l'air dans la partie vide du tube située en avant de la tête de la roquette, lorsque celle-ci est en retrait de la section avant du tube. Cet échauffement est très rapide et très important. Il dépend de la position de la roquette dans le tube, de la vitesse de l'écoulement aérodynamique. Ce phénomène est très sensible sur les petits calibres mais n'intéresse pas les gros calibres de 100mm ou plus. Des températures de 200°C ont été mesurées en vol au niveau de la tête sur des roquettes de 68mm de calibre, à une vitesse de 530 Kt.

On se protège de ces phénomènes en obturant le tube à l'avant. La roquette doit alors traverser la protection au tir.

3.5. - Contraintes liées au stockage, et aux manipulations

Les propulseurs doivent supporter sans dommages les conditions d'environnement particulières au stockage et aux manipulations. Plus précisément, ils devront supporter:

- les variations de températures journalières et saisonnières pendant toute la durée de leur vie,
- les secousses et les vibrations de transport par camion, chemin de fer ou bateau,
- les chocs consécutifs aux manipulations en emballage pendant les chargements et déchargements,
- les chocs sur roquette nue consécutifs aux opérations de destockage et de préparation d'une mission,
- l'exposition à l'air salin.

Ils doivent pouvoir supporter, éventuellement avec dommages, mais sans mettre en cause la sécurité des chutes accidentelles toujours possibles en utilisation.

3.6. - Durée de vie

La durée ne doit pas être inférieure à 10 ans en climat tempéré. Au bout de cette période, les propulseurs doivent pouvoir encore fonctionner en toute sécurité.

4. - CONCLUSION - PERSPECTIVES D'AVENIR

Du fait des progrès des défenses anti-aériennes rapprochées des objectifs au sol, l'utilisation des roquettes classiques d'aviation comporte des risques accrus pour l'avion tireur, dans les conditions actuelles d'emploi.

La détermination de nouvelles conditions d'emploi, ou l'adjonction de dispositifs de guidage rustiques permettant le tir à plus grande distance, sont des solutions susceptibles de résoudre ce problème.

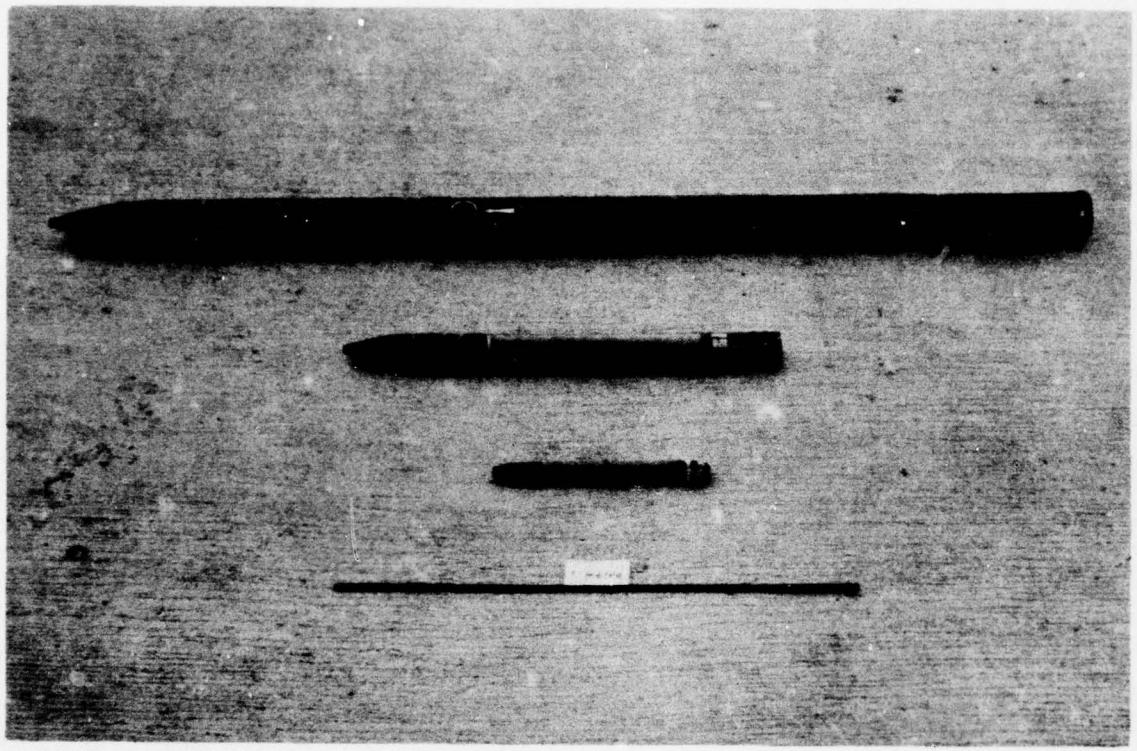

En arrière	roquette de 100 mm	masse : 30 kg	impulsion : 2400 daN.S	temps de combustion : 1,30
Au milieu	roquette de 68 mm	masse : 6,3 kg	impulsion : 310 daN.S	temps de combustion : 0,8
Devant	roquette de 37 mm	masse : 1 kg	impulsion : 45 daN.S	temps de combustion : 0,250

FIG.1 EXEMPLES DE ROQUETTES

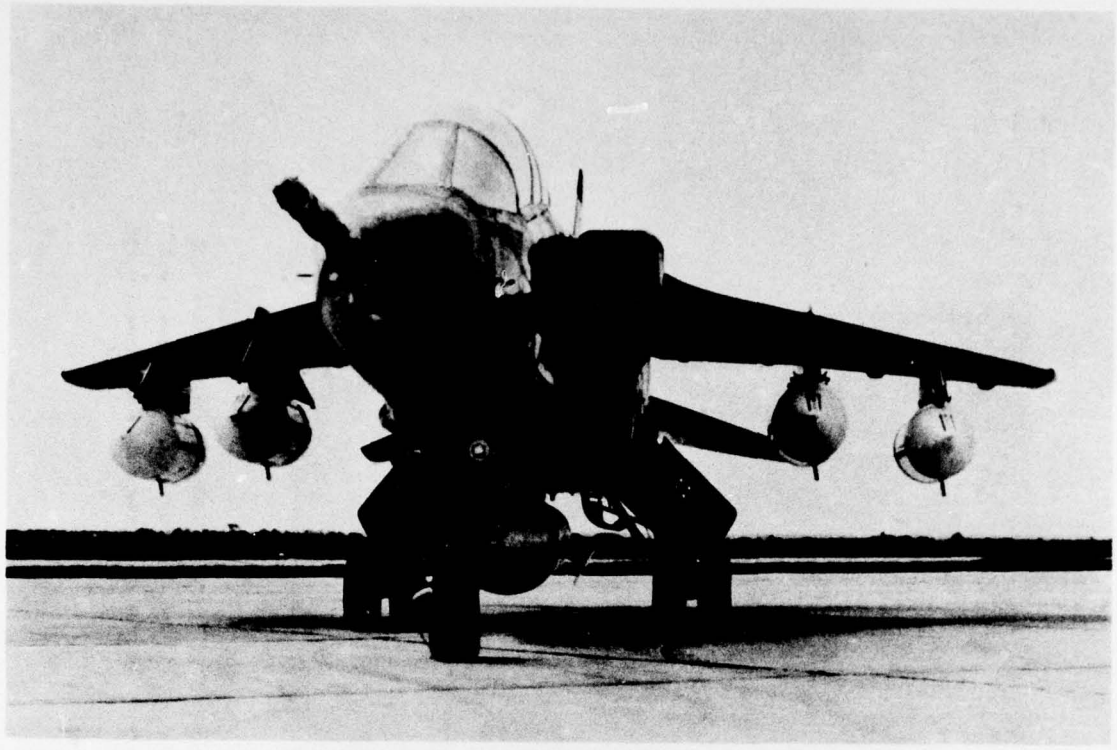

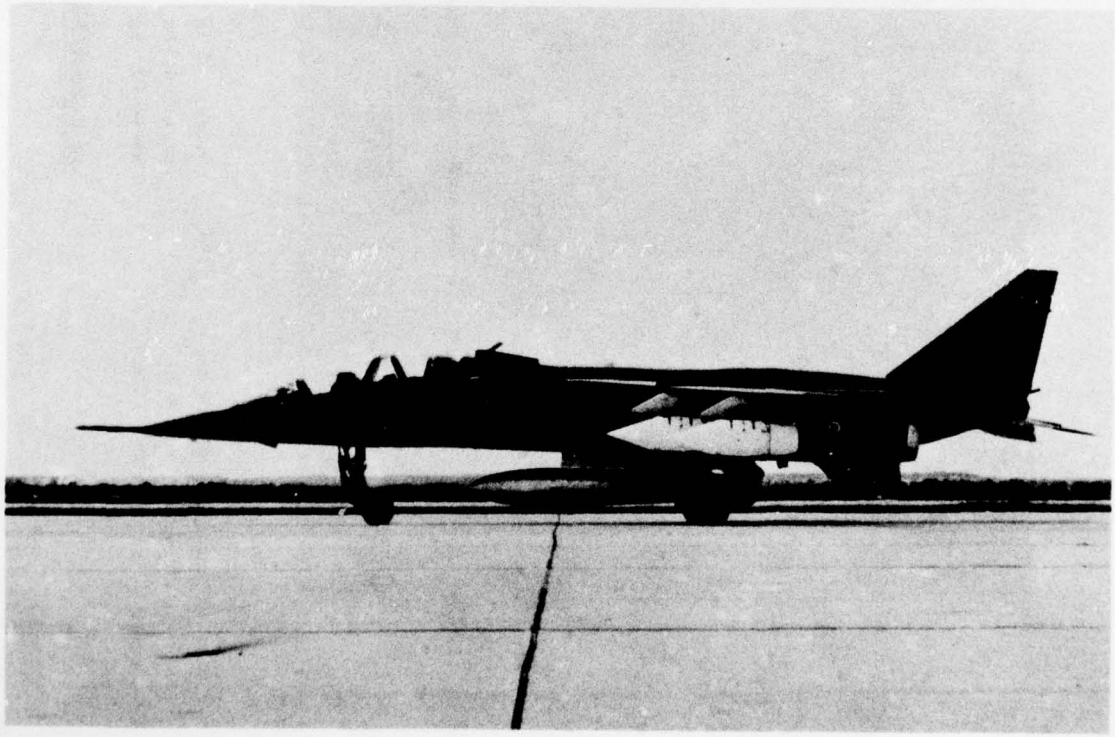

FIG.2 AVION JAGUAR EQUIPE DE 4 LANCE-ROQUETTES de 36 roquettes de 68 mm sous les points d'emport de voilure.

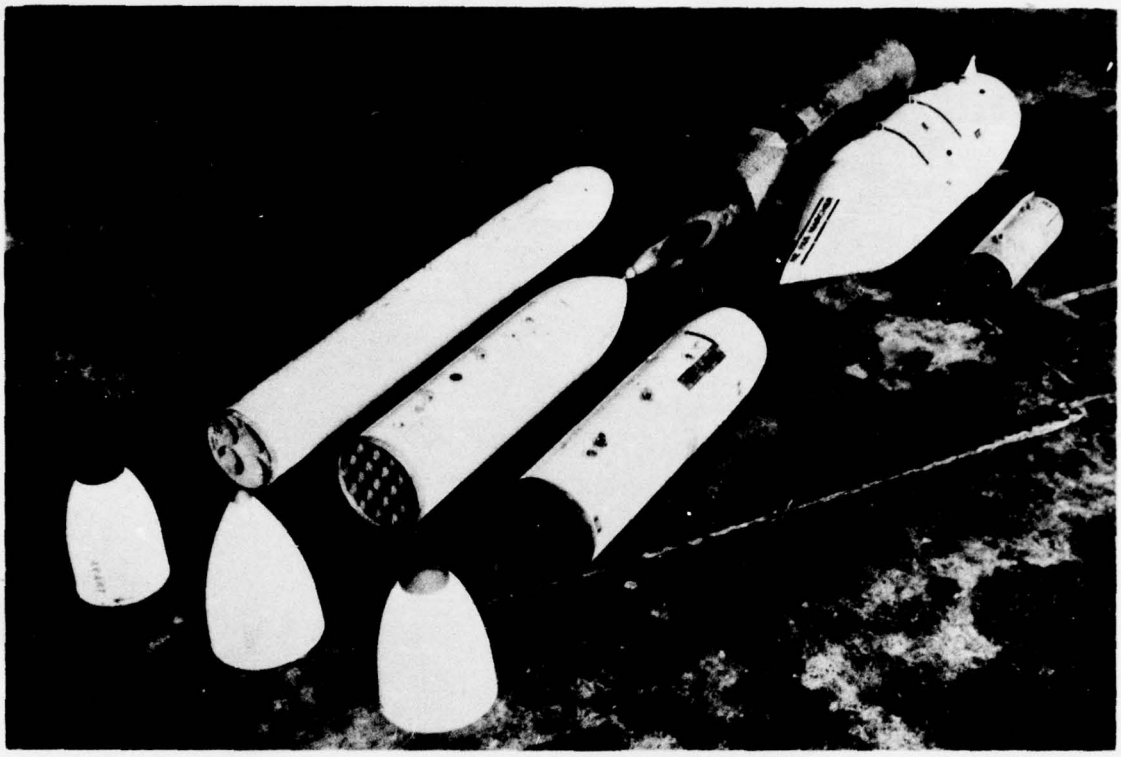

A l'arrière de gauche à droite : - lance-roquettes de 100 mm à 6 roquettes
- lance-roquettes de 68 mm à 36 roquettes
- lance-roquettes de 68 mm d'entraînement à 6 roquettes

A l'avant de gauche à droite : - lance-roquettes à cône friable (cône avant démonté)
lance-roquettes de 5" à 4 roquettes
lance-roquettes de 2,75" à 19 roquettes

FIG.3 EXEMPLES DE LANCE-ROQUETTES

SPECIFICATIONS DES SYSTEMES DE PROPULSION DES ROQUETTES ANTI-CHARS

par
Alain Fournier
Direction Technique des Armements Terrestres
Etablissement Technique de Bourges
Centre Technique Armes et Munitions
Carrefour de Zéro-Nord
Route de Guerry
18015 Bourges
France

RESUME

Les propulseurs d'accélération des futures roquettes anti-chars devront utiliser un propergol de pression de fonctionnement élevée avec un coefficient de température acceptable pour l'emploi tout temps, de vitesse de combustion aussi élevée que possible, de sensibilité à la combustion érosive diminuée par rapport à celle des propergols actuels.

Il est nécessaire dans les futurs programmes de mettre davantage l'accent sur les caractéristiques de discrétion vis à vis de l'ennemi et de gène pour le côté ami ainsi que sur les caractéristiques de fiabilité et de coût.

LISTE DES SYMBOLES UTILISES.

Cd : coefficient de débit du propulseur (dans la formule débit $\dot{m} = Cd.\ P.\ At$)
Isp : impulsion spécifique du propergol
L : longueur du tube de lancement
P : pression de fonctionnement
M : masse de propergol brûlé correspondant à la vitesse V
Mo : masse du projectile correspondant à la vitesse V
S : aire de la section droite intérieure disponible pour le chargement propulsif
T : durée de combustion
V : vitesse du projectile en fin de combustion
g : accélération de la pesanteur
l : longueur disponible pour le chargement propulsif
ln : logarithme népérien
β : rapport d'autoserrage (rapport de la surface de passage terminale du chargement Ap à la surface au col de tuyère At)
ρ : masse volumique du propergol

Nous nous limiterons dans cet exposé aux propulseurs d'accélération c'est à dire aux propulseurs comportant un seul étage de propulsion et à courte durée de combustion tels ceux utilisés dans les armes légères antichar du type roquette et associés à une tête militaire constituée en général par une charge creuse.

Ces propulseurs doivent en principe répondre aux critères suivants concernant :

- les performances :
  - . portée utile de combat
  - . efficacité terminale
  - . encombrement
  - . poids
- la fiabilité :
  - . probabilité de bon fonctionnement et en particulier d'allumage à un instant donné
  - . durée de vie minimale (conservation des performances initiales) au stockage
- la sécurité :
  - . sûreté de l'emploi
  - . discrétion vis à vis de l'ennemi
  - . absence de gêne pour l'entourage de l'utilisateur
- le coût :
  - . ensemble du système armes et munitions.

Nous examinerons successivement les contraintes imposées notamment au propergol par ces différents critères.

Pour ce qui concerne les performances :

La roquette est placée dans un tube de lancement de longueur L et un système de mise à feu déclenche le fonctionnement du propulseur. La roquette est accélérée dans le tube et le quitte avec une vitesse V. Il est généralement admis que la combustion du propulseur doit être terminée lorsque la roquette sort du tube afin que le tireur ne reçoive pas les jets de gaz du propulseur.

Il en résulte immédiatement une condition sur la durée de fonctionnement T du propulseur qui si si l'accélération est constante peut être représentée par la relation $T = \frac{2L}{V}$

Cette relation n'est qu'approchée lorsque l'accélération n'est pas constante mais elle traduit clairement dans tous les cas la façon dont varie la durée de combustion en fonction de la longueur du tube et de la vitesse de sortie.

Il est d'autre part bien connu qu'en l'absence de guidage, la probabilité d'atteinte est liée à la durée de trajet du projectile qui doit rester au dessous d'une certaine valeur.

La propulsion additionnelle sur trajectoire permet de réduire cette durée de trajet mais elle introduit surtout si le gain de vitesse est grand un facteur de sensibilité au vent latéral.

Il y aura donc toujours intérêt pour augmenter la portée utile de combat des roquettes antichars à augmenter la vitesse initiale ce qui conduit à rechercher la diminution de la durée de combustion du propulseur d'accélération puisque la longueur du tube ne peut croître indéfiniment.

Il faut donc rechercher simultanément une diminution de la durée de combustion des propulseurs et une augmentation de la vitesse des roquettes. Nous allons montrer que ces conditions se contrarient ce qui rend le problème très difficile et limite les progrès que l'on pourra faire pour ce qui concerne les propulseurs d'accélération par rapport aux réalisations actuelles telles que la roquette antichar française AC 89 modèle F1 dont la vitesse initiale est de 300 m/s environ.

Examinons le problème de la réduction de la durée de combustion.

Les vitesses de combustion des propergols dont on dispose actuellement en France sont limitées à des valeurs de l'ordre de 30 mm/s pour des pressions de 200 à 400 bars. Il existe en étude des propergols dotés de vitesse de combustion supérieure mais seuls sont évoqués ici les propergols homologués ayant des bonnes caractéristiques mécaniques et dont le coefficient de température est faible.

Il en résulte que les épaisseurs de propergols sont très faibles: 0,75 mm dans le cas du chargement propulsif de l'AC 89 qui brûle par les deux faces.

Ces chargements sont également caractérisés par une grande surface de combustion. Il est en effet nécessaire de générer de gros débits gazeux pour obtenir les poussées et les niveaux d'accélération requis.

Si l'on ajoute à ces caractéristiques les conditions sévères imposées par l'emploi comme munitions d'infanterie, (fonctionnement à haute et basse températures, chutes, vibrations, stockage de campagne etc...) ainsi que la condition nécessaire de tenue à une accélération de plusieurs milliers de g, on imagine aisément la difficulté du problème et les efforts d'ingéniosité déployés qui sont attestés par de nombreux brevets.

Il est d'autre part nécessaire de progresser dans la connaissance des mécanismes de combustion de ces chargements à courte durée de combustion. Dans ce type de chargement la phase de combustion en régime permanent est très brève, parfois, presqu'inexistante (roquettes antichar) et l'ensemble de la combustion est alors régi par les phases transitoires (allumage du chargement, vidage du propulseur). L'objectif est d'établir un modèle de combustion qui puisse permettre de prévoir les performances de ce type de propulseur en tenant compte des effets de combustion érosive et d'instationnarité de l'écoulement.

Il est donc peut être possible d'améliorer encore l'architecture des chargements propulsifs mais les réalisations actuelles présentent déjà à cet égard des performances satisfaisantes.

On peut penser cependant que la problème serait sérieusement simplifié s'il était possible de disposer de propergols à vitesse de combustion et propriétés mécaniques supérieures.

Augmentation de la vitesse initiale :

La vitesse V d'un projectile autopropulsé à élément non largable est donnée par la formule :

$$V = g.\ Isp.\ \ln\left(1 + \frac{M}{Mo}\right)$$

Il résulte immédiatement de cette formule que l'on pourra augmenter la vitesse en augmentant Isp ou M ou en réduisant Mo.

Le sens de variation indique donc les axes d'efforts. Il est souhaitable de diminuer la masse transportée c'est à dire alléger la tête militaire et le corps de propulseur. L'allègement de la tête militaire ne devant pas s'effectuer au détriment de son efficacité il est probable vu les progrès réalisés sur les blindages que les gains effectifs de masse seront peu significatifs.

Pour le propergol il est souhaitable d'augmenter l'Impulsion Spécifique et la masse du chargement propulsif. La première condition est évidente, la deuxième mérite d'être commentée.

On peut montrer en effet moyennant certaines hypothèses simplificatrices que la masse M de propergol peut être exprimée par la formule suivante :

$$M = \frac{\rho . l . S}{1 + \frac{2\beta . \rho}{Cd} . \frac{1}{P.T} . l}$$

A calibre donné, S est une fonction décroissante de la pression de fonctionnement.

De cette formule il est possible de déduire les résultats suivants : la masse de poudre décroît

avec la durée de combustion et augmente avec la pression de fonctionnement.

Pour un volume donné $l.S$ constant, la masse de poudre la plus forte est obtenue pour le minimum de longueur.

La masse de poudre augmente avec la masse volumique du propergol et lorsque β, donc la senbilité à la combustion érosive diminue.

L'augmentation de pression qui permet d'accroître la masse de poudre entraine évidemment un alourdissement de la masse de l'enveloppe donc un effet antagoniste. Il est vraisemblable que pour les petites roquettes antichars l'optimum de pression se situe à une valeur assez élevée comprise entre 500 et 1000 bars.

A titre d'exemple des calculs effectués sur l'AC 89 avec des hypothèse très simplifiées, à longueur de tube de lancement constante donc en maintenant le produit (VT) constant, donnent une pression optimale d'environ 800 bars et un gain de vitesse initiale d'environ 15% avec une augmentation de la densité de chargement d'environ 30% et un alourdissement du projectile de l'ordre de 20%.

En définitive les améliorations de performances des roquettes antichars indépendamment des progrès sur les têtes militaires sont conditionnées par des progrès sur les propergols portant sur :

- l'augmentation de l'impulsion spécifique.
- l'augmentation de la masse volumique.
- l'augmentation de la pression de fonctionnement (en restant dans un domaine de fonctionnement à toutes températures).
- l'augmentation de la vitesse de combustion.
- la diminution de la sensibilité à la combustion érosive (diminution du coefficient β acceptable).

Pour l'allégement des structures (corps de propulseur, tuyère, empennage...) donc de la masse transportée il est bien évident qu'il faille utiliser des matériaux à haute résistance spécifique (rapport de la limite élastique à la masse volumique). On peut penser, que vu les durées de combustion très courtes envisagées, la tenue à la flamme ne doit pas présenter de gros problèmes. Les matériaux composites filamentaires ainsi que des matériaux comme le titane peuvent, à cet égard, être très intéressants.

La fiabilité et la sécurité.

L'augmentation des performances des propergols conduira sans doute entre autres à l'emploi d'oxydants plus énergétiques, de produits de granulométrie plus fine, de nouveaux additifs. Dès lors il paraît évident que certains problèmes comme ceux liés à la fiabilité et à la sécurité du système d'arme se poseront avec davantage d'acuité tels :

- la compatibilité des éléments du propergol entre eux et avec les éléments constitutifs du propulseur, qui a des conséquences directes sur la durée de vie au stockage.

- l'aptitude du propergol à transiter de la déflagration à la détonation lors d'agressions telles que : l'incendie, les impacts de projectiles, les détonations proches... avec leurs conséquences sur la sureté d'emploi.

- la discrétion vis à vis de l'ennemi pour éviter le repérage du point de tir par les fumées, les flammes ou le bruit.

- la gène pour le tireur et les servants par le bruit, les effets de souffle, et leurs éventuelles conséquences thermiques, les projections arrières directes (débris du système d'allumage, particules de propergol imbrûlées) et indirectes (sable, cailloux soulevés du sol par le souffle du propulseur).

Le programme optimum correspond à un compromis entre les caractéristiques techniques, économiques et opérationnelles.

Afin de pouvoir faire ce choix en toute connaissance de cause il paraît souhaitable d'entreprendre des études complémentaires. Ces études devraient porter sur la génération des bruits et des flammes, les moyens de les réduire et la détermination des maximum admissibles.

De même il conviendrait d'examiner plus complètement les effets de souffle et de projection sur le tireur et sur l'environnement de la pièce.

L'objectif est d'établir des spécifications définissant les niveaux acceptables pour le tireur et son entourage de ces divers effets environnant des propulseurs, spécifications qui devraient être prises en compte par le bureau d'étude lors de la conception des propulseurs.

De telles études devraient permettre de définir les possibilité de tir dans des configurations particulières (tir en cave, devant un mur etc...) et le gabarit de sécurité arrière pour les tirs en terrain découvert.

Le coût :

Il semble évident que la satisfaction de ces différentes contraintes conduise à une majoration du prix du propulseur. Il est souhaitable cependant que cet aspect soit présent dans l'esprit des concepteurs lors du choix par exemple de matériaux nouveaux ou des procédés de mise en oeuvre.

En conclusion on peut dire pour ce qui concerne le propulseur d'accélération des futures roquettes antichars qu'il devra utiliser un propergol de pression de fonctionnement élevée (supérieure à 500 bars) avec un coefficient de température acceptable pour l'emploi tout temps, de vitesse de combustion aussi élevé que possible, de sensibilité à la combustion érosive diminuée par rapport à celle des propergols

actuels.

Il est nécessaire dans les futurs programmes de mettre davantage l'accent sur les caractéristiques de discrétion vis à vis de l'ennemi et de gène pour le côté ami - cette amélioration ne concernant pas seulement le propergol, mais l'ensemble du propulseur notamment les inhibiteurs de combustion et les protections thermiques - ainsi que sur les caractéristiques de fiabilité et de coût.

Il ne faut pas s'attendre cependant compte-tenu des contraintes énoncées plus haut à une augmentation considérable des vitesses de sortie de tube de lancement. Il sera donc nécessaire pour les grandes portées d'utiliser une propulsion additionnelle avec éventuellement une correction de la trajectoire.

DEVELOPMENT OF A SMALL SOLID PROPELLANT ROCKET MOTOR FOR FLEXIBLE RANGE REQUIREMENTS

by

Walter Helmut Diesinger
Dynamit Nobel AG, ES-FG
Waltherstrasse 80
D-5000 Köln 80
Germany

SUMMARY

The conventional light artillery rocket has the following drawbacks:

- The ratio of minimum to maximum range is about .6 and should be smaller.

- Near minimum range trajectories cause large longitudinal dispersions.

- The thrust program is far from optimum for maximum range.

These disadvantages may be avoided to some extent by a solid propellant rocket motor with two propulsive charges and two independent thrust periods of equal thrust levels. The charges are ignited in sequence by an electronic timing circuit at a predetermined time of delay for optimum results e. g. one of the following alternatives:

- maximum range,

- minimum range,

- favourable ballistic data at impact,

- high velocity trajectory for minimum dispersion.

The feasibility of such a rocket motor has been demonstrated by software, hardware and successful flight tests. Application of this concept to other missiles may be advantageous, too.

NOTATIONS

A	altitude
A_r	aerodynamic reference area
A_t	nozzle throat area
d	diameter of missile
D	aerodynamic drag
I_{tot}	total impulse
m_o	launching mass
m_b	burn out mass
m_p	propellant mass
M	Mach number
R	range
t	flight time
t_{tot}	total flight time
t_b	burning time of rocket engine
Δt	time delay between ignition of the first and the second charge of a dual impulse motor
T	thrust
$\bar{T}$	average thrust, thrust level
V	tangential velocity on flight path
$\bar{V}$	mean velocity
Θ_o	elevation of launcher
$\Theta_o(R_{max})$	Θ_o for R_{max}

The studies have been sponsored in part by the Ministry of Defence of the Federal Republic of Germany

appreviations:

DIM	dual impulse motor
LAR I	light artillery rocket (conventional), 1rst generation
DIM-LAR II	light artillery rocket, 2nd generation, with DIM propulsion

subscripts:

1	first thrust phase
2	second thrust phase
min	minimum value
max	maximum value

1. INTRODUCTION

Progress in solid propellant rocket technology during the last five years has been considerable. Methods for control of thrust vector and thrust program have been developed [1, 2, 3] in addition to new composite propellants and light-weight cases. This is true for space applications and for medium or large rockets for military use.

Since the expenses for the vehicle should be in reasonable relation to the expenses for the payload or the warhead most of this progress is not applicable to small solid propellant rockets for field use such as the light artillery rocket (LAR).

2. BALLISTIC PROPERTIES OF THE CONVENTIONAL LIGHT ARTILLERY ROCKET

As well known the range of the conventional light artillery rocket is only controlled by the elevation of the launcher. Thus, for each range only one elevation with one trajectory is available with typical dispersional deviations from the theoretical point of impact. Trajectories with elevations $\vartheta_o > \vartheta_o(R_{max})$ are excluded because of the unacceptable flight times t_{tot} and dispersions.

In order to minimize the dispersion due to cross wind in the initial phase of flight a light artillery rocket engine is designed to deliver a comparatively high thrust during a short action time causing for instance a medium acceleration of 450 m/s² (≈ 45 g's) during two seconds of burning time t_b.

These design characteristics effect the ballistic properties of the light artillery rocket. Figure 1 shows a set of trajectories for the light artillery rocket with different elevations ϑ_o.

The major observations from this figure are:

i) The ratio of minimum to maximum range is about $R_{min}/R_{max} = .6$

ii) Because of wind, gusts and other atmospheric disturbances in addition to statistical deviations of the missile data all probable trajectories for a given elevation are covered by a cone of dispersion. Thus, large longitudinal dispersions for small ranges R are to be expected.

The next figure (fig. 2) shows the aerodynamic drag D and the velocity V on the flight path vs flight time t for the maximum range trajectory.

The figure demonstrates that the discharge of the whole total impulse

$$I_{tot} = \int_0^{t_{tot}} T(t)dt$$

during the initial few seconds after ignition effects large velocity reduction due to aerodynamic drag D. Thus, the maximum range R_{max} is considerably inferior to the potential maximum range $R_{max}(I_{tot})$ which could be realized by a more "economic" velocity distribution over the flight path or the flight time t_{tot}.

Moreover, the comparatively high maximum velocity $V(t_b)$ or Mach number $M(t_b)$ requires a corresponding large fin area because of stability limits. This means high dependency to cross wind in the initial thrust phase causing a comparatively large transversal dispersion.

At small ranges high speed impact is inevitable. This limits e. g. the application of secondary warheads.

3. MILITARY REQUIREMENT

The military requirement for the second generation of the light artillery rocket (LAR II) can be concisely summarized as follows:

i) Use of existing launchers and packages. This means that the thrust to weight ratio and the dimensions of the existing LAR I must not be exceeded.

ii) The rocket exhaust gases should be smokeless, without toxic agents and without an electrolyte such as hydrogen chloride. In any case this is necessary because of the operators and the proper function of the incorporated electronic circuits of the missile warhead.

Thus, at least in the first thrust phase double base propellants instead of higher performance composites should be used.

iii) The light artillery rocket LAR II must have a maximum range of at least $R_{max} = 20$ km with a minimum range of $R_{min} = 4$ km. A range of $R_{max} = 25$ km should be aimed, the minimum range being $R_{min} \geq 5$ km, that is to say a ratio $R_{min}/R_{max} \simeq .2$.

4. FEASIBILITY AND COST EFFECTIVENESS

The conventional German Light Artillery Rocket LAR I has a maximum range of $R_{max} \simeq 14.2$ km. The new missile must exceed this range by 40 - 80 % within the geometric and volume constraints given by the LAR I.

This challenge can be more or less met by several concepts such as (fig. 3):

4.1 A conventional concept with a single chamber solid propellant rocket engine as applied to the LAR I, but using a high performance cast composite propellant together with a suitable cast double base propellant for the initial thrust phase. Thus, the exhaust gases in the environment of the launcher are smokeless and non-toxic.

However, this concept has a lot of disadvantages, e. g.:

- unknown influence of the electrolyte during composite burning,
- the lack of information upon the life time of two different types of propellants cast one into the other,
- problems in meeting the minimum range requirement by one of the following measures:

  i) use of an aerodynamic brake, which needs additonal structure and may cause unacceptable dispersion due to atmospheric disturbances because such a brake works like a highspeed parachute,

  ii) use of a device to cut-off thrust before regular burn out time. This may be achieved by extinguishment of the propellant or by thrust compensation. Both methods require highly developed additional structures and a special electronic timing circuit since the longitudinal dispersion is very sensitive to the total impulse I_{tot} delivered. This means comparatively high production and development costs and a decay in maximum range.

  iii) use of a gasdynamic brake, which does not need the timing circuit mentioned above. Such a device diminishes the specific impulse, that is to say the thrust level, by turning off an amount of the exhaust gases from the axial direction. This method also requires additonal structure. Another consequence is a comparatively low axial velocity at the end of the launcher favouring the cross-wind influences on dispersion.

All these disadvantages prevented us from developing a conventional concept with additional devices to meet military requirements.

4.2 Figure 4 shows a concept with two solid propellant rocket engines, a booster for launching and velocity build up and a sustainer for economic velocity distribution on the flight path.

Minimum range requirement at small elevation is met because the sustainer cannot deliver its full total impulse I_{tot}. The missile is in the target before the sustainer's end of burning time.

For maximum range this concept is the best if the thrust program only is considered without regard to the additonal structure raising total mass of the missile at ignition and diminishing the usable volume for the propellant. System analysis for light artillery rockets has revealed that these drawbacks in cost and structure cannot be compensated by a better thrust program.

4.3 Keeping this in mind we looked for a concept characterized by the simplicity, necessary for small rockets, together with a compromise in the thrust program. The result of our investigations is our DIM concept [4]. DIM is the appreviation for Dual Impulse Motor, that is a rocket engine with two action phases of equal thrust levels.

5. DIM-LAR II CONCEPT

5.1 MODE OF ACTION

Figure 5 reveals that the DIM concept differs from a conventional solid propellant rocket engine by its two combustion chambers each incorporating a solid propellant charge. The igniter for the rear charge is located in the nozzle throat and is jettisoned after ignition by the rising pressure in the rear combustion chamber.

During the first thrust phase the second charge is prevented from burning by a separating closure which opens only when the second thrust phase is initiated by a timing device at a predetermined time Δt of delay. During the second thrust phase the rear combustion chamber acts as a blast-tube.

With this concept a thrust program as indicated in figure 5 can be realized with arbitrary ignition time delay $\Delta t > t_{b1}$ for the second charge.

Within the internal ballistic constraints given by the fixed nozzle throat area A_t and the propellant properties the thrust levels $\bar{T}_1$ and $\bar{T}_2$, the burning times t_{b1} and t_{b2} and the total impulse ratio I_{tot1}/I_{tot2} of the grains may differ and be optimized.

5.2 COMPONENTS

In comparison to conventional solid propellant rocket engines using end or radial burning grains the DIM engine needs the following additional or specially designed components:

i) timing device for the ignition of the second charge (electronic, mechanical or pyrotechnic),

ii) rear combustion chamber acting as blast-tube during the second thrust phase,

iii) closure separating both chambers during the first thrust phase which converts to a sufficiently large orifice at the beginning of the second thrust phase.

5.3 BALLISTIC PROPERTIES

Let us return to figure 2 and exchange the conventional solid propellant rocket engine by a DIM engine where the mass ratio of both charges is $m_{p1}/m_{p2} = 1$, that is to say both charges are equal in mass.

In figure 6 aerodynamic drag D and velocity V on the flight path vs time t are plotted for a maximum range trajectory and compared with the conventional light artillery rocket. The maximum values of aerodynamic drag D_{max} and Mach number M_{max} are inferior to these of the conventional light artillery rocket.

This means that

i) the fins of the DIM missile may be comparatively small with little cross-wind influence in the initial flight phase,

ii) the more "economic" velocity distribution on the flight path will result in an elevated maximum range R_{max} in comparison to the conventional light artillery rocket.

This can be readily seen from figure 7 where the elevation θ_o vs range R is plotted for several values of ignition delay time Δt. The dotted line is for $\Delta t = t_{b1}$, that is to say for the conventional light artillery rocket, since both thrust phases are merged into one.

The following most important features of our DIM concept can be derived from figure 7:

i) Compared with the conventional light artillery rocket the maximum range R_{max} is extended and the minimum range R_{min} diminished, thus easily meeting the flexible range requirement. In the special case presented the ratio of minimum to maximum range is about R_{min}/R_{max} = 4.55 km/25.76 km = .18 instead of 12.88 km/23.53 km = .55 for the conventional design.

ii) The maximum range is extended by about 9 %.

iii) The minimum range is reduced by about 65 %.

iv) For range control two parameters are available, elevation θ_o and ignition time delay Δt of the second charge. For any range R between R_{min} and R_{max} an infinite number of combinations of elevation θ_o and time delay Δt is optional. Thus, the optimum trajectory may be chosen, characterized by one of the following or other conditions (fig. 8):

- minimum flight time,

- minimum dispersion,

- special ballistic data at impact,

- flight over an obstacle.

5.4 INFLUENCE OF DESIGN DATA

To get exact data for preliminary design of DIM engines systematic ballistic investigations have been carried out including variations in missile diameter, launching weight, aerodynamic cleanness and mass ratio m_{p1}/m_{p2} of the propellant charges.

All results, which may be interesting for design, cannot be discussed in this paper. The investigations showed, that the advantages of the DIM concept compared with a conventional radial burning solid propellant engine, increase with the potential influence of aerodynamic drag D, that is to say with diminishing ratio of burn out mass to aerodynamic reference area m_b/A_r and diminishing aerodynamic cleanness (fig. 9).

The limits of minimum and maximum range of a DIM missile shown in figure 9 have been computed for $m_{p1}/m_{p2} = 1$. Variation of this ratio shifts these limits, that is to say m_{p1}/m_{p2} may be optimized for maximum range R_{max} or other requirements.

The influence on dispersion of deviations from the design data has been investigated, too. It has been shown, that compared with a conventional LAR II a DIM-LAR II is less sensitive to deviations in specific impulse and aerodynamic cleanness but more dependent on deviations in launching mass m_0, but adjusting this mass is not very difficult. Deviations in delay time Δt are no problem, too. In the most unfavourable case a ratio $\Delta R/\Delta t < 1$ m/ms has been determined for a DIM-LAR II.

Moreover, the atmospheric influences on dispersion of a DIM-LAR II are comparatively small, since

i) the mean velocity $\bar{V}$ on the flight path is higher,

ii) the flight path and the flight time t_{tot} are shorter (for medium ranges)

and

iii) the fin area is smaller

in comparison to the conventional LAR II.

6. STATE OF ART

A German Government sponsored technology and development program carried out at Dynamit Nobel Company in 1973 and 1974 revealed that a DIM solid propellant rocket engine is feasible with conventional technology and limited development cost and risk. Three experimental DIM-LAR missiles were flown successfully on 21 May 1975.

Our know-how in software and hardware in this special field of solid propellant rocket technology would enable us to develop a DIM Light Artillery Rocket which meets all military requirements perfectly. This could be done within a comparatively short time and with moderate funds. The new components mentioned above, which are electronic timer, rear combustion chamber with thermal insulation and the closure dividing both chambers, are hardware and need no additional development efforts. In figure 10 the components of a DIM-LAR II are shown.

7. CONCLUSION

The performance of the DIM-LAR II light artillery rocket agrees with the military requirements and can be easily fitted to new or other requirements.

The ballistic data of the DIM-LAR II missile for a given range R can be chosen for best efficiency since two parameters of range control are available.

The over-all dispersion of a DIM-LAR II due to internal or external deviations is small compared with a conventional LAR II.

The new components required for a DIM-LAR II as compared with the conventional design do not need additional development efforts or unusual production devices. The other components such as propellant and hardware are standard. All present launchers can be used without any modification. The production costs are moderate in comparison with the elevated performance.

8. REFERENCES

1. Zarin, N. A.: Controlling the thrust of rocket engines. Space World H-5-89 (1971), No. 5, pp. 30 - 34.

2. Mc Donald, A. J.: On-off and acceleration control of solid rockets. SAE Paper 710767 (1971).

3. Diesinger, W. H.: Methods for approximate optimum thrust programming of solid propellant rockets for spacecraft applications. ESA TT-186, Technical Translation, Sept. 1975.

4. Diesinger, W. H.: Solid propellant rocket motor. US Patent 3,888,079 (June 10, 1975).

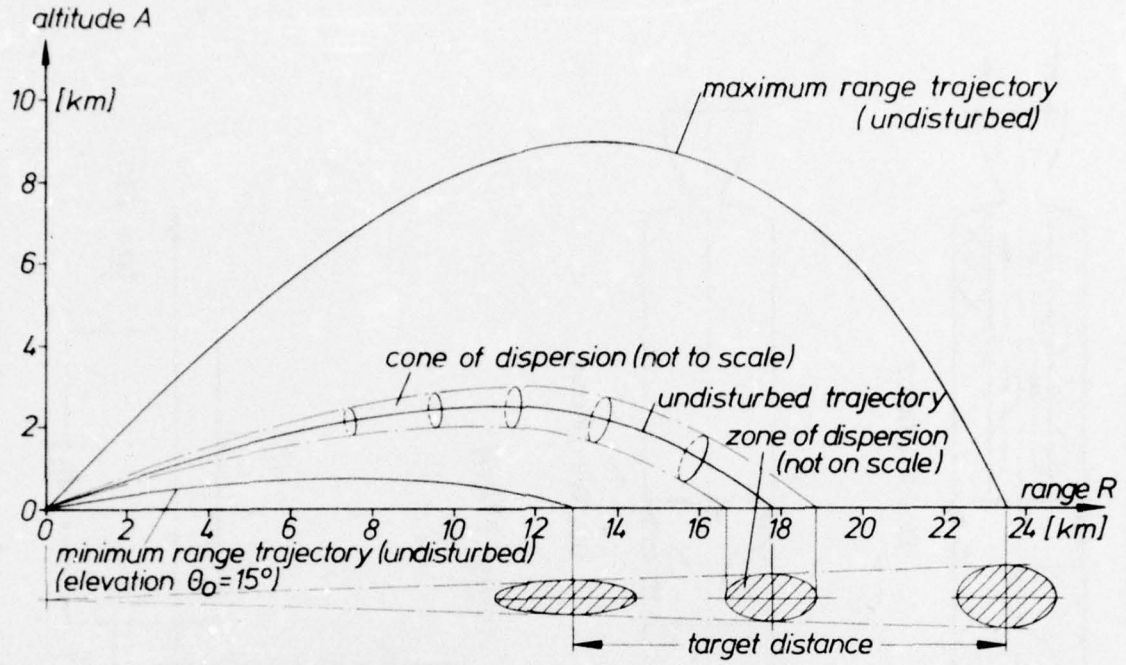

Fig. 1 Trajectories of a conventional light artillery rocket.

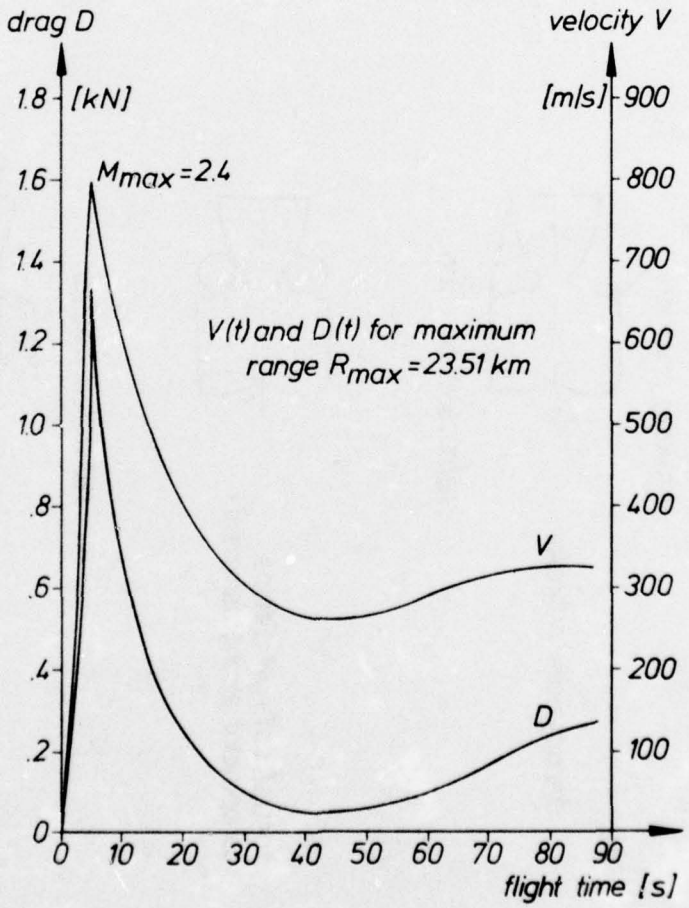

Fig. 2 Aerodynamic drag D and velocity V on the flight path for maximum range R_{max} vs flight time t ; conventional light artillery rocket.

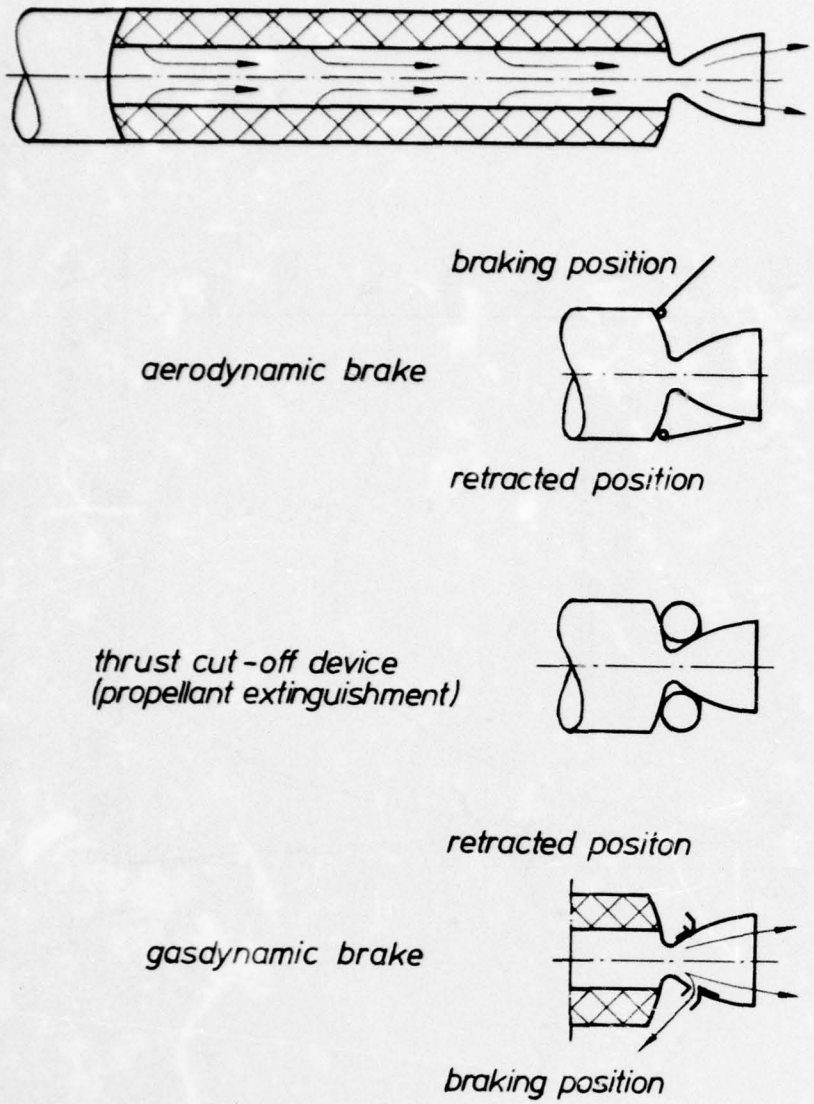

Fig.3 Conventional concept to meet military range requirements.

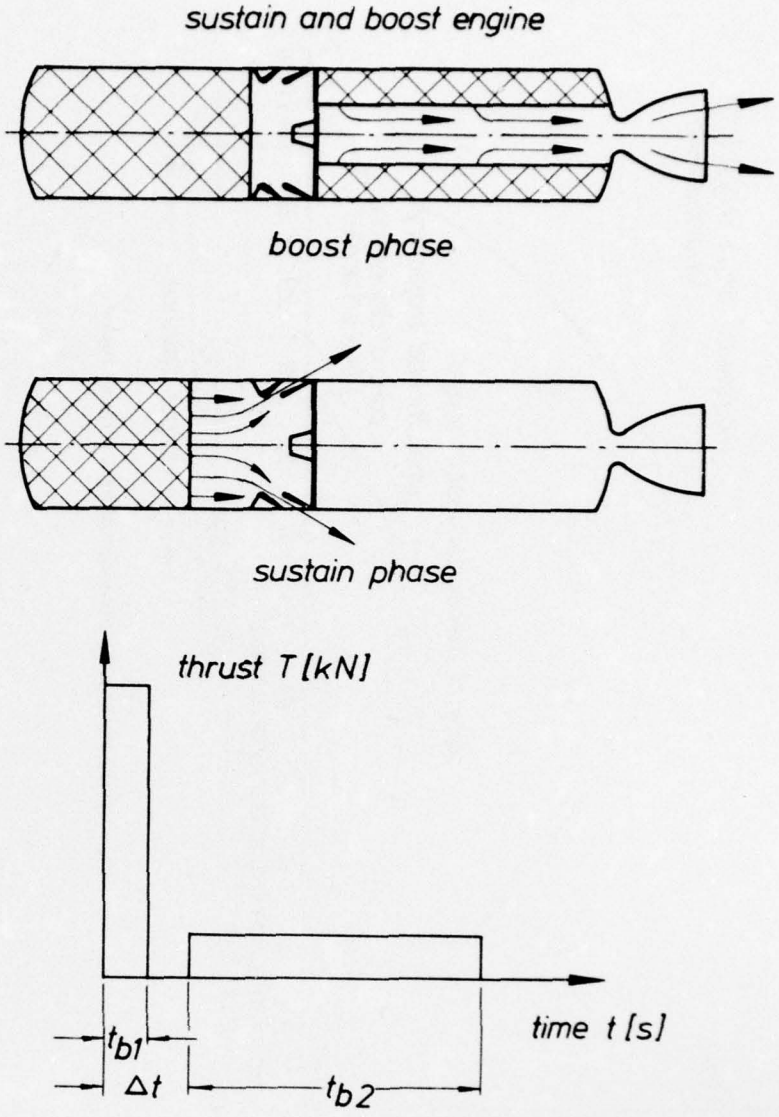

Fig.4 Application of two separate engines for boost and sustain phases.

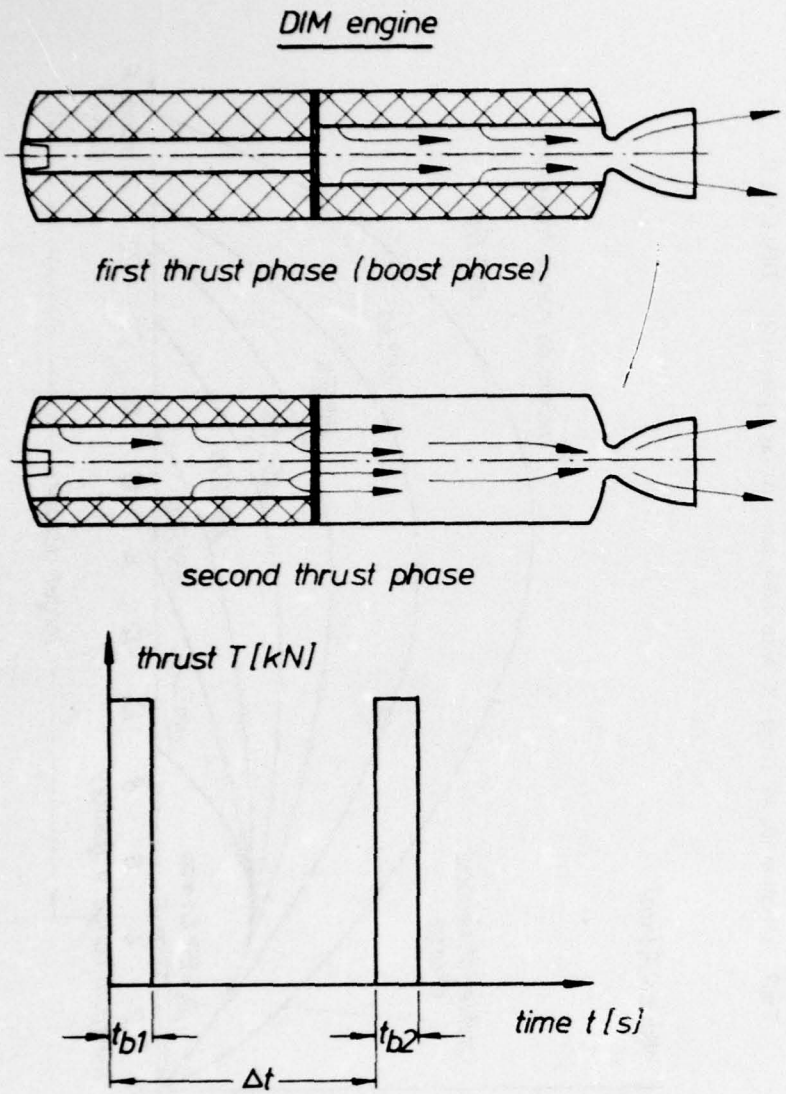

Fig.5 Solid propellant rocket engine with two separate action phases of equal thrust levels (DIM engine).

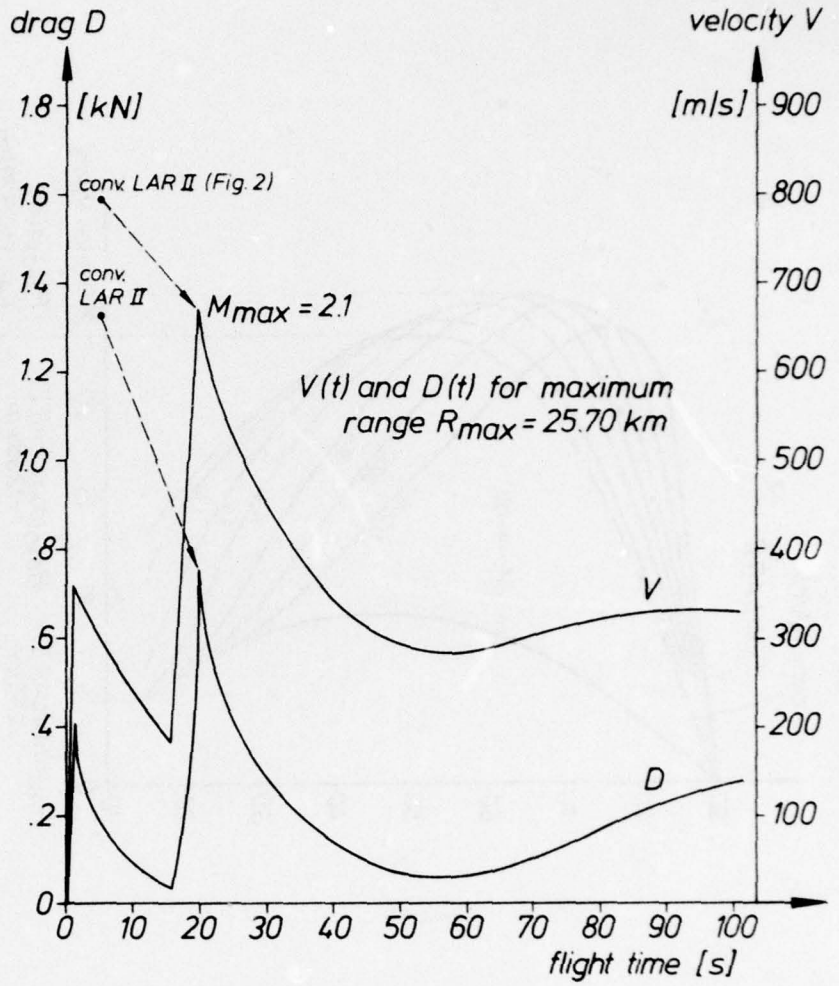

Fig.6 Aerodynamic drag D and velocity V on the flight path for maximum range R_{max} vs flight time t ; DIM light artillery rocket (DIM-LAR II).

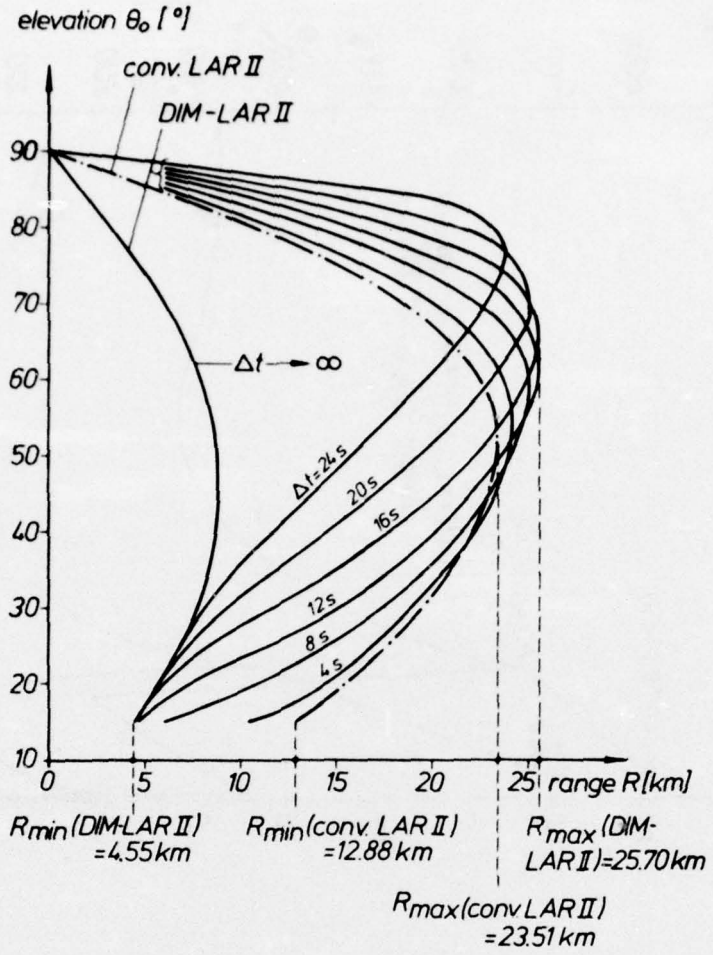

Fig.7 Elevation θ_o vs range R with delay time Δt as a parameter ; DIM-LAR II.

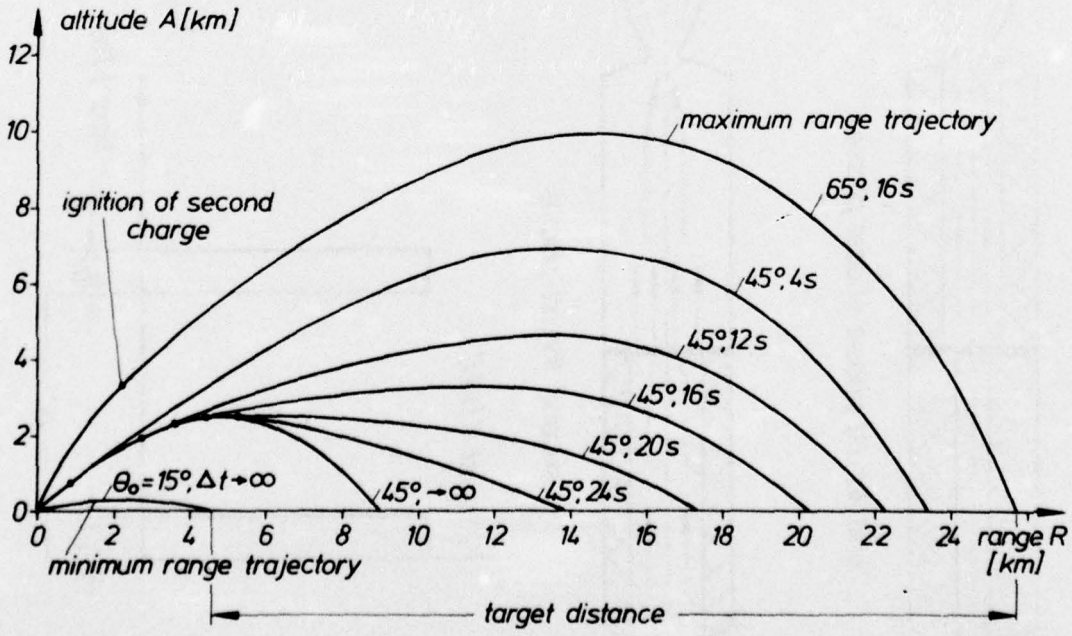

Fig.8 Trajectories of the DIM light artillery rocket (DIM-LAR II).

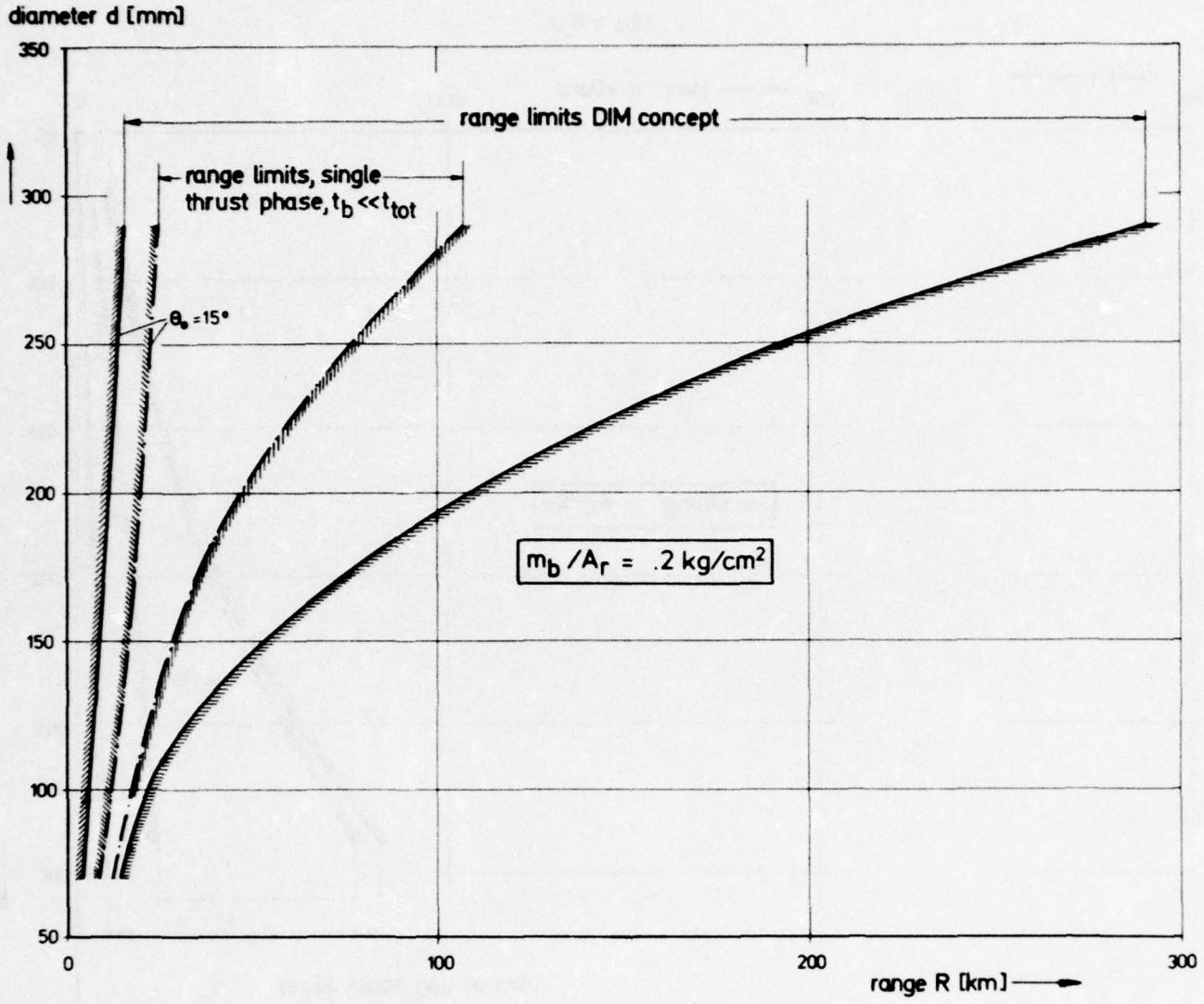

Fig.9 Minimum and maximum range R_{min} and R_{max} vs diameter d for conventional and DIM artillery rockets; (a) m_b/A_r = ·2 kg/cm² and (b) m_b/A_r = ·5 kg/cm².

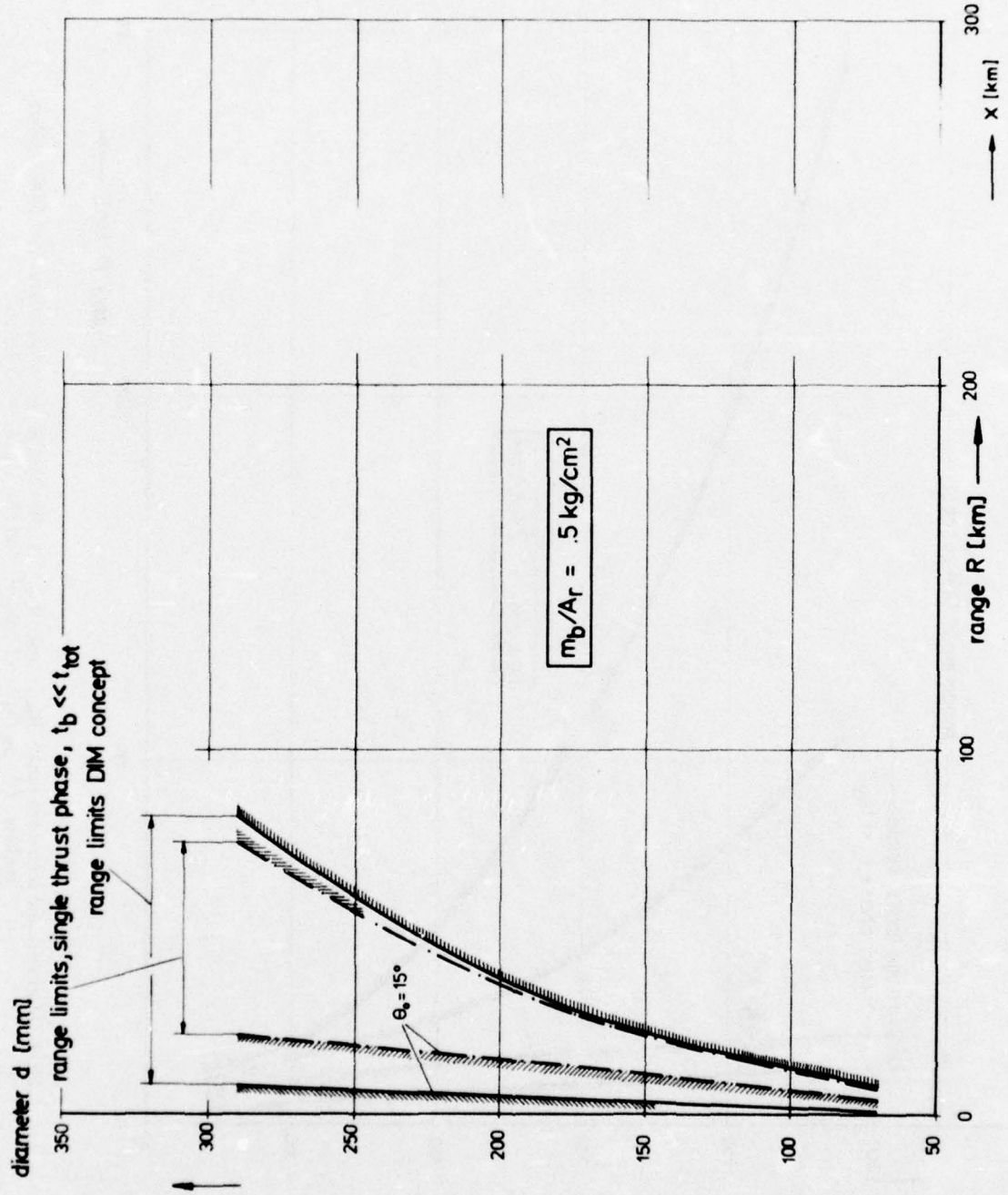
diameter d [mm]
range limits, single thrust phase, $t_b << t_{tot}$
range limits DIM concept
m_b/A_r = .5 kg/cm²
θ_e = 15°
range R [km]
x [km]
350
300
250
200
150
100
50
0
100
200
300

Figure 9(b)

Fig.10 Components of the DIM light artillery rocket (DIM-LAR II).

OPTIMIZATION OF THE PROPULSION AND BALLISTICS OF AN ANTI-TANK HAND WEAPON UTILIZING THE GLIDING EFFECT

by

Lothar STIKLORUS

MESSERSCHMITT-BÖLKOW-BLOHM GMBH
Unternehmensbereich Apparate
Wehrtechnik
8000 München 80
Postfach 801149

SUMMARY

A gliding projectile has several crucial advantages in comparison to a ballistic one. With equal starting velocity, the flight path flattens. This gives the gliding projectile a higher hit probability in the vertical plane. With equal flight path curvature, its starting velocity would be essentially lower, which would allow a lower weapon weight. In order to eliminate the cross-wind error and to keep the flight time short, a sustainer could be employed. Gliding effect and sustainer, however, also provide new errors. The purpose of this report is to give a survey of aerodynamic and mass dynamical means to reduce these errors. The increase of stability reduces certain errors. It does not affect, however, error sources such as cross wind and initial roll.

1. INTRODUCTION

The anti-tank hand weapon is basically a tube from which the projectile is launched. In order to eliminate the recoil, a body with mass equal to the projectile is ejected to the rear (fig. 1). It disintegrates rapidly in air. Essentially there are three requirements for this weapon:

- It should be as light in weight as possible
- It should be easy to operate by the gunner
- It should exhibit a high hit probability.

With increasing operational range it becomes more and more difficult to meet these requirements. Provided that over the entire operational range the tank height is not to be exceeded, and a distance measurement with subsequent launch angle adjustment is to be avoided, the flight path must flatten with increasing operational range. For a ballistic projectile this would involve a higher starting velocity and, in consequence, a greater weight for the launch tube to meet the increasing strength requirements.

In order to extend the flight path of the projectile without increasing the starting velocity and the weapon weight, the gravitation, for instance, can be compensated for entirely or in part by a lift force. Deceleration during flight may be counterbalanced by a sustainer. For purposes of comparison, fig. 2 shows the flight paths in the vertical plane of a ballistic projectile, of a gliding projectile without and of a gliding projectile with sustainer. A scale distortion was chosen for better display of the flight paths, i.e. vertical distances are presented in larger scale

than horizontal distances. Gliding effect and sustainer are new error sources which cast doubt on the success of these devices. However, promising possibilities exist for reducing these and other disturbances. All these means are of a design nature and in some way alter the aerodynamics or mass dynamics of the projectile. In consequence, different new projectile versions were designed. Their flight paths were calculated using a three-dimensional flight path program. This was based on the most important disturbances, choosing magnitudes which appear realistic.

2. GLIDING PROJECTILE AND VARIANTS

The basic version of the projectile is shown in fig. 3. The projectile data are presented in table I. A pair of fins at the nose produces the lift. This provides a positive pitching moment, which is compensated for by an equally large, contrarily acting one of the aft body. This is accompanied by the build-up of a positive angle of attack which produces the lift to counterbalance gravitation (fig. 4).

In order to reduce the starting velocity and to compensate for cross wind the projectile was equipped with a sustainer (version B in fig. 5). The keel fin of version C1 causes the projectile to turn with lift in the case of cross wind and initial yaw, such that the lateral lift component counteracts the lateral displacement. It turned out that the initial yaw was overcompensated in case of version C1. Therefore version C2 was provided with a keel fin, which can be dropped. A release of this fin at an appropriate instant permits compensation of cross wind as well as of initial yaw. Version D carries an upper fin. This is intended to diminish initial roll. However, an adverse effect as far as cross wind and yaw are concerned cannot be avoided. Version E features a mass rotor which can only turn about its axis of rotational symmetry, which points in y-direction. The gyro effect is intended to transfer the rolling motion of the projectile into a less critical pitching or yawing motion. In version F (fig. 6) the part of the projectile carrying the mass rotor was designed as a rotary nose. This reduces the angular momentum and the mass of the rotor. In version G the rotor is provided with a gimbal. In this way it has 3 degrees of freedom with regard to the projectile. Version H has a rotary nose with a roll-stabilizing fin to diminish roll. In addition there is a sustainer for cross-wind compensation. Version I is similar to version H except for a rotor with gimbal (as in version G) instead of the roll-stabilizing fin at the rotary nose.

3. FLIGHT PATH SIMULATION INCLUDING DISTURBANCE PARAMETERS

Using a three-dimensional flight path program based on the complete differential equations of motion with aerodynamic coefficients obtained in the wind tunnel, flight paths were computed with an IBM computer 370/165. Each version was subjected to each of the mentioned disturbances. The disturbance parameters with their standard deviations are given in table II. For initial roll two values were chosen. This is done to compensate for the great uncertainties attached to the roll parameter, which has a strong influence on the deviations. The chosen parameters for initial roll also take roll errors during flight into consideration. The paths of the versions without a sustainer were computed with a starting velocity of V_i = 200 m/s. In the case of the versions with a sustainer the starting velocity V_i = 172 m/s was chosen to obtain approximately the same flight time (1.73 s). In case of a decrease of starting velocity to 150 m/s the condition of equal flight time can no longer be satisfied, as the

deviations become too large. A decrease of sustainer momentum caused an increase of flight time to 1.96 s. A change of mass and moment of inertia data due to the addition of a sustainer was not taken into account in the flight path computations. This is permitted, as the flight path is rather insensitive to changes of mass and moments of inertia. Furthermore, a very low momentum (approx. 40 Ns) is required for propulsion.

4. RESULTS

In order to evaluate the performance of the various versions of the projectile, deviations at a horizontal distance of 300 m are examined. Fig.7 shows the pattern on target for the basic projectile (version A), i.e. the dispersion of hits due to various disturbances on a square target with an area corresponding to a circular disk of 2 m in diameter. The deviations apply for the 1σ values of the disturbances, that is, in 68 % of the cases the disturbance results in a deviation as shown in the figure, or in a smaller value. The various disturbances and their effect on the different versions of the projectile are summarized in figs. 9 to 11. Table III gives an evaluation of the various variants in comparison with the original version with regard to their effect on the disturbance parameters. At a first glance it is seen that the cross wind and initial roll cause the greatest deviations, provided the numerical value of the initial roll is a realistic one. For this reason, main attention is paid to the influence of these two disturbance parameters when judging the remaining versions.

As can be seen from the computer results, the following design features help to compensate the two most important disturbances best:

a) cross-wind effects may be diminished by
   - a sustainer
   - a droppable keel fin, and
   - a mass rotor with 1 degree of freedom;

b) initial roll effects may be diminished by
   - a mass rotor in a rotary nose with 3 degrees of freedom, and
   - a roll-stabilizing fin on a rotary nose.

Each design feature by itself did not show effective compensation of both cross wind and initial roll. Therefore combinations of a and b were investigated. The addition of a sustainer to a mass rotor in a rotary nose with 3 degrees of freedom proved to be the most effective combination (fig. 8). Fig. 12 indicates that version I is particularly advantageous compared to the others when the initial roll disturbance amounts to 10 °/s or more. When the latter is equal to or less than 3 1/3 °/s, the versions E, B and C2 are also suitable. These three versions provide compensation of cross wind by mass rotor, sustainer or dropping the keel fin, respectively. Of these versions, B has the advantage of a lower starting velocity (172 m/s as against 200 m/s). Fig. 13 illustrates the influence of the starting velocity on the overall mass of the weapon. For instance, the weapon mass decreases by about 1 kg when the starting velocity can be reduced from 240 to 160 m/s.

Versions C1, D, F and H are not suitable at all. With version C1 a fixed keel fin designed for cross-wind compensation will overcompensate the initial yaw to an unacceptable degree. The upper fin of version D slightly reduces roll. With D, however, the effect of the remaining disturbances, particularly of initial yaw and of the lateral aerodynamic malalignment, is increased. In the case of version F which carries

a rotor in a rotary nose, extreme roll of the nose is induced by cross wind via yawing. The lift obtains a large lateral component causing a large lateral deviation. The gyro exerts no stabilizing effect as it has merely 2 degrees of freedom. At launch the roll-stabilizing fin attached to the rotary nose of version H is turned sideways due to the cross wind and especially to initial yaw. In this way a lateral lift component is produced. Version B using a sustainer shows increasing deviation with decreasing starting velocity. This is mainly caused by the longer flight time, as the effect of certain disturbances (roll, thrust error) grows with flight duration. The longer flight time has an additional disadvantage when combating moving targets. These can cover a considerable distance from the moment the projectile is launched.

Stability has the following effect on the disturbances: greater stability diminishes the influence of disturbing moments caused by aerodynamic and thrust malalignment. Pitch and yaw disturbance are favourably affected as well. The deviations in case of initial pitch are much larger than with initial yaw, as the pitch stability is lower than the yaw stability. The low pitch stability originates from the destabilizing trimming fins. To the most important disturbances such as cross wind and roll, however, the stability effects are almost negligible.

5. CONCLUSION

In order to compensate gravitational forces which influence the flight path curvature unfavorably, a projectile was designed with a pair of fins at the nose. In this way, in addition to gravitational force compensation a trimming of the projectile is achieved. New disturbances arise, mainly initial roll. Means were investigated to keep the influence of the disturbances to a minimum. Special attention was paid to the most serious sources of error, which are cross wind and initial roll. No individual means by itself could be found to reduce both these disturbances. A sustainer was considered to be particularly suitable with regard to cross wind. It also permits a lower starting velocity and thus a reduction in weight of the weapon. Further devices for cross-wind compensation are a droppable fin and a mass rotor. A gyro-stabilized nose is advisable for diminishing initial roll. A combination of sustainer and gyro-stabilized nose is suitable in the event of large initial roll (10 ^{o}/s or more). In case of slight initial roll equal to or less than 3 1/3 ^{o}/s, one of the three alternatives for cross-wind compensation suffices. Further investigations by the MBB company will concentrate mainly on the feasibility of a gyro-stabilized nose with respect to large accelerations (up to 20,000 g) during launch.

Table I

Projectile Data

Mass m	1 kg
Moments of inertia about the transverse axis I_y, I_z	0.0136 kgm^2
Moment of inertia about the longitudinal axis I_x	0.002463 kgm^2
Overall length l	0.415 m
Largest diameter d	0.0674 m
Largest cross-sectional area S	0.003568 m^2
Position of centre of gravity $x_{c.g.}$ (from nose)	0.205 m
Diameter of pin d_p	0.018 m
Chord,of trimming fins c_{ft}	0.0125 m
Span of trimming fins s_{ft}	0.043 m
Angle of incidence ot trimming fins η_{ft}	3^o

Table II

Standard Deviations of the Disturbances (1σ -Values)

Cross wind v_w	3.9 m/s
Initial roll p_i	10 ^{o}/s or 3 1/3 ^{o}/s
Initial yaw r_i	20 ^{o}/s
Lateral aerodynamic malalignment $C_{n_{am}}$	0.001
Lateral thrust malalignment ε_y	1 ^{o}/oo
Lateral aiming error δ_y	3 1/3 cm/300 m
Roll attitude Φ_i	1^o
Initial pitch q_i	20 ^{o}/s
Vertical aerodynamic malalignment $C_{m_{am}}$	0.001
Vertical thrust malalignment ε_z	1 ^{o}/oo
Vertical aiming error δ_z	3 1/3 cm/300 m

Table III

Effect of the various design measures on the specific disturbance parameters

Design measure \ Disturbance	Cross wind	Initial yaw	Initial roll	Initial pitch	Lateral aerodynamic malalignment	Vertical aerodynamic malalignment	Roll attitude
Sustainer	++	-	-	-	-	-	-
Keel fin	+	--	-	0	+	0	0
Keel fin, droppable	++	++	+	0	0	0	0
Upper fin	--	--	+	0	--	0	+
Rotor, 1 degree of freedom	++	-	-	0	-	0	+
Rotor in rotatable nose, 2 degrees of freedom	--	--	-	0	++	++	-
Rotor in rotatable nose, 3 degrees of freedom	0	0	++	0	++	++	0
Upper fin on rotatable nose, incl. sustainer	+	--	++	-	++	++	-

++ favourable -- unfavourable 0 no effect

+ somewhat favourable - somewhat unfavourable

Fig.: 1 Anti - tank hand weapon

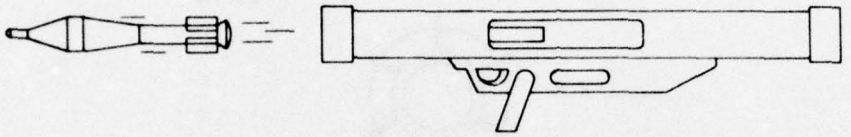

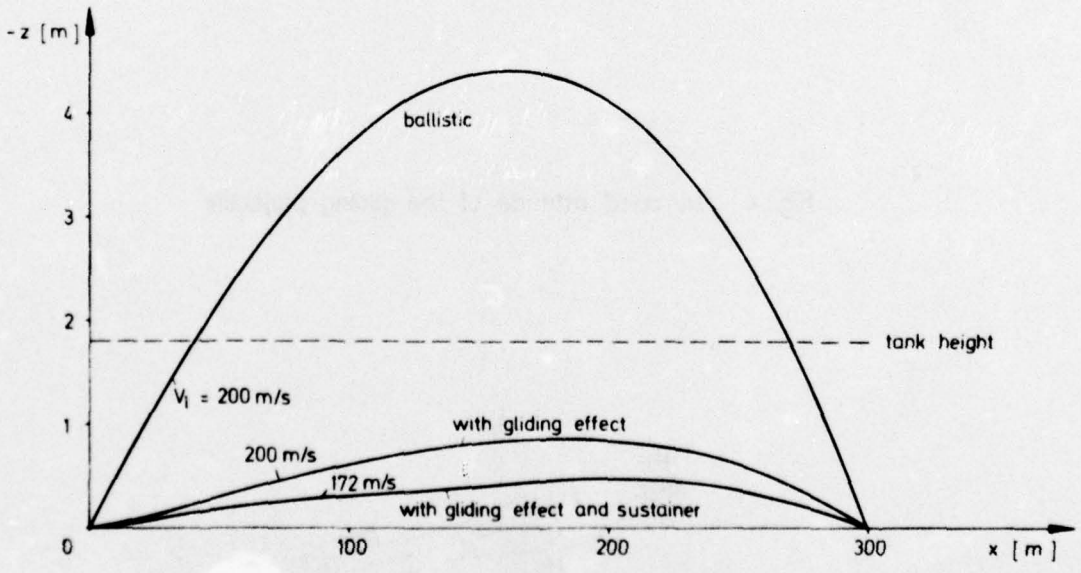

Fig.: 2 Influence of the gliding effect on the flight path

Fig.: 3 Basic configuration version A

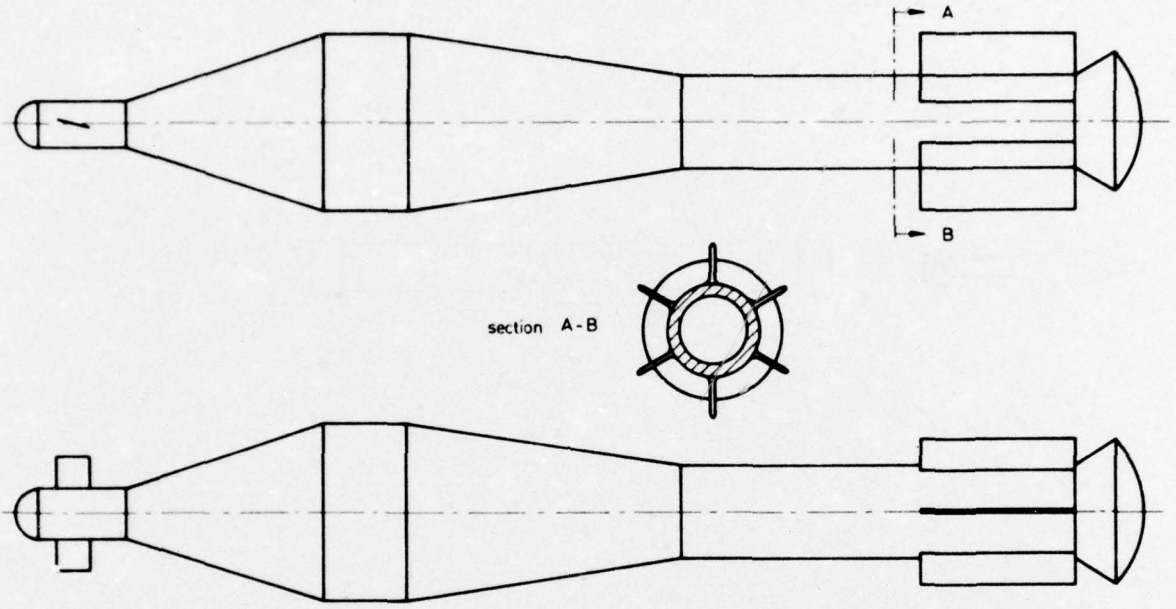

Fig.: 4 Trimmed attitude of the gliding projectile

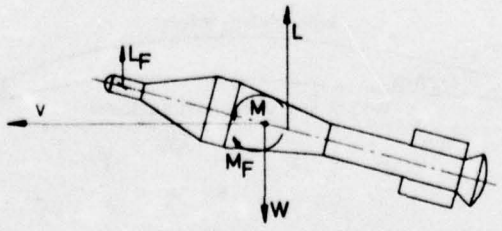

Fig. 5 Examined projectile versions I

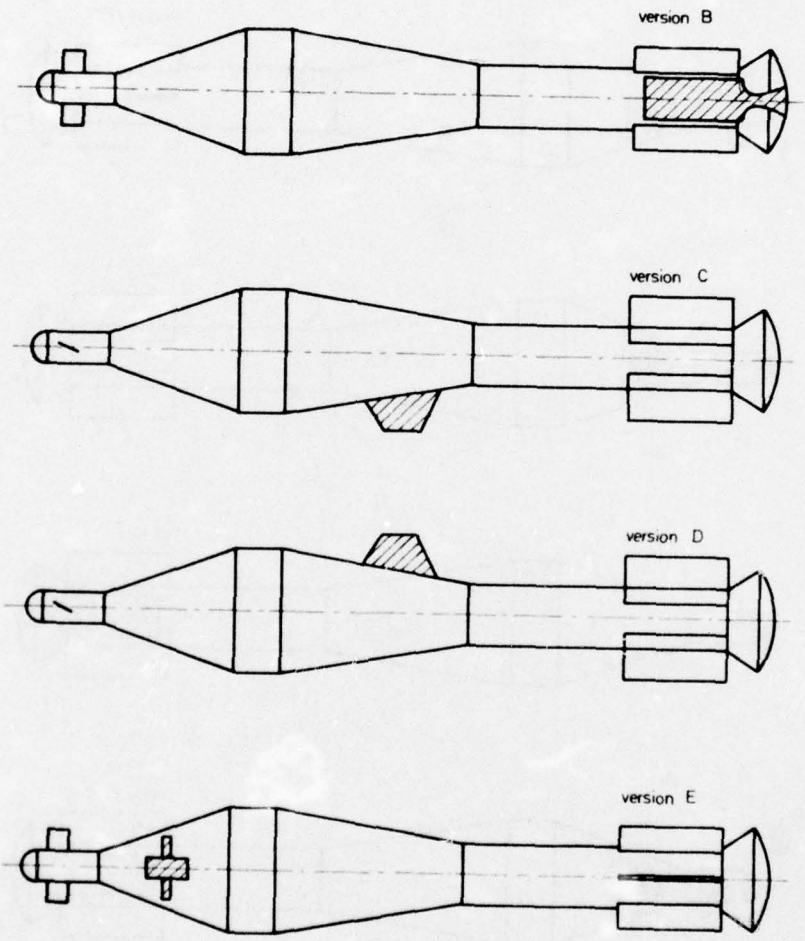

Fig.: 6 Examined projectile versions II

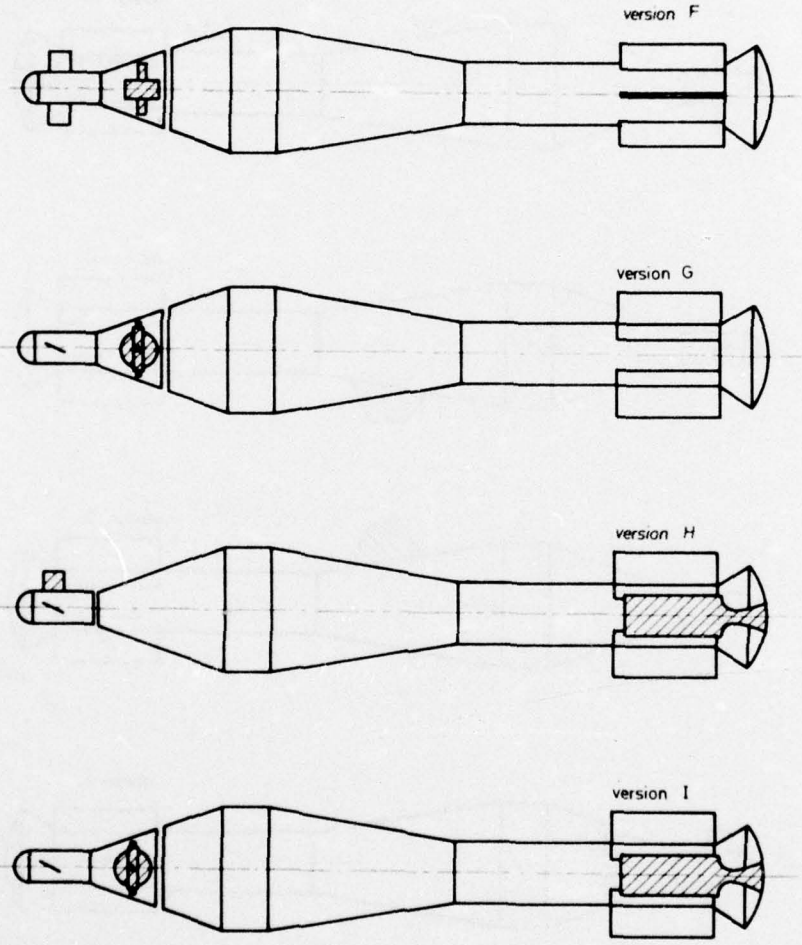

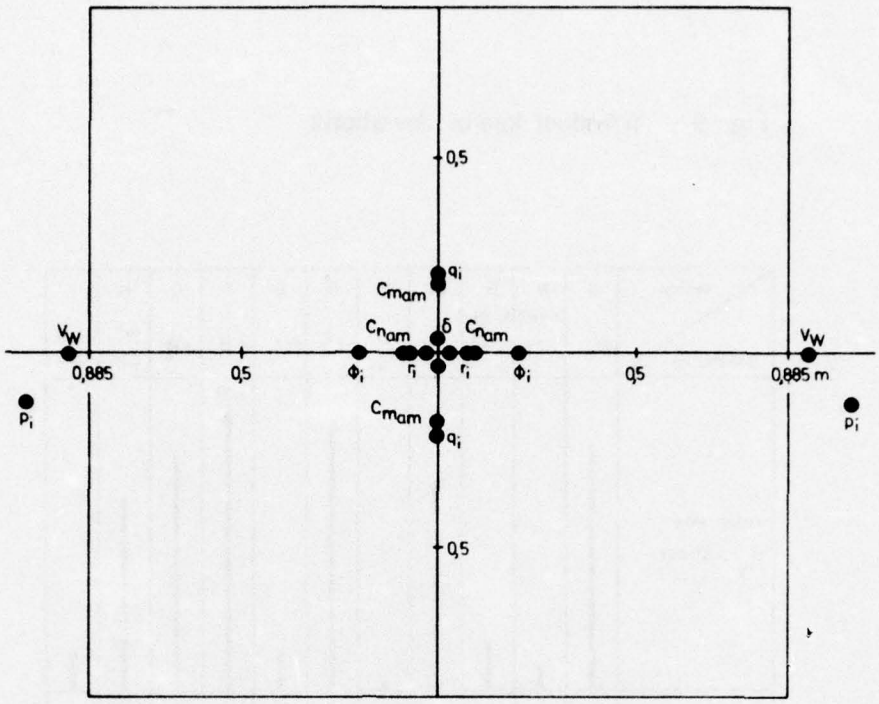

Fig.: 7 Pattern on target version A 1σ - deviations

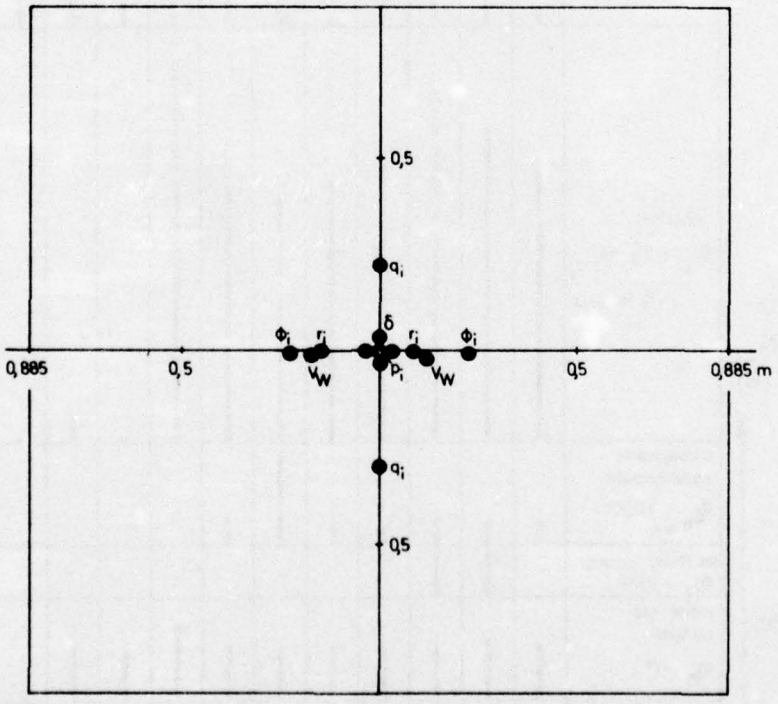

Fig.: 8 Pattern on target version I 1σ - deviations

Fig.: 9 Individual lateral deviations

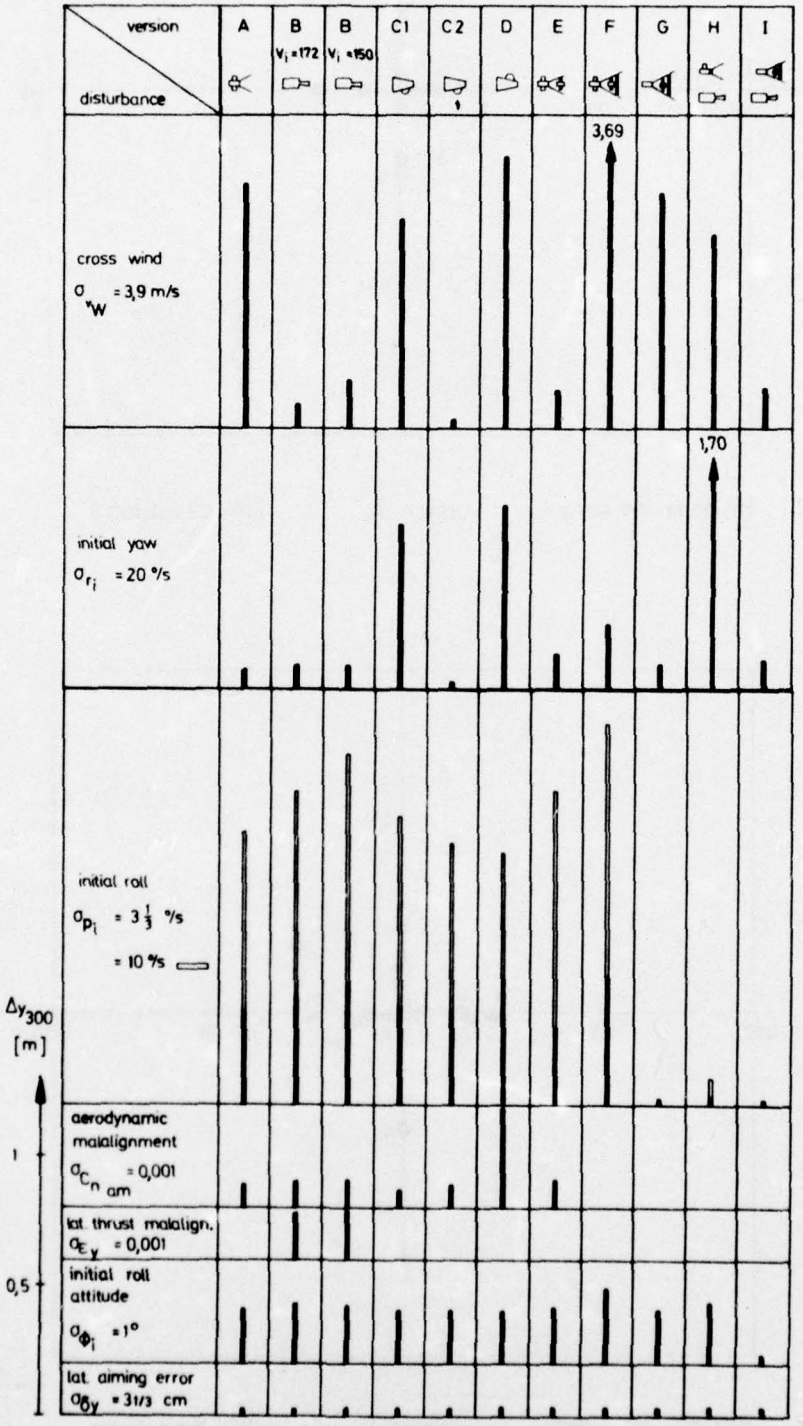

Fig.: 10 Total lateral deviations

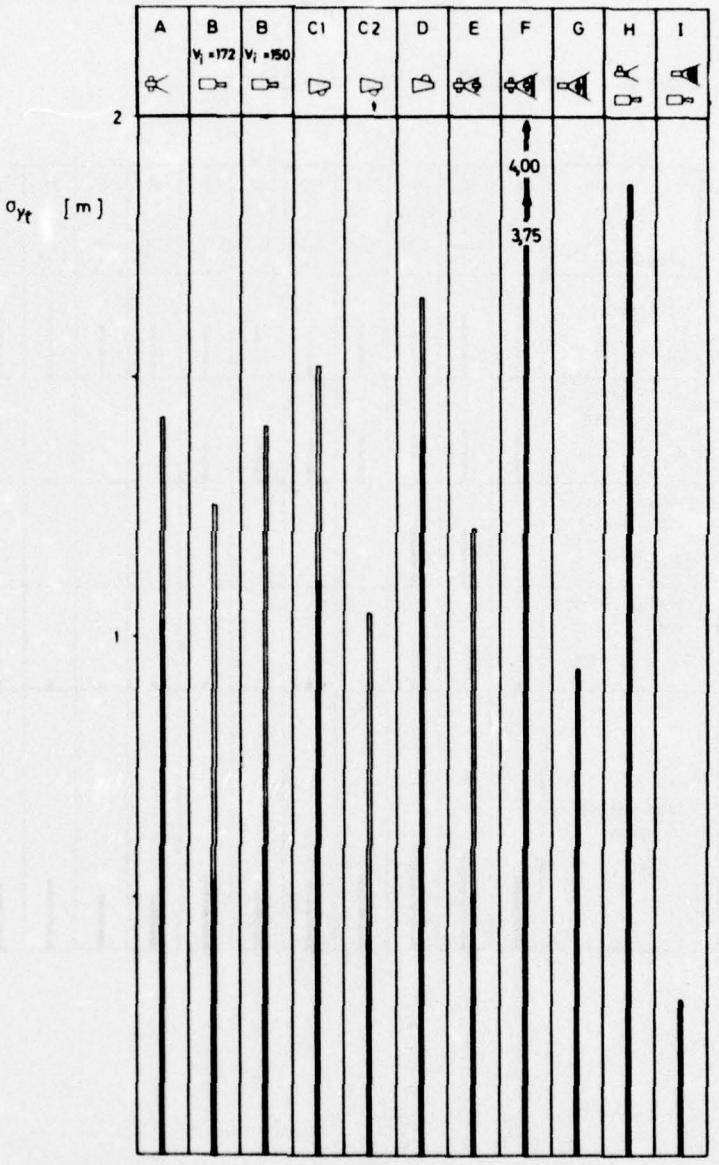

Fig.: 11 Individual vertical deviations

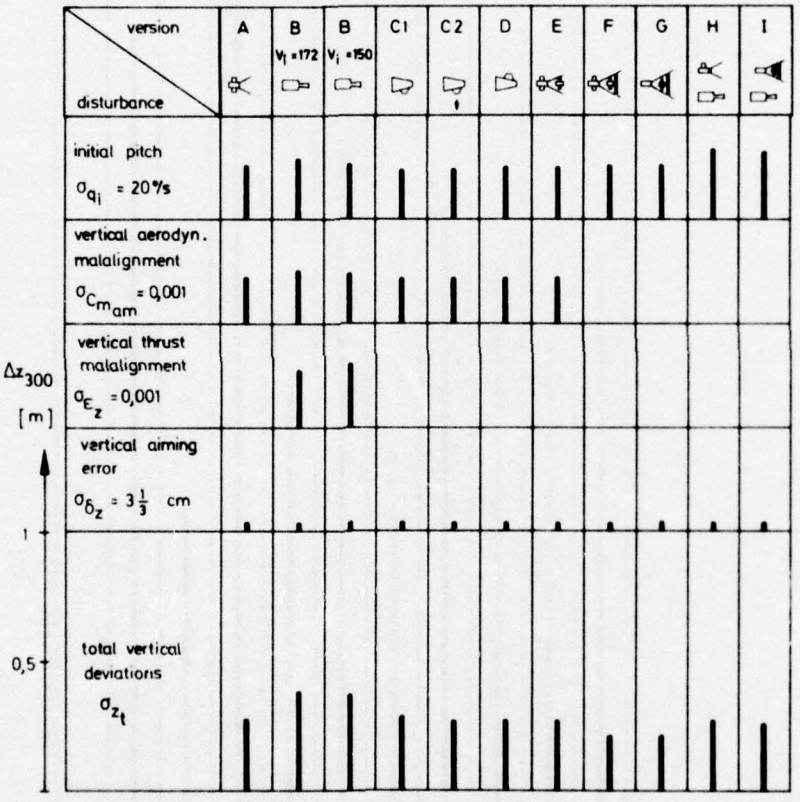

Fig.: 12 Hit probabilities P_h for a circular target of 2m in diameter

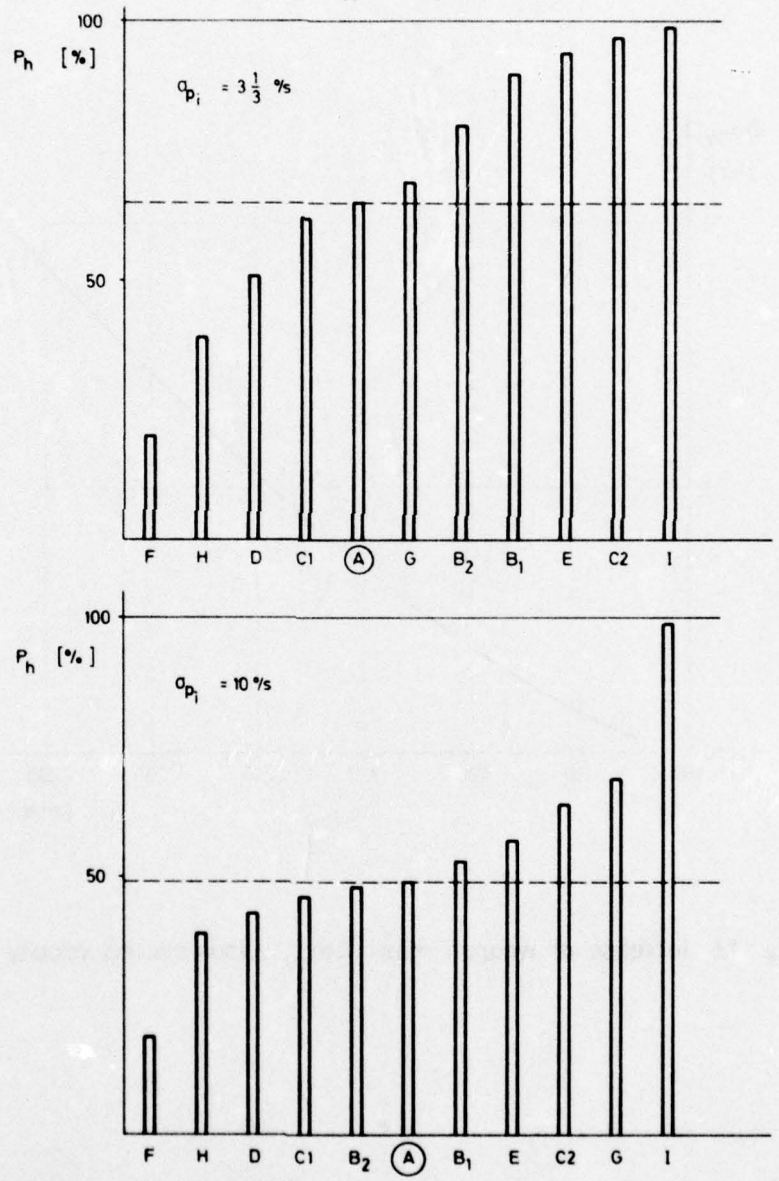

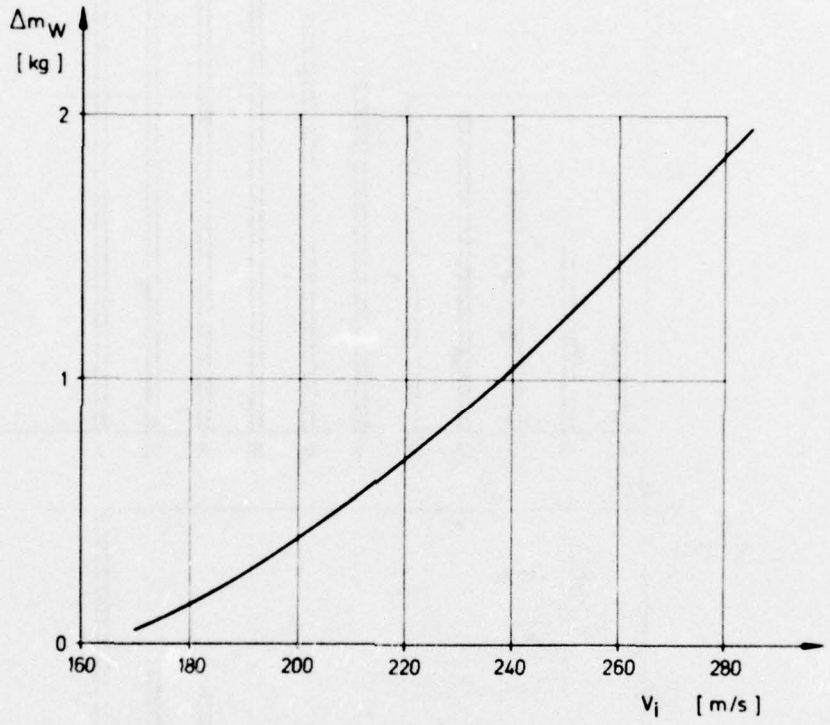

Fig. : 13 Increase of weapon mass Δm_W versus starting velocity V_i

HIGH ENERGY COMPOSITE DOUBLE BASE SOLID PROPELLANTS

by

W. Klöhn

Institut für Chemie der Treib- und Explosivstoffe, 7507 Pfinztal-Berghausen, Germany

AGARD-PEP 47th Meeting on SMALL SOLID PROPELLANT ROCKET FOR FIELD USE

1. Introduction

The so-called composite double base or CDB solid propellants have been developed and tested at our Institute for the past fifteen years or so. Their main constituents may be ammonium perchlorate, nitrocellulose fluid balls, nitroglycerin, aluminum, and a crosslinked polyurethane binder.

These propellants, which are prepared in a slurry process, are characterized by very high energy, highly variable burning rates from presently 12 to 70 mm/s at 130 bar pressure, and good visco-elastic properties.

A number of problems, which can occur in an aggravated form in composite propellants, are caused by the highly corrosive hydrogen chloride in the combustion gases formed from ammonium perchlorate. Consequently, it would be desirable to replace ammonium perchlorate in these propellant systems by other oxidants, in particular organic oxidants. Suitable substances for these purposes are the stable and very powerful compounds known in explosives technology in the group of cyclic nitramines, such as hexogen or RDX and octogen or HMX which are processed into CDB propellants with HCl-free offgases together with the other propellant constituents, such as nitrocellulose fluid balls. nitroglycerin, aluminum, and polyurethane binder. Similar concepts have been described in the literature as solid propellants or, without aluminum, as gun powders. There are some differences probably in the fabrication techniques or the properties of the propellants.

2. Spectrum of Properties of CDB Propellants

In the course of this concept CDB solid propellants were produced with a number of interesting characteristics which will be described below.

- The specific energies of modern composite propellants with polybutadiene binders are reached or even exceeded by these CDB propellants, the densities of the propellants being roughly comparable.
- The CDB propellants have excellent visco-elastic properties and can therefore be produced as case-bonded propellant charges.
- The propellant masses to be prepared in a slurry process can be produced in the same mixers and casting equipments as composite propellants, if vertical mixers are used.
- The offgases of the propellants contain no corrosive components that might result in rapid corrosion of the launchers or inadmissible exposure of the operating personnel.

3. Preparation of Propellants

CDB propellants are prepared in vertical mixers with the necessary devices for heating, cooling and vacuum (Fig. 1). Following the flowsheet shown in Fig. 2, the necessary quantity of nitroglycerin phlegmatized with the polyurethane prepolymer is loaded in the vertical mixer, and the dried nitrocellulose fluid balls, the catalysts, stabilizers and wetting agents are stirred

into the solution.

At temperatures of approximately 50°C, stirring initiates a swelling process of the nitrocellulose fluid balls with the nitroglycerin which is interrupted when the viscosity has reached approximately 500 decipascal-seconds (poise).

Then the aluminum powder and hexogen or octogen is added, and mixing is continued while cooling to 25°C under a vacuum of 13,3 millibar.

After addition of the diisocyanate curing agent the mixture ready for casting with viscosities between 1000 and 4000 decipascal-seconds is cast at 25°C. The relatively small solid fraction and the use of non-fibrous nitrocellulose are the reasons for the low viscosity and the unproblematic preparation technique.

Also casting is carried out under a vacuum (Fig. 3).

The reaction of the curing agent with the prepolymer gives rise to crosslinked propellants with visco-elastic properties. CDB propellants cure within 72 to 120 hours at temperatures between 30 and 50°C.

4. Properties

4.1. Theoretical Calculation of Performance

Table 1 is a summary of a number of propellant combinations obtained from performance calculations.

With the aluminum content kept constant, the hexogen or octogen was increased in 10% steps, while the nitrocellulose/nitroglycerin fraction was reduced and the polyurethane binder fraction was kept unchanged.

Fig. 4 is a plot of the performance data calculated, with the hexogen fraction as the abscissa and the specific impulse as the ordinate. Up to 12% aluminum the specific impulses increase linearly with the hexogen content.

At 14 to 18% aluminum there may be a drop in the specific impulse with increasing hexogen content.

The following results can be deduced from the calculations:

- With the aluminum content kept constant, a decrease of the adiabatic flame temperature was calculated with increasing hexogen or octogen fractions.
- The specific impulse of an equilibrium flow increases with the aluminum content. Optimum values are found between 12 and 16% at hexogen or octogen concentrations of 50 to 70%.
- The specific impulse of most combinations was calculated to be between 2550 and 2650 Ns/kg. These performance levels are in the range of composite propellants with high solid fractions.

4.2. Burning Properties

The burning properties of similar types of propellants are described already in the literature. This indicates that the presence of hexogen or octogen in double base propellants destroys the plateau behavior and can cause the pressure exponent n in Vielle's equation, $r = a \cdot P^n$, to rise strongly.

With hexogen bearing double base propellants, pressure exponents 0,7 have been obtained in the pressure range of up to some 250 bar.

We will discuss the burning properties of propellants with hexogen fractions of 30 and 40 %. The mean grain size of the hexogen used was 11 µm after grinding in a colloid mill.

The values of the burning rates as a function of pressure can be seen from Tables 2 and 3.

Fig. 5-6 show the burning diagrams of the propellants listed in the tables in a log-log coordinate system.

In the absence of catalysts a pressure exponent of 0.76 can be calculated from the straight burning line also for these propellants.

As a consequence, various metal compounds of lead, tin, chromium, iron, copper, vanadium, zirconium, molybdenum and selenium were added to the propellants in concentrations of 1-3%.

The effectiveness of the compounds used differed greatly. In most cases, only the rates increased, whereas the pressure exponents did not change greatly.

Some results obtained in this series with lead, copper and tin compounds will be indicated (Table 2).

In addition to the metal ion also the organic residue is of major significance as far as effectiveness is concerned.

While the two lead betaresorcyclates only brought about an increase in the burning rate, the lead salicylates were able to reduce the exponent to values of 0.6 in the pressure range between 70 and 180 bar.

Another interesting feature to note was the burning behavior of propellants with 40% hexogen and a slightly modified binder composition (Table 3).

Compounds such as tin octoate increase the burning rate, but the pressure exponents are at a value of 0.85. Also lead octoate and copper diresorcyclate would be suitable only to a limited extent.

However, lead monosalicylate and monobasic copper betaresorcylate will raise the exponents to levels of 0,45 in the pressure range between 100 and 180 bar, which is so important for rocket motors; in those cases, high increases of 0.8 were measured below 100 bar and above 180 bar.
Extended studies will be necessary to allow the burning behavior to be modified on an even larger scale.

4.3. Mechanical Properties

The mechanical properties were determined in tensile tests with a Zwick-type tensile tester employing crosshead rates of 50 mm/min. The JANNAF specimen form with a measuring length of 50 mm was used. The values quoted are mean values taken from five assays. Before the test specimens were conditioned for 168 hours at 20°C and relative humidities of the air of 5%. In the tests referred to, the maximum tensile strengths corresponded to the ultimate tensile strenghts, and so did the respective strains.

The mechanical properties of the CDB propellants described in this paper are determined by various factors. Earlier experiments had indicated that the reaction of the prepolymer with the diisocyanate and the swelling of the nitrocellulose fluid balls with nitroglycerin made an additive contribution to the overall properties of the propellants. In this respect, also the effect upon the polyurethane formation reaction of the catalysts used for burning must be taken into account.

Where curing of the polyurethane binder was inhibited by a catalyst and mainly swelling reactions occurred, propellants were generated which had bad elastic properties.

It is evident from Table 4 that for the same propellant compositions the catalyst has a major influence upon curing and, hence, upon the ultimate tensile strength and strain. Monobasic copper salicylate and iron octoate, for instance, result in propellants with unsatisfactory mechanical properties. Improvements in these values are brought about as a result of the use of iron acetyl acetonate and lead octoate, in which cases strain values in excess of 50 % were obtained.

Excellent visco-elastic properties are achieved with monobasic copper betaresorcylate at 6.2 bar and 73.0 %. A reduction of the catalyst fraction further increases the strain values. Accordingly, also the polyurethane binder fraction can still be reduced. However, it has become apparent that mixtures of various catalysts, which had different influences upon the mechanical properties, resulted in propellants with high strain values.

The influence of temperature upon the mechanical properties is evident from Table 5. The propellant was cast as a block and cured. The test specimens were punched from slabs.

This propellant is characterized by remarkably good visco-elastic properties in the low temperature region. For its mechanical behavior, this propellant could be used as a case-bonded type also at extreme temperature.

4.4. Thermal Stability

The thermal stability of CDB propellants is determined chiefly by the nitrocellulose - nitroglycerin components. Because of the dilution with hexogen, aluminum and the polyurethane binder, however, excellent values may be expected for the short term tests. The following values have been found for various compositions:

Deflagration temperature	= 180 - 188°C
Holland test	= 0.9 - 1.2 % loss of weight
Bergmann-Junk test	= 1.0 - 3.3 ml $\frac{n}{100}$ NaOH/g feed mat.

It should be added that these stability values may deteriorate significantly as a result of the presence of some burning catalysts. Long time storage at 90°C is shown in Fig. 7. A loss of weight of 3 % is reached after 44 days. After 62 days, when the loss of weight is 5.8 %, the reaction occurs autocatalytically. This behavior is typical of the decomposition characteristics of nitrocellulose and is found also in double base propellants

Practical Energy Assessment in Combustion Chambers

The performance was determined in practice in combustion chambers with approximately 11.6 kg of propellant mass.

In these experiments, which served only for testing the propellants and their insulations, no emphasis was put on optimizing the weight. An internal star burner was used as shown in Fig. 8.

For the combustion experiments steel burning chambers of a lightweight construction capable of flying were used (Fig. 9).

The insulation of the chambers was manufactured by the rotational molding process with a thickness between 0.8 and 1.2 mm. Filled HTPB polymers were used as the insulation. Figure 10 lists some data of the combustion chamber, the propellant charge, the nozzle, and

the ignition system. The results obtained with a propellant containing 30 % hexogen are listed in Table 6. The thrust and pressure diagrams of a typical propellant are shown in Fig. 11 and 12.

The propellants listed, which still exhibit differences in composition and in the catalysts, were fired in the pressure range between 140 and 190 bar.

In the examples quoted specific impulses of 2316 to 2367 Ns/kg, characteristic velocities of 1489 to 1560 m/s, and thrust factors of 1.497 to 1.556 were obtained. These performance data can be improved further if the hexogen fraction is increased from at present 30 to 40 or 50 %.

5. Concluding Remarks

The propellants described in this paper lend themselves particularly well to the use in ballistic rockets requiring long operating times of the launcher, especially because of their high performance and the absence of corrosive gases. The visco-elastic properties allow the fabrication of case-bonded propellant charges adhering to the chamber walls and, hence, the achievement of high volumetric efficiencies. The simple processing capabilities also allow the production of complicated geometric shapes of the burning surfaces. We regard the types of propellant described here as interesting additions to the proven line of double base and composite propellants.

TABLE 1

Calculated Thermodynamic Properties of CDB-Propellants with Herogen or Octogen (Expansion Ratio 70:1)

Propellant Components	Composition in %																	
Aluminium	5	5	5	5	5	5	5	5	5	10	10	10	10	10	10	10	10	10
RDX or HMX	–	10	20	30	40	50	60	70	85	–	10	20	30	40	50	60	70	80
NC Fluid Balls	42.5	37.5	32.5	27.5	22.5	17.5	12.5	7.5	–	40	35	30	25	20	15	10	5	–
Nitroglycerin	42.5	37.5	32.5	27.5	22.5	17.5	12.5	7.5	–	40	35	30	25	20	15	10	5	–
Polyurethane Binder	10	10	10	10	10	10	10	10	10	10	10	10	10	10	10	10	10	10
Adiabatic Flametemperature T_c in K	3110	3099	3089	3078	3067	3056	3045	3034	3018	3313	3304	3295	3285	3276	3266	3256	3246	3236
Specific Impulse I_s equil. in Ns/kg	2468	2475	2483	2491	2498	2505	2511	2519	2530	2527	2538	2549	2556	2567	2577	2586	2595	2604
Molenumber of Gases n in mol/kg	38.1	38.7	39.3	39.9	40.4	41.0	41.6	42.2	43.1	36.6	37.2	37.8	38.3	38.9	39.5	40.1	40.7	41.2

TABLE 1 (Continued)

Propellant Components	Composition in %																	
Aluminium	12	12	12	12	12	12	12	12	12	14	14	14	14	14	14	14	14	14
RDX or HMX	–	10	20	30	40	50	60	70	78	–	10	20	30	40	50	60	70	76
NC Fluid Balls	39	34	29	24	19	13	9	4	–	38	33	28	23	18	13	8	3	–
Nitroglycerin	39	34	29	24	19	13	9	4	–	38	33	28	23	18	13	8	3	–
Polyurethane Binder	10	10	10	10	10	10	10	10	10	10	10	10	10	10	10	10	10	10
Adiabatic Flametemperature T_c in K	3253	3253	3253	3253	3253	3253	3253	3253	3253	3253	3253	3253	3253	3253	3253	3253	3253	3253
Specific Impulse I_s equil. in Ns/kg	2565	2573	2582	2590	2599	2607	2615	2624	2630	2591	2600	2608	2617	2625	2633	2640	2645	2639
Molenumber of Gases n in mol/kg	36.3	36.8	37.4	37.9	38.6	39.0	39.6	40.2	40.6	35.8	36.4	36.9	37.5	38.0	38.6	39.2	39.8	40.1

TABLE 2

Burning Rate in mm/s of CDB-Propellants in the Presence of Different Catalysts

Composition of Propellants in %

Hexogen	:	30.0
Aluminium	:	14.0
NC/Ngl	:	44.1
PU Binder	:	9.9
Catalyst	:	2.0

Catalysts :	without Catalyst	Normal Lead Betaresorcylate	Monobasic Lead Betaresorcylate	Lead Monosalicylate	Lead Disalicylate
Pressure in bar					
40	3.9	4.3	4.6	4.7	5.2
70	6.2	6.0	6.9	7.4	8.0
100	7.2	8.0	9.0	9.2	9.7
130	8.4	9.4	10.5	10.5	11.0
180	11.2	12.2	13.3	12.6	13.4
250	14.5	16.0	17.0	16.2	16.7
Pressure Exponent n in the Pressure Range of bar	100 - 250	70 - 250	40 - 250	70 - 180	70 - 250
	0.76	0.78	0.72	0.56	0.58

TABLE 3

Burning Rate in mm/s of CDB-Propellants in the Presence of Different Catalysts

Composition of Propellants in %

Hexogen	:	40.0
Aluminium	:	14.0
NC / Ngl	:	34.1 - 33.1
PU - Binder	:	9.9
Catalyst	:	2.0 - 3.0

Catalysts	Stannic Octoate	Cupric Diresorcylate	Lead Octoate	Lead Monosalicylate	Monobasic Cupric Beta resorcylate
Pressure in bar					
40	4.4	4.2	4.9	4.4	5.2
70	6.0	6.4	7.2	7.0	8.1
100	7.5	8.5	8.9	9.6	11.3
130	9.5	10.1	10.5	10.8	12.8
180	12.0	13.0	13.1	12.3	14.3
250	16.4	16.5	17.5	17.0	19.5
Pressure Exponent n in the Pressure Range of bar	100 - 250	70 - 250	40 - 180	100 - 180	100 - 180
	0.85	0.64	0.65	0.44	0.42

TABLE 4

Mechanical Properties of CDB-Propellants at 20 °C

Bindercomposition in %								
Prepolymer	9.0	9.0	9.0	9.0	9.0	9.0	8.0	7.5
Diisocyanate	0.9	0.9	0.9	0.9	0.9	0.9	0.8	0.7
Catalyst	Cupric Salicylate 2.0	Ferric Octoate 2.0	Ferric Acetyl Acetonate 2.0	Lead Octoate 2.0	MCBR * 2.0	MCBR * 1.0	MCBR * 1.0	MCBR * 1.0
Stress at Break in bar	4.7	7.5	11.0	9.5	6.2	7.7	6.4	7.0
Strain at Break in %	20.8	23.7	51.0	56.0	73.0	87.0	90.0	77.0

* MCBR = Monobasic Cupric betaresorcylate

TABLE 5

Mechanical Properties of a CDB-Propellant at Different Temperatures

	Temperature in °C				
Mechanical Properties	− 40 °C	− 10 °C	+ 20 °C	+ 50 °C	+ 70 °C
Stress at Break in bar	19.9	8.7	6.2	5.4	4.7
Strain at Break in %	80.0	94.0	80.0	57.0	53.0

TABLE 6

Performance Determination of CDB-Propellants

m p (kg)	Throat Diameter (mm)	$\bar{p}$ (bar)	t 50% P (s)	$\int p \cdot dt$ (bar.s)	$\bar{F}$ (N)	t 50% F (s)	$\int F \cdot dt$ (N.s)	J s (Ns/kg)	C * (m/s)	C F —	τ (mm/s)
11.62	29.00	171	1.525	262	17822	1.510	26911	2316	1489	1.556	14.6
11.76	29.00	178	1.630	274	18308	1509	27892	2355	1538	1.542	14.5
11.67	30.00	138	1.796	250	15103	1.783	27082	2320	1514	1.533	12.4
11.55	30.00	166	1.517	255	17871	1.505	26974	2335	1560	1.497	14.6
11.67	30.00	164	1.488	251	18633	1.462	27357	2364	1533	1.543	14.9
11.54	30.00	190	1.324	261	20768	1.314	27315	2367	1537	1.540	16.8

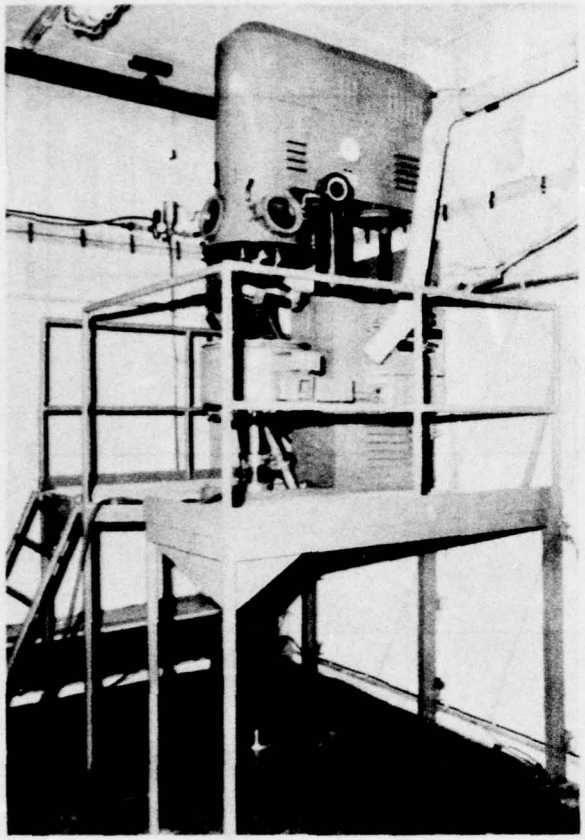

Fig.1 Vertical mixer

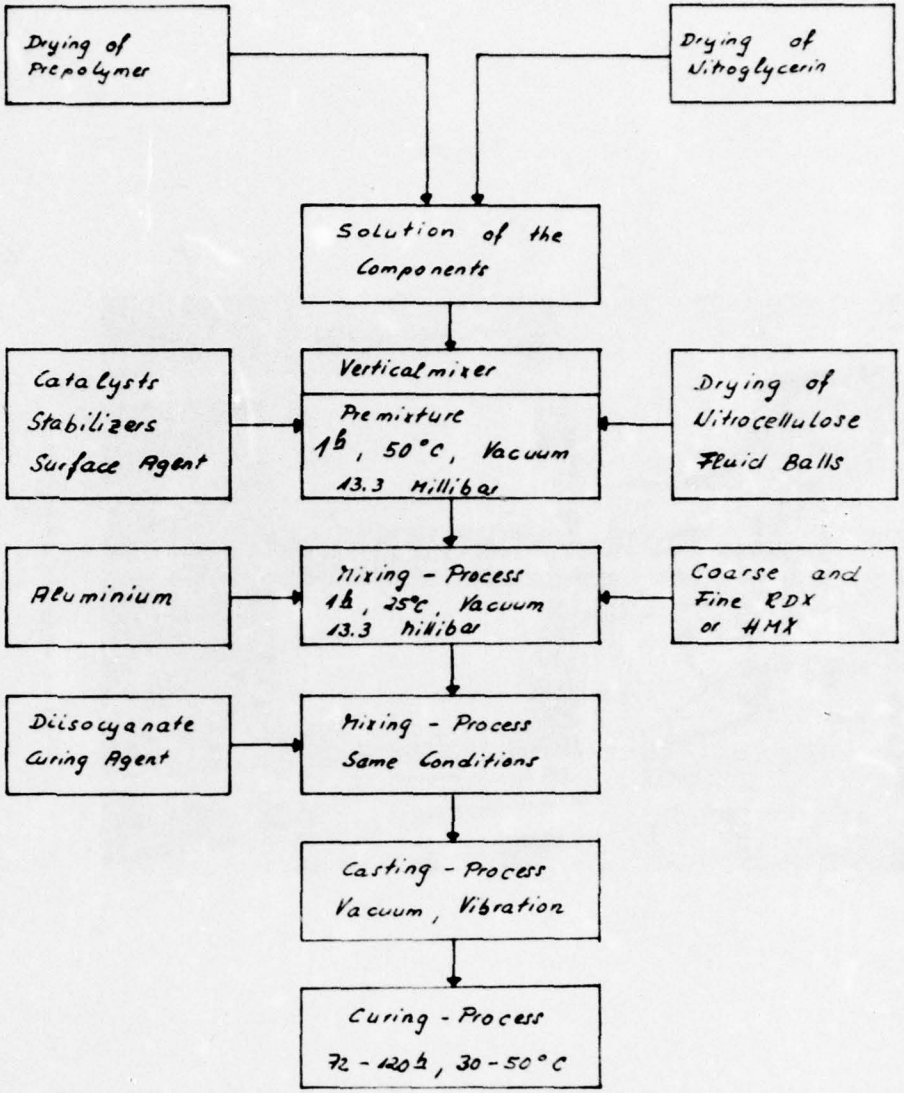

Fig.2 Diagram of the CDB-propellant production method

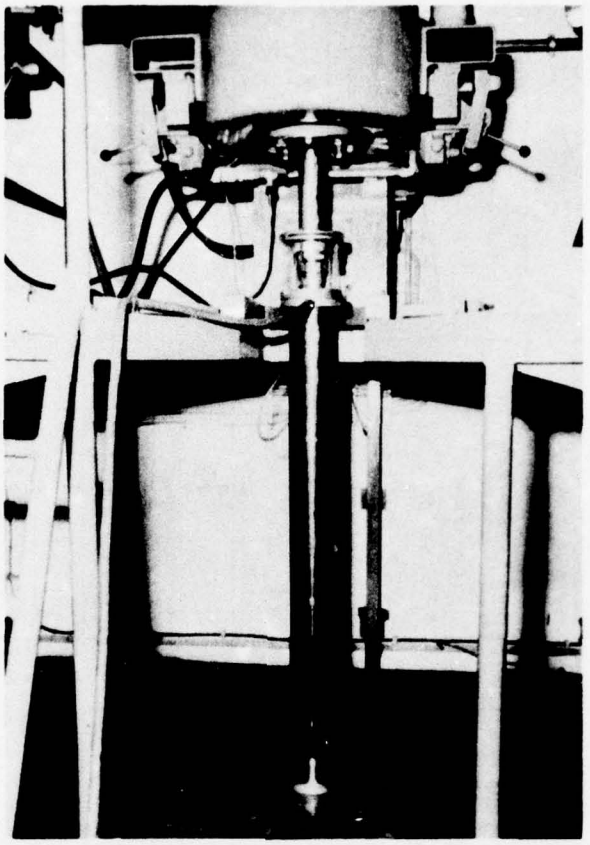

Fig.3 Casting of CDB-propellant

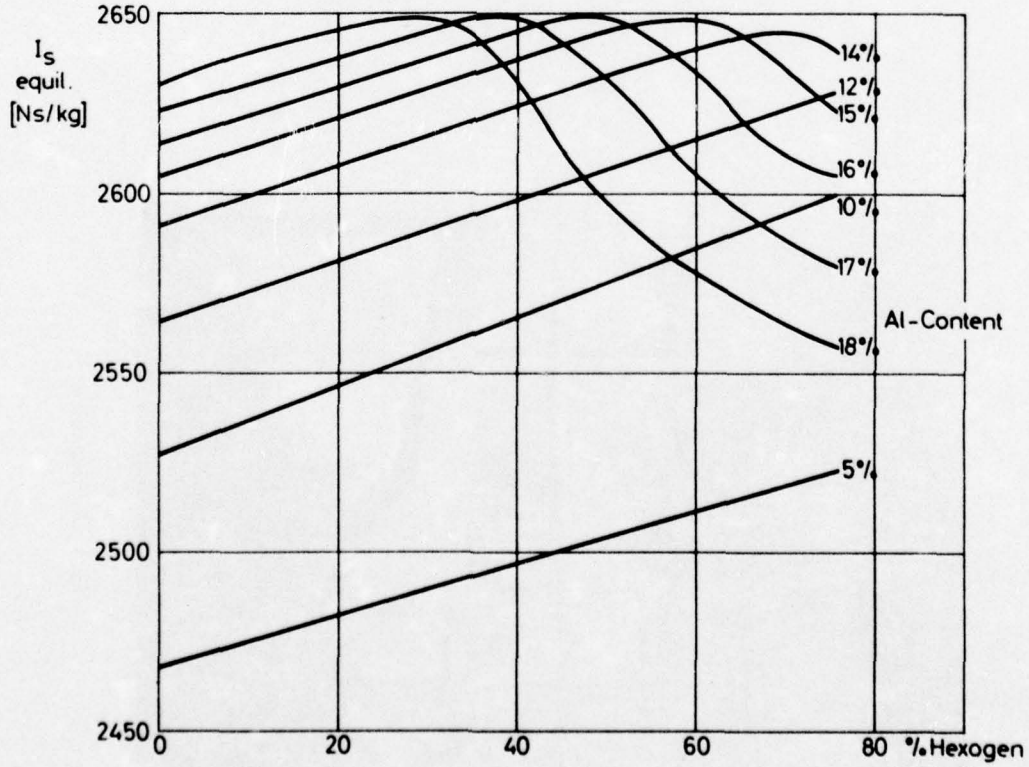

Fig.4 CDB-propellants

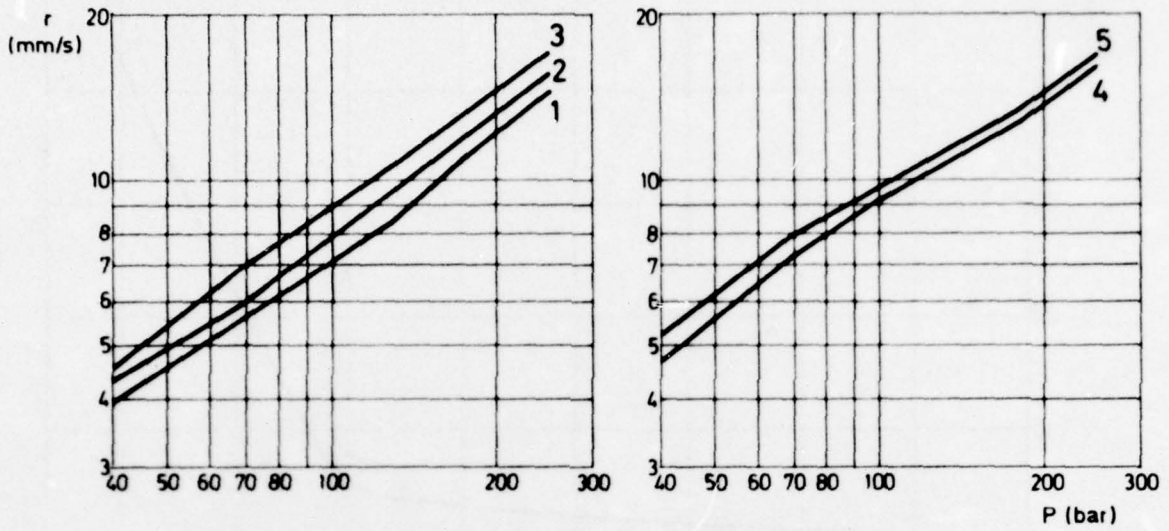

1 Without Catalyst

2 Normal Lead Betaresorcylate

3 Monobasic Lead Betaresorcylate

4 Lead Monosalicylate

5 Lead Disalicylate

Fig.5 CDP-propellants

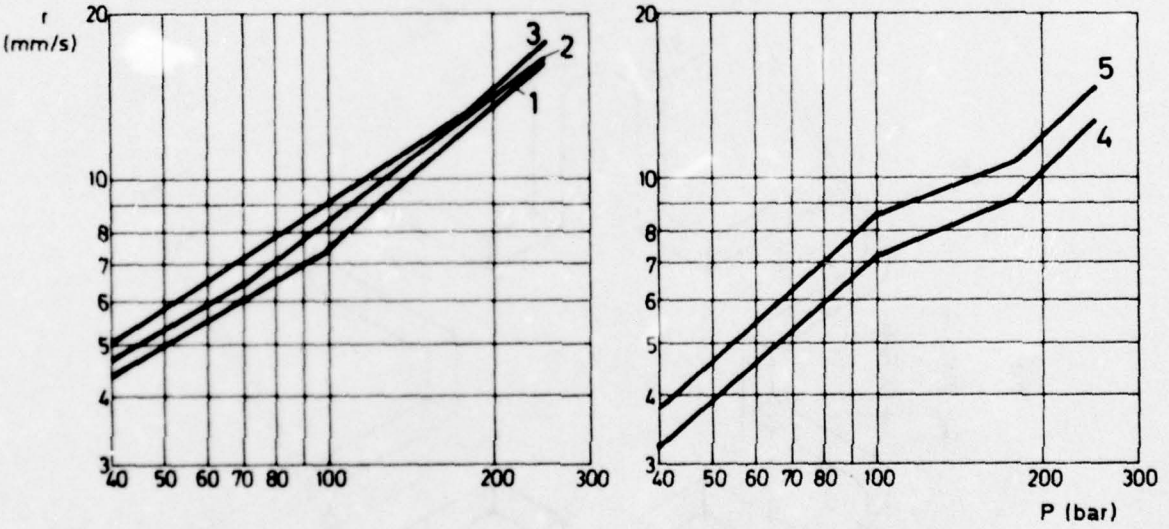

1 Stannic Octoate

2 Cupric Diresorcylate

3 Lead Octoate

4 Lead Monosalicylate

5 Monobasic Cupric Betaresorcylate

Fig.6 CDB-propellants

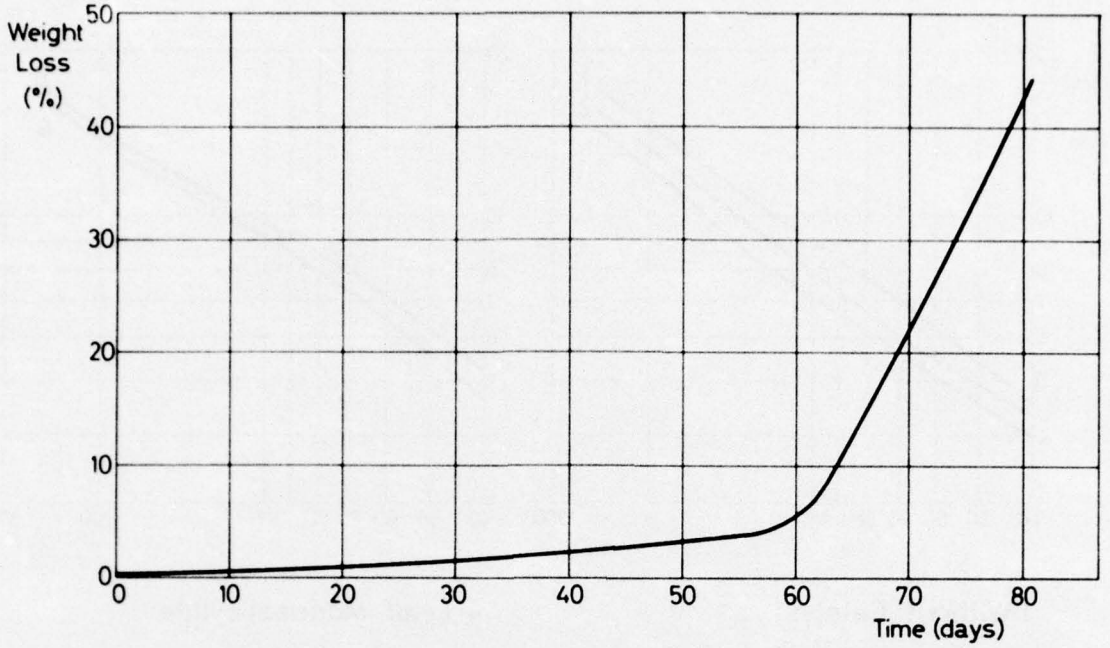

Fig.7 CDB-propellants

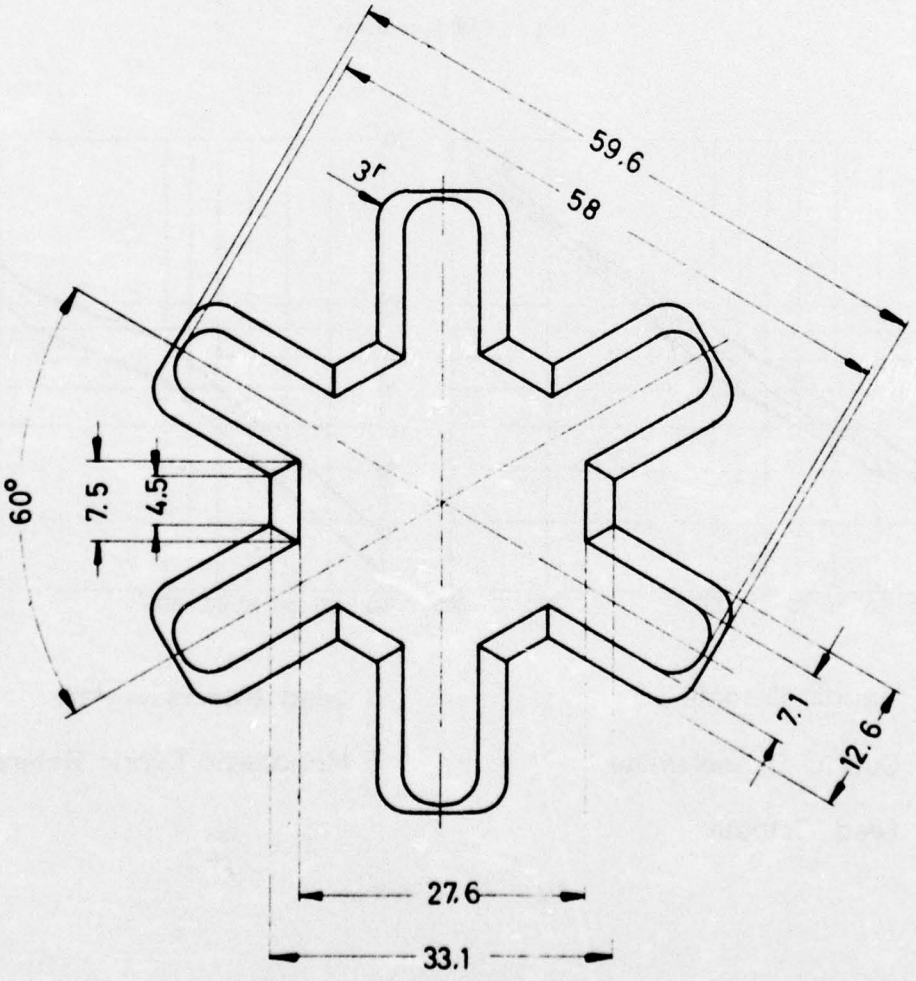

Fig.8 CDB-propellants

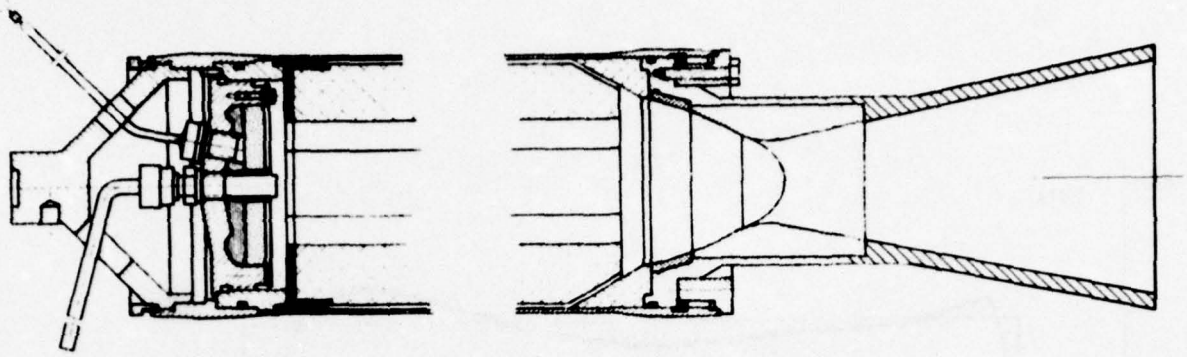

Fig.9 CDB-propellants

1. Chamber

Length	1144 mm
Inner Diameter (without Insulation)	105 mm
Wall Thickness	1.5 mm
Insulation Thickness	0,8 - 1.2 mm
Free Chamber Volume	9.901 l

2. Propellant Charge

Length	1039 mm
Diameter	103 mm
Burning Surface	269400 mm^2
Web Thickness	22.2 mm
Mandrel Volume	1.614 l
Propellant Mass	~ 11.6 kg

3. Nozzle

Length	201 mm
Throat Diameter	29 - 30 mm
Throat Area	660 - 707 mm^2
Exit Area of Nozzle	6361 mm^2
Area Ratio ε	9.00 - 9.64

4. Ignition

Squib	ZK 1
Main Charge	15g AR 2C

Figure 10

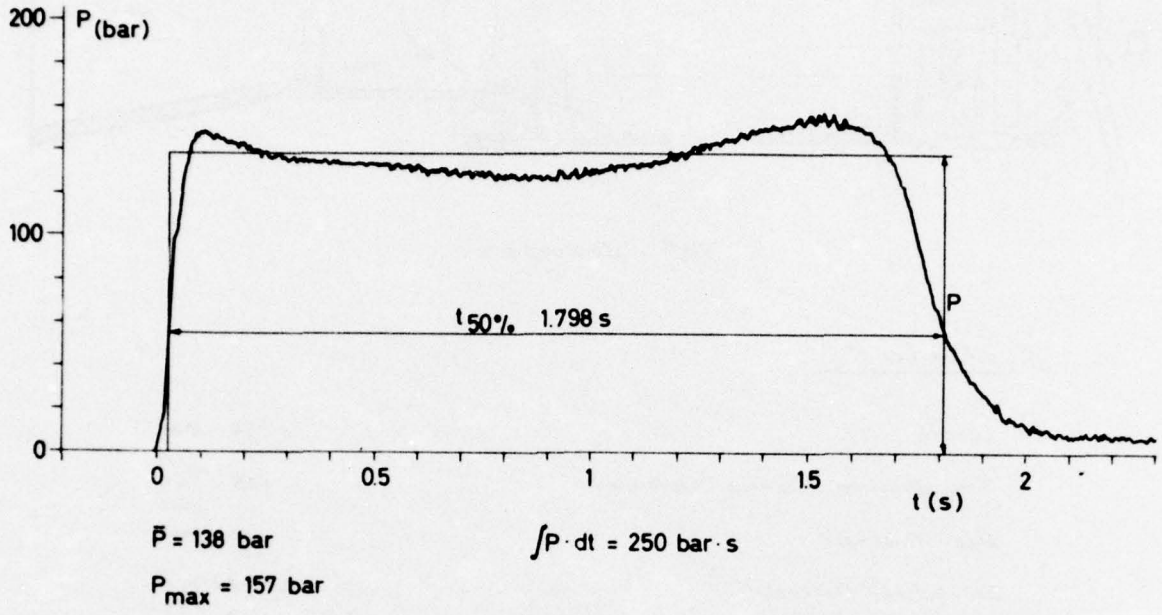

Fig.11 CDB-propellants

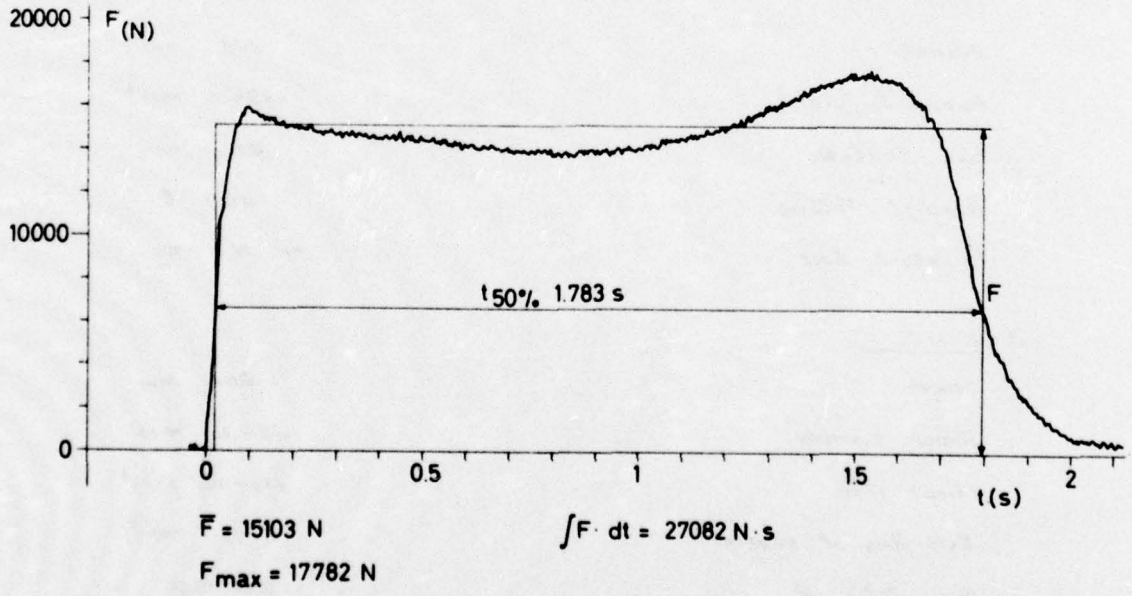

Fig.12 CDB-propellants

PROPERGOLS NOUVEAUX POUR ENGINS TACTIQUES
LES SILILANES

G. DORIATH - Ingénieur chimiste au Centre de Recherches du Bouchet
B.P. n° 2 Le Bouchet 91710 VERT LE PETIT

Les sililanes, propergols composites à liant silicone, chargés avec du perchlorate d'ammonium et de l'aluminium, ont été caractérisées des points de vue propriétés mécaniques et balistiques. Ces propergols se distinguent par une vitesse de combustion élevée (jusqu'à 35 mm/s) pour une impulsion spécifique en moteurs de 40 kg maximum voisine de 233 s. Le liant silicone confère à ces propergols une remarquable stabilité des propriétés mécaniques dans un large domaine de température -mais ces propriétés ne sont pas suffisantes pour permettre d'utiliser la technique du "moulé-collé"- La tenue en ambiance prolongée à haute température (au moins 130°C),liée aux propriétés des liants silicones,est excellente.

1. INTRODUCTION

Les sililanes sont des propergols composites à liant silicone utilisant le perchlorate d'ammonium comme charge oxydante et l'aluminium comme charge réductrice. Ces propergols sont obtenus par un procédé classique de fabrication de propergols composites :

- mélangeage des ingrédients dans un malaxeur. Le liant est introduit sous la forme d'un prépolymère liquide réticulable à température modérée. Les charges sont sous forme pulvérulente.

- coulée dans un moule aux dimensions du bloc à réaliser

- cuisson dans une étuve.

- démoulage et usinage du bloc.

Les blocs obtenus peuvent être,soit "moulés-collés" si l'inhibiteur de combustion est collé à l'enveloppe (le propulseur),ou "libres" si cet inhibiteur est uniquement collé au bloc propulsif. Dans le cas des sililanes on verra que les propriétés mécaniques de ces compositions n'ont pas permis de réaliser des blocs "moulés-collés".

On examinera dans la suite les propriétés mécaniques (et de collage sur inhibiteur), cinétiques et énergétiques de ces compositions.

2. PROPRIETES MECANIQUES

On s'est efforcé de déterminer les propriétés mécaniques de traction-allongement de ces propergols ainsi que les limites de tenue en relaxation et fluage.

21. Forme de la courbe de traction

Cette courbe est obtenue à 20°C sur machine INSTRON à la vitesse de 10 mm/s pour une éprouvette 1/2 Janaf. (fig. 1)

On constate une rupture de pente dès les faibles allongements attribuable aux mauvaises propriétés de l'adhésion liant-charge de ces propergols. En effet, dès un allongement ε_a on voit apparaître sur l'éprouvette de nombreuses fissures qui auraient pour origine les vides créés autour de chaque grain de perchlorate au cours de la traction. Ceci a pu être confirmé par les observations suivantes :

- déchaussement très facile des grains de perchlorate en surface du propergol (au simple toucher)

- des mesures de variation de volume au cours de la traction faites au dilatomètre à gaz, montrent un accroissement rapide du volume de l'éprouvette jusqu'à ε_a suivi d'une chute instantanée à V = 0 (pénétration du gaz dans les fissures).

Après ε_a on a la propagation de ces fissures au cours de la traction, et le matériau a subi des dommages irréversibles.

Du point de vue pratique les valeurs S_a et ε_a n'étant pas faciles à déterminer on repère les propriétés du propergol par :

Sm : valeur de la contrainte maximale en général $\simeq 2\ S_a$

ε : allongement "élastique"

em : allongement à traction maximale (avec environ $em \simeq 10\varepsilon$).

Ces valeurs évoluent selon la formule du propergol (croissance du module lorsque le taux de charges croît ou que le taux de réticulation croît) et les conditions de traction (température et vitesse de traction).

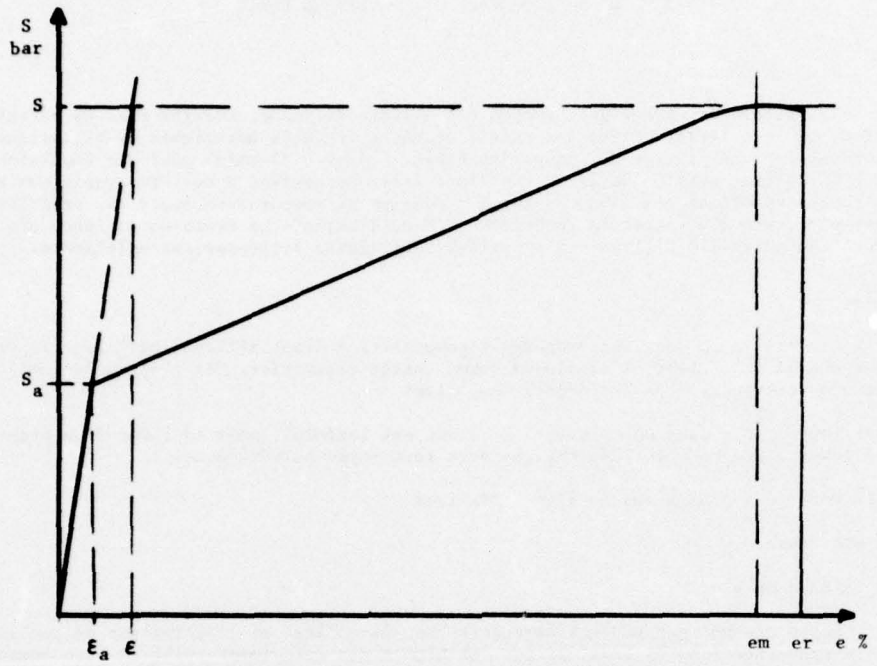

Figure 1 : COURBE DE TRACTION D'UNE SILILANE APPAREIL INSTRON 10 mm/mn

22. Influence de la température

Les propriétés mécaniques de ce type de propergol sont particulièrement stables dans une large plage de température. Elles sont représentées pour une sililane 13/61/26 par les courbes de la figure 2 (traction Instron 10 mm/mn, éprouvettes 1/2 Janaf).

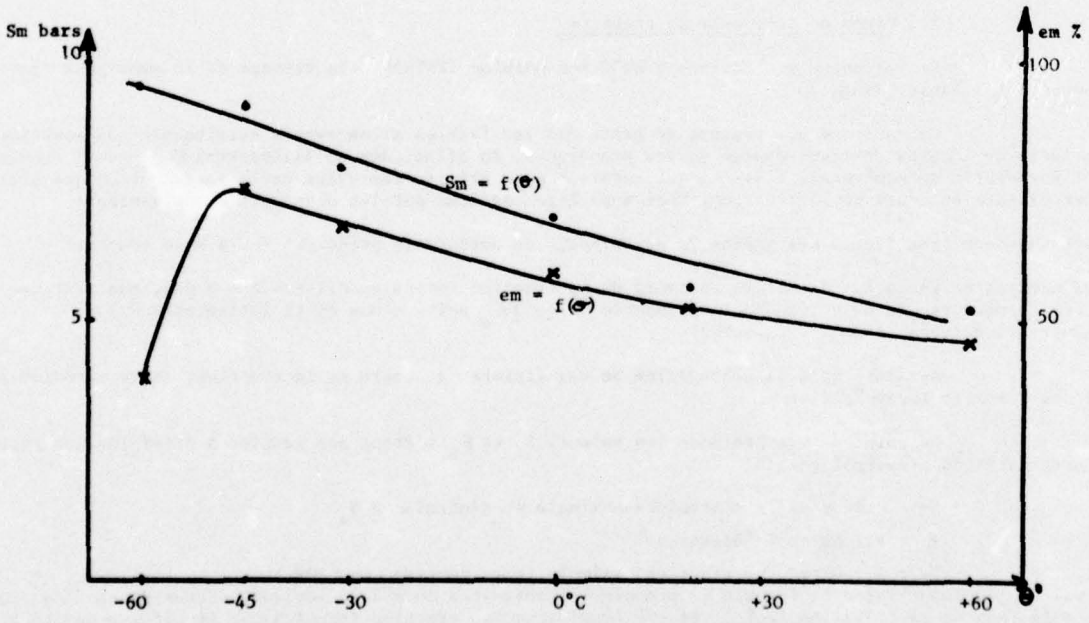

Figure 2 : Propriétés mécaniques en fonction de la température d'une sililane 13/61/26 (INSTRON 10 mm/mn)

Les courbes d'évolution de la contrainte maximum et de l'allongement correspondant montrent :

- que la contrainte maximum croît quand la température s'abaisse. Cependant cette croissance reste faible 85 % entre + 60 et - 60 °C, soit 3 à 4 fois moins qu'un autre propergol composite.

- que l'allongement à la contrainte maximum évolue peu dans ce même domaine de température, puisque toutes les valeurs se situent entre 27,5 et 35 %. Le maximum se situant à ~ 45 °C.

23. Influence de la vitesse de traction

Les résultats (sur une composition 16/76/8) confirment les valeurs précédentes à savoir que les propriétés mécaniques dépendent peu de la vitesse de traction. Traction INSTRON à + 20°C éprouvette 1/2 Janaf.

vitesse de traction en mm/mn	Sm bars	ε %	em %
0,05	5,4	1,8 %	22 %
0,5	5,6	1,8	22
5	6,8	2,1	29
50	8,2	2,6	29
500	8,6	1,9	29

24. Tenue au fluage et en relaxation

La limite de tenue en fluage est obtenue en soumettant des éprouvettes, à une température fixée, à des charges constantes. Ces éprouvettes sont des "1/2 Janaf". La limite est la valeur de la charge pour laquelle au bout de 2 mois aucune éprouvette ne casse.

De même la limite de tenue en relaxation est obtenue en soumettant des éprouvettes à un allongement constant. Au bout de 2 mois la valeur à partir de laquelle aucune éprouvette n'est cassée est définie comme la "limite de relaxation".

Pour une composition 22/62/16 ces valeurs sont à 20 °C
- limite de rupture en fluage 4 bars
- limite de tenue en relaxation 47,5 %
propriétés mécaniques de traction allongement de ce propergol :
Sm = 7,7 bars em = 61 %

3. VIEILLISSEMENT

Les essais effectués montrent l'excellente tenue à la température de ces propergols.

31. Tenue à haute température (vieillissement court)

On a réalisé un vieillissement court à 130°C d'une composition sililane 16/76/8

	Sm	ε	em	er
Temps zéro	5 bars	3 %	84 %	86 %
Temps 15 j	7 bars	5 %	67 %	67 %

On note une diminution des allongements, accompagnée d'une augmentation de la contrainte maximum, mais dans des proportions très acceptables.

32. Vieillissement long

Un vieillissement (sur trois ans) a été réalisé sur la composition 16/63/21. Les résultats sont les suivants aux différentes températures. Traction Lhomargy 28 mm/mn.

A 20°C la contrainte maximum reste stable sur la période envisagée
A 60°C elle augmente constamment
A 100°C elle augmente rapidement pendant un mois puis décroît lentement pour revenir à sa valeur de départ après 18 mois

En ce qui concerne l'allongement :

A 20 et 60°C il reste constant sur les 36 mois étudiés
A 100°C il décroît lentement : 50 % en 18 mois

Ce comportement pourrait s'expliquer par un phénomène de surréticulation rapide à 100°C, et plus lente à 60°C.

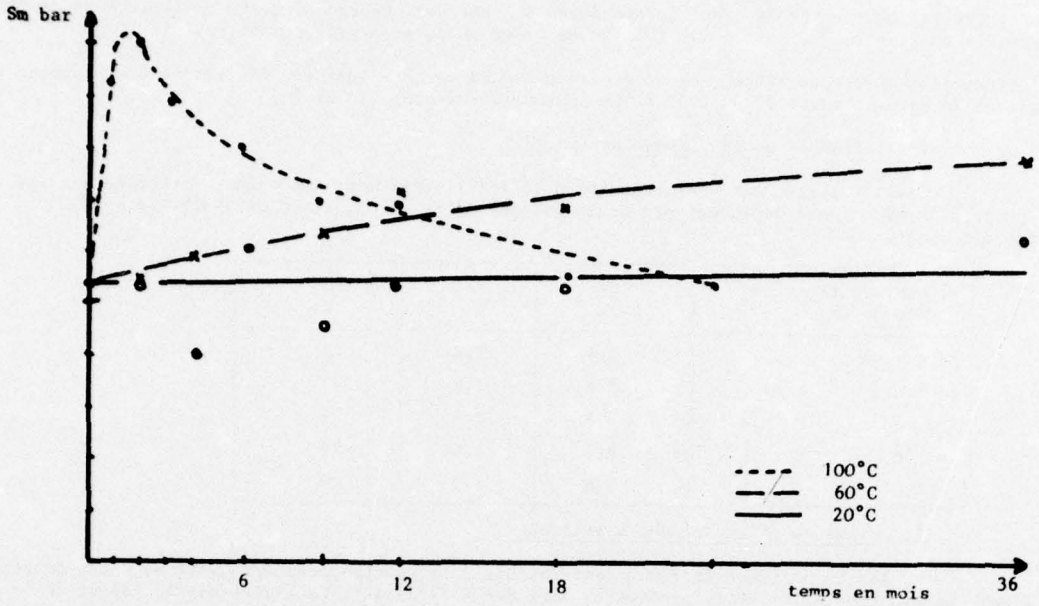

Figure 3 : VIEILLISSEMENT D'UNE SILILANE 16/69/21 Evolution du Sm à différentes températures

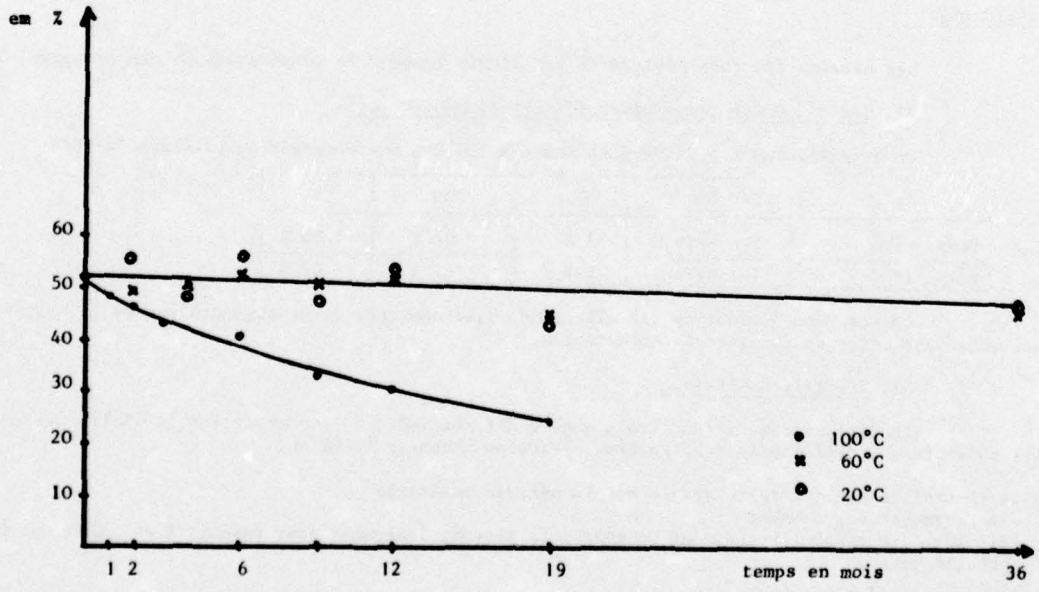

Figure 4 : Vieillissement d'une sililane 16/63/21 Evolution de em à différentes températures

4. INHIBAGE

Les premiers tirs de sililane en blocs libres Mimosa (blocs de 3 kg), diamètre 90 mm, longueur 300 mm, se sont accompagnés de plusieurs anomalies de pression. Il s'agissait de l'existence d'une surpression apparaissant vers le tiers ou le quart du temps de combustion normal.

L'origine de ces incidents a pu être attribuée à l'existence d'un jeu trop important entre bloc et propulseur pouvant conduire à des déchirements en fond de dent lors de la mise en pression, grâce à des essais de mise en pression de rondelles et à des tirs où ce jeu a été éliminé par un garnissage de résine ou un surbobinage du bloc par un ruban adhésif.

Dans ces conditions nous n'avons observé aucun tir défectueux durant toute l'étude. Ce comportement paraît lié à la faible valeur de ε des compositions sililanes et paraît exclure la possibilité de fabriquer des blocs moulés-collés. En effet les contraintes auxquelles est soumise le propergol dans ces blocs engendreraient des fissures et donc des incidents au cours du tir.

5. PROPRIETES BALISTIQUES

51. *Vitesse de combustion*

511. Influence du taux de charge

L'ensemble des résultats a été reporté sur la figure 5 sous la forme d'un diagramme ternaire où les courbes tracées sont les courbes d'isovitesse à 70 bars. On note l'importance du taux de liant sur la vitesse. Celle-ci croît lorsque le taux de liant diminue.

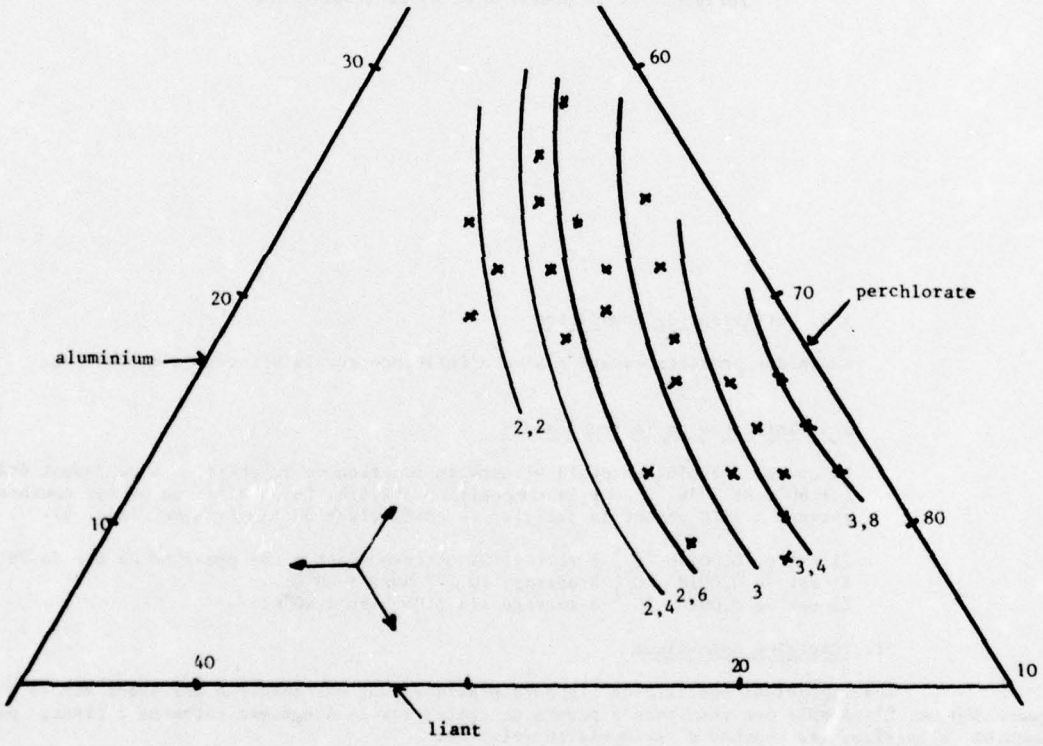

Figure 5 : VITESSE DE COMBUSTION DES SILILANES A 70 BARS (blocs de 3 kg) en cm/s
Influence de la composition

512. Influence de la pression

La courbe de vitesse-pression a été tracée au Strand Burner pour la composition 14/64/22 L'exposant de pression de la loi $V = ap^n$ est de 0,25 entre 20 et 100 bars.

Cette même courbe a été obtenue pour la composition 16/76/8 à partir de résultats de tirs de bloc mimosa de diamètre 90 mm, longueur 300 mm. L'exposant de pression entre 50 et 150 bars est de 0,37 (fig. 6).

La courbe a pu être tracée entre 7,5 et 144 bars sans problème d'allumage.

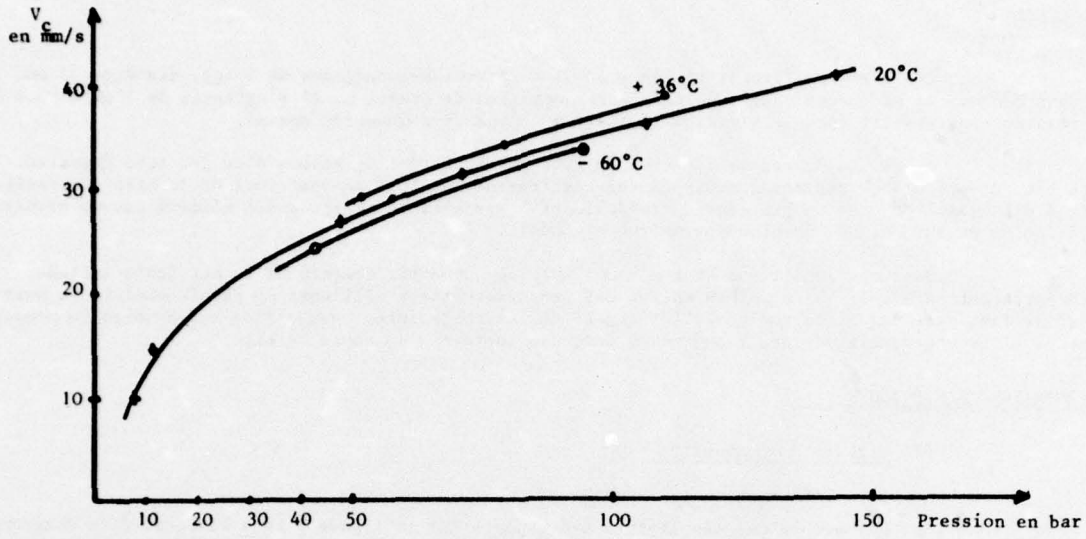

Figure 6 : VITESSE DE COMBUSTION D'UNE SILILANE 16/76/8 EN BLOCS DE 3 KG
Influence de la pression et de la température

513. Catalyseur de combustion

Aucun des produits essayé n'a eu d'influence sur la vitesse de combustion.

514. Influence de la température

La courbe d'évolution de la vitesse en fonction de la pression a également été établie à + 60°C et - 36 °C pour la composition 16/76/8. La comparaison de ces courbes avec celle obtenue à 20°C permet de calculer le coefficient de température (fig. 6).

Il est de 0,00168 $°C^{-1}$ à serrage 92 correspondant à une pression de tir de 70 bars à 20°C.
Il est de 0,0018 $°C^{-1}$ à serrage 70 (47 bars à 20°C)
Il est de 0,0016 $°C^{-1}$ à serrage 118 (105 bars à 40°C)

52. Impulsion spécifique

Les impulsions spécifiques standard pratiques ont été mesurées sur blocs Mimosa Ø 90 mm, longueur 300 mm. L'ensemble des résultats a permis de tracer sur le diagramme ternaire : liant, perchlorate d'ammonium, aluminium, les courbes d'isoimpulsion (fig. 7).

Tout comme les courbes d'isovitesse, les courbes d'isoimpulsion sont grossièrement parallèles aux droites de même taux de liant. L'impulsion maximum sera donc définie par les critères de fabricabilité Ainsi, en limite de fabricabilité, l'impulsion maximum est obtenue pour la composition 16/76/8 avec 229,1 secondes d'impulsion spécifique 70/1.

La corrélation habituelle entre Mimosa de diamètre 90 mm, longueur 300 mm et Mimosa de diamètre 203 mm (blocs de 40 kg), longueur 1000 mm, permet d'avancer avec ce dernier une impulsion spécifique pratique de l'ordre de 233 secondes pour la composition 16/76/8 dans les conditions standard (on évalue à 17 secondes le gain d'impulsion obtenu pour un tir à 150 bars et 22 secondes pour 200 bars).

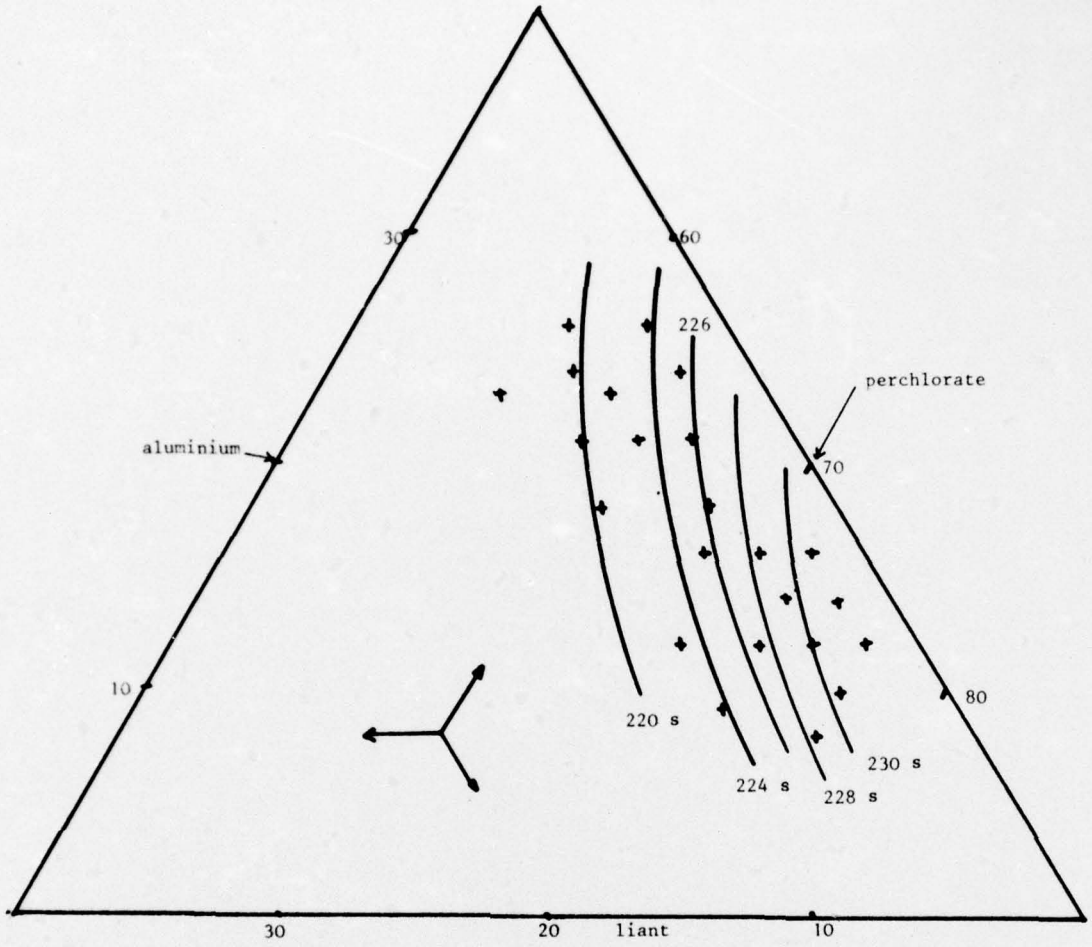

Figure 7 : IMPULSION SPECIFIQUE DES SILILANES (70/1) en blocs de 3 kg
Influence de la composition

6. CONCLUSION

Un nouveau type de propergol utilisable en bloc libre a pu être mis au point avec les propriétés suivantes :

- une résistance au séjour à haute température (130 °C)
- des propriétés mécaniques stables dans une large plage de température (- 60°C, + 60°C)
- un bon vieillissement
- des vitesses de combustion élevées
- une impulsion spécifique moyenne variable en fonction du taux de liant.

PROPERGOLS A FORTE IMPULSION SPECIFIQUE ATTENUANT PEU LES ONDES RADIOELECTRIQUES

G. PRIGENT Ingénieur de recherche
Chef de programme des études de propergols transparents aux ondes radioélectriques
SNPE Centre de Recherches du Bouchet 91710 VERT LE PETIT

Cet exposé a pour but de présenter, plus particulièrement, des résultats expérimentaux obtenus lors d'essais, sous vide en caisson (ou soufflerie) ou à l'air libre, pour déterminer les propriétés balistiques de propergols telles que l'impulsion spécifique ou la vitesse de combustion et caractériser ces mêmes compositions du point de vue atténuation radar hautes fréquences 10 GHz par des mesures d'atténuation transversales ou diagonales. Les chargements de missiles tactiques effectués avec ces propergols nécessitent de connaître les propriétés mécaniques de ces propergols. Quelques résultats sont présentés et permettent de juger de l'influence des additifs anti-atténuants indispensables sur des propriétés mécaniques Sm, em et er (Annexe A) de ces propergols. Outre les compositions à 82 % d'oxydant, quelques résultats sont présentés sur une composition à 89 % d'oxydant dont 15 % d'octogène, l'objectif recherché étant la discrétion dans le visible de ce type de compositions.

Introduction

La mise au point de propergols pour le chargement du missile MASURCA a conduit, il y a dix ans, la direction des Poudres à s'intéresser à la transparence du jet d'un propulseur aux ondes radar hautes fréquences. Lorsque l'illuminateur de la cible est un radar continu, les missiles équipés d'un autodirecteur semi-actif ont besoin, pour mesurer la fréquence Doppler à bord de l'engin, d'une référence. Dans ce cas un récepteur auxiliaire capte par l'intermédiaire d'une antenne placée à l'arrière des missiles le rayonnement direct provenant du radar illuminateur. Les ondes électromagnétiques issues de ce radar en traversant le jet subissent une atténuation définie par $\alpha = -8{,}686 \frac{\omega}{c} \beta$ (1)

ω : fréquence du signal radar (rd/s)

c : vitesse de la lumière (m/s)

β : indice d'extinction du milieu de propagation

α : coefficient d'atténuation (dB/m)

Dans la forme la plus générale l'indice β a pour expression :

$$\beta = \frac{1}{\sqrt{2}} - \left[\left(1 - \frac{\omega_p^2}{\omega^2 + \nu^2}\right) + \left(1 - \frac{\omega_p^2}{\omega^2 + \nu^2}\right)^2 + \left(\frac{\omega_p^2}{\omega(\omega^2 + \nu^2)}\right)^2 \right]^{1/2} \qquad (2)$$

avec m masse de l'élection

ε_o permittivité du vide

$$\omega_p = \sqrt{\frac{n_e e^2}{m \varepsilon_o}} \qquad (3)$$

L'atténuation est, en particulier, dépendante selon (2) et (3) de la densité électronique n_e et de la fréquence de collision électron neutres ν. Dans un jet de propulseur il y a en général une décroissance de la pression sur l'axe à partir du plan de sortie de tuyère et la densité électronique sur l'axe dépend fortement de ce gradient de pression.

Dans certains cas, selon la composition du mélange gazeux issu de la combustion du propergol il existe une zone annulaire dans laquelle des gaz réducteurs du mélange rebrûlent avec l'oxygène de l'air et créent un phénomène appelé post-combustion. L'élévation de température résultante provoque un accroissement de la densité électronique donc de la valeur d'atténuation.

De nombreux auteurs ont proposé des modèles théoriques pour expliquer et interpréter la post-combustion qui est la cause principale de l'atténuation.

A la SNPE des études sont effectuées depuis plusieurs années pour :

- mesurer l'atténuation de l'onde électromagnétique dans le jet

- caractériser et comparer les compositions de propergols composites peu atténuants. Chronologiquement, les premières compositions de propergols étudiées pour résoudre ce type de problème utilisaient un liant polyuréthanne avec un taux d'oxydant, généralement du perchlorate d'ammoniaque, compris entre 75 et 82 %. Les résultats expérimentaux montraient que l'atténuation minimum était obtenue pour une composition à 75 % d'oxydant (isolite 30). L'industrialisation d'une composition voisine a constitué l'étape pour la définition du chargement de l'étage croisière du missile Masurca. L'amélioration des performances balistiques s'est poursuivie par l'utilisation de liant polybutadiène, moins oxygéné. L'obtention d'un équivalent en oxygène pour la composition de propergol, nécessite un taux d'oxydant supérieur à 75 %. Cette conséquence a conduit à la formulation de propergol à 82 % de ClO_4NH_4 (butalite) puis l'augmentation simultanée du taux d'oxydant et éventuellement du taux d'octogène dans la composition n'a eu ensuite pour but que l'amélioration des propriétés balistiques.

2. PROPERGOLS BUTALANE A 82 % DE PERCHLORATE D'AMMONIAQUE

La composition de départ était à 18 % de liant polybutadiène. Compte-tenu des travaux effectués aux USA par LD Smoot [1] et son équipe nous avons étudié l'influence des faibles taux d'aluminium 0,5 ; 2 et 4 % incorporés dans un propergol (butalane) à taux d'oxydant constant 82 % sur les propriétés balistiques et mécaniques et sur les valeurs du coefficient d'atténuation de ces compositions.

21. Généralités

L'incorporation d'aluminium, à faible taux, dans une composition à 82 % de ClO_4NH_4 présente trois avantages :

- augmenter l'impulsion spécifique
- augmenter la densité du propergol
- augmenter la charge de la composition donc diminuer les valeurs du coefficient d'atténuation

et des inconvénients dont le principal est la diminution du taux de transmission dans le visible et le proche infra-rouge d'un signal lumineux à travers le jet.

22. Caractéristiques théoriques des compositions à 82 % de ClO_4NH_4

221. Impulsion spécifique, température de combustion

2211. Calculs

A partir des données sur le propergol telle que son enthalpie de formation et sa composition atomique, et connaissant la pression de fonctionnement du moteur, les calculs sur la détente des gaz dans la tuyère peuvent s'effectuer suivant deux hypothèses soit en supposant la composition du mélange gazeux constant et égale à celle dans la chambre (détente figée) soit en recalculant cette composition dans chaque section de tuyère (détente en équilibre).

2212. Résultats

La figure 1 présente les résultats de calcul de l'impulsion spécifique (Isp) en fonction du taux d'aluminium dans les deux hypothèses formulées ci-dessus. Les valeurs obtenues montrent que l'Isp en détente figée est inférieure à l'Isp en équilibre ; l'écart entre ces deux courbes allant croissant quand le taux d'aluminium augmente. La figure 2 présente les résultats de calculs de l'Isp et de la température de combustion en fonction du taux de perchlorate d'ammoniaque dans l'hypothèse de la détente figée.
Les valeurs obtenues montrent l'accroissement de l'Isp avec le taux d'oxydant tant que le taux de liant reste supérieur à 10 %. On observe, la même évolution pour la température Tc.
Notons dans cette figure que la composition à 82 % de perchlorate possède une Isp (70/1) de 234,8 s et une Tc de 2600 °K.

222. Pouvoir réducteur

2221. Définition

Si l'on admet le processus suivant :

post-combustion ⟶ ionisation accrue ⟶ atténuation augmentée

il apparait important de connaître les causes de la post-combustion pour expliquer les conséquences sur les valeurs de l'atténuation.
Il est intéressant pour cela de définir le pouvoir réducteur du mélange gazeux produit par la combustion du propergol. Ce peut être :

$$P = \frac{Z_{CO} + Z_{H2}}{Z}$$

Z est le nombre total de moles dans le plan de sortie de la tuyère calculée pour une détente en équilibre.

2222. Résultats

La figure 3 présente les valeurs calculées de P pour des compositions de 82 % de perchlorate et à faible pourcent d'aluminium.
Entre 0 et 4 % d'aluminium P décroît de 37 à 27 %.
Ces résultats peuvent être rapprochés de ceux que nous verrons plus loin et permettront de montrer la relation existant entre pouvoir réducteur et atténuation.

23. Propriétés balistiques

231. Impulsion spécifique standard mesurée (Isms)

2311. Moyen de mesure

L'Isms est un paramètre balistique caractéristique du propergol obtenu après mesure d'une intégrale de poussée et d'un poids de poudre brûlée.
Au banc fixe, le moteur standard type utilise un bloc de propergol étoilé de diamètre 203 mm et de longueur 1000 mm.
Pour des raisons de commodités, il est aussi employé un autre moteur standard utilisant un bloc de propergol étoilé de diamètre 90 mm et de longueur 300 mm.
Par type de composition il existe des corrélations entre les différentes Isms obtenues à l'aide de ces deux moteurs.
Quel que soit le moteur, la pression de fonctionnement doit être de 70 bars et la pression dans le plan de sortie de la tuyère égale à 1 bar. Les essais s'effectuent toujours dans des conditions voisines de celles indiquées ci-dessus et des corrections doivent être effectuées sur la valeur de l'impulsion calculée. Le rapport des aires utilisé pour ce type de composition est constant et égal à 8,02 :

$$\varepsilon = \frac{As}{At}$$

As aire de sortie de tuyère
At aire du col
Cette valeur correspond dans le graphique théorique (C_F, ε) au maximum du C_F lorsque la pression de fonctionnement du moteur est de 70 bars (Annexe B).

2312. Résultats

La figure 4 donne l'évolution de l'Isms en fonction du taux d'aluminium pour un taux de perchlorate fixé.
Il existe un palier peu significatif tant que le taux d'aluminium reste inférieur à 0,5 %. Au-delà l'Isms croît régulièrement avec ce taux d'aluminium. Les courbes en pointillés rappellent les valeurs théoriques de la fig.1 et permettent de les comparer aux valeurs expérimentales obtenues à l'aide d'un moteur de diamètre203.

232. Vitesse de combustion

La figure 5 donne des valeurs de vitesses de combustion à 35 bars de ces compositions. L'accroissement de vitesse pour des compositions dans lesquelles ne varie que le taux d'aluminium est de 27 % quand ce taux passe de 0 à 4 %.
On a porté sur le graphique des valeurs de vitesse obtenues avec des compositions utilisant des additifs anti-atténuation (A et B). Ils accroissent la vitesse des compositions d'autant plus que le taux d'aluminium croît.

24. Propriétés mécaniques

Les propriétés mécaniques à 20° de ces propergols sont données au tableau de la figure 6. L'introduction d'additifs anti-atténuation présente l'inconvénient de détériorer les propriétés mécaniques du produit fini. Malgré cela nous n'avons éprouvé aucune difficulté pour effectuer avec ce type de compositions des chargements moulés-collés.

25. Atténuation radar

251. Rappel

Selon Jensen et Webb [6] la post-combustion apparait s'il y a formation de radicaux H et OH en excès. Certains métaux présentent la particularité d'accélérer les processus de recombinaison des radicaux actifs tel qu'H et OH empêchant aussi l'apparition de la post-combustion. L'intérêt est donc d'incorporer dans les compositions de propergols des additifs métalliques qui jouent le rôle de catalyseur de recombinaison des radicaux H et OH.

252. Moyens

Les montages expérimentaux [3] pour mesurer l'atténuation radar dans les jets sont :

- un banc mobile utilisant un moteur de diamètre 90 cm dans un caisson de 100 m3. Un tir effectué dans le caisson permet d'obtenir les courbes d'atténuation en fonction du temps, en différents points du jet.
- un banc mobile utilisant un moteur de diamètre 203 à l'air libre. Un tir effectué sur ce banc permet d'obtenir les valeurs d'atténuation uniquement sur l'axe du jet.

Les compositions présentées dans ce texte ont des niveaux d'atténuation très faibles et les tirs effectués dans le caisson donnent des grandeurs mesurables à la limite de détectabilité des capteurs. Cette installation permet d'obtenir des diamètres du jet plus importants et des niveaux d'atténuation plus élevés.

- une installation utilisant un moteur horizontal tournant autour d'un axe vertical permet d'obtenir des valeurs d'atténuation diagonales dans le jet.
- une installation utilisant les veines de souffleries de l'ONERA à Modane nous permet d'obtenir des valeurs d'atténuation transversales dans un jet de propulseur pour un missile en mouvement.

253. Résultats

La figure 7 présente le résultat de 2 tirs dans le caisson de simulation d'altitude (CSA). La composition étudiée est une butalane 82/2. La pression de départ dans le caisson est dans les deux cas égale à 520 mm de Hg. En fin de tir elle a 720 mm Hg. Les courbes en pointillés se rapportent au tir de la composition sans additif. Les courbes en trait continu concernent le tir de la composition avec additif. Les courbes 1 et 2 se rapportent aux valeurs d'atténuation en fonction du temps. Les courbes 3 et 4 se rapportent aux valeurs de pression de fonctionnement du moteur en fonction du temps. Les courbes 5 et 6 réprésentent le mouvement pendulaire du moteur en fonction du temps.
Nous concluons au vu des formes des courbes 1 et 2 du mode opératoire du dépouillement [3] à l'intérêt de l'additif anti-atténuant dans la butalane 82/2. La figure 8 présente des résultats identiques et permet dans le cas de la butalane 82/4 de conclure à une plus grande efficacité de l'additif A par rapport à l'additif B. Les figures 9 et 10 présentent chacune respectivement 3 courbes :

- atténuation en fonction du temps
- pression de fonctionnement des propulseurs en fonction du temps
- poussée du propulseur en fonction du temps

Une butalane 82/4 possède un niveau d'atténuation moyen de 0,8 dB (fig. 9), la même composition avec additif tirée dans des conditions identiques a un niveau d'atténuation de 0,15 dB (fig. 10).

Le tableau de la figure 11 présente des résultats obtenus par des tirs avec mesures de l'atténuation diagonale. C'est l'expérience se rapprochant le plus près de l'essai sur missile réel mais c'est également la plus chère à mettre en oeuvre. On constate à taux d'additif constant et pour des pressions de fonctionnement voisines, que l'atténuation est maximum entre 0 et 2 % d'aluminium et décroît ensuite quand ce taux augmente.
On juge également de l'intérêt des additifs en comparant les valeurs d'atténuation de la butalane avec A ou B.
La décroissance de l'atténuation quand le taux d'aluminium augmente est en relation avec la décroissance du pouvoir réducteur du mélange gazeux issu de la combustion. On observe cette décroissance sur des mesures effectuées en transversales. Préalablement il est nécessaire de corriger les valeurs obtenues au cours du tir. Pour obtenir a on divise les valeurs A d'atténuation par le diamètre Ds en mm du plan de sortie tuyère et on corrige les valeurs obtenues dans le rapport des débits, en prenant une des compositions comme référence.

Le tableau de la fig. 12 donne les valeurs a obtenues comme indiquées ci-dessus, pour les 3 compositions butalanes à 0,5-2 et 4 % d'aluminium en prenant comme débit de référence celui de la butalane à 0,5 % d'aluminium.
On constate que le minimum d'atténuation se situe au-delà de 4 % d'aluminium dans la composition à 82 % d'oxydant.

26. Corrélation expérience théorique

Parallèlement aux expériences effectuées sur ce type de composition la mise au point de programmes de calcul permet actuellement de prédire le niveau d'atténuation (fig. 13). Tous les programmes de calcul de concentration électronique puis d'atténuation dans les jets admettent des hypothèses simplificatrices.

Le mélange des gaz de combustion avec l'air ambiant dépend des valeurs données aux coefficients de transfert tels que nombre de Schmidt ($C_p\mu/k$) et nombre de Prandlt ($\mu/\rho D$) qui dépendent de la viscosité μ du mélange gazeux résultant donc du modèle retenu a priori compte-tenu de la température et de la composition du milieu. L'écart entre les maxima observés sur la fig. 13 est en partie du au mauvais choix de valeur de ces coefficients.

On a pu constater par calcul que le taux d'alcalins (Na, K) modifiait considérablement les niveaux d'atténuation maximum dans un jet. Pour une butalane à 4 % d'aluminium et 18 % de liant l'atténuation maximum passe de 0,02 dB à 1 dB quand les impuretés en K passe de 0 à 400 ppm dans la composition du propergol.

La connaissance de ces valeurs entraine les actions suivantes :
- en ce qui concerne les compositions, diminuer le taux d'impuretés alcalines dans les constituants du propergol et plus particulièrement dans l'oxydant,
- en ce qui concerne l'agencement du moteur, utiliser des composants (liner, protection thermique, tube de flamme) possèdant de faibles taux en alcalins.

Cette deuxième action est d'autant plus nécessaire que la destruction par combustion ou ablation de ces produits pendant les essais et pendant les tirs réels est importante et risque de rendre inopérantes les dispositions prises au niveau de la formulation du propergol.

3. PROPERGOLS A CARACTERISTIQUES AMELIOREES

31. Généralités

D'après Smoot [8] et d'après les quelques expériences que nous avons effectuées dans ce domaine nous savons que l'atténuation diminue avec le taux de charge et qu'à taux de charge constant l'atténuation augmente avec le taux d'aluminium.

En vertu de ces deux constatations il est possible de formuler des compositions plus énergétiques que les butalites à 82 % de ClO_4NH_4 et atténuant moins. Notre recherche a porté sur des compositions à plus de 88 % en taux de charge dans lesquelles on a en plus substitué le perchlorate par de l'octogène (15%). Pour des raisons de fabricabilité, toutes ces compositions utilisent un liant à base de PBHT. Ces compositions présentent en outre l'avantage de donner très peu de solides dans les gaz de combustion. Elles sont du type "primarly smokeless".

La figure 2 indique que les butalites à 11 % de liant possèdent une Isp 70/1 théorique figée de 243 s et une température T°K de 3080°. Une butalite à même taux d'oxydant dont 15 % d'octogène possède une Isp (70/1) théorique figée de 246,5s et une température de combustion identique à la précédente. L'évaluation pour ces deux compositions de l'indice de performance Isp x ρ donne respectivement 421,8 pour la butalite et 426,7 pour la butalite à l'octogène.

32. Isms et vitesse de combustion

321. Vitesse de combustion

L'utilisation du liant PBHT à la place du liant PBCT a eu pour conséquence d'abaisser la vitesse de combustion à 70 bars d'environ 20 %. C'est ainsi que les valeurs obtenues en Strand Burner pour une butalite 88 passe de 11,7 mm/s à 9,3 mm/s et pour une butalite 89 de 12,3 mm/s à 9,3 mm/s.
Des mesures de vitesse de combustion effectuées sur deux compositions, l'une avec un liant PBCT, l'autre avec un liant PBHT, contenant toutes deux un accélérateur de combustion tel que le chromite de cuivre montrent que l'effet signalé ci-dessus n'est plus vrai.
Pour la composition contenant 15 % d'octogène les essais sur blocs fournissent la valeur 9,7 mm/s à 70 bars (fig. 14). D'une manière générale l'octogène à granulométrie identique ou voisine de celle de ClO_4NH_4 a tendance en absence de l'aluminium à abaisser la vitesse de combustion du propergol.

322. Impulsion spécifique standard mesurée

En petits blocs (Ø 90 L = 300 mm) la composition à 89 % d'oxydant dont 15 % d'octogène possède une Isms de 238,1 s ce qui équivaut en gros bloc (Ø 203 L = 1000 mm) à une Isms de 243,1 s.
Rappelons qu'une butalite à 89 % de ClO_4NH_4 possède une Isms en gros bloc de 240 s. On peut remarquer que les écarts théoriques et expérimentaux sont identiques : 3 s (la théorie donne 243,2 et 264,4 pour les compositions ci-dessus).

33. Propriétés mécaniques

Après avoir effectué une cuisson en 14 j à 50°C les propriétés mécaniques permettent de constater qu'avec le liant PBHT Sm croît et em décroît quand on augmente le taux de charge de 88 à 90 %. Ces variations de Sm et de em sont identiques quand le taux d'octogène augmente (fig. 13).

34. Atténuation radar

Les premiers essais effectués en utilisant des petits blocs donnent des résultats tels que les valeurs transversales d'atténuation restent inférieures à la limite de détectabilité des capteurs dans la chaîne de mesures, qui est de 0,1 dB.

4. DISCRETION DANS LE VISIBLE

La présence d'aluminium diminue le taux de transmission. C'est ainsi que 0,5 % d'aluminium fait descendre [redacted] de 100 à 30,2 %. De même que l'augmentation du taux de charge parait diminuer la transmission, cf 82/0.5 et 85/0.5 de la fig. 14.

5. CONCLUSION

Il est possible de fabriquer des propergols impulsifs et relativement transparents aux ondes électromagnétiques. Accessoirement, on trouve dans la gamme proposée des propergols discrets dans le domaine du visible et du proche infra-rouge. Par rapport aux propergols les plus performants industrialisables, leur densité est un peu faible. Les résultats auxquels nous aboutissons et le cheminement de la recherche pour les prochaines années nous conduit à espérer avec des compositions à 10 % en liant d'atteindre le cap des meilleures Isp actuelles et des densités voisines de 1,78 g/cm3.

[1] DUFOUR
Etudes de l'atténuation des ondes électromagnétiques par les gaz d'échappement des fusées à propergols solides.
Note technique n° 772 Laboratoire de balistique de Sevran 1ère partie : moyens d'études

[2] DUFOUR
Etudes de l'atténuation des ondes électromagnétiques par des gaz d'échappement des fusées à propergols solides
Note technique n° 962 Laboratoire de Balistique de Sevran 2ème partie : étude expérimentale

[3] PRIGENT. JUILLE
Etude théorique et expérimentale de l'ionisation dans les jets de propulseurs
ICT Jahrestagung 1974 27-29 juin p 227 à 250

[4] PERGAMENT. DE JENSEN
Influence of Chemical kinetic and turbulent transport coefficients on afterburning rocket plumes
J spacecraft Vol. 8 n° 6 june 1971 p 643 à 649.

[5] SMOOT, SIMONSEN
Exhaust plume prediction model for a low altitude supersonic missile
AIAA paper n° 72.1170

[6] JENSEN. WEBB
Afterburning predictions for metal-modified propellant motor exhausts
AIAA paper n° 75.1232

[7] EDWARD. MC HALE
Experimental evaluation of chemical agents in suppressing missile plume afterburning
AIAA paper 75.1233

[8] SMOOT
Investigation of high performance solid propellant with favorable attenuation characterisation mechanisms which cause radar attenuation
LPC Report 756 F Lockeed Redlands Californie Janv. 1967

THE MEASUREMENT OF IGNITER HEAT FLUX IN SOLID PROPELLANT ROCKET MOTORS

I.E. Smith
Reader in Engineering Thermodynamics
Cranfield Institute of Technology,
Cranfield, Bedford.

and

K.M. Siddiqui
Research Officer
Council of Scientific & Industrial
Research, Karachi.

SUMMARY

Using platinum thin film gauges, the temporal and axial distribution of heat flux from two different types of igniter compositions and two different igniter geometries has been measured. The parameters employed were different igniter masses, tube lengths and nozzle throat diameters. The size distribution of the particulate matter arising due to combustion of pyrotechnic materials has also been investigated and deducations have been made regarding its contribution towards total heat. Whereas radiation plays a relatively insignificant part in the total heat transfer process, the 'point' heat flux due to particulate heat transfer has been found to be one of the most important modes of heat transport during an igniter action and which may, in fact, be responsible for the first appearance of ignition flame in a solid propellant rocket motor.

NOMENCLATURE

A_p	=	area of the conduit
b	=	coefficient of burning
c_p	=	specific heat
D_p	=	port diameter
d_c	=	crater diameter
d_p	=	particle diameter
H_c	=	heat of dissociation of cellulose acetate
h	=	heat transfer coefficient
k	=	thermal conductivity
L	=	motor length
m_p	=	particle mass
N	=	total number of particles
n	=	pressure index
Q	=	total heat absorbed by the motor body
q	=	heat transfer J/m^2
$\dot{q}$	=	heat flux, W/m^2
r	=	rate of burning, mm/s
T_c	=	temperature of cellulose acetate
T_{p_o}	=	initial particle temperature
T_{p_t}	=	particle temperature after time, t
t	=	time
X	=	axial distance from igniter
ρ_c	=	density of cellulose acetate
ρ_p	=	density of the particle

INTRODUCTION

The ignition of a solid propellant rocket motor is achieved by the transfer of thermal energy from an igniter to the propellant surface. The pyrotechnic type of igniter, generally a combination of finely divided metallic powders intimately mixed with an inorganic oxide, is sometimes made into pellets or granules to alter its burning rate characteristics to suit various ignition requirements. Todate, data regarding heat-transfer from igniters is extremely meagre with the result that rocket designers depend on past experience, and in order to achieve reliable 'first-time' ignition, tend to provide an over-sufficiency of the thermal impulse. This sometimes results in the fracture of the propellant grain due to the sudden pressure rise and consequently to unpredictable performance or even failure of the rocket motor casing.

Recently several investigators (refs. 1, 2, 3, 4 and 5) attempted to measure the heat-flux from igniters to the summy propellant surface using various types of igniter compositions and varying sizes of rocket motors. However, most of these investigators contented themselves with the measurement of convective heat flux assuming it to be the dominant mode of heat-transfer. Only two investigators (Refs. 3, 5) attempted to measure the radiative component, and none has considered the contribution of solid particles to the heat transport from igniter to the propellant.

The following work was undertaken to measure the heat flux in a rocket motor and its variation in space and time, using two currently employed pyrotechnic compositions, and to study in particular the contribution of particulate matter emitted by the igniter combustion to the total heat transfer. In addition, the effects of such parameters as igniter mass, motor length and motor port to nozzle throat area ratios on heat transfer to the propellant have also been examined.

EXPERIMENTAL DETAILS

To measure the spatial as well as the temporal distribution of heat flux from igniters, two separate rigs were designed to simulate conditions in a rocket-motor. One rig was built to measure the distribution of total heat flux as contributed by convection, conduction and radiation and also to measure the radiative component separately. The second was designed to measure the size distribution and heat contribution of the particulate matter emitted during igniter action.

Total Heat Flux Rig

This consisted of a 0.30 m long mild steel tube which was extendable to 0.45 or 0.60 meters in separate stages (Fig. 1). A cellulose acetate liner, 3 mm thick, was used to simulate the thermal properties of the propellant.

Thin platinum film heat flux gauges (Fig. 2), fabricated in the laboratory, were used to measure wall temperatures. These were prepared by coating of Hanovia Liquid Bright Platinum Paint, 05-X, on round discs of pyrex glass of similar curvature as that of the motor conduit, and baking them at 720^{0}C in a furnace (ref. 6).

The heat flux was calculated using Eq. 1, based on one-dimensional theory of heat-conduction in a semi-infinite slab (refs. 7, 8).

$$\dot{q} = \frac{\rho c k}{\pi} \frac{T(t)}{\sqrt{t}} + \int_0^t \frac{T(t) - T(\tau)}{(t - \tau)^{3/2}} d\tau \qquad \ldots\ldots(1)$$

The errors due to the singularity at $t = \tau$ were reduced by using a numerical technique described by Cook and Felderman (ref. 9).

These gauges were mounted flush along the conduit at positions P1 and P9 at distances from the igniter of 50, 100, 150, 200, 250, 350 and 530 mm respectively. During a firing the platinum film gauge output was recorded on either a 12-channel U.V. recorder or an ampex FR-1300 magnetic analogue tape recorder via a multi-channel constant current generator. The recorded data was digitized using an M 16.2 analogue computer and processed on an ICL 1903 digital computer.

To record the chamber pressure a pressure transducer having a response time of better than 1m sec was placed facing position P3, 150 mm from the igniter.

In order to study the effect of nozzle-throat area on the amount of heat absorbed by the motor body, three convergent nozzles with port to throat area ratios of 56, 20 and 10 were employed.

Measurement of Heat Flux due to Radiation

For the measurement of thermal radiation, the platinum resistance thermometers were modified so that they could act as radiometers. The gauge surfaces were coated with a film of carbon soot less than 2μm in thickness. To protect the carbon film, it was covered with a 2 mm thick glass disc. These radiometers were calibrated using a Spembly carbon tube furnace. During a test, these gauges were receded by 20 mm from the conduit surface and a nitrogen sweep was introduced to protect their surfaces from particulate deposits.

Particulate Heat Transfer Rig

This rig was designed to obtain the size distribution of particles emanating from an igniter, both in time and space, inside a rocket motor. The principle was to have a narrow slot rotating with respect to an outer liner which acted as a shutter so that igniter particles could be sampled along the conduit (Fig. 3). It consisted of an inner rocket-motor tube 0.3 meters long and of similar dimensions to that of the total heat flux rig. A slot 4 mm wide and 220 mm long was machined on its top side. On the outside of this tube a lead-bronze concentric cylinder was arranged to rotate on bearing surfaces formed at either end of the tube. Other than at the bearing surfaces, there was a gap of 1.6 mm between the outer rotating cylinder and the inner stationery rocket-tube.

A cellulose acetate sheet 220 mm x 245 mm x 0.5 mm thick was lined inside the outer cylinder so that it rotated with the outer cylinder and effectively reduced the gap between the stationery inner and the rotating outer cylinder to 1.1 mm. The speed of revolution of the concentric cellulose acetate liner was maintained at 1360 revs/min. At this speed the 4 mm wide slot gave a scanning time of 44 ms with a resolution of 0.5 ms. After the firing, the CA sheet was carefully removed. Firstly the deposited

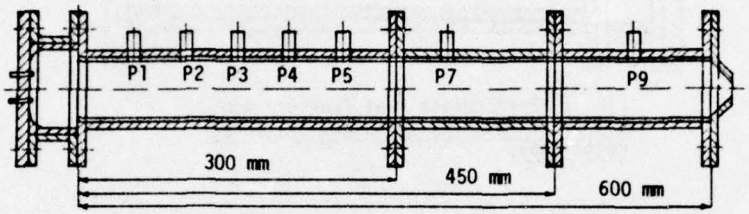

FIG. 1 Total Heat Transfer Rig

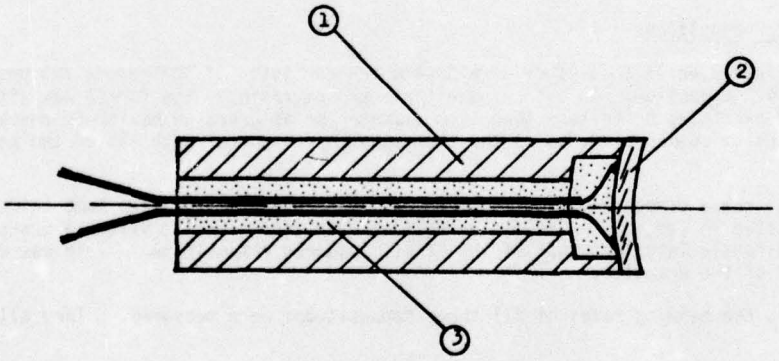

FIG. 2. Construction of a thin platinum film gauge.
(1)teflon cylinder, (2)glass disc, (3)araldite

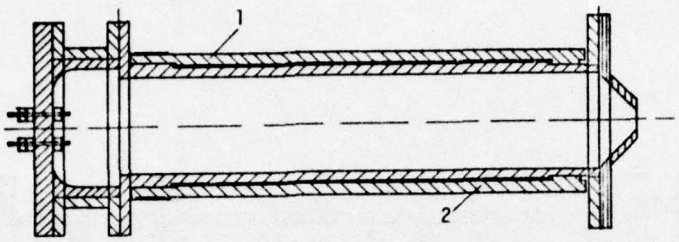

FIG. 3 Particulate Heat Transfer Rig. (1) Outer rotating cylinder. (2) Inner motor tube.

particulate matter and the loose particles were carefully brushed off the sheet on to microscope slides for particle sizing. Secondly, the sheet was washed and dried. The craters due to particle impacts on the sheet at each corresponding gauge position were counted using a Quantimet 720 Particle Size Analyser. The size distribution of loose particles was matched with carter sizes to find a correspondence between the two.

RESULTS AND DISCUSSION

Properties of Igniter Compositions

The pyrotechnic materials used in this study were SR44 which consisted of 30% boron, 70% potassium nitrate, and SR371C which was 42% magnesium, 50% potassium nitrate and 8% resin. The former was either in powder form, the majority of particles being less then 4 μm diameter or as granules having an average diameter of 700 μm. The magnesium composition was in the form of a coarse powder with 75% of the particles less than 10 μm.

Heats of combustion of these compositions were determined using a nitrogen-filled bomb calorimeter, the average values are listed in Table 1. It will be noticed that the calorific value of granulated SR44 was found to be consistently less than that of the finely powdered composition. This was due to the incomplete combustion of the granules.

Using a strand burner, the burning rates of all three compositions were measured. They all followed the burning rate law

$$r = b\,p^{n} \qquad \ldots\ldots(2)$$

where burning rate, r, is in mm/sec and pressure, p, is in atmospheres. The values of burning coefficient, b, and pressure exponent, n, are also listed in Table 1.

Composition	Burning rate coefficient b	Burning rate exponent n	Heat of Combustion
SR44 granulated	219.0	0.68	7540 x 10^3J/Kg
SR44 fine power	20.5	0.27	8250 x 10^3J/Kg
SR371C Coarse Powder	11.0	0.48	7460 x 10^3J/Kg

TABLE 1 CHARACTERISTICS OF PYROTECHNIC COMPOSITIONS

Total Heat Transfer

Figures 4, 5 & 6 show the total heat flux received from the three forms of pyrotechnic. Several general observations can be made regarding thses plots. The heat flux peaks at different positions along the conduit do not occur at the same time but they are all registered during the first 12 ms after which period the situation stabilises and almost smooth falling gradients of the heat flux, $\frac{d\dot{q}}{dt}$, converge to insignificent value of heat flux. The gradient of heat flux, $\frac{d\dot{q}}{dt}$, is almost always a maximum at position P1 nearest to the igniter. The ratio of the heat flux gradient $\frac{1}{\dot{q}}\frac{d\dot{q}}{dt}$ for the first three positions, P1 to P3 is invariably greater than the corresponding ratio of pressure gradient $\frac{1}{p}\frac{dp}{dt}$. But after the initial fast rise of the heat flux gradients, their decay corresponds with the decay in pressure.

The Magnitude & Location of Maximum Heat Flux

The location and magnitude of $\dot{q}_{max}$ for different tube lengths, igniter compositions and masses are listed in Table 2. Although the gradient of $\dot{q}$ is always a maximum at P1, the maximum heat flux does not necessarily occur at P1. In a 0.3 m long tube, its location is invariably at or near P1, but for longer tubes, this site generally shifts doenstream to P3, P5 or even P7. The reason for this would seem to be that with longer tubes, owing to the greater free volume, complete combustion of the powder takes place further downstream in the tube.

The variation in igniter mass appeared to have no consistent effect on the magnitude of maximum heat flux peaks. In fact, in some tests the heat flux peaks obtained by a .002 kg mass of igniter were found to be higher in magnitude than those obtained from .005 mg of the same composition.

The magnitudes of $\dot{q}_{max}$ appear to increase with nozzle diameter. This may be due to the occurrence of greater convective heat transfer because of a larger nozzle throat area.

			0.30m tube		0.45m tube		0.60m tube	
Composition Type	Port To Throat Area Ratio	Weight of the Composition	$\dot{q}_{max}$	Location of $\dot{q}_{max}$	$\dot{q}_{max}$	Location of $\dot{q}_{max}$	$\dot{q}_{max}$	Location of $\dot{q}_{max}$
		(Kg)	(MW/m^2)		(MW/m^2)		(MW/m^2)	
SR44 Granular	56	.002	8.4	P1	8.4	P1	8.4	P2
		.005	9.5	P3	6.0	P3	10.5	P5
"	20	.002	8.9	P1	8.5	P1	6.9	P1
		.005	13.8	P1	10.4	P3	8.0	P2
"	10	.002	15.8	P1	11.5	P1	6.2	P1
		.005	18.0	P1	5.9	P1	8.5	P7
SR44 Powder	20	.002	8.3	P3	10.0	P3	7.1	P3
		.005	11.2	P3	10.5	P3	7.9	P4
SR371C Coarse Powder	20	.002	8.2	P1	6.6	P4	6.8	P1
		.005	10.0	P2	8.0	P5	6.0	P1

TABLE 2 MAGNITUDE AND LOCATION OF MAXIMUM TOTAL HEAT FLUX

Heat fluxes were integrated with respect to time after 5, 10, 20, 40 and 80 ms to obtain heat transfer rates at different positions along the conduit. Fig. 7 is a typical plot of heat transfer rate against non-dimensional length, $\frac{X}{D}$. The initial sharp downward gradients became smoother as the mass of igniter was increased, until almost linear curves tending to become horizontal, were obtained from igniter masses greater than 0.005 kg.

The heat transfer rates were further integrated over the entire area of the motor conduit to obtain total heat delivered to the motor-body. Total heat against mass of the igniter is plotted in Fig. 8, for a motor length of 0.30 m. There appears to be a linear relationship between igniter mass and the total heat received by the motor body, provided the igniter mass is less than a certain limiting quantity. The optimum limit in this case was found to be 0.004 Kg. The reason that this linear relationship breaks down at higher masses appears to be that beyond a certain value, uncombusted material is ejected from the nozzle. The evidence for this was that traces of uncombusted powder were noticed outside the nozzle when tests using .005 kg or more of igniter compositions were conducted.

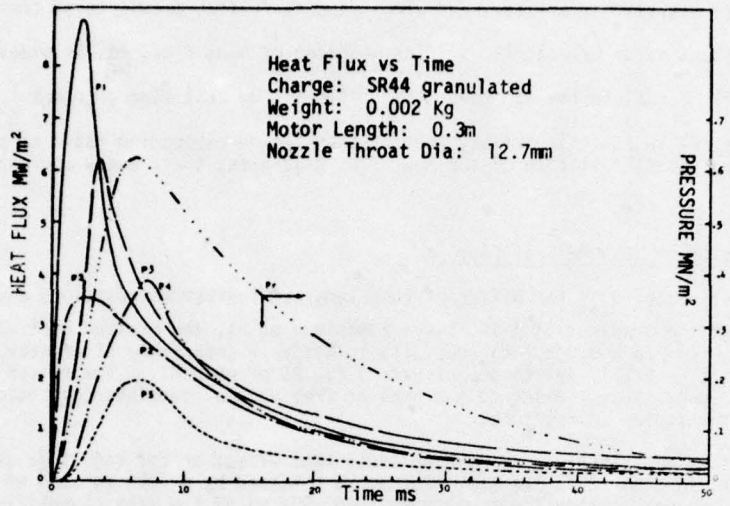

FIG. 4

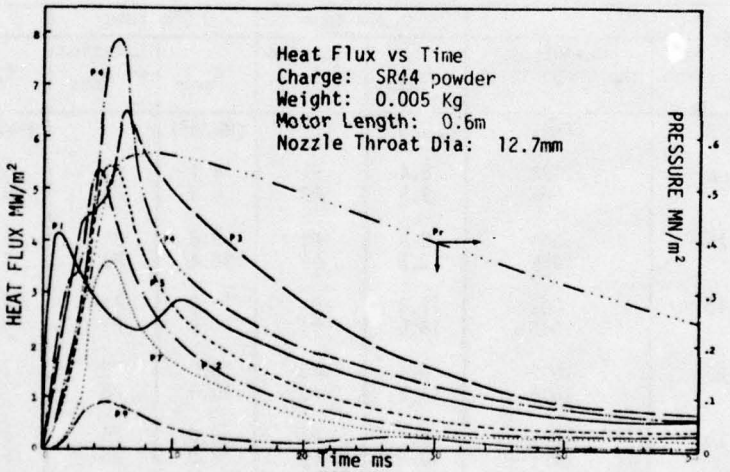

FIG. 5

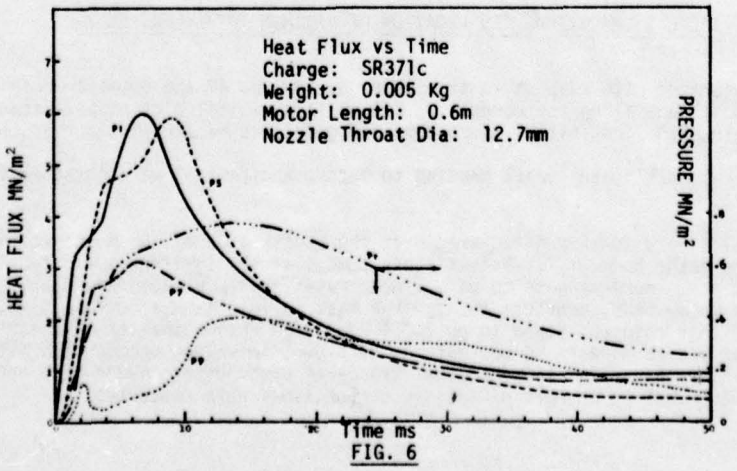

FIG. 6

Taking average values for the heat absorbed in each tube length after 80 ms, Table 3 gives the amount of heat lost through the nozzle (port-to-throat area ratio of 20) based on the bomb-calorimeter measurements of the heats of combustion for each type of composition.

Composition	%age Heat Lost
SR44 granular	72%
SR44 fine powder	80%
SR371C coarse powder	71%

TABLE 3 HEAT LOST THROUGH THE NOZZLE

The effect of port-to-throat area ratio on the total heat absorbed by the motor body is illustrated in Fig. 9, using SR44 granular compositions. It appears that a port-to-throat area ratio of 20 is an optimum from the point of view of heat transferred to the motor conduit, although the dependence is not a strong one.

The total amount of heat absorbed by the motor tube increased with tube length, although not markedly when SR44 compositions were used. However, with SR371C composition, this increase was as high as 33% when the motor tube was lengthened from 0.30 m to 0.6 m. It is believed that this phenomenon is due to the slower rate of burning of the Mg/KNO_3 powder, the greater residence time of the longer tube allowing it to combust more fully.

Radiative Heat Transfer

Fig. 10 provides a typical comparison between total heat flux and radiative heat flux at position P1 in a 0.3 m long tube. The total heat flux peak occurs 4.5 ms before the pressure peak whereas the radiative peak occurs at the same time as the pressure peak. After 18 ms, when the pressure is half its peak value, the radiative heat flux is also halved but the total heat flux falls to 1/6th of its peak value. The radiant flux is clearly dependent upon pressure and hence the density of gases within the motor.

The maximum gradients of heat flux occur at P1 in cm 0.3m tube but as the tube length is increased the sites of maximum gradient as well as of the largest heat flux peaks shift downstream. Table 4 summarises the axial distribution of the sites of heat flux and their magnitudes.

Composition Type	Charge Weight (Kg)	0.30m tube			0.45m tube			0.60m tube		
		$\dot{q}_{max}$ (MW/m^2)	Location of $\dot{q}_{max}$	Time to $\dot{q}_{max}$ (M Sec)	$\dot{q}_{max}$ (MW/m^2)	Location of $\dot{q}_{max}$	Time to $\dot{q}_{max}$ (M Sec)	$\dot{q}_{max}$ (MW/m^2)	Location of $\dot{q}_{max}$	Time to $\dot{q}_{max}$ (M Sec)
SR44 Granular	.002	1.44	P1	6	0.60	P5	11	0.65	P2	12
	.005	3.62	P1	8	2.00	P5	19	2.05	P4	7
SR44 Powder	.002	1.20	P1	7	1.07	P5	12	0.49	P2	10
	.005	3.10	P1	9	0.81	P7	13	1.55	P1	9
SR371C Coarse Powder	.002	1.61	P1	5	0.44	P5	13	0.49	P4	13
	.005	7.50	P2	7	1.56	P7	11	0.62	P3	9

TABLE 4: MAGNITUDE AND LOCATION OF MAXIMUM RADIATIVE HEAT FLUX

Port-to-Throat Area Ratio: 20

The average radiative heat absorbed by the motor body is 3% of the total integrated heat at t = 5 ms but after t = 40 ms, it increases to 18% of the total heat. However, it must be assumed that by this time ignition will have already taken place.

Particulate Heat Transfer

A typical particle impingement pattern obtained on a cellulose acetate sheet after a test is shown in Fig. 11. In a 0.3 m tube the first particle impact and the area of maximum impact of it occurred between positions P1 and P3, i.e. in the first half of the motor length. However, for the longer tubes the first and the maximum impact area lay between P2 and P7. Thus for longer tubes the particle impact spectrum moved downstream, just as did the region of greatest total heat flux noted previously.

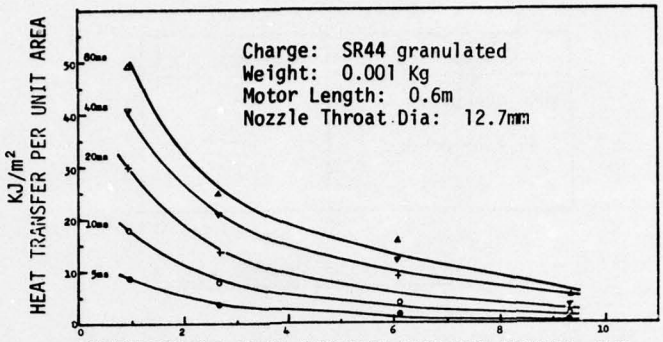

FIG. 7 Axial variation of Heat Transfer per unit area along conduit

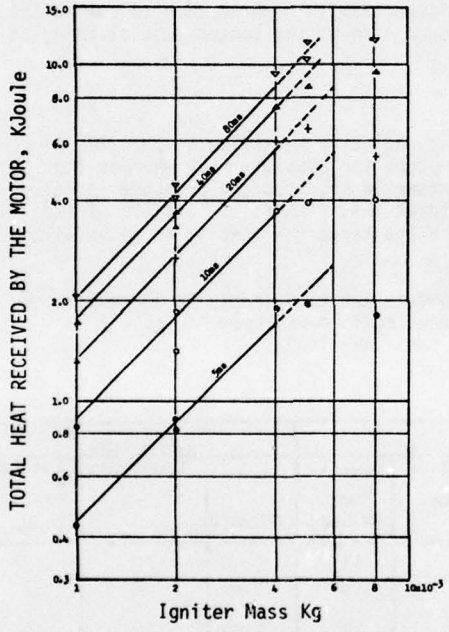

FIG. 8 Total Heat received by the motor as a function of Igniter Mass

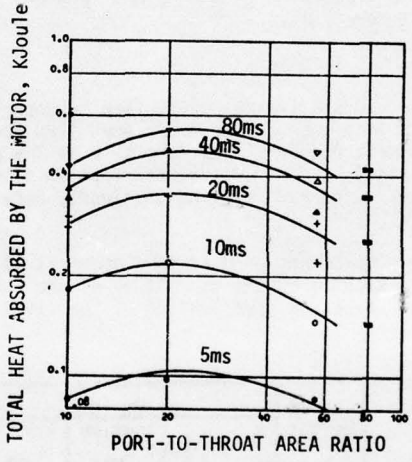

FIG. 9 Total Heat received as a function of port/throat area.

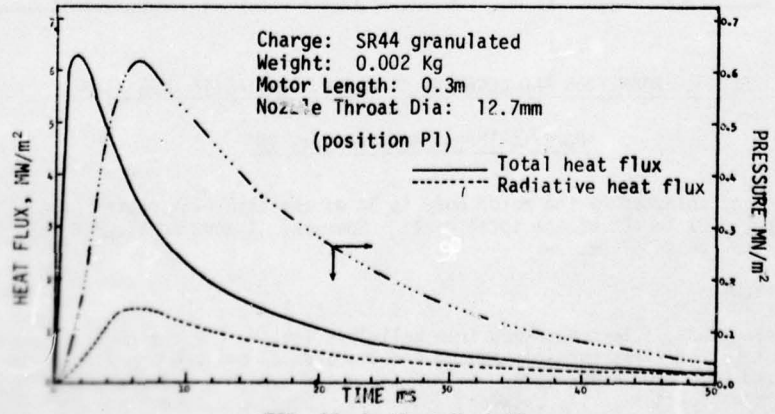

FIG. 10 Radiant Heat Flux

It was also observed that virtually all the particle impact occurred during the first 10 ms of a test, corresponding approximately to the pressure rise time.

Temporal and Axial Distributions of Craters

The particle impact period of approximately 10 ms was divided into equal segments of 2.5 ms each and craters in each segment of the cellulose acetate sheet were counted separately. No general trend in the variation of particle size distribution with time could be observed.

Based on average values at each position, the axial distribution of carters is given in Table 5 for a typical test. The general effect of the axial distance on the crater distribution appears to be to increase the number of smaller craters. No craters of size greater than 125 microns were observed.

Crater/ Particle sizes in Microns	0.005 Kg SR371C Composition 0.60m tube					Average Distribution of Loose Particles Scraped from the CA Sheet
	Crater Distribution at					
	P1	P3	P5	P7	P9	
0 - 5	61.8%	63.3%	67.8%	76.4%	70.9%	32.5%
5 - 10	14.0%	14.2%	15.6%	11.9%	15.2%	17.4%
10 - 15	9.4%	7.8%	8.1%	3.4%	7.0%	11.8%
15 - 20	5.4%	4.7%	3.5%	8.0%	3.3%	8.2%
20 - 25	4.2%	3.7%	1.9%	0.2%	1.5%	5.4%
25 - 30	1.9%	2.1%	1.6%	0.1%	1.1%	5.4%
30 - 35	1.7%	1.4%	0.9%	-	0.6%	3.8%
35 - 40	0.6%	0.8%	0.3%	-	0.1%	2.6%
40 - 50	0.6%	0.9%	0.3%	-	0.1%	4.2%
50 - 60	0.2%	0.7%	-	-	0.1%	1.9%
60 - 70	0.1%	0.3%	-	-	0.1%	1.6%
70 - 80	0.1%	0.1%	-	-		1.0%
80 - 90						0.5%
90 - 100						1.3%
100 - 125						0.5%
125 - 150						0.6%
150 - 175						0.4%
175 - 200						0.3%
200 - 225						0.2%
225 - 250						0.2%
250 - 275						0.1%

TABLE 5: AXIAL DISTRIBUTION OF CRATER SIZES COMPARED WITH AVERAGE DISTRIBUTION OF LOOSE PARTICLES

Correlation between Combustion Particles & Crater Size

Fig. 12 is a typical plot of %age less than stated size against size of the combusted particles, and the correspondong craters obtained in that test. Based on the reasonable assumption that the particle size distribution has a close correspondence with the crater size distribution, correlations have been obtained between particle size and crater size for different igniter masses for a tube length of 0.6 m. A typical correlation is plotted in Fig. 13, which suggests that particles obtained from a combustion of .005 kg of igniter produce larger craters than those produced by particles obtained from .002 Kg mass of igniter. Crater-particle correlations based on .005 Kg of igniter mass are listed in Table 6.

Particulate Heat Transfer

If a particle of diameter d_p impinges on the cellulose acetate sheet to produce a crater of diameter d_c and assuming that the particle is half embedded in the sheet, the heat transferred per unit area would be given by:

$$q = \frac{d_p \rho_p C_{p_p}}{3} (T_{p_p} - T_{p_t}) \quad \ldots\ldots (3)$$

Since the particle is only partially embedded, the heat input to the sheet can be approximated by

$$Q = \frac{\pi}{12} \rho_p C_{p_p} d_p d_c^2 (T_{p_o} - T_{p_t}) \quad \ldots\ldots (4)$$

Assuming that the crater is a perfect half sphere, and it would be nearly so if vaporisation of cellulose acetate takes place at the hot interface, the heat used to pyrolise the sheet is given by:

$$Q = \frac{\pi}{12} \rho_c d_c^3 C_p (T_c - T_o) + H_c \quad \ldots\ldots (5)$$

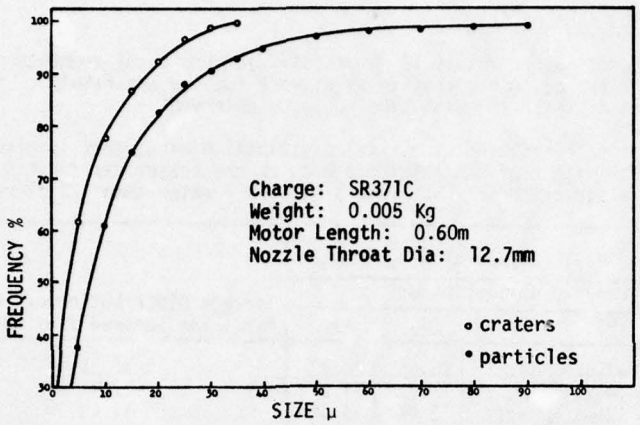

FIG. 12 Distribution of Particle Size & Crater Size

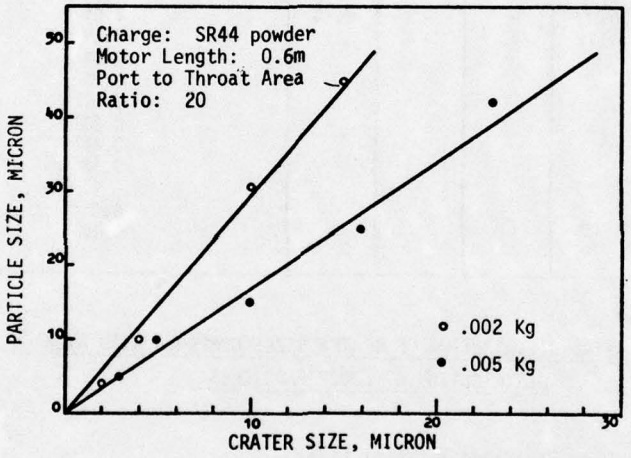

FIG. 13 Correlation between Particle and Crater Size

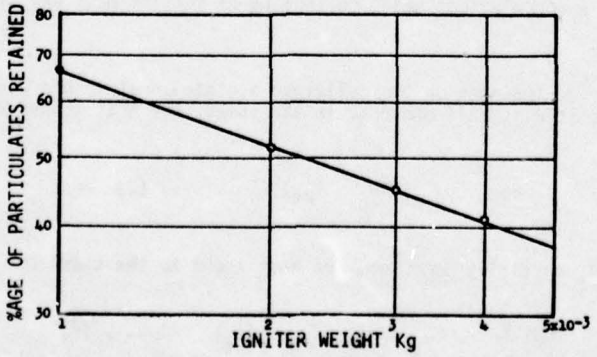

FIG. 14 Weight %-age of Igniter Particulates retained inside the motor After a Firing vs Igniter Mass

If the particle is allowed to transfer its entire heat to the sheet and assuming that it is entirely utilized in the formation of the crater, then it would be reasonable to assume that:

$$T_{p_t} = T_c \qquad \ldots\ldots (6)$$

Particle Sizes (Microns)	Corresponding Crater Sizes		
	SR44 Granular	SR44 Powder	SR371C Coarse Powder
5	2.0	3	2.5
10	4	5.5	5.0
15	5.5	8.5	7.5
20	7.5	11	10
25	9.5	14	12.5
30	11	17	15
40	15	22	20
50	19	28	25
60	23	33	30
70	26	39	35

Igniter mass = .005 Kg Tube length = .6m

TABLE 6: CORRELATION BETWEEN PARTICLE SIZE AND CRATER SIZE

Using Eqs. (4), (5) and (6) the initial temperature of the particle is given by:

$$T_{p_o} = \frac{d_c}{d_p} \frac{1}{C_{p_p}} (T_{p_t} - T_o) + H_c + T_{p_t} \qquad \ldots\ldots (7)$$

Once the particle temperature is known, the particulate heat flux per unit area is given by

$$\dot{q} = h (T_{p_o} - T_{p_t}) \qquad \ldots\ldots (8)$$

The average value of the heat transfer coefficient was found to be 2.1 kW/m^2 ^oC (ref 10). The heat of dissociation of cellulose acetate was experimentally found to be 6 x 10^6 KJ/Kg. Using specific heat values of B_2O_3 and Mg O from Thermodynamic Tables (ref 11)., Eq. 7 was employed to calculate particle temperatures. These together with estimated particulate heat fluxes and heat inputs are given in Table 7.

Frequency of Particle Impingement

Based on the mass of igniter and distribution of particles found deposited on the inside of the motor, an estimate as to the total number of particles striking the conduit-surface can be made. Let the mass of igniter particulate matter deposited in the tube be m_p and let N be the total number of particles constituting this mass. Assuming n_1% particles have diameters d_1 and so on, it can be shown that

$$N = \frac{600}{\pi \rho_p} \frac{m_p}{\sum_{i=1}^{n} n_i d_i^3} \qquad \ldots\ldots (9)$$

Let the motor conduit surface area be A_p and since almost all the particles impact within 10 ms with a uniform density, the rate of particle impact per millisecond comes to

$$r_p = \frac{60}{\pi \rho A_p} \frac{m_p}{\sum_{i=1}^{n} n_i d_i^3} \qquad \ldots\ldots (10)$$

The amount of igniter material retained inside the motor, m_p, was found experimentally. It is plotted as a function of igniter mass in Fig. 14.

Assuming that all the combusted particles are oxides of boron or of magnesium in the respective cases of SR44 and SR371C combustion, the total number of combusted particles is estimated to be 8 x 10^9 and 4 x 10^9 per Kg respectively. This means that a combustion of .005 kg of SR44 composition gives rise to an average impact rate of 31 particles/mm^2 m sec. Similarly SR371C gives rise on combustion to an average impact rate of 16 particles/mm^2 m sec. Since each particle continues to transfer heat for several milliseconds, it is estimated that at any given moment, more particles are transferring heat than the particles impact rate would indicate.

Composition	Estimated Particle Temperature	Particulate Heat Flux	Heat Transfer from Particles of Sizes				
			5 microns	10 microns	20 microns	50 microns	100 microns
	(^{O}K)	(MW/m^2)	(KJ/m^2)	(KJ/m^2)	(KJ/m^2)	(KJ/m^2)	(KJ/m^2)
SR44 Granular	1800	2.5	5.4	10.8	21.6	54.0	108.0
SR44 Powder	2200	3.5	7.4	14.9	29.7	74.3	148.6
SR371C Coarse Powder	1300	1.6	5.9	11.8	23.6	58.9	117.8

TABLE 7: PARTICULATE HEAT TRANSFER BASED ON ESTIMATED TEMPERATURES

CONCLUSIONS

From the foregoing, it is evident that convection and conduction due to particle impingement are the two most dominant modes of heat transport from an igniter to the propellant during ignition of a rocket-motor. The contribution of the radiative component of heat flux, although significant in motors with length to diameter ratios of 6 or less, becomes far less significant with longer motors. The particulate heat flux is comparable to the average convective heat flux during the first and the most crucial 10 ms of a rocket ignition. In fact, in addition to the particles escapting through the nozzle, 3 to 5 million particles from the combustion of .001 Kg of pyrotechnic material strike and stick to the propellant surface. Although about half of these particles are less than 5 micron in size, at least 12% are greater than 20 micron. These alone are sufficient to cause ignition (ref 10). Smaller particles i.e., in the 5 micron range will not, of themselves, give rise to ignition but with rates of impact of between 8 and 15 particles per mm^2 per millisecond, they do contribute at least one third of the ignition energy. It is, therefore, most likely that in conjunction with the convective heat supplying a steady background, the first ignition sites in a rocket motor will occur at these point-sources of energy.

Since in rocket motor tubes with non-dimensional length parameter, $\frac{X}{D} > 6$, the site of maximum heat flux shifts downstream near the middle of the motor body, it is reasonable to assume that the first ignition flame in longer motors usually appears in the middle regions of the motor conduit.

It has already been shown that the total heat is a linear function of igniter mass until an optimum is reached, beyond which the improvement in heat-flux is not proportional to the increase in mass, because increasing amount of uncombusted material escapes through the nozzle. Thus providing a rocket motor with a larger than optimum igniter mass results only in a small increase in heat input.

The rate of burning rather than the calorific value of a pyrotechnic material is a more important factor in determining its combustion efficiency. B/KNO_3 composition when finely powdered and packed has a much lower rate of burning than when it is in a granular form. Although calorimetric measurements give a higher value for the heat of combustion of finely powdered B/KNO_3 than when it was in a granulated shape but in motor firings, the slower burning powder gave as much as 40% less heat than the much faster burning granules.

REFERENCES

1. Nanigian, J., "Rocket Igniter Characteristics", Instruments and Control Systems, Vol. 40, May 1967, PP. 121-124.

2. Keller, J.A. and Ryan, N.W., "Measurement of Heat Flux from Igniters for Solid Propellants", Journal of American Rocket Society, Vol. 31, No. 12, Oct. 1961, PP. 1375-1379.

3. Allan, S.D., Bastress, E.K. and Smith, K.A., "Heat Transfer Processes during Ignition of Solid Propellant Rockets", J. Spacecraft & Rockets, Vol. 4, No. 1, Jan. 1967, PP. 95-100.

4. Peleg, I. and Manheimer-Timnat, Y., "A Study of Solid Propellant Rocket Motor Ignition", Israel Jour. Technology, Vol. 6, No. 1-2, 1968, PP. 32-45.

5. Scaqnetti, M. and Crabol, J., "Measure des Flux de Chaleur Pendant la Phase D'Allumage d'un Propergol Solide", La Recherche Ae'rospatiale, No. 123, Mars-Avril 1968, PP. 45-61.

6. Siddiqui, K.M., "The Measurement of Heat Flux from Igniters in Solid Propellant Rocket Motors", Ph.D. Thesis, 1975, School of Mechanical Engineering, Cranfield Institute of Technology, Cranfield, Bedford.

7. Carslaw, H.S. and Jaeger, J.C., "Conduction of Heat in Solids", 2nd ed., Oxford at the Clarendon Press, 1959.

8. Schultz, D.L. and Jones, T.V., "Heat Transfer Measurements in Short Duration Hypersonic Facilities, AGARDograph No. 165.

9. Cook, W.J. and Felderman, E.J., "Reduction of Data from Thin Film Heat Transfer Gauges. A Concise Numerical Technique", AIAA Journal, Vol. 14, No. 3, 1966, PP. 561-564.

10. Siddiqui, K.M. and Smith, I.E., "The Ignition of Double-Base Propellants by Hot Particles Arising in the Igniter Products", AIAA/SAE 10th Propulsion Conferences, San Diego, Oct. 1974, Paper No. 74-1087.

11. McBride, B.J., Heimel, S., Ehlers, J.G. and Gordon, S., "Thermodynamic Properties to 6000°K for 210 Substances Involving the First 18 Elements", NASA SP-3001, 1963.

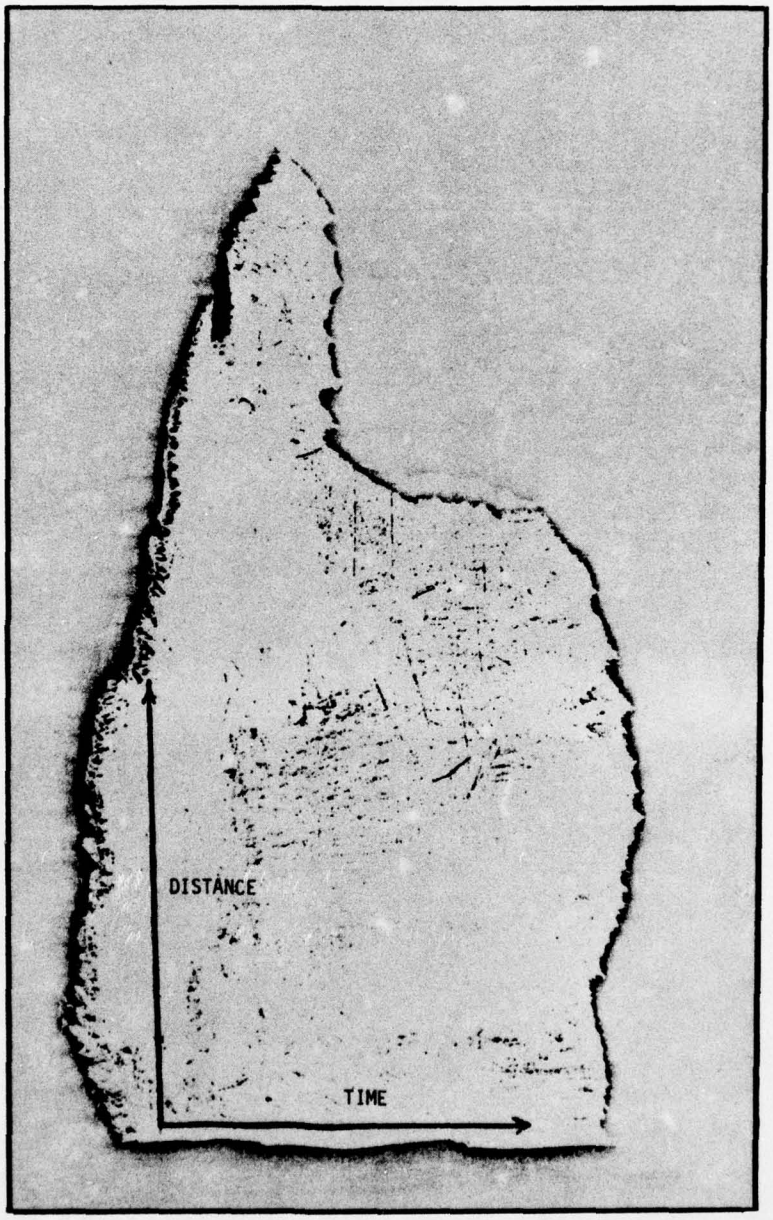

FIG. 11 Typical Particulate Deposit

AN INTERIOR BALLISTICS MODEL FOR A SPINNING ROCKET MOTOR

Carl W. Nelson
Research Physical Scientist
Interior Ballistics Laboratory
U. S. Army Ballistic Research Laboratories
Aberdeen Proving Ground, Maryland 21005 USA

Summary

A computer model was developed for the spinning rocket motor used in an artillery projectile. Lumped parameter equations for conservation of mass and energy are solved numerically. Departures from standard procedures are made in treating 1) the gas properties by mixing the input from two different propellant grains, 2) the gas dynamic effects due to swirling of the gases through a single central nozzle as predicted by Mager (1961), 3) increase in radial burning rates due to radial acceleration and swirling gases. A formula for radial burning rates was derived from reducing pressure-time data for 40mm and 80mm rocket motors at spin rates up to 340 rps. The code is applied to motors for a 155mm projectile and a 203mm projectile at spin rates of 170 rps and 250 rps. For the 155mm agreement is good between code predictions and firing tests at 170 rps; at 250 rps the agreement is not as good because of suspected slow ignition. For the 203mm projectile, agreement was good for the one spin rate compared.

List of Symbols

a_o	sound speed at stagnation conditions (cm/sec)
A	geometric nozzle area (cm^2)
M	gas molecular weight
P	chamber pressure (MPa)
r	linear burning rate of propellant (cm/sec)
R_i	grain inner radius (cm)
R	universal gas constant ($kgm^2/sec^2 gmol°K$)
S	burning surface (cm^2)
t	time (sec)
T	chamber temperature (°K)
V	chamber gas volume (cm^3)
γ^*	chamber specific heat ratio
ρ	propellant density (kg/cm^3)
ω	spin rate (rps)

Introduction

Modeling of spinning rocket motors requires departures from standard rocket interior ballistics. Swirling of the flow through a central nozzle causes vortex effects which have been calculated by Mager (1) and by Norton (2) among others (3). Cold flow experiments by Farquhar (4) confirmed the predictions. The combination of radial acceleration and swirling gas flow increases the burning rate of the propellant principally in the radial direction. Some data are available on the effects of spin on double base propellants which are of interest in this study.

Combining these two main effects into a computer model has been previously attempted with limited success. When Ulloth and Guthrie (5) attempted a computer program to model a high spin motor (10000 rpm), they were unable to predict a runaway pressure rise after half the grain was burned. They accounted for

---

1 *A. Mager, "Approximate Solution of Isentropic Swirling Flow Through a Nozzle," ARS 31, (8) pp 1140-1148, 1961.*

2 *D. J. Norton, "An Analytical Investigation of the Fluid Mechanics of Rotating Flows in Rocket Motors," Ph.D. Thesis, Purdue University, Lafayette, IN, 1968.*

3 *D. J. Norton, D. N. Farquhar, J. D. Hoffman, "Analytical Studies of the Interior Ballistics of Spinning Rocket Motors - A Literature Survey," Jet Propulsion Center, Report TM-67-1, Purdue University, 1967.*

4 *D. N. Farquhar, D. J. Norton, J. D. Hoffman, "An Experimental Investigation of Swirling Flow in Nozzles," Jet Propulsion Center Report TM-67-9, Purdue University, 1968.*

5 *D. R. Ulloth, W. D. Guthrie, "A Study of Vortex Effects in Spinning Rocket Motors," USAMICOM Report RK-TR-66-8, April 1964 (AD 374624).*

the gas dynamic effects through Mager's analysis. They did predict surface regression profile which agreed with static firing tests. Glick (6) studied the gas dynamic effects in a simulated central perforated motor by a one-dimensional quasi-steady analysis. Local burning rates were computed as a function of acceleration and local gas velocity. Krier, et al (7) wrote a prediction code for a tri-segmented grain design with no gas dynamic effects of spinning but with a radial burning rate augmentation proportional to grain inner diameter. Maximum augmentation was 30 percent.

The present study was motivated by a need to study range dispersion of a rocket assisted projectile for a 155mm howitzer. It was hoped that a computer model would permit numerical experiments to identify the source of the variability in delivered impulse shown in flight test data (8). It was later found that the dominant cause of the variability lay in the exterior ballistics of the base region (9).

Analysis

For the chamber gases, the simultaneous conservation equations for mass and energy are integrated numerically for a lumped parameter system by a modified Euler scheme. Quasi-steady isentropic flow for an ideal gas is assumed. Because at least one motor of interest has two propellant grains of different size and composition, effective values for the thermodynamic properties of the gas mixture are obtained by assuming isentropic mixing of the two gas sources.

Mass flow rate through the nozzle must be corrected for the effect of swirling flow. Mager's analysis for a free vortex flow should be applicable to a cylindrical port motor. The presence of the slots and a steel spacer between the grains are ignored for simplicity. Mager's controlling parameter for the mass flow reduction is

$$\alpha^* = \frac{R_i^2 \omega}{a_o R_t} \sqrt{\frac{\gamma^* - 1}{2}}$$

Tabular values of mass flow efficiency versus α^* and γ^* are found in Glick and Kilgore (10). The efficiency is treated as an effective throat area factor. The effect is two-fold in that it 1) reduces the mass flow rate and therefore the thrust, and 2) increases the effective area expansion ratio and therefore the thrust while the flow is still underexpanded. The net effect is to change the ratio of thrust to chamber pressure. For the purposes of this code, the burning radius was assumed to be that of the aft grain instead of an average value over the entire motor length.

Burning rates of the different propellant surfaces is the second substantial departure. All surfaces except the inner radii and the narrow slots are assumed to regress at the usually published rates for the given propellant. In the slots, erosive burning is assumed proportional to mass velocity.

Spinning the motor induces burning rate changes beyond that expected from reducing the effective throat area to thus raise the equilibrium pressure. Some combinations of local gas velocity and acceleration increase the radial burning rate. Data on these double base propellants at 10 krpm are not directly available. Bulman and Netzer (11) found a decrease with acceleration alone. Guthrie and Chen (12) reported an increase of 75 percent at 10000 g's in a spinning motor.

---

6 *R. L. Glick, "An Analytical Study of the Effects of Radial Acceleration upon the Combustion Mechanism of Solid Propellant," NASA Report CR-66218, December 1966 (N67-13189).*

7 *H. Krier, S. Shimpi, E. Meister, "An Interior Ballistics Prediction of the M549 Rocket Assited Projectile," Technical Report AAE 75-10, University of Illinois, October 1974.*

8 *R. D. Botticelli, "Effect of Actual and Induced Propellant Inhibiting on M549 Flight Performance," Picatinny Arsenal, TM2159, September 1974.*

9 *R. D. Botticelli, "Range Precision of Rocket Assisted Projectiles as Affected by Base Pressure Variations During Burning," JANNAF Propulsion Meeting, Anaheim, CA, October 1975.*

10 *R. L. Glick, M. S. Kilgore, "Effect of Specific Heat Ratio on Mass Flow for Swirling Nozzle Flow," J. Spacecraft and Rockets, p. 1099, August 1967.*

11 *M. J. Bulman, D. W. Netzer, "Burning Rates Acceleration Sensitivity of Double Base Propellants," AIAAJ 8 (6) p 1155-1156, June 1970.*

12 *W. D. Guthrie, C. M. Chen, "Effects of Acceleration on Burning Rates of Solid Propellants," USAMICOM Report RK-TR-63-22, October 1963 (AD345491).*

Pressure-time records are available from a AVCO developed 40mm motor with multiple nozzles spin up to 330 rps. Similar data are also available from a Picatinny Arsenal 80mm motor spun to 75 rps. Figure 1 shows the pressure-time history of the 40mm motor at several spin rates, and Figure 2 shows the 80mm motor.

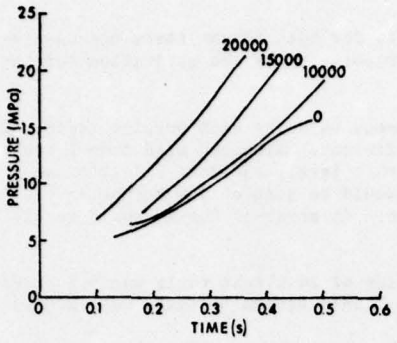

Figure 1. Effect of Spin on Pressure-40mm Motor.

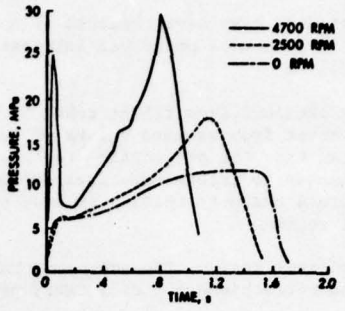

Figure 2. Effect of Spin on Pressure-80mm Motor.

The continuity equation for a constant temperature rocket chamber may be rearranged to give

$$r = \frac{1}{\rho S} \left[C\ A\ P + \frac{M}{R_o T} \left(P \frac{dV}{dT} + V \frac{dP}{dt} \right) \right].$$

The burning rate is thus expressed as a function of known parameters and of parameters which must be computed from the burning rate history [S, V, dV/dt, all functions of distance burned]. For internally perforated cylindrical grains, these parameters can be specified by simple expressions. For a central nozzle, Mager's results can be applied to compute a virtual throat area as a function of spin rate and instantaneous grain inner radius.

For both motors there was a decided trend to higher burning rates at higher spin rates. No simple relationship with acceleration seemed derivable because the trend within data sets at different spin rates was not consistent. A more consistent trend was noted when the relative burning rate was plotted against the tangential velocity (WR) of the grain inner radius. In Figure 3, which shows the trends, the ellipsoidal areas enclose the data points for the cited spin rate for the 40mm motor. Because there were only two tests with the 80mm motor, the entire history is shown by the two labeled curves.

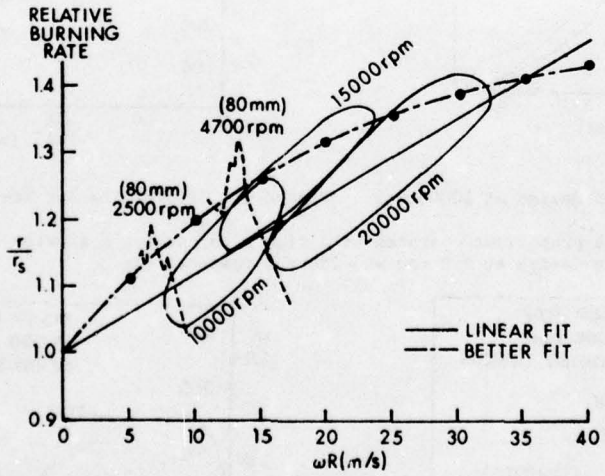

Figure 3. Correlation of Relative Burning Rate with Tangential Velocity.

One element of bias was introduced in the analysis when an initial grain radius was picked. In all data reductions, the computations were started at a minimum in the pressure-time history after pre-ignition spike. An assumption had to be made on the amount of propellant consumed in the ignition process. The 40mm motors had a screw thread initial surface to aid ignition and the 80mm had a smooth initial surface. Somewhat arbitrarily, the no-spin tests were subjected to trial and error reduction until the assigned initial radius yielded an approximate relative burning rate of 1.0 at the pressure minimum. To the extent that the ignition transient depends on spin rate, the assumption introduces a systematic error.

Two lines were drawn on Figure 3 to represent the trend of the results. When the linear fit was used for a computer model of a RAP with (WR) values beyond the tested range, the radial burning rate was apparently overstated by about 25%. There were too many other uncertainties in the motor simulation to allow any firm conclusions about the real validity of the linear expression. For convenience in that model, a limiting value of relative burning rate of 1.5 gave reasonable argument with test firings. The form of the correlation used there is shown as a broken line in Figure 3.

Total impulse correction has been made by using a constant efficiency factor to adjust the predicted value to the test value. In effect, pressure and impulse predictions were considered together before adjustment factors were selected. Numerical values are shown in the section on comparison of predicted and test performance.

Comparison with Tests

Firing test data have been obtained from Picatinny Arsenal (8) for both flight tests and captive tests. Thrust data were of principal interest because impulse variability was the motivation for the code development.

Impulse is obtained from flight tests by measuring instantaneous velocity with doppler radar and inferring the thrust from assumed values of aerodynamic drag coefficient. Although wind tunnel tests (9,13) have shown that the projectile drag also depends on the thrust level, the data reduction scheme has not been changed to incorporate that dependence. The effect would be seen at low thrust levels (below about 1 kN) where a sharp transition in base pressure ratio occurs. An error of 0.1 kN could result in this low thrust regime.

For the original design, the average total impulse for a series of 24 flight tests was 5.85 kN-sec. The code with no corrections for efficiency predicted 6.42 kN-sec. This series of tests was adopted as the standard.

Comparisons between computed and test performance are shown in Figures 4 through 7 for two configurations. The original production standard configuration with OGK aft grain and spun at 170 rps was the basis for computing impulse efficiency. Figure 4 compares test data with two computed profiles: one with a simple grain and ideal thermodynamics and one with a real grain and losses.

The simple grain analysis ignores the geometry of the aft grain end and assumes a fully inhibited outer radius and sharp corners of all interacting surfaces.

Figure 5 compares the computed profile with test data for the original design. Note the differences in the early profile among two typical flight tests and a typical spin stand test.

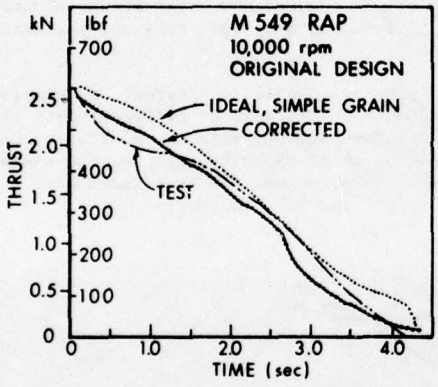

Figure 4. Thrust for Original Design at 10000 rpm

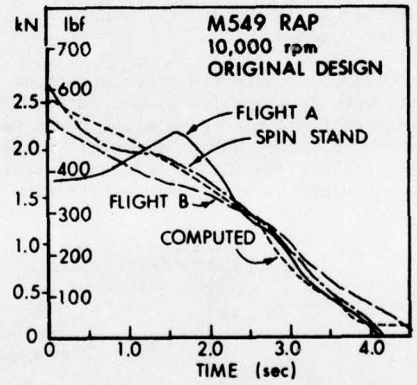

Figure 5. Original Design Test Comparisons.

The final design with one propellant operates at a higher thrust for a shorter time. Figures 6 and 7 present comparisons for this design at 170 rps and 250 rps respectively.

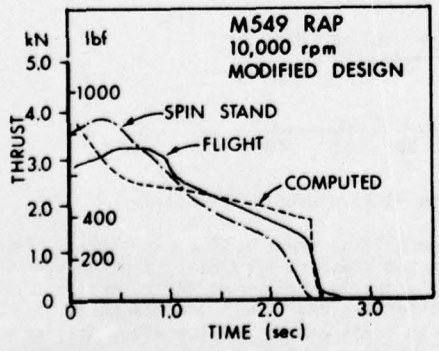

Figure 6. Comparisons of Final Design at 10000 rpm.

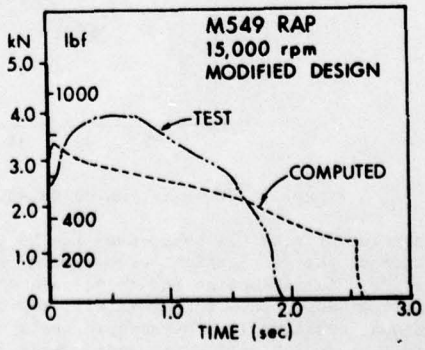

Figure 7. Comparisons for Final Design at 15000 rpm.

[13] *C. E. Brazzel, "Estimated Power-On Base Drag for a Rocket Assisted Projectile," USAMICOM Report RD-TM-70-7, July 2970 (AD874580).*

Several attempts were made to match the profiles by reasonable changes in early burning rate behavior with no success. The barrier is that the forward grain geometry cannot burn progressively unless the radial regression is much greater than the non-radial rate (ratio exceeds 20). A progressive pressure trace must then arise from some other source than grain geometry. A definitive model would require a description of the entire flow field during the flame spreading phase. The phenomenon does not hurt motor operation but does bar a lumped parameter simulation.

Application

Some parametric studies were conducted for the 155mm motor for variations in burning rates and grain inhibition. Some conclusions drawn from these studies were that: 1) expected variation in the nominal burning would not cause the observed variation in delivered impulse; 2) expected impulse variations could result from variation in radial burning rates which decrease the predicted rate by more than 10%, 3) all predicted impulse variations result from unburned propellant, 4) inhibiting the ends of both grains should lessen the impulse variation, 5) variation in an motor with one propellant would be lower. These studies pointed to a probable cause for the observed impulse variation outside the motor interior ballistics although using a one propellant motor with inhibited ends should minimize the contribution from the motor. The motor was modified to such a configuration and the delivered impulse variability was sharply reduced although most of the credit must go to the exterior ballistics of a higher thrust level (9).

The code was also tested for a RAP has a nominal outer diameter of 171mm. The interior ballistic performance should be similar except for the different contraction ratio near grain burnout. Correction factors derived for the 155mm RAP were used. Figure 8 presents the comparisons for the computed solution and two different flight tests. Figure 9 presents the comparison for assumed inhibition of the grain ends. No explanation is offered for the different behavior in the flight tests.

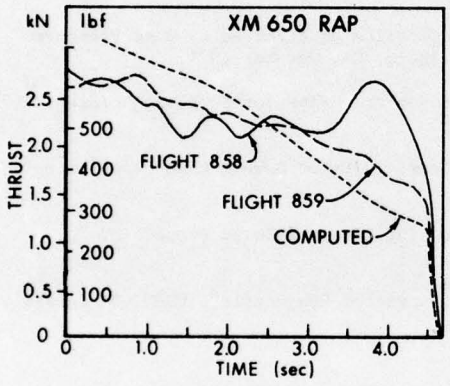

Figure 8. Comparisons for 171mm, RAP, Standard Design

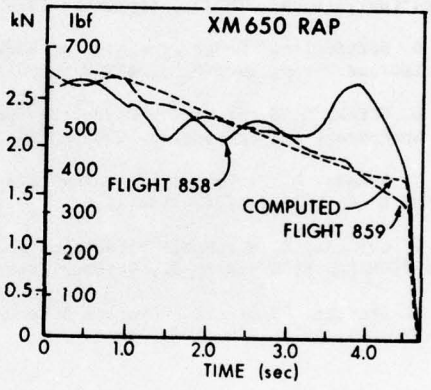

Figure 9. Comparisons for 171mm, RAP, Inhibited Grain Ends Assumed

References

1. A. Mager, "Approximate Solution of Isentropic Swirling Flow Through a Nozzle," ARS 31, (8) pp 1140-1148, 1961.

2. D. J. Norton, "An Analytical Investigation of the Fluid Mechanics of Rotating Flows in Rocket Motors", Ph.D. Thesis, Purdue University, Lafayette, IN, 1968.

3. D. J. Norton, D. N. Farquhar, J. D. Hoffman, "Analytical Studies of the Interior Ballistics of Spinning Rocket Motors - A Literature Survey", Jet Propulsion Center, Report TM-67-1, Purdue University, 1967.

4. D. N. Farquhar, D. J. Norton, J. D. Hoffman, "An Experimental Investigation of Swirling Flow in Nozzles", Jet Propulsion Center Report TM-67-9, Purdue University, 1968.

5. D. R. Ulloth, W. D. Guthrie, "A Study of Vortex Effects in Spinning Rocket Motors", USAMICOM Report RK-TR-66-8, April 1964 (AD374624).

6. R. L. Glick, "An Analytical Study of the Effects of Radial Acceleration upon the Combustion Mechanism of Solid Propellant", NASA Report CR-66218, December 1966 (N67-13189).

7. H. Krier, S. Shimpi, E. Meister, "An Interior Ballistics Predictionthe M549 Rocket Assisted Projectile," Technical Report AAE 74-10, University of Illinois, October 1974.

8. R. D. Botticelli, "Effect of Actual and Induced Propellant Inhibiting on M549 Flight Performance", Picatinny Arsenal, TM2159, September 1974.

9. R. D. Botticelli, "Range Precision of Rocket Assisted Projectiles as Affected by Base Pressure Variations During Burning", JANNAF Propulsion Meeting, Anaheim, CA, October 1975.

10. R. L. Glick, M. S. Kilgore, "Effect of Specific Heat Ratio on Mass Flow for Swirling Nozzle Flow", J. Spacecraft and Rockets, p 1099, August 1967.

11. M. J. Bulman, D. W. Netzer, "Burning Rates Acceleration Sensitivity of Double Base Propellants", AIAAJ 8 (6) p 1155-1156, June 1970.

12. W. D. Guthrie, C. M. Chen, "Effects of Acceleration on Burning Rates of Solid Propellants", USAMICOM Report RK-TR-63-22, October 1963 (AD345491).

13. C. E. Brazzel, "Estimated Power-on Base Drag for a Rocket Assisted Projectile", USAMICOM Report RD-TM-70-7, July 1970 (AD874580).

DETERMINING THE SHELFLIFE OF SOLID PROPELLANTS

F. V O L K
Institut für Chemie der Treib- und Explosivstoffe
D-7507 Pfinztal-Berghausen, der Fraunhofer-Gesellschaft

Paper presented at the AGARD-PEP 47th Meeting on
SMALL SOLID PROPELLANT ROCKET FOR FIELD USE

1. Introduction

Shelflife is the time for which all functions of a propellant charge remain intact, within given tolerances, although some aging processes have already occurred. In general, two different periods of shelflife can be defined for solid propellants: the chemical shelflife or safe shelflife, and the physico-mechanical shelflife. The chemical shelflife is determined by the chemical reactions occurring in the propellant. The physico-mechanical shelflife is a function of physical and mechanical events, respectively, which can be felt as cracking, dissociation of materials, straining, diffusion of plasticizers, influences of moisture etc.

This contribution will be limited to the chemical shelflife of double base solid propellants. It will be shown by a few selected examples in what way the aging processes can be detected analytically which occur during the storage of double base solid propellants at elevated temperatures.

2. Factors influencing shelflife

The stability of double base solid propellants is a function of various factors. The main preconditions to good stability first of all lie in the use of stable basic products in the fabrication process. This applies in particular to nitrocellulose and nitroglycerin. In addition, there must also be good compatibility between the propellant matrix and other components, such as burning modifiers, plasticizers and other substances, in order to achieve satisfactory stability conditions. Studies carried out at our Institute, dealing with the influence of various burning modifiers upon the stability of double base solid propellants, have indicated that especially the copper salts of salicylic acid have a clearly deteriorating effect upon stability[1)]

In composite and composite double base solid propellants compatibility includes also such substances as aluminum, ammonium perchlorate, hexogen, octogen etc. In addition to satisfactory compatibility it is important to have a propellant which is optimally stabilized. This means that a stabilizer compatible with the propellant is applied in an optimum ratio. Other factors of interest relate to the impact of stabilizer reaction products upon the stability of the propellants.

As far as the propellant charge is concerned, it es particularly important to know the diffusion processes of plasticizing agents and nitroglycerin, which occur between the propellant and the insulation[1)].

Attention should be devoted also to the influences, especially upon the mechanical properties, of such factors as moisture, storage, transport etc.

3. Determining the Aging of Double Base Solid Propellants

There are various methods of determining the aging of double base solid propellants. Here are a few important examples:

(a) Measurement of the rate of heat generation during storage at elevated temperature as, for instance, in the method according to van Geel[2].

(b) Assessment of the thermal decomposition curve through the loss of weight.

(c) Determination of the stabilizer reaction products during storage at elevated temperature.

In all these cases a factor of decisive importance is the possibility of establishing a correlation between results achieved at higher and those achieved at lower temperatures in order to determine characteristic shelflife data for practical purposes.

The studies outlined below are carried out by the methods referred to under (b) and (c) above.

3.1 Types of studied propellant

The studies were carried out on specially prepared double base propellants which contained different stabilizers, while the composition of the propellants remained unchanged, see Fig.1.

The propellant consists of the following main components:

50 % nitrocellulose
35 % nitroglycerin
10 % diethylphthalate
2 % stabilizer
3 % burning modifier.

Q_{ex} = 850 cal/g

This basic composition was used to produce seven types of propellant by means of different stabilizers, which contained the following alternative stabilizer fractions:

- 2 % diphenylamine
- 2 % nitrodiphenylamine
- 2 % acardite I (asymmetrical diphenylurea)
- 2 % acardite II (asymmetrical methyldiphenylurea)
- 2 % ethyl centralite
- 6 % ethyl centralite
- 1 % ethyl centralite + 1 % acardite II.

3.2 Test Performance

In order to find out whether the results obtained at elevated temperatures (90°C) correlate with those obtained at the lower temperatures (65°C), the studies were carried out at several temperatures within this temperature range. The propellant specimens were stored in metal block thermostats each holding 4 grams of substance in test tubes with glass stoppers loosely put in place. Five specimens each were stored parallel to produce a representative mean value. The studies were carried out with two purposes in mind:

(a) The specimens were stored at the temperature applied in a specific case until autocatalytic decomposition occurred, which could be detected from a sudden loss of weight and the formation of nitrous gases, respectively.

(b) In another part of the study propellant specimens, which had been stored for different periods of time at various temperatures, were extracted with dichloromethane and the extracts were analyzed by thin layer chromatography to determine the stabilizer reaction products.

AD-A033 497 ADVISORY GROUP FOR AEROSPACE RESEARCH AND DEVELOPMENT--ETC F/G 21/8.2
SMALL SOLID PROPELLANT ROCKETS FOR FIELD USE.(U)
1976

UNCLASSIFIED AGARD-CP-194 NL

2 OF 2
AD
A033497

END

DATE
FILMED
2-77

3.3 Test Results

3.3.1 Temperature Correlation for Autocatalysis

In order to obtain a correlation for the autocatalytic decomposition between higher and lower storage temperatures, the weight losses were studied for the propellants in question. In these investigations, the loss of weight was followed in $5^{o}C$ steps between $65^{o}C$ and $90^{o}C$ until self-accelerated decomposition occurred, which was detectable by the formation of nitric oxides and a spontaneous major loss of weight.

Fig. 2 und 3 show two typical results. The diagrams are plots of the losses of weight as a function of the storage period. It is seen from the result obtained at $80^{o}C$ that the propellant containing diphenylamine reaches autocatalysis at an early point in time. As the storage period goes on, this is followed by the propellants containing ethylcentralite, 2-nitrodiphenylamine, acardite I, centralite I + acardite II, and acardite II. From this it es seen that acardite II has the best stabilizer properties.

The propellant containing 6 % centralite differs from the others in havíng a very high rate of decomposition and reaches the autocatalysis region only at a loss of weight above 10 %.

To indicate the temperature dependence of the thermal decomposition Fig. 4 and 5 show the results obtained for propellants with diphenylamine and 2-nitrodiphenylamine.

The dependence on storage period of the loss of weight is shown here with the temperature as a parameter.

Similar curves were obtained also for the other types of propellant; hence, there is no need to explain them in greater detail.

For better assessment of the results with respect to the losses of weight the time at which autocatalytic decomposition set in were plotted as a function of temperature. At the same time, the activation energy for the propellants stabilized in different ways was calculated by means of the Arrhenius equation, i.e.,

$$E = 4.572\ (\log k_2 - \log k_1)\ \frac{T_1 \cdot T_2}{T_2 - T_1}$$

where k_1, k_2 = decomposition rates at temperatures T_1 and T_2

T = temperature in K.

k_1 and k_2 are the reciprocal storage times to onset of autocatalysis.

Fig. 6 shows the result obtained for the propellant containing diphenylamine, with a plot of the times to the onset of autocatalysis as a function of temperature. As is evident from the diagram, there is a straight line relation between autocatalysis and temperature, if the storage time is plotted logarithmically. Accordingly, this constitutes a temperature correlation for the time of autocatalysis.

The activation energy as determined by means of the Arrhenius equation is 33.2 kcal/mol.

Fig. 7 shows the results obtained with the propellant stabilized with 2-nitrodiphenylamine. In order to show the effect on the results of different surfaces, both compact and ground specimen materials were studied.

Again, this is a straight line curve, both for the ground and for the compact propellant material. At the same time this shows that, especially at higher temperatures, the time at which autocatalysis starts is slightly earlier for the ground specimen material than for the compact ones.

In double base solid propellants ethylcentralite is also used as a plasticizer besides its stabilizing properties. In order to show the effect upon stability of a concentration of this substance (6 %) higher than usually employed as a stabilizer (2 %). the storage results will be compared as shown in Fig. 8. Again, there is a straight line relationship between the temperature and the storage period. The losses of weight measured at the time

of autocatalytic decomposition are much greater in the propellant with 6 % ethylcentralite than with the same stabilizer containing 2 % of that substance.

To indicate the time limits within which the safe life of the propellants stabilized in different ways can be found, the respective results are compared with each other in Fig.9. It is remarkable that acardite II shows the best stability values, that is, has a stabilizing action slightly better than that of the mix of stabilizers acardite II + centralite I. By far the most unstable propellant is that stabilized with diphenylamine (DPA). It is a well known fact that DPA is not especially qualified to be used as a stabilizer for double base propellant. This stabilizer was included in this research program only for the sake of completeness. For better clarity, the results obtained from the propellants with 2-nitrodiphenylamine and ethylcentralite were not indicated in the diagram.

3.3.2 Stabilizer Reaction Products as a Measure of Aging

The aging process of double base solid propellants and gun propellants is known to become apparant in the change of the stabilizer. The stabilizer continues to be degraded more and more as storage goes on, which gives rise to a number of reaction products[3].

Since the stabilizer is subjected to constant changes as a result of nitration and hydrolysis events, is should be possible to draw conclusions as to the aging condition from the reaction products of the stabilizer found in a propellant.

In order to elaborate some systematic criteria in this field, extensive studies have been conducted at our Institute. They were concerned primarily with analyses of the reaction products formed during the aging process of double base solid propellants with different stabilizers. The separation of these products was done mainly by thin layer chromatography. Unknown stabilizer reaction products were identified by means of field ion mass spectrometry.

Finally, the propellants referred to above, which contained different stabilizers within the same propellant composition, were aged artificially at different temperatures. In order to be able to follow the change in the stabilizer reaction products as a function of time during storage, propellant samples were taken from the materials stored in accordance with a precise schedule and extracted with dichloromethane. The extract was finally separated by means of the method of two-dimensional thin-layer chromatography. The following solutions were used as developer liquids for two-dimensional chromatographic separation:

(1) Benzene: tetrachloromethane: 1,2-dichloroethane = 5 : 3 : 2,5

(2) ethylacetate: petroleum ether = 20 : 80

For better identification, the following spraying agents were used:

(1) p-diethylaminobenzaldehyde
1 g in 75 ml of methanol + 25 ml of concentrated sulfuric acid

(2) 0,8 g of potassium bichromate in 100 ml of 60 % sulfuric acid.

Fig. 10 is a diagram showing the most important reaction products of diphenylamine as separated by means of thin layer chromatography. Obviously, these are almost all nitration products including the fully nitrated end product, hexanitrodiphenylamine and picric acid.

Considerable work was needy for identification of the reaction products of ethylcentralite, mainly because the preparation of the different stabilizer derivatives of ethylcentralite was much more complicated than in the case of diphenylamine. Another aggravating factor was the fact that derivatives of centralite do not undergo the characteristic color reactions as do DPA products when sprayed on the thin-layer plate.

Fig. 11 shows the main reaction products of ethylcentralite.

For identification of the components the thin-layer plate was briefly heated to 130° following chromatographic analysis and subsequently sprayed with a solution of potassium bichromate in sulfuric acid.

From the chromatogram it is seen that the reaction products are more in the nature of nitrated saponification products than direct nitration products of ethylcentralite. The main products generated are the derivatives of ethylaniline.

From the next figures it is evident that the reaction products of the stabilizer is much more identical with the aging condition of the respective propellant than is expressed in any other type of stability examination. The diagrams show the stabilizers with their stabilizer reaction products schematically in the way they can be generated in colors on the thin-layer plate.

Fig. 12 shows the change in the stabilizer reaction products of the double base propellant stabilized with DPA at 90°C. After only one day all the DPA has reacted. In addition to other reaction products resulting from continued nitration, such as the dinitro-,trinitro- and tetranitro-derivatives, finally, as aging of the propellant continues, penta- and hexanitro-DPA and picric acid are formed. The latter two products were detected above all before the onset of autocatalytic decomposition during aging double base propellants.

An analogous reaction series, but spread over a longer period of time, is obtained at 85°C, see Fig. 13. This correspondingly holds also for even lower temperatures, see Fig. 14. This is a diagram showing the aging products obtained at 80°C.

A similar decomposition mechanism as with DPA is shown also by 2-nitro-DPA, as is seen in Fig. 15. In the course of storage at 90°C the following products can be detected: after one day dinitrodiphenalamines; after two days trinitrodiphenylamines; after two weeks tetranitro-DPA; after 23 days pentanitro-DPA; after 27 days hexanitro-DPA and picric acid.

The results obtained with acardite I as a stabilizer are of special interest, because this stabilizer continues to react as the propellant continues to age, mainly forming the reaction products of diphenylamine, see Fig. 16. In the propellant stabilized with acardite II aging at 90°C, in addition to the DPA reaction products 2- and 4-nitroacardite II are formed, see Fig. 17.

A behavior by far different from that of diphenylamine, 2-nitrodiphenylamine and the acardites is exhibited by ethylcentralite in the course of aging of double base propellants. In addition to nitro- and dinitrocentralite, mainly the nitro- and nitroso-derivatives of ethylaniline are formed in this case, see Fig. 18.

While ethylcentralite with a 2 % fraction in the propellant has been completely consumed after only 14 days of storage at 90°C, autocatalytic decomposition does not occur before storage for 28 days. This behavior of double base propellants containing centralite, namely the fact that the stabilizer has been consumed at approximately half the storage period, with respect to autocatalysis, has been observed also at lower temperatures,e.g., at 85°C, see Fig. 19. This means that the time at which ethyl centralite has just been consumed is equal to half the safe life.

4. Summary

While stored at various temperatures between 65°C and 90°C, several double base propellants with the same composition, differing only in the stabilizer, were aged artificially to the onset of autocatalytic decomposition. A correlation between the temperature and the storage period has been established for the results obtained at the respective temperatures.

Moreover, studies were conducted on the chromatographic analysis of stabilizer reaction products of the type occurring in particular in propellants with diphenylamine, 2-nitrodiphenylamine, acardite I, acardite II and ethylcentralite as a result of storage at elevated temperatures due to reactions with the decomposition products of nitric acid esters.

It has been shown that continuing aging of the propellant gives rise to stabilizer reaction products which are quite characteristic of the respective aging condition. These reaction products may be used as a criterion for different stages of aging within the safelife of solid propellants.

5. Literature

1) Volk, F., Schmitt, D., Wunsch, G.: Untersuchungen über die Lebensdauer von Raketentreibsätzen ICT-Bericht 5/74

2) Van Geel, J.L.C.: The heat generation test for the determination of the self ignition and the ballistic stability of nitrate ester propellants Jahrestagung 1971, Institut für Chemie der Treib- und Explosivstoffe, Karlsruhe

3) Yasuda, St.K.: Identification of N-nitroso- and nitrodiphenylamines by two-dimensional thin-layer chromatography J.Chromatog.14 (1964) 65-70

4) Yasuda, St.K.: Identification of ethylcentralite-nitrogen tetroxide reaction products J.Chromatog. 16 (1964) 488-493

6. Abbreviations

1. Reaction Products of Diphenylamine

1)	DPA	diphenylamine
2)	2-N-DPA	2-nitro-DPA
3)	N-Ns-DPA	N-nitroso-DPA
4)	N,4-DNs-DPA	N,4-dinitroso-DPA
5)	N-Ns-4-N-DPA	N-nitroso-4-nitro-DPA
6)	3-N-DPA	3-nitro-DPA
7)	2,6-DN-DPA	2,6-dinitro-DPA
8)	2,4-DN-DPA	2,4-dinitro-DPA
9)	N-Ns-2,4-DN-DPA	N-nitroso-2,4-dinitro-DPA
10)	2,2'-DN-DPA	2,2'-dinitro-DPA
11)	2,4,6-TN-DPA	2,4,6-trinitro-DPA
12)	2,4'-DN-DPA	2,4'-dinitro-DPA
13)	N-Ns-2-N-DPA	N-nitroso-2-nitro-DPA
14)	N-Ns-4,4'-DN-DPA	N-nitroso-4,4'-dinitro-DPA
15)	4-Ns-2-N-DPA	4-nitroso-2-nitro-DPA
16)	4-N-DPA	4-nitro-DPA
17)	2,2'-4,6-TeN-DPA	2,2',4,6-tetranitro-DPA
18)	N-Ns-2,4'-DN-DPA	N-nitroso-2,4'-dinitro-DPA
19)	N-Ns-2,2'-DN-DPA	N-nitroso-2,2'-dinitro-DPA
20)	2,2',4-TN-DPA	2,2',4-trinitro-DPA
21)	N-Ns-2,2',4-TN-DPA	N-nitroso-2,2',4-trinitro-DPA
22)	N-Ns-2,4,4'-TN-DPA	N-nitroso-2,4,4'-trinitro-DPA
23)	2,4,4'-TN-DPA	2,4,4'-trinitro-DPA
24)	2,4,4',6-TeN-DPA	2,4,4',6-tetranitro-DPA
25)	2,2',4,4'-TeN-DPA	2,2',4,4'-tetranitro-DPA
26)	2,2',4,4',6-PN-DPA	2,2',4,4',6-pentanitro-DPA
27)	4-Ns-DPA	4-nitroso-DPA
28)	4,4'-DN-DPA	4,4'-dinitro-DPA
29)	2,2',4,4',6,6'-HN-DPA	2,2',4,4',6,6'-hexanitro-DPA
30)	2,4,6-TN-Ph	2,4,6-trinitrophenol (picric acid)

2. Reaction Products of Ethylcentralite

1)	NB	nitrobenzene
2)	2-NEA	2-nitroethylaniline
3)	1,3,5-TNB	1,3,5-trinitrobenzene
4)	2,4,6-TNEA	2,4,6-trinitroethylaniline
5)	1,3-DNB	1,3-dinitrobenzene
6)	EA	ethylaniline
7)	N-NsEA	N-nitrosoethylaniline
8)	N-Ns-4-NEA	N-nitroso-4-nitroethylaniline
9)	N,2,4,6-TeNEA	N,2,4,6-tetranitroethylaniline
10)	2,4-DNEA	2,4-dinitroethylaniline
11)	2-NA	2-nitroaniline
12)	4-NEA	4-nitroethylaniline
13)	N-Ns-2-NEA	N-nitroso-2-nitroethylaniline
14)	4-NA	4-nitroaniline
15)	2,2',4,4'-TeNEC	2,2',4,4'-tetranitroethylcentralite
16)	2,4-DNA	2,4-dinitroaniline
17)	4-NEC	4-nitroethylcentralite
18)	2-NEC	2-nitroethylcentralite
19)	4-NPh	4-nitrophenol
20)	2,4-DNEC	2,4-dinitroethylcentralite
21)	4,4'-DNEC	4,4'-dinitroethylcentralite
* 22)	EC	ethylcentralite
23)	2,4-DNPh	2,4-dinitrophenol
24)	2,6-DNPh	2,6-dinitrophenol
25)	2,4,6-TNPh	2,4,6-trinitrophenol (picric acid)

Composition of Double base propellants

50 %	nitrocellulose
35 %	nitroglycerine
10 %	diethylphthalate
2 %	stabilizer
3 %	burning modifier

Stabilizers:

- 2 %	diphenylamine
- 2 %	nitrodiphenylamine
- 2 %	acardite I (asymmetrical diphenylurea
- 2 %	acardite II (asymmetrical methyldiphenylurea
- 2 %	ethylcentralite
- 6 %	ethylcentralite
- 1 %	ethylcentralite + 1 % acardite II

Figure 1

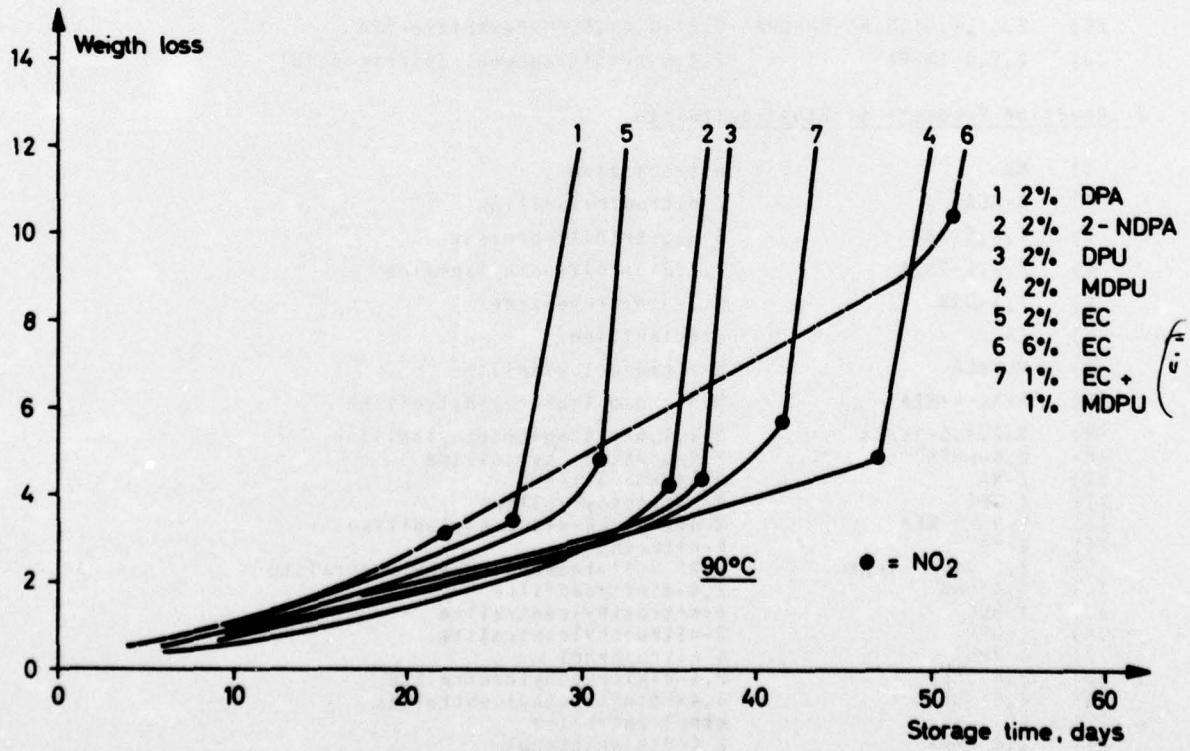

Fig.2 Propellants with different stabilizers

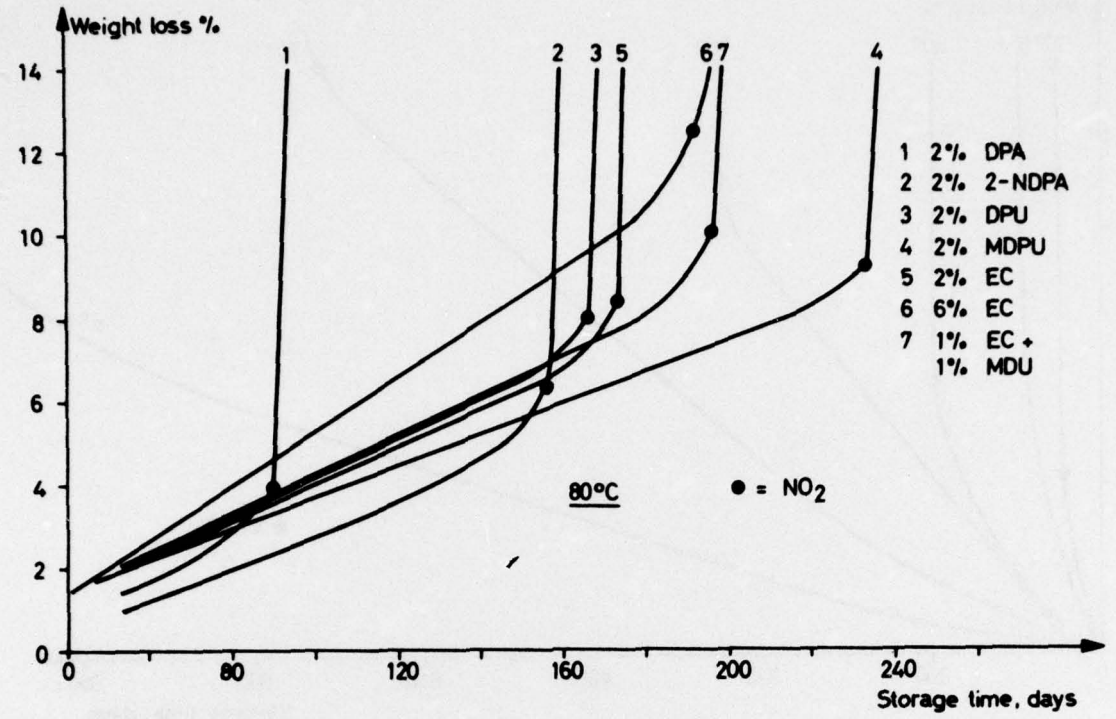

Fig.3 Propellants with different stabilizers

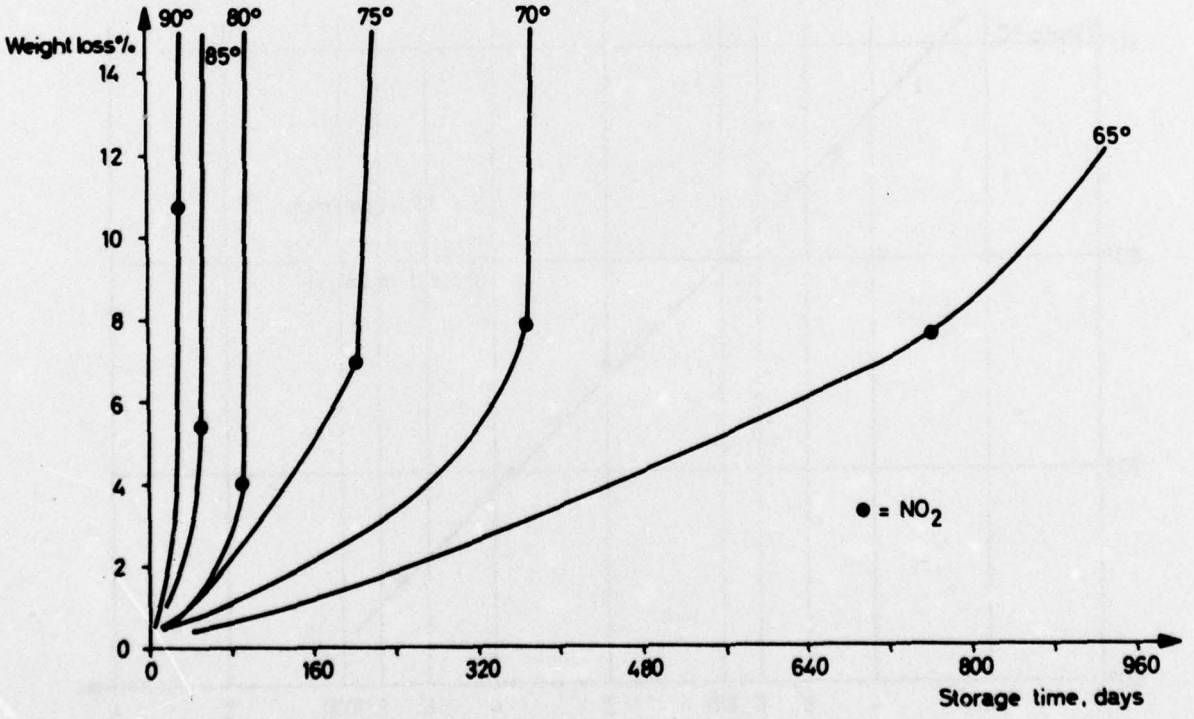

Fig.4 Propellant with 2% diphenylamine

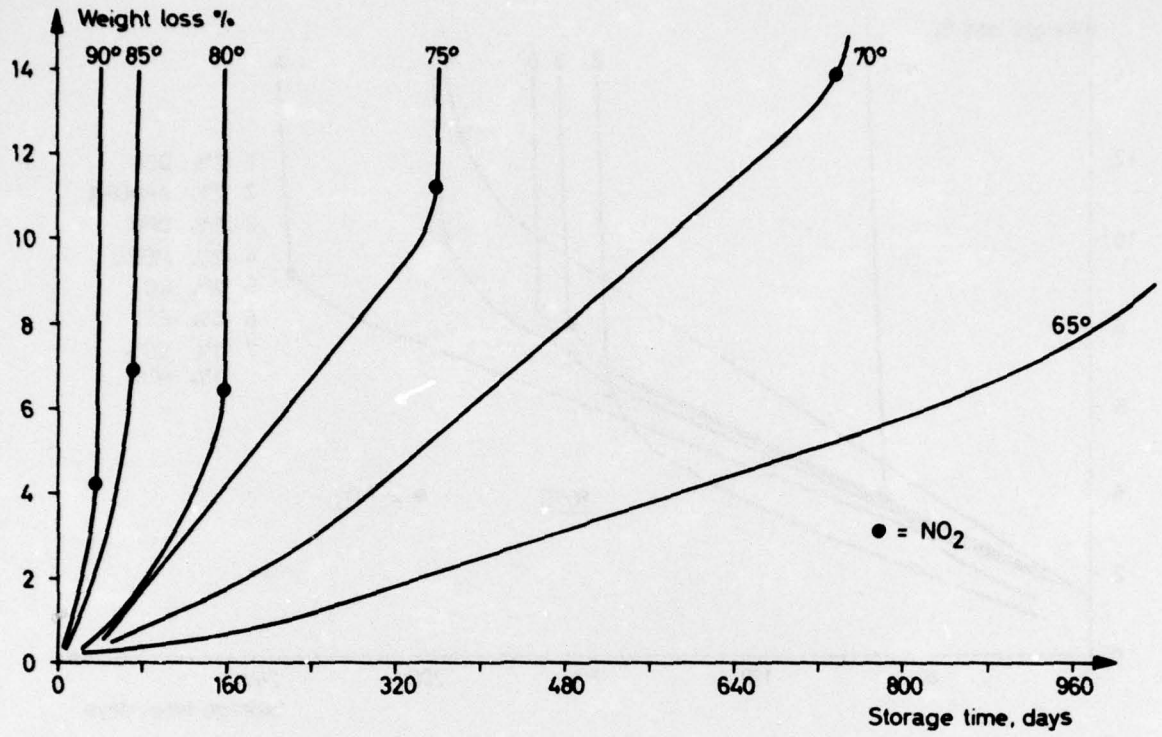

Fig.5 Propellant with 2% Nitrodiphenylamin

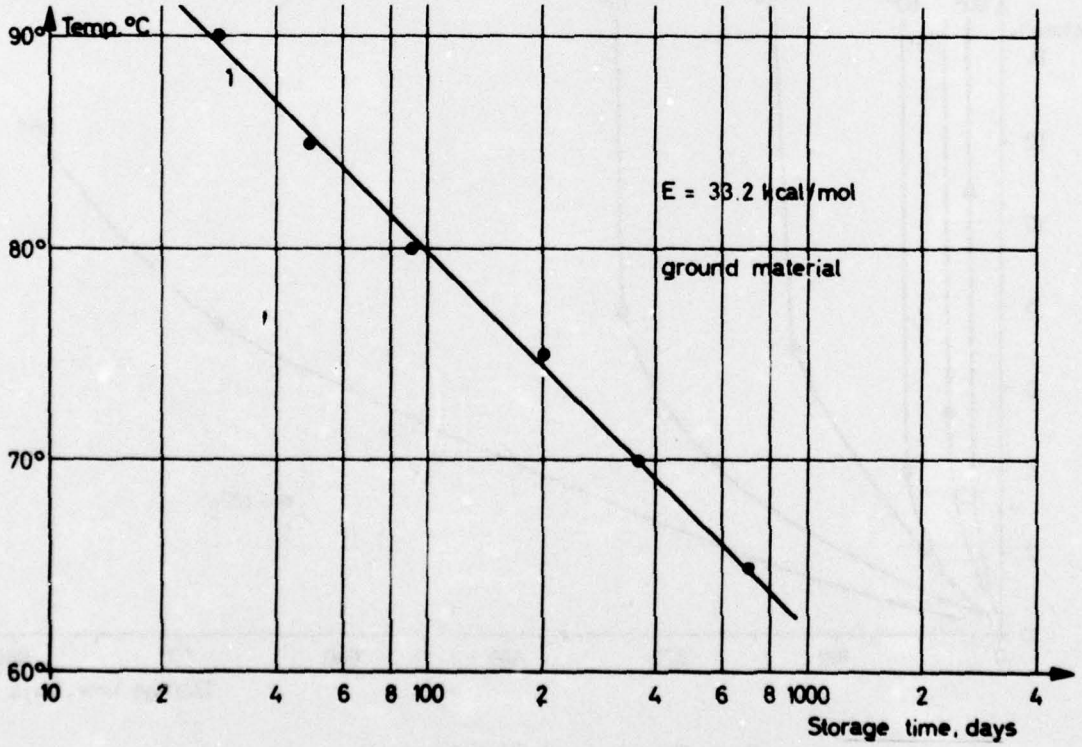

Fig.6 Autocatalysis of double base propellant with 2% DPA

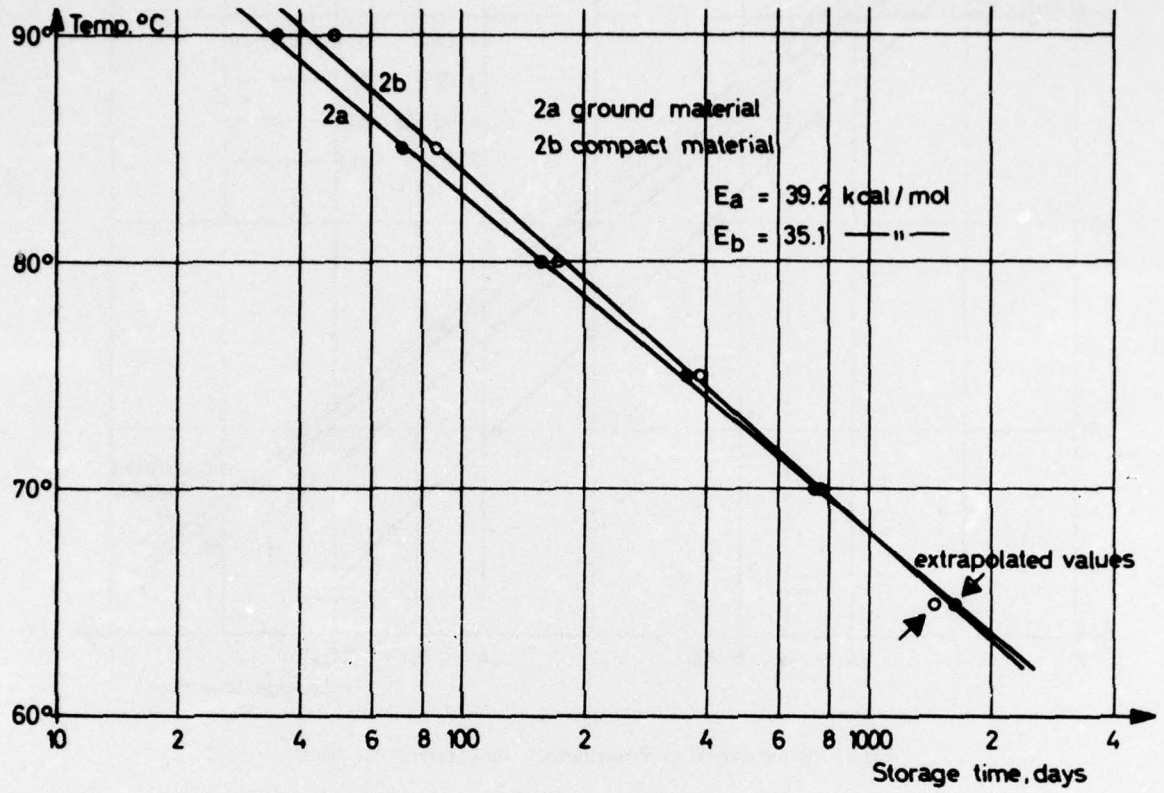

Fig.7 Autocatalysis of double base propellant with 2% of 2-NDPA

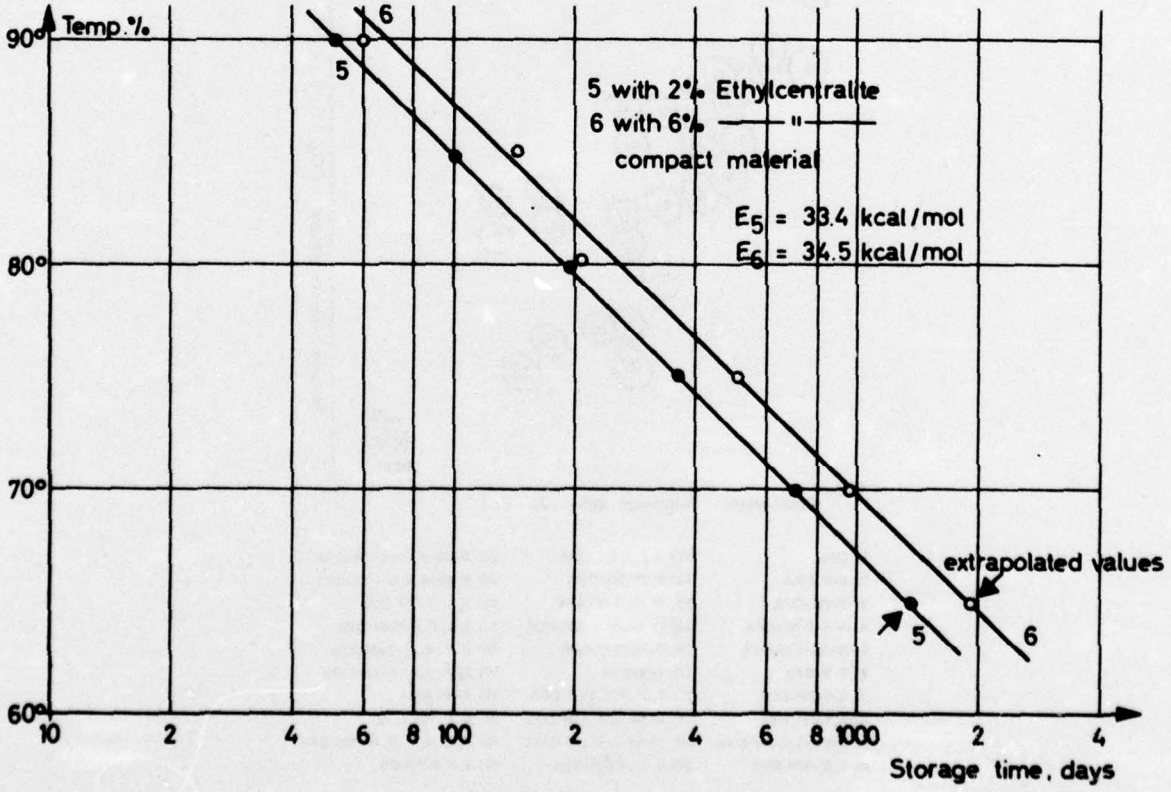

Fig.8 Autocatalysis of double base propellants

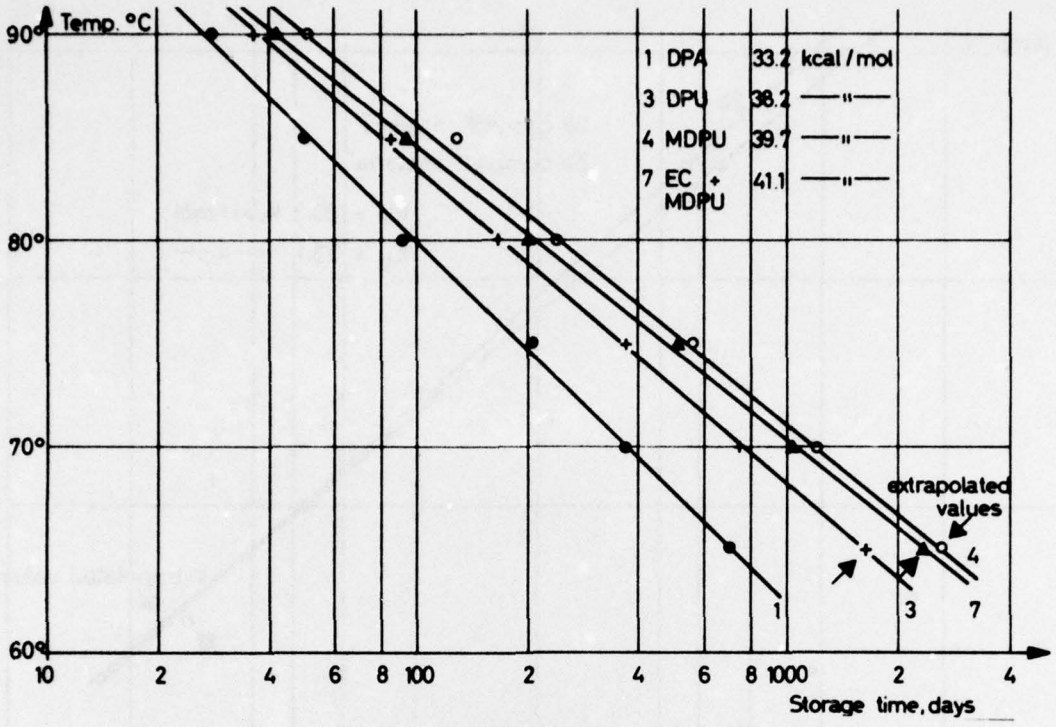

Fig.9 Autocatalysis of Propellants with different stabilizers

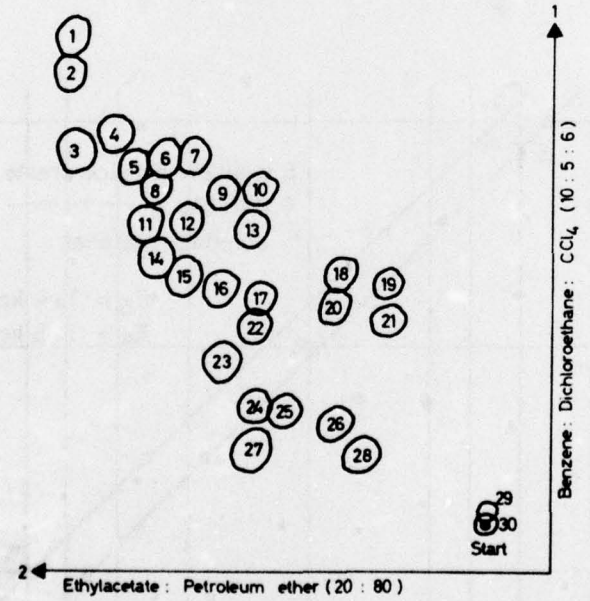

1) DPA	11) 2, 4, 6-TN-DPA	21) N-Ns-2, 2', 4-TN-DPA
2) 2-N-DPA	12) 2, 4'-DN-DPA	22) N-Ns-2, 4, 4'-TN-DPA
3) N-Ns-DPA	13) N-Ns-2-N-DPA	23) 2, 4, 4'-TN-DPA
4) N, 4-DNs-DPA	14) N-Ns-4, 4'-DN-DPA	24) 2, 4, 4', 6-TeN-DPA
5) N-Ns-4-N-DPA	15) 4-Ns-2-N-DPA	25) 2, 2', 4, 4'-TeN-DPA
6) 3-N-DPA	16) 4-N-DPA	26) 2, 2', 4, 4', 6-PN-DPA
7) 2, 6-DN-DPA	17) 2, 2', 4, 6-TeN-DPA	27) 4-Ns-DPA
8) 2, 4-DN-DPA	18) N-Ns-2, 4'-DN-DPA	28) 4, 4'-DN-DPA
9) N-Ns-2, 4-DN-DPA	19) N-Ns-2, 2'-DN-DPA	29) 2, 2', 4, 4', 6, 6'-HN-DPA
10) 2, 2'-DN-DPA	20) 2, 2', 4-TN-DPA	30) 2, 4, 6-TN-Ph

Fig.10 Two dimensional thin-layer chromatogram of the aging products of diphenylamin

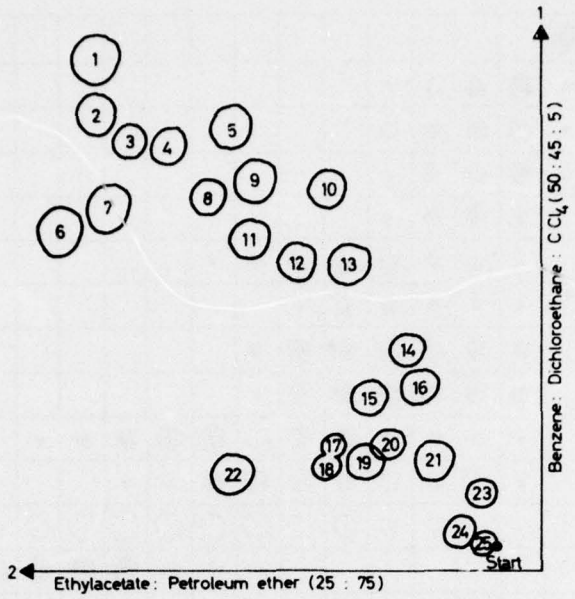

1) NB
2) 2-NEA
3) 1,3,5-TNB
4) 2,4,6-TNEA
5) 1,3-DNB
6) EA
7) N-NsEA
8) N-Ns-4-NEA
9) N,2,4,6-TeNEA
10) 2,4-DNEA
11) 2-NA
12) 4-NEA
13) N-Ns-2-NEA
14) 4-NA
15) 2,2',4,4'-TeNEC
16) 2,4-DNA
17) 4-NEC
18) 2-NEC
19) 4-NPh
20) 2,4'-DNEC
21) 4,4'-DNEC
22) EC
23) 2,4-DNPh
24) 2,6-DNPh
25) 2,4,6-TNPh

Fig.11 Two dimensional thin-layer chromatogram of the aging products of ethylcentralite

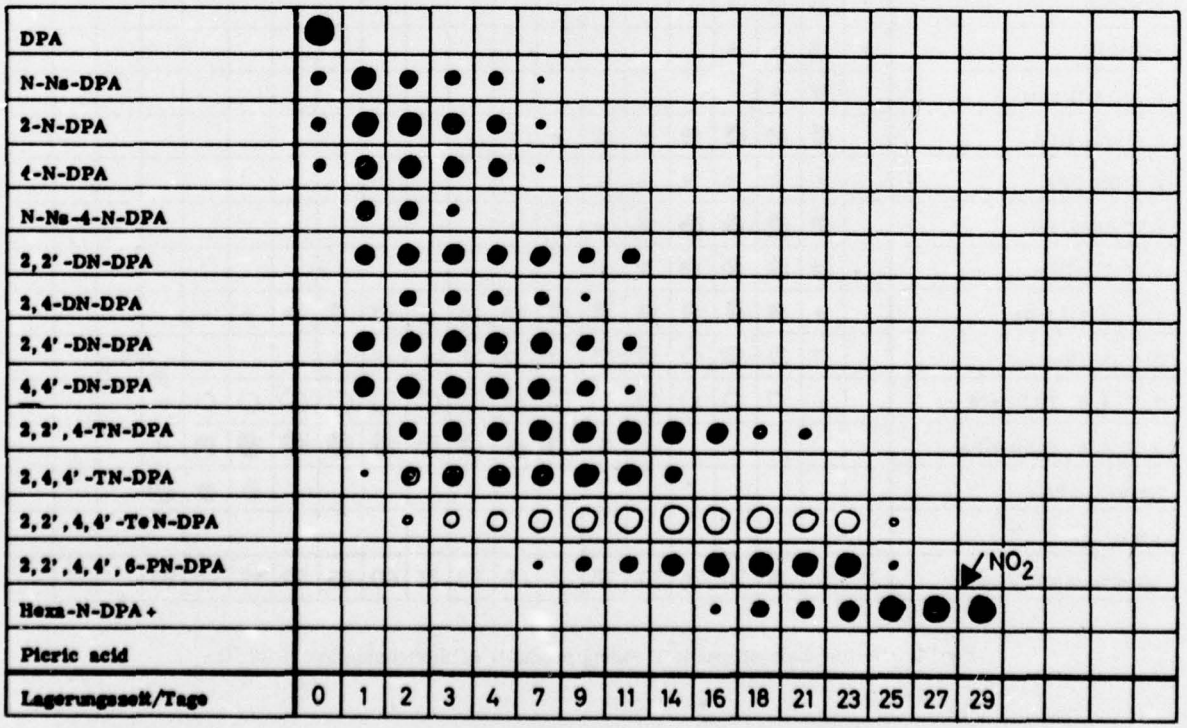

Fig.12 Double base propellant. Aging products of diphenylamine at 90 °C

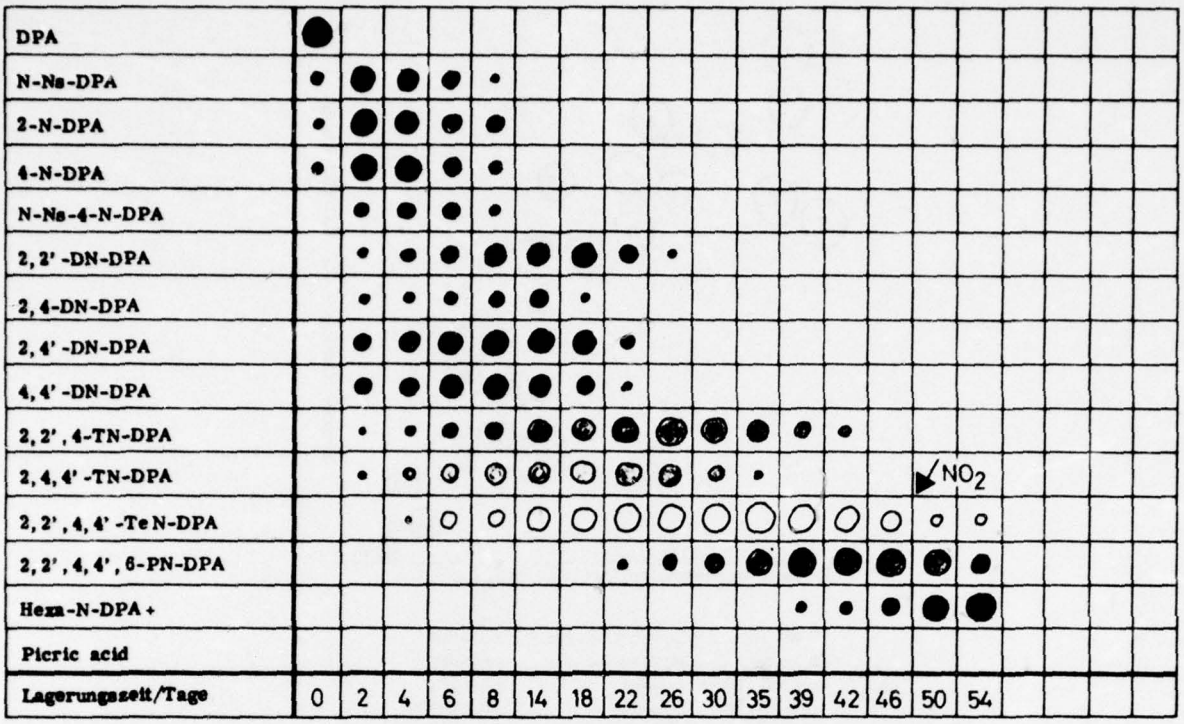

Fig.13 Double base propellant. Aging products of diphenylamine at 85 °C

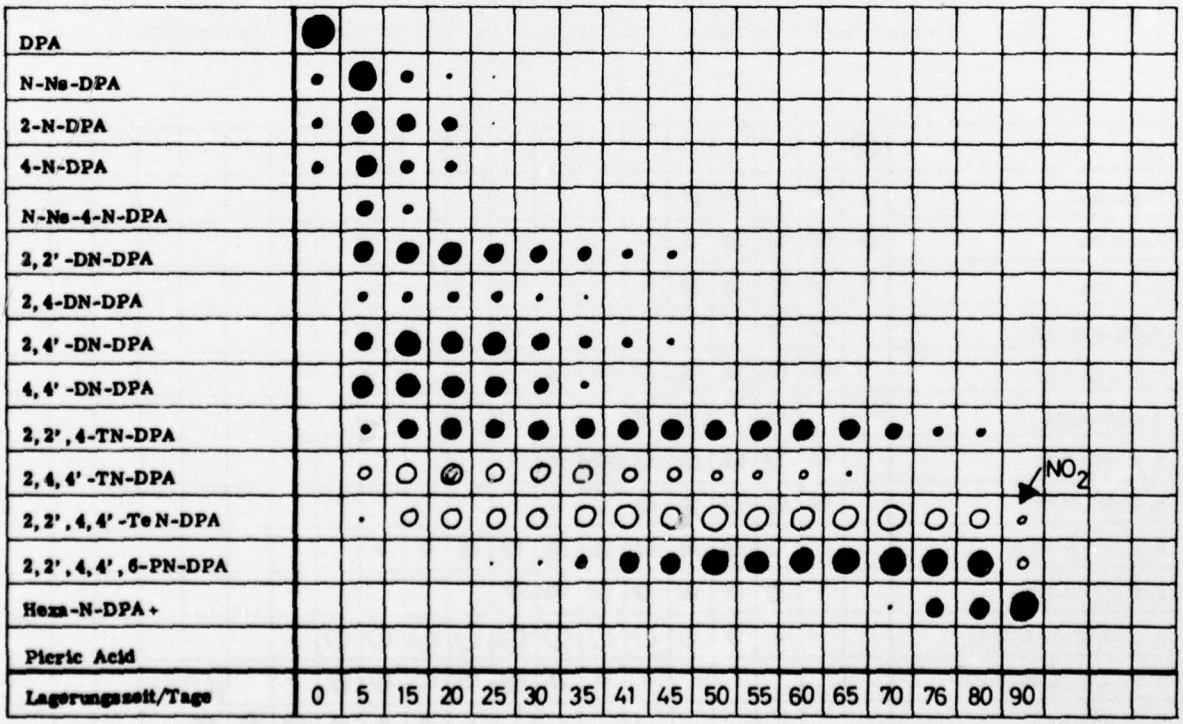

Fig.14 Double base propellant. Aging products of diphenylamine at 80 °C

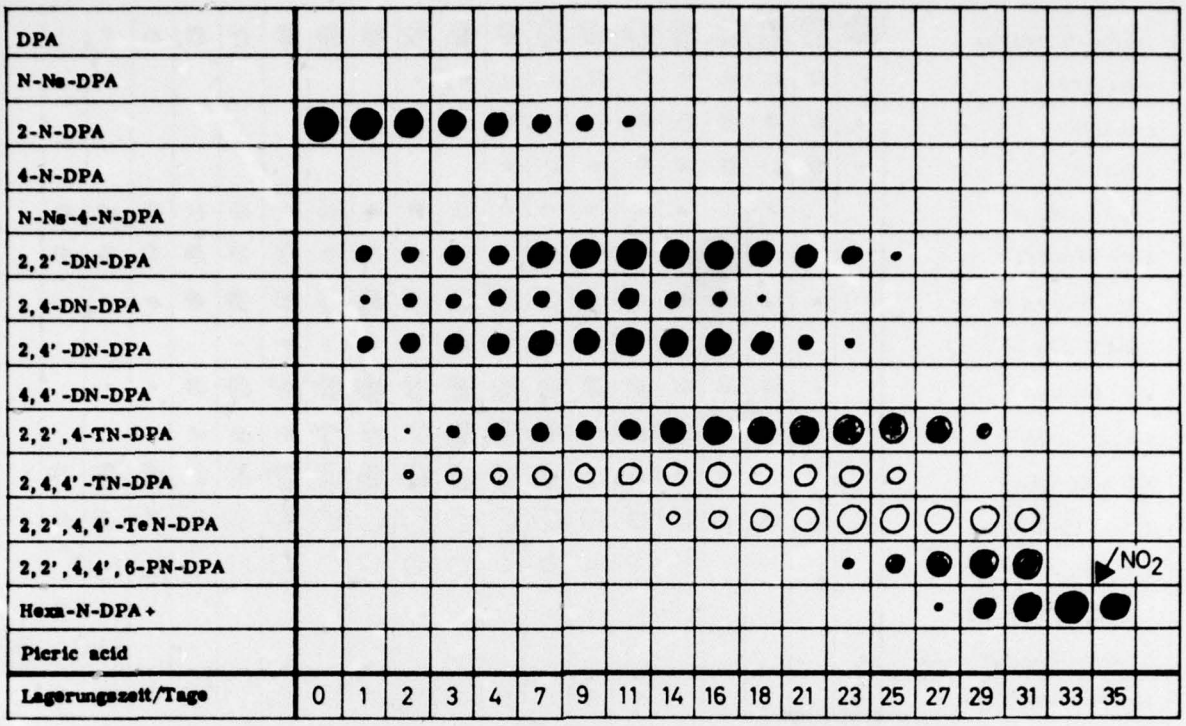

Fig.15 Double base propellant. Aging products of 2-nitrodiphenylamine at 90 °C

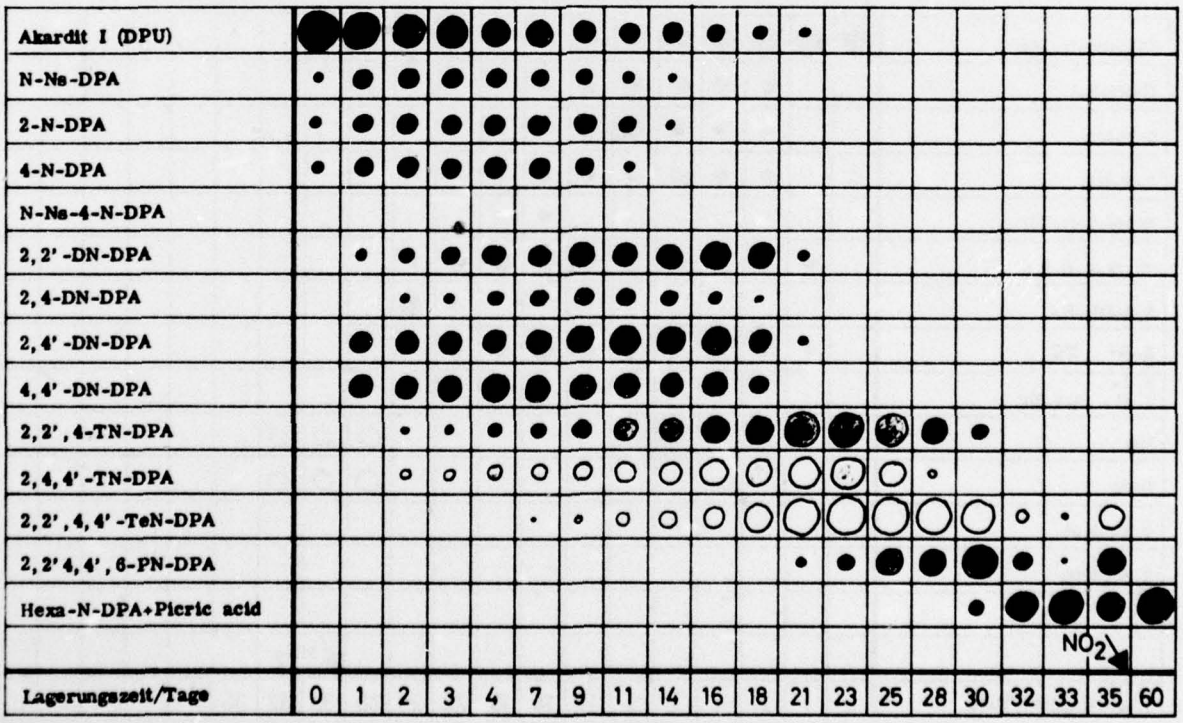

Fig.16 Double base propellant. Aging products of akardite I (diphenylurea) at 90 °C

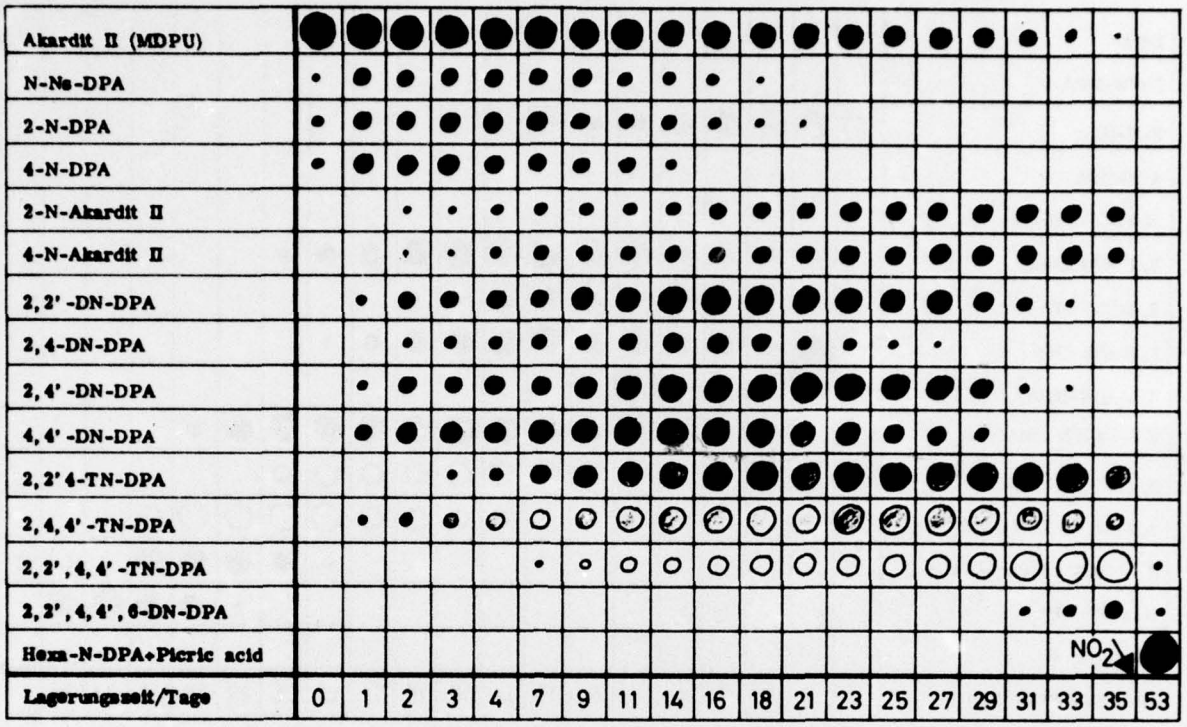

Fig.17 Double base propellant. Aging products of akardite II (methyldiphenylurea) at 90 °C

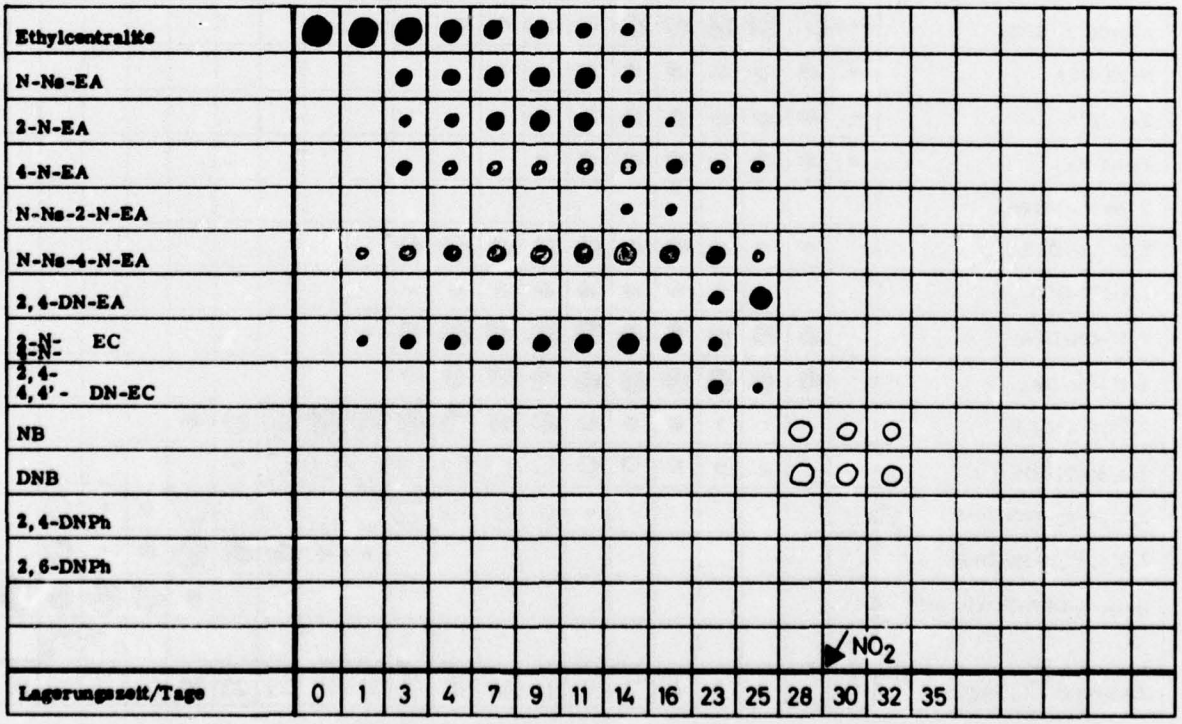

Fig.18 Double base propellant. Aging products of ethyl centralite at 90 °C

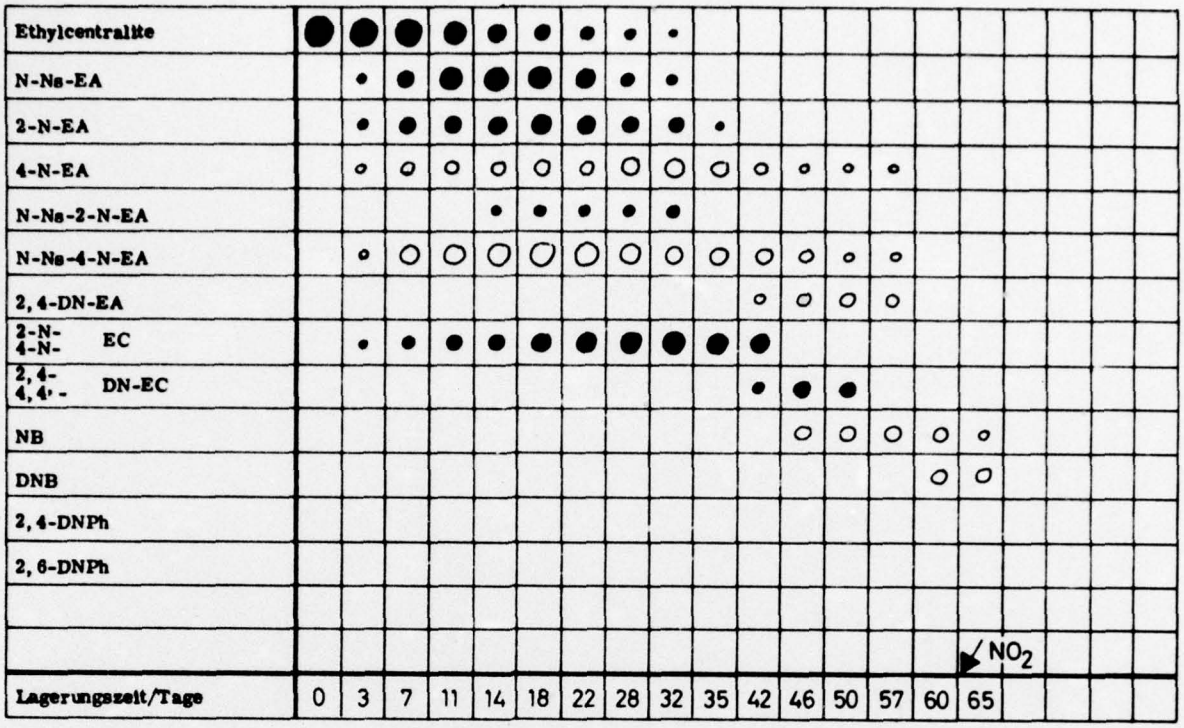

Fig.19 Double base propellant. Aging products of ethyl centralite at 85 °C

Activation energies

Double base propellant with

- 2 %	DPA	33,2 kcal/mol	
- 2 %	2-nitro-DPA	39,2 "	"
- 2 %	acardite I	38,2 "	"
- 2 %	acardite II	39,7 "	"
- 2 %	ethylcentralite	33,4 "	"
- 6 %	ethylcentralite	34,5 "	"
- 1 %	ethylcentralite +	41,1 "	"
1 %	acardite II		

Figure 20

SIMPLE DETERMINATION OF THE MECHANICAL BEHAVIOUR OF DOUBLE BASE ROCKET PROPELLANTS UNDER HIGH LOADING RATES

by
P.J. Greidanus
Rocket Section
Technological Laboratory TNO
P.O. Box 45
Rijswijk-2100
The Netherlands

SUMMARY

Solid rocket propellants are subject to high loading rates, e.g. by the pressure rise during ignition of rocket motors. Therefore, the mechanical properties at high loading rates are important for a reliable performance of rocket motors. Mostly the mechanical behaviour is determined by tensile testing, but this technique is complicated and costly.

In the Technological Laboratory TNO two methods have been applied and evaluated for double base rocket propellants: uniaxial impact compression by an instrumented drop weight apparatus, and determination of elastic constants by ultrasonic measurements.

In both methods specimen preparation and test execution are simple. Ultrasonic measurements for the determination of elastic constants can possibly by applied directly to small rocket propellant grains.

The ultrasonic equipment is used in two ways: determination of elastic constants, and localization of defects in the propellant grain.

In this paper the investigation of the mechanical properties of some double-base rocket propellants by forementioned methods will be considered.

LIST OF SYMBOLS

E	Young's modulus	MN/m^2
F	force	N
G	shear modulus	MN/m^2
G^*	complex shear modulus[1)]	MN/m^2
G'	real part of complex shear modulus[1)] ≡ storage modulus	MN/m^2
G''	imaginary part of complex shear modulus[1)] ≡ loss modulus	MN/m^2
K	compression modulus	MN/m^2
M	uniaxial compression modulus ≡ longitudinal wave modulus	MN/m^2
O	surface on which force acts	m^2
T_g	glass transition temperature	^oC
T_g'	secondary transition temperature	^oC
U	particle displacement	m
U_o	particle displacement at t=0[1)]	m
a	deceleration	m/s^2
c	sound velocity in liquid	m/s
c_s	transverse sound velocity[1)]	m/s
c_ℓ	longitudinal sound velocity[1)]	m/s
$c_{\ell,m}$	longitudinal sound velocity in sample[1)]	m/s
$c_{s,m}$	transverse sound velocity in sample[1)]	m/s
d	thickness of sample	m
g	acceleration by gravity	m/s^2
h	drop height	m
i	$\sqrt{-1}$	
ℓ	specimen length	m
m	mass	kg
p	pressure	MPa
q	$= c\,\Delta t/d$	
r	$= \alpha_{s,m}\, c_{s,m}/\omega$	
t	time	s
t_1	time to travel a distance in sample	s
t_2	time to travel same distance in liquid	s
Δt	$t_2 - t_1$	s
v	velocity	m/s
w	strain rate	1/s
x	distance	m
$\alpha_{s,m}$	attenuation	Nepers/m
δ	phase difference between stress and strain	
ε	strain	
ε_{max}	maximum strain	
ε_{el}	elastic strain	
ε_{pl}	plastic strain	
ε_{rec}	recovered strain after 30 days	
γ	shear strain	
ω	angle velocity	rad./s
ρ	density	kg/m^3
σ	stress	MN/m^2
θ	angle of incidence for waves	rad.
$\theta_{g,\ell}$	limit angle of incidence for longitudinal waves	rad.
$\theta_{g,s}$	critical angle for transverse waves	rad.
ϕ	angle of refraction	rad.

[1)] Subscripts, superscripts, etc are also used with other symbols.

INTRODUCTION

For reliable rocket motor performance the mechanical properties of propellants are very important. The more the mechanical properties of the solid rocket propellant will deteriorate, the bigger the chance of mechanical failure or permanent deformation of the propellant grain; failure and permanent deformation are bound to influence interior ballistic properties of the rocket motor. Any type of defect in the propellant grain will cause pressure-fluctuations in the rocket motor; if pressure deviates too much from the pressure-equilibrium of the deflagration, there is a chance of continuous increase in chamber pressure and burning rate of the rocket propellant. In that case explosion by bursting of the rocket motor case is possible.

Very important characteristics which will influence the mechanical properties of the rocket propellant grain are the chemical composition, the internal structure or texture, the shape, the propellant processing technique and the history of the propellant grain. Common types of solid rocket propellants are double base propellants and composite propellants; both with polymeric material as their main component, i.e. cellulose nitrate in the former type of propellant and polyurethane, polyvinylchloride or polybutadiene in the latter type. Both types are regarded as filled polymers. Because of the polymeric backbone these solid propellants act rheologically as visco-elastic materials.

The internal structure or texture is also an important variable of the mechanical behaviour of the propellant grain. Texture describes approximately the strength between the components of the propellant. Special shapes of propellant grains have been designed for a programmed gas production during the burning time of the rocket motor. Dependent on the shape and processing technique internal stresses are introduced into the propellant grain. Some mechanical properties of the propellant grain such as failure properties could deteriorate drastically by internal stresses in the propellant.

Also environmental and transport history of the propellant grain could influence the mechanical behaviour. During storage gravity forces and thermal stresses in the propellant grain will occur while loading by vibrations and shocks will act during transport.

Failure of the solid propellant grain will mainly occur during the fast pressure rise on ignition. For example pressure may rise from 0 through 5 MPa in the first five milliseconds. It is evident that the mechanical behaviour of the propellant grain at high loading rates is very important for reliable rocket performance.

Also, it is expected that the mechanical properties of propellants at high loading rates are more age-sensitive than the mechanical properties at lower loading rates, e.g. in normal tensile tests (Ref.1). Because the Netherlands is not manufacturing rocket motors, our laboratory is specialized in surveillance testing of old rocket motors. Within the scope of surveillance testing the determination of age-sensitive mechanical properties, such as mechanical properties at high loading rates is interesting.

The mechanical properties of solid rocket propellants are both temperature and strain rate sensitive. Rate sensitivity of mechanical properties is a typical feature of visco-elastic materials. No failure would occur if during the short loading time energy could dissipate. Energy dissipation mainly occurs by molecular motions. The quantity of energy that dissipates is dependent on the relaxation time.

A complete structural analysis of a solid rocket propellant grain would be complicated, because of the complex shape of the charge, especially at high loading rates. Exact laboratory simulation of the loading on the charge during action time of the rocket motor would require very complicated techniques. In the Technological Laboratory TNO simple techniques are used for the determination of mechanical properties of materials at high loading rates.

EXPERIMENTAL

For the estimation of the mechanical properties of a material no difference exists at molecular scale between uniaxial compression deformation or uniaxial tensile deformation (Ref.2,3). Loading of a specimen by uniaxial compression has experimental advantages over tensile loading. Besides the fact that machining of the specimen is more simple, also clamprupture often occurs in tensile tests. At uniaxial compression tests, however, no clamping is necessary. For the determination of the mechanical properties at high loading rates the Technological Laboratory is using an impact test with uniaxial compression loading, i.e. the drop weight impact method along with a non-destructive method based on ultrasound, the ultrasound method.

Ultrasound techniques are frequently used in product control and surveillance tests for determining internal defects in propellant charges.

Mechanical and ultrasonic properties of materials are closely related (Ref.4,5). The measurement of the sound velocities is used to determine the elastic properties of solid materials (see Appendix A1).

Propagation of ultrasound waves through materials causes dynamic loading. Because of the short duration of the loading it can be assumed that deformation occurs only within the elastic region.

Contrary to the drop weight impact method, no failure properties could be determined with the ultrasound method.

Drop weight impact method

The drop weight impact method is based on impact of a cylindrical specimen by a dropping weight. In the Technological Laboratory a modified Rotterapparatus is used for this purpose. In Figure 1 an outline of the system is given.

Measuring procedure

The loading rate could be varied from 1 through 8 m/s by dropping the weight from different heights. The load during the impact deformation of the specimen causes a signal from the load-cell, with natural frequency of 8 KHz. The loading signal is amplified by a strain gauge amplifier (Peekel, type GRL-1) and monitored on an oscilloscope (Tektronix, type 564 Storage Oscilloscope); the oscilloscope is triggered by a photo-cell. The impact experiment is approximately similar to a dynamic experiment at 0,2 KHz.

The load-time curve is photographed from the oscilloscope screen. From the load-time relationship of the impact experiment a stress-strain relationship is derived by using numerical calculation techniques (see Appendix A2-a).
Young's modulus, maximum strain, maximum stress and failure criteria are derived from the stress-strain relationship.

Simulation of loading during ignition

By rough calculation it can be shown that loading during ignition of a solid propellant rocket motor may approximately be simulated by dropping a weight on a cylindrically shaped specimen: $\int_0^t p\,dt$, acting on a solid propellant charge during a pressure rise from 0,1 to 10,1 MPa in 10 ms would be $0,5 \times 10^5$ (Ns/m^2), if the average chamber pressure is 10 MPa.

By dropping a weight, m (kg), from a height, h (m), on a cylindrically shaped specimen with diameter 12,5 (mm) the pressure-impulse is:

$$\int_0^t \frac{F}{0}\,dt = 0,36 \times 10^5 \times m\, h^{\frac{1}{2}}$$

Simulation of the loading during ignition of forementioned solid propellant charge will occur, if the relation $0,5 \times 10^5 = 0,36 \times 10^5 \times m\, h^{\frac{1}{2}}$ holds.
This relation will hold if m = 1 (kg) and h = 1,93 (m)
m = 2 (kg) and h = 0,48 (m)
m = 3 (kg) and h = 0,21 (m)
m = 5 (kg) and h = 0,08 (m)

Ultrasound method

Short pulses of ultrasonic waves are sent through a sample with a repetition frequency of 65 Hz. An outline of the apparatus is shown in Figure 2.

The ultrasonic part of the apparatus consists of the Ultrasonic Flaw Detector MK III (CNS Instruments Ltd., London). The four transducers are identical and are arranged in two pairs. The working frequency of the lead zirconate titanate crystals in the transducers is 0,351 MHz. Both the transducers and the sample are immersed in a contact liquid in a thermostated bath. The temperature can be varied between -40°C and +60°C with an accuracy of ± 0,1°C. The sample is placed in a sample holder at the bottom of the bath. The bath is attached to a table which can be turned in a horizontal plane. This enables the sample to be set under any desired angle with the sound beam.
In Figure 2 the sample is placed between one pair of test transducers. There are two liquid-solid transitions between the test transducers. Between the others, the so-called reference transducers, only the contact liquid is present. To eliminate possible effects from liquid-solid transitions, there are also samples of which a thinner part extends between the reference transducers. Then the thickness of the sample is the only difference in sound path between test transducers and reference transducers.

When the sample is placed perpendicular to the sound beam, only longitudinal waves are transmitted through the solid. If the sample is placed at an oblique angle with the sound beam, both longitudinal and shear waves are generated in the sample. Since the longitudinal sound velocity in the solid sample ($c_{\ell,m}$) is always higher than the sound velocity in the contact liquid (c), there will exist a critical angle at which longitudinal waves are totally reflected, while shear waves are still transmitted through the sample and the shear wave velocity ($c_{s,m}$) can be measured.
The critical angle for longitudinal waves ($\theta_{g,\ell}$) follows from Snellius' law (Equations 1 and 2)

$$\frac{\sin\theta_{g,\ell}}{c} = \frac{\sin\phi}{c_{\ell,m}} \qquad (1)$$

and $\phi = \pi/2$ gives

$$\sin\theta_{g,\ell} = \frac{c}{c_{\ell,m}} \qquad (2)$$

If $c_{\ell,m} > c$ and $c_{s,m} < c$, then the measurement of the shear wave velocity is possible for every $\theta > \theta_{g,\ell}$. Otherwise, if $c_{s,m} > c$, then θ has to fulfil the condition $\theta_{g,\ell} < \theta < \theta_{g,s}$, where $\theta_{g,s}$ is the critical angle for shear waves.

Measuring procedure

The temperature and the sound velocity of the contact liquid in the bath are measured. The sample is placed in the liquid while perpendicular or under an angle θ with the sound beam, and the time difference (Δt) in travelling the same distance between both pairs of transducers is measured.

The following equations are used (Equations 3, 4, and 5).

$$q = \frac{c\Delta t}{d} \tag{3}$$

$$c_{\ell,m} = \frac{c}{1-q} \tag{4}$$

$$c_{s,m} = c\left[1-2q\cos\theta + q^2\right]^{-\frac{1}{2}} \tag{5}$$

(Equation 5 is derived in Appendix A2-b).

Before rotating the sample from the perpendicular position, the critical angle ($\theta_{g,\ell}$) is calculated. About 15 to 20 circle degrees are added to $\theta_{g,\ell}$ and then the shear wave velocity is measured. This addition is necessary, because the sound beam is diverging. It is also necessary to shift the position of the receiver transducer perpendicularly to the direction of the sound beam (see also Appendix A2-b).

From the sound velocities measured at different temperatures several elastic constants, such as shear modulus, bulk modulus and Poisson ratio could be calculated, with the aid of the following relations

$$G = \rho\, c_{s,m}^2 \tag{6}$$

$$K = \rho\left(c_{\ell,m}^2 - \frac{4}{3}\, c_{s,m}^2\right) \tag{7}$$

$$\mu = \frac{1-2\left(\frac{c_{s,m}}{c_{\ell,m}}\right)^2}{2-2\left(\frac{c_{s,m}}{c_{\ell,m}}\right)^2} \tag{8}$$

It should be mentioned, that because of the dynamic loading of viscoelastic materials the forementioned variables are complex quantities. However, in this investigation the assumption is made, that deformations are small and occur only within the pure elastic region, so that the solid could be considered pure elastic. This means no damping will occur (see Appendix A1).

From all materials the expansion coefficients must be known for calculation of the density at different temperatures. Expansion coefficients of several double base propellants by dilatometer experiments are given in Reference 6.

SAMPLES

At 20°C and 50% RH experiments were carried out on double base rocket propellant N-4 using the drop weight impact method. The chemical composition of this 11-year-old propellant is listed in Table I. The cylindrically shaped specimens had a diameter of 12,5 mm and a length of 25 mm. All 42 specimens were sawn from a Sidewinder rocket motor (M17) charge and subsequently machined in a lathe to the above dimensions.

Experiments, using the ultrasound method were carried out on polymethylmethacrylate (PMMA) and on four double base rocket propellant types, namely JPN, NK865, OGK and N4. In Table I the chemical composition of these propellants is listed. Plane-parallel specimens of 80 mm x 140 mm were sawn and machined from the different rocket motor charges.

RESULTS AND DISCUSSION

Drop weight impact method

The impact experiments have been carried out with drop weights of 1,2,3 and 5 kg; drop heights were varied from 0,572 through 3,194 m. In Table II 42 experiments with N-4 propellant are listed and Figure 3 shows some specimens 30 days after the impact experiment.

The stress-strain diagram has been determined and several mechanical properties of

the propellant, such as maximum strain, maximum stress, Young's modulus and failure criteria have been calculated. (Table II).

From Figure 4 it appears that experiments with drop weights of 1 and 2 kg result in a scattering of the values of the Young's modulus. The scattering is mainly caused by a decreasing strain rate during the elastic deformation of the specimen. With the 3 and 5 kg drop weights the strain rate will be approximately constant during the deformation in the elastic region.

According to the rheological theory of viscoelastic materials the Young's modulus increases with increasing strain rate. Inaccurate centering of the specimen on the load cell and inhomogeneities of the propellant could explain the extreme difference between some results.

Maximum strain (ε_{max}) and maximum stress (σ_{max}) are reached when the strain rate has decreased to zero. From Figures 5 and 6 it appears that ε_{max} and σ_{max}, as the Young's modulus with increasing strain rate and with increasing mass of the drop weight. The kinetic energy of the drop weight is mainly used for deformation of the specimen.

Maximum strain is divided into two types of strain, the elastic strain (ε_{el}) and the plastic strain (ε_{pl}). Elastic strain will be the sum of any type of elastic deformation, e.g. pure elastic deformation, but also viscoelastic deformation. Plastic strain is that part of the strain which will cause permanent deformation.

Mostly the deformation within the elastic region will recover completely, so that the recovered strain, (ε_{rec}) is equal to the elastic strain (ε_{el}). For the plastic strain the following relation will hold:

$$\varepsilon_{pl} = \varepsilon_{max} - \varepsilon_{rec}$$

From Figure 7 it appears that plastic deformation starts at $\varepsilon \approx 0{,}32$, the yield point, and that the plastic deformation increases with increasing impact energy. The marked symbols refer to the experiments with failure. A part of the elastic energy will be consumed by failure of the propellant; this part of the elastic energy is not used for recovering, so that the recovered strain is lower in experiments with failure of the specimen.

It appears from Figure 8 that a nearly linear relation exists between maximum stress (σ_{max}) and maximum strain (ε_{max}). For N-4 propellant specimens with permanent deformation approximate calculation of σ_{max} is possible, using this linear relationship between σ_{max} and ε_{max} and assuming that plastic deformation will occur at $\varepsilon > 0{,}32$.

Failure criteria for N-4 propellant specimen are $\varepsilon_{max} > 0{,}50$ and $\sigma_{max} > 80$ MN/m^2. No failure of an N-4 propellant grain could be concluded on the basis of the following arguments. During functioning many solid propellant rocket motors have an average pressure of approximately 10 MPa; the bulk compression loading of the solid propellant grain will be 10 MN/m^2 *). From the impact experiments at 20°C it appears that failure of the N-4 propellant specimens by uniaxial compression loading occurs when stress will exceed 80 MN/m^2. Mears et al. (Ref.7) found that failure by uniaxial compression loading occurs at lower stresses than by bulk compression loading, so that no failure of the N-4 propellant grain during functioning is expected. Also, considering the pressure impulse will lead to this conclusion. Impact experiments with failure occur within 5 ms and have a pressure impulse of more than $1{,}75 \times 10^5$ Ns/m^2, while ignition of a Sidewinder rocket motor at 20°C will give in the first 5 ms a pressure impulse of $0{,}18 \times 10^5$ Ns/m^2 (Ref.8).

Determination of the Poisson ratio at 20° of N-4 propellant gives a value of approximately 0,40 , which is in agreement with the Poisson ratio expected via the ultrasound method.

Ultrasound method

In Figures 10a,b,c and d the results of measurements of PMMA are compared with values from literature. Measurements with PMMA were carried out as a check of the apparatus and of the measuring procedure. By comparing curves 2 and 3 of Figure 10a, it appears that a correction is desirable when the solid-liquid transitions between the reference transducers are absent. Moreover, a difference (3%) appears when different contact liquids are used.

PMMA has a glass transition temperature T_g of 105°C (Ref.9). Besides this transition Wada (Ref.10) observes a secondary transition at temperature T_g' ($T_g' \simeq 67$°C), about 30°C lower than T_g. There are two possible interpretations for the molecular mechanism involved in this phenomenon, namely, the rotation of side groups of chain polymers, the so-called "β-transition", and the rotation of the end parts of backbone chains.

Besides, the transition temperatures just mentioned are measured statically and will increase with increased loading rates of the dynamic-mechanical measuring techniques, according to the rheological theories of viscoelastic materials. The almost horizontal curve of Figure 10c and 10d refers to the glassy state of PMMA in this temperature range.

---

*) Loading of the uniaxial compression of N-4 propellant is parallel to the extrusion direction of the propellant grain. During ignition mostly radial loading occurs; results from other investigations show that for example, for JPN-propellant no difference in failure criteria exists by radial loading and by loading in extrusion direction.

Sorokin et al. (Ref.11) studied the cellulose nitrate-glycerol trinitrate system with the aid of DTA-techniques. They found a secondary transition at about 35°C for 30-40% (by weight) GN. In Figures 11a,b,c and d the longitudinal and transversal velocity, the shear modulus and the compression modulus are plotted against temperature for the four propellant types.

Contrary to the results of PMMA there is a marked downward slope of the curves with increasing temperature but in Figures 11c and 11d there is no strong evidence of a β- or γ-tranistion in the range in which measurements were done. The curves of the shear modulus are much steeper than the curve of the shear modulus of PMMA.

This slope of the shear modulus suggests a transition region. Normally, the shear modulus of polymers decreases several decades in a short temperature range or time range when passing the glass transition. The double base rocket propellants are to be considered polymers with a large amount of fillers. Such compositions show a broadening of the glass transition.

The ratio of weight percentage of cellulose nitrate (CN) and glycerol trinitrate (GN), weight % CN/weight % GN, is 1,20 for JPN propellant; for N-4, NK865 and OGK propellant this ratio is 1,55, 2,18 and 2,33 respectively (see Table I). The glycerol trinitrate and the other compounds are more likely to show interaction with the water/glycol contact liquid than with the silicone oil. See for instance Figure 11a. The longitudinal sound velocity of JPN, measured with water/glycol as contact liquid is about 5% higher than with silicone oil. There are also differences in the transversal sound velocities, but these are smaller and are not significant for the given figures.

It should be mentioned that all samples are regarded as pure elastic solids. Damping does not occur in that case. In Appendix A1 the influence of the damping properties on the measured mechanical properties is introduced. It appears from recent damping investigations that the accuracy of the calculated moduli will decrease to approximately 5% of the corresponding storage moduli with increasing temperature. Consequently the suggested transition region at about 35°C by Sorokin et al. will become more significant.

This investigation has to be considered within the scope of the investigation into the possibility of non-destructive determination of sound velocities and damping by the application of ultrasound method directly to small propellant charges.

Because the mechanical properties at high loading rates are expected to be more age-sensitive than at lower loading rates it is suggested to introduce these types of methods in product testing. Then, the specimens need not be moulded, but have to be sampled from final propellant charges. Surveillance testing will thus become more reliable and valuable.

APPENDIX A1

RELATIONS OF ULTRASOUND PROPERTIES AND VISCOELASTIC PROPERTIES

In solids longitudinal and transversal waves may occur. If the dimensions of the sample in all directions are large as compared with the wavelength then the propagation of the waves through the solid causes uniaxial compression loading (Ref. 4,5). For the uniaxial compression modulus or longitudinal modulus the following equation holds:

$$M = \rho\, c_\ell^2 \qquad \text{(A1-1)}$$

Analogous to Equation A1-1 will hold for the shear modulus,

$$G = \rho\, c_s^2 \qquad \text{(A1-2)}$$

It should be borne in mind that in the derivation of the elastic properties three assumptions have been made (Ref.12).

1. The solids are isotropic.
2. The deformations are small so that the applied force is proportional to the resulting deformation (Hooke's law).
3. The superposition principle of Boltzmann holds:
   The total deformation resulting from different forces applied at different times is equal to the sum of these deformations.

Using these assumptions different types of moduli such as the Young's modulus, bulk modulus, the Poisson modulus or Poisson ratio, can be calculated. The different moduli are related by the following equations (Ref.13):

$$E = 2G(1+\mu) \qquad \text{(A1-3)}$$

$$K = E/3(1-2\mu) \qquad \text{(A1-4)}$$

$$M = K + \frac{4}{3} G \qquad \text{(A1-5)}$$

From Equations A1-3, A1-4 and A1-5 the Poisson ratio is derived

$$\mu = \frac{M-2G}{2(M-G)} \qquad \text{(A1-6)}$$

However, as mentioned before solid rocket propellants act rheologically as viscoelastic materials.

For viscoelastic substances the relationships between the different moduli are more complicated. In ultrasound measurements a sinusoidal strain is imposed on a viscoelastic

solid. The strain is written in complex notation as follows:

$$\gamma^{*} = \gamma_o \exp(i\omega t) \qquad \text{(A1-7)}$$

Because of the viscoelasticity the resulting stress amounts to:

$$\sigma^{*} = \sigma_o \exp\{i(\omega t+\delta)\} \qquad \text{(A1-8)}$$

If $\delta=0$, then the sample is elastic and if $0 < \delta < \Pi/2$ the sample is viscoelastic.
In dynamic-mechanical experiments, such as ultrasound experiments all moduli are complex. For example the complex shear modulus will amount to:

$$G^{*} = \sigma^{*}/\gamma^{*} = (\sigma_o/\gamma_o)\exp(i\delta) =$$

$$= (\sigma_o/\gamma_o)(\cos\delta+i\sin\delta) = G' + iG'' \qquad \text{(A1-9)}$$

G' is the storage modulus which represents the elastic response of the material and G'' is the loss modulus which describes the viscous behaviour. The deformation energy in the viscous region is lost as heat. The quotient of G'' and G' is the damping or loss factor.
In order to apply Equations A1-1 and A1-2 to viscoelastic solids the moduli are replaced by complex quantities, e.g.

$$G^{*} = \rho c_s^{*2} \qquad \text{(A1-10)}$$

The complexity of the shear wave velocity $c^{*}_{s,m}$ amounts to:

$$c_s^{*} = c_s' + ic_s'' \qquad \text{(A1-11)}$$

Combining Equations A1-10 and A1-11 gives:

$$G' = \rho\{(c_s')^2 - (c_s'')^2\} \qquad \text{(A1-12)}$$

$$G'' = 2\rho c_s' c_s'' \qquad \text{(A1-13)}$$

In the complex notation the wave equation can be written as Equation A1-14:

$$U = U_o \exp\{i\omega(t-\frac{x}{c_s^{*}})\} = U_o \exp\{i\omega t\}\exp\left\{-\frac{i x}{c_s'+ic_s''}\right\} =$$

$$= U_o \exp\{i\omega t\}\exp\{-\alpha_{s,m}x\}\exp\left\{\frac{-i\omega x}{c_{s,m}}\right\} \qquad \text{(A1-14)}$$

From Equation A1-14 it follows that the linear absorption coefficient for shear waves ($\alpha_{s,m}$) and the shear wave velocity ($c_{s,m}$) determined experimentally are given by:

$$\alpha_{s,m} = \frac{\omega c_s''}{c_s'^2+c_s''^2} \qquad \text{(Nepers/m)} \qquad \text{(A1-15)}$$

$$c_{s,m} = \frac{c_s'^2+c_s''^2}{c_s'} \qquad \text{(A1-16)}$$

Equations A1-12, A1-13, A1-15 and A1-16 can be rewritten in the following form:

$$G' = \rho c_{s,m}^2 \frac{(1-r^2)}{(1+r^2)^2} \qquad \text{(A1-17)}$$

$$G'' = 2\rho c_{s,m}^2 \frac{r}{(1+r^2)^2} \qquad \text{(A1-18)}$$

where

$$r = \frac{\alpha_{s,m}\, c_{s,m}}{\omega} \qquad \text{(A1-19)}$$

N.B. Analogous relations are obtained for the determination of M' and M''.

The total attenuation can be divided into attentuation by reflection losses from the liquid solid transitions and attenuation by viscous losses from energy dissipation in the sample, described by $\alpha_{s,m}$.

Mostly suitable liquids are chosen so that the former type of attenuation will be negligible. However, Waterman (Ref.14) and recent investigations in our laboratory have shown that attenuation by reflection losses from the liquid solid transitions become very important if $c \cong \sqrt{2}\, c_{s,m}$. In that case determination of $\alpha_{s,m}$ and $c_{s,m}$ is not possible anymore.

It should be mentioned that in experiments with low attenuation G" will be negligible and G' will be approximately equal to $G(= \rho c_{s,m}^2)$.

N.B. The linear absorption coefficient is usually determined in dB/m; this quantity is 8,686 times as large as used in forementioned relations, which are expressed in Nepers/m.

APPENDIX A2-a

CALCULATION STRESS-STRAIN RELATIONSHIP

During deformation of the material the drop weight decelerates. The velocity of the weight with mass m will decrease to zero.

At any time t during the deformation holds:

$$F(t) = m\, a(t) \qquad \text{(A2-a-1)}$$

Deceleration and velocity are related by the following relation:

$$v(t) = v(0) + \int_0^t a(t)\, dt \qquad \text{(A2-a-2)}$$

Combination with Equation A2-a-1, gives:

$$v(t) = v(0) + \frac{1}{m} \int_0^t F(t)\, dt \qquad \text{(A2-a-3)}$$

The velocity at t=0 is defined by drop height and

$$v(0) = (2\, g\, h)^{\frac{1}{2}} \qquad \text{(A2-a-4)}$$

The displacement of the drop weight during the deformation at time t is:

$$\ell(t) = \int_0^t v(t)\, dt \qquad \text{(A2-a-5)}$$

Also $\ell(t)$ is the deformation of the specimen.
Strain at time t amounts to:

$$\varepsilon(t) = \ell(t)/\ell(0) \qquad \text{(A2-a-6)}$$

Combining Equations A2-a-3, A2-a-5 and A2-a-6 will result in the following expression for the strain at time t:

$$\varepsilon(t) = \left[v(0)\, t + \frac{1}{m} \int_0^t \left(\int_0^t F(t)\, dt \right) dt \right] / \ell(0) \qquad \text{(A2-a-7)}$$

For the stress at time t holds:

$$\sigma(t) = F(t)/O \qquad \text{(A2-a-8)}$$

At any time t $\sigma(t)$ and $\varepsilon(t)$ can be calculated. For calculation of the double integrals numerical techniques were used.

Numerical calculation of the strain was carried out on a PDP-11 computer (Digital Equipment Corporation). Control of the calculation was done by high speed filming of the impact experiment. For this purpose a HYCAM 150 M high-speed camera producing 8000 frames per second was used. From Figure 9 it appears that the numerical calculation of strain gives results within the measuring accuracy of the system.

APPENDIX A2-b

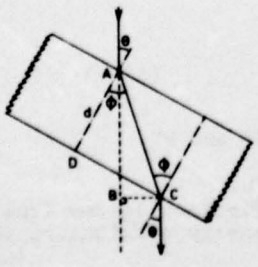

DERIVATION OF $c_{s,m} = c \left[1 - 2q \cos\theta + q^2 \right]$

According to Snellius' law:

$$\frac{\sin\theta}{c} = \frac{\sin\phi}{c_m} \qquad \text{(A2-b-1)}$$

In ΔADC : $AC = d/\cos\phi$ (A2-b-2)

and in Δ ABC:

$$AB = AC \cos(\phi-\theta) = d \cos(\phi-\theta)/\cos\phi \qquad \text{(A2-b-3)}$$

If there is no sample present, the sound wave will travel a distance through the liquid,

so $$AB = c\ t_2 \qquad \text{(A2-b-4)}$$

where t_2 is the travelling time. In the sample the sound wave will follow path AC.

so $$AC = c_m\ t_1 \qquad \text{(A2-b-5)}$$

where t_1 is again the travelling time. Hence the time difference, Δt, with and without sample, is:

$$t_2 - t_1 = \Delta t = \frac{AB}{c} - \frac{AC}{c_m} = \frac{d}{\cos\phi}\left[\frac{\cos(\phi-\theta)}{c} - \frac{1}{c_m}\right]$$

or:

$$\frac{\Delta t\ c}{d} = q = \frac{1}{\cos\phi}\left[\cos(\phi-\theta) - \frac{c}{c_m}\right] \qquad \text{(A2-b-6)}$$

Combining Equation A2-b-6 with Equation A2-b-1 yields

$$q\cos\phi = \cos\phi\cos\theta + \sin\phi\sin\theta - \frac{\sin\theta}{\sin\phi}$$

or:

$$\cos\phi(\cos\theta-q) = \sin\theta\left(\frac{1}{\sin\phi} - \sin\phi\right) = \sin\theta\frac{\cos^2\phi}{\sin\phi} \qquad \text{(A2-b-7)}$$

Rearranging gives:

$$\tan\phi = \frac{\sin\theta}{\cos\theta-q} \qquad \text{(A2-b-8)}$$

Using again Equations A2-b-1 and A2-b-8 this results in:

$$\tan^2\phi = \frac{\sin^2\phi}{1-\sin^2\phi} = \frac{(c_m/c)^2\sin^2\theta}{1-(c_m/c)^2\sin^2\theta} = \frac{\sin^2\theta}{(\cos\theta-q)^2} \qquad \text{(A2-b-9)}$$

or:

$$c_m = c\left[q^2 - 2q\cos\theta + 1\right]^{-\frac{1}{2}} \qquad \text{(A2-b-10)}$$

With $\theta = 0$, Equation A2-b-10 becomes

$$c_m = \frac{c}{1-q} \ . \qquad \text{(A2-b-11)}$$

It is easy to derive that the shift of the sound beam, BC, equals:

$$BC = d\,\frac{\sin(\phi-\theta)}{\cos\phi} \qquad \text{(A2-b-12)}$$

REFERENCES

1. R.B.Beyer, N.Fishman, "Solid Propellant Aging Studies(U)", Report No.22, Contract No.AF33(616)-5806, Stanford Research Institute,Menko Park, California,March 17,1960.
2. L.E.Nielsen, "Mechanical Properties of Polymers and Composites", Vol.2, Ch.5, Marcel Dekker, Inc., New York, 1974.
3. H.Schubert, D.Schmitt, Explosivstoffe 15(1) 1 (1967).
4. G.L.Gooberman, "Ultrasonic Theory and Application", English Univ. Press Ltd., London, 1968.
5. H.J.Mc Skimin, "Principal Acoustics - Principles and Methods", Vol.I,Part A,p.271, Acad.Press, New York/London,1964.
6. J.H.Gouda, "Secondary Transitions of Double Base Propellants", Ass.TL 8318-V2, Proj.No.A64/KL/097,Techn.Lab.TNO,Rijswijk,15-12-1972.
7. D.R.Mears, K.D.Pae, J.A.Sauer, J.Appl.Phys.40,4229(1969).
8. R.S.de Boer, W.F.J.van Altena, "Surveillance Testing of European Produced Sidewinder Rocket Motors", Ass.TL 9536-I,Contract No.NAMSA MU 3513,Techn.Lab.TNO,Rijswijk, 18-2-1974.

9. M.C.Shen, A.Eisenberg, Rubber Chem. and Techn. 43,95(1970).
10. Y.Wada, H.Hirose, T.Asano, S.Fukutomi, J.Phys.Soc.Japan, 14(8)1064(1959).
11. G.A.Sorokin, I.V.Tishumin, E.N.Fominikh, Vysokomol.Soedin, Ser.B11,522(1969).
12. H.J.Sutherland, R.Lingle, J.Appl.Phys.43(10)4022(1972).
13. J.D.Ferry, "Viscoelastic properties of polymers", John Wiley, New York, 1961.
14. H.A.Waterman, Kolloid-Z. u.Z. Polymere 192,1(1963).
15. R.Kono, J.Phys.Soc.Japan, 15(4)718(1960).
16. J.R.Asay, J.Appl.Phys., 40(4)1768(1969).
17. B.Hartmann, J.Jarzynski, J.Acoust.Soc.Am., 56(5)1469(1974).

TABLE I. Composition of the investigated, double base rocket propellants

constituent	per cent. by weight			
	JPN	NK 865	OGK	N-4
cellulose nitrate	51,1	59,2	56,7	50,9
glycerol trinitrate	42,75	27,2	24,3	32,9
diethyl phtalate	3,3			10,7
dioctyl phtalate			3,1	
diphenylamine		0,9		
2-nitrodiphenylamine			1,7	2,1
N,N'-diethyl-N,N' diphenylurea	1,1	4,9		
triacetine			10,2	
methyl phenylurethane		4,9		
potassium sulfate	1,23			1,5
lead stearate			3,3	0,7
graphite	0,19	0,1		0,1
vaseline		2,9		
moisture	0,23		0,5	0,5
solvent	0,10		0,2	0,2
specific gravity (kg/m^3)	1630	1550	1560	1553

TABLE II. Drop weight impact experiments with N-4 propellant

Specimen no.	Drop weight mass m	Drop height h	Initial strain rate w	Impact energy (t=0)	Pressure impulse	Strain (after 30 days) ε	Maximum strain ε_{max}	Maximum stress σ_{max}	Young's modulus E
	kg	m	s^{-1}	Nm	$Ns/m^2 x 10^5$			MN/m^2	MN/m^2
528	1	0,588	135,9	5,77	0,278	0,00	0,110	21,78	493,0
571		0,588	137,0	5,77	0,278	0,00	0,116	20,46	427,7
526		1,088	183,4	10,68	0,348	0,02	0,154	27,77	677,1
530		1,088	185,6	10,68	0,348	0,00	0,174	25,79	421,5
532		1,776	234,3	17,43	0,482	0,00	0,222	33,05	586,1
564		1,776	237,1	17,43	0,482	0,00	0,219	32,91	686,6
558		2,483	280,4	24,36	0,570	0,00	0,268	41,16	577,9
547		2,483	280,4	24,36	0,570	0,01	0,268	41,40	463,2
525		3,187	317,6	31,27	0,646	0,00	0,276	50,96	800,0
594		3,187	316,3	31,27	0,646	0,02	0,314	48,94	723,0
599	2	0,573	134,7	11,25	0,547	0,00	0,153	28,85	659,1
593		0,573	135,2	11,25	0,547	0,00	0,160	28,68	508,4
596		1,033	-	-	-	0,00	-	-	-
582		1,083	-	-	-	0,00	-	-	-
517		1,768	234,7	21,25	0,962	0,03	0,329	53,00	864,8
577		1,768	235,6	21,25	0,962	0,00	0,336	52,85	678,9
520		2,272	268,2	34,70	1,091	0,01	0,370	62,70	720,1
549		2,272	268,2	34,70	1,091	0,06	0,379	65,70	999,6
595		2,767	294,8	44,59	1,203	0,09	0,414	76,21	842,3
583		2,767	296,0	44,59	1,203	0,07	0,413	71,99	815,5
537		3,180	317,3	62,41	1,290	0,11	0,441	83,18	811,2
523		3,180	318,6	62,41	1,290	0,13	0,441	79,41	829,6
591	3	0,572	134,0	16,84	0,820	0,00	0,238	32,10	487,4
527		0,572	134,6	16,84	0,820	0,00	0,241	31,51	424,4
585		1,080	184,2	31,79	1,127	0,06	0,323	48,99	591,0
543		1,080	184,2	31,79	1,127	0,03	0,303	52,51	1068,1
529		1,790	237,0	52,70	1,452	0,08	0,405	72,52	587,1
512		1,790	237,0	52,70	1,452	0,09	0,411	70,52	612,7
590		2,489	279,6	73,28	1,712	0,19	0,485	87,04	731,6
515		2,489	281,8	73,28	1,712	0,24	0,505	81,36	780,4
539+		2,795	297,5	82,28	1,815	0,24	0,502	84,96	744,1
592+		2,795	296,3	82,28	1,815	0,25	0,490	87,04	764,8
578+		3,194	316,7	94,03	1,940	0,38	0,539	90,63	793,7
524		3,194	-	-	-	0,50	-	-	-
542	5	0,577	134,6	28,31	1,376	0,05	0,317	44,68	534,0
560		0,577	135,2	28,31	1,376	0,07	0,315	46,83	577,0
541		1,084	184,5	53,15	1,882	0,11	0,403	73,80	1363,8
551+		1,084	-	-	-	0,09	-	-	-
514+		1,781	237,4	87,39	2,412	0,34	0,541	86,17	728,3
559+		1,781	236,5	87,39	2,412	0,39	0,567	85,54	643,7
548+		1,881	245,8	92,29	2,498	0,45	0,582	87,02	691,7
562+		1,973	248,9	96,81	2,539	0,42	0,584	89,52	789,9

+Specimens with failure.

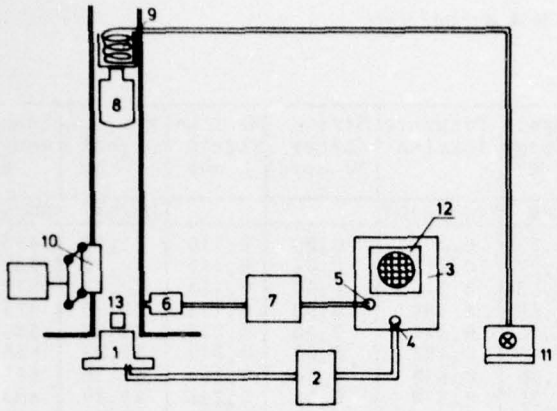

Fig.1 Outline of the drop weight impact apparatus and measuring system. 1.Load cell, 2.Strain gauge amplifier, 3.Oscilloscope, 4.Signal input, 5.Trigger input, 6.Photocell, 7.Power supply, 8.Drop weight, 9.Electromagnet, 10. Pneumatic recapture system for drop weight, 11. Switch, 12. Photocamera, 13.Sample.

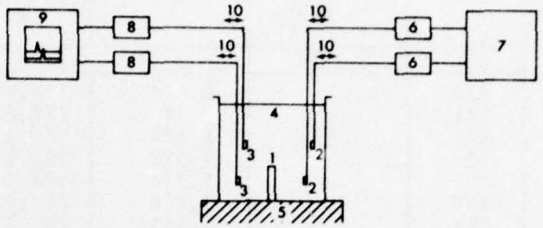

Fig.2 Outline of the Ultrasonic Flaw Detector MK III and the sample mounting. 1.Sample, 2.Transducer(sender), 3.Transducer(receiver), 4.Thermostated bath, 5.Indexed turntable, 6.Amplifier, 7.Power supply, 8.Attenuator, 9.Oscilloscope, 10.Transducer displacement device.

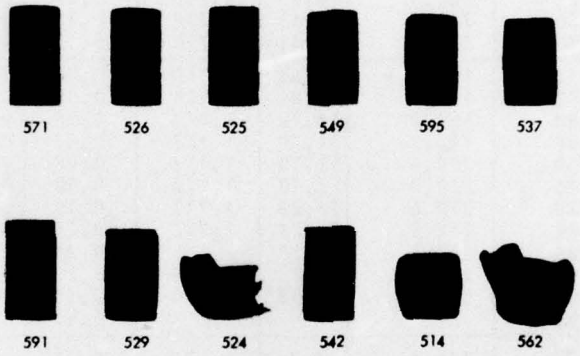

Fig.3 Some N-4 propellant samples 30 days after the drop weight impact experiments.

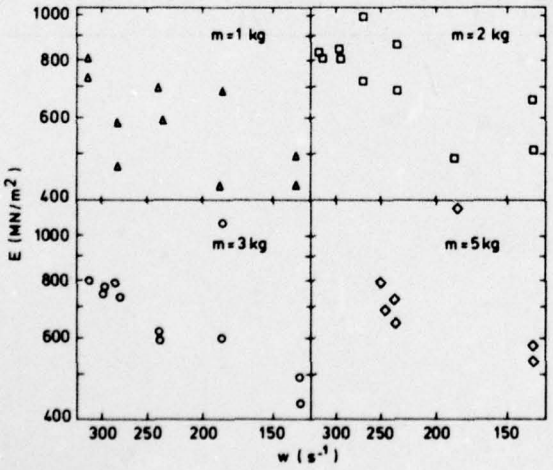

Fig.4 Young's modulus versus strain rate for different drop weights. (N-4 propellant)

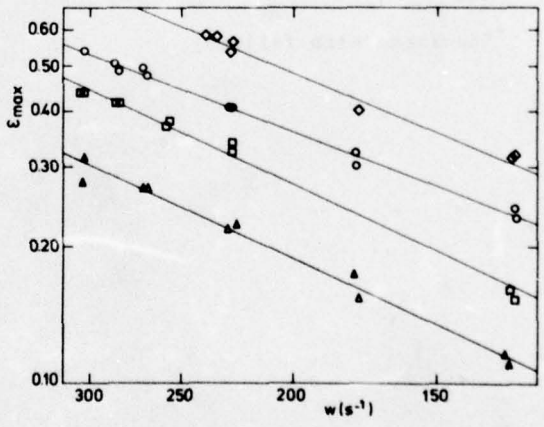

Fig.5 Maximum strain versus strain rate for drop weight masses of 1 kg (Δ), 2 kg (□), 3 kg (0) and 5 kg (◇). (N-4 propellant)

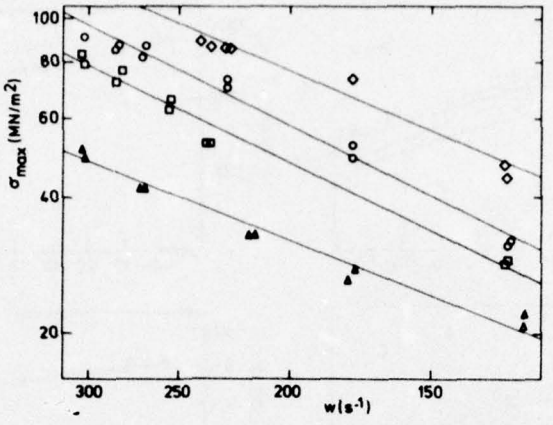

Fig.6 Maximum stress versus strain rate for drop weight masses of 1 kg (Δ), 2 kg (□), 3 kg (0) and 5 kg (◇).

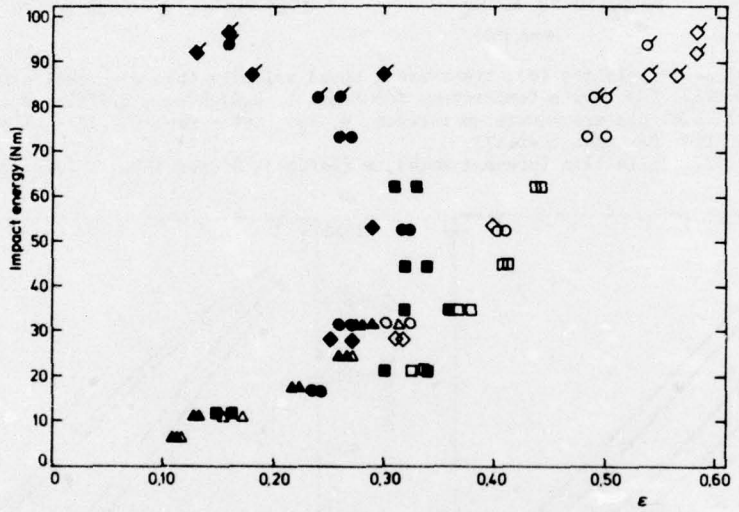

Fig.7 Impact energy versus maximum strain (open symbols) and recovered strain (solid symbols). (Δ 1 kg, □ 2 kg, 0 3 kg, ◇ 5 kg). N.B. Marked sympols refer to failure.

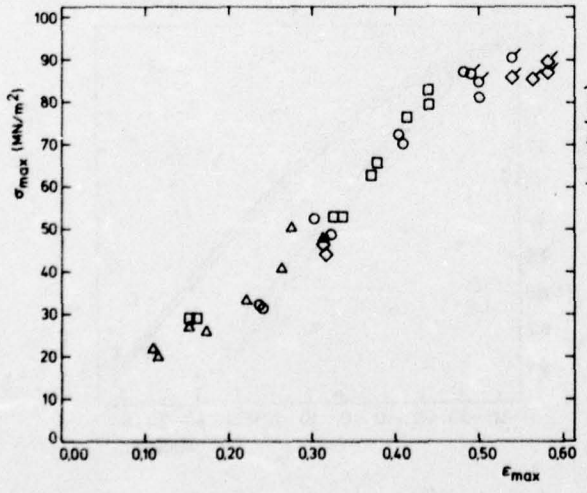

Fig.8 Maximum stress versus maximum strain for drop weight masses of 1 kg (Δ), 2 kg (□), 3 kg (0) and 5 kg (◇).
N.B. Marked symbols refer to failure.

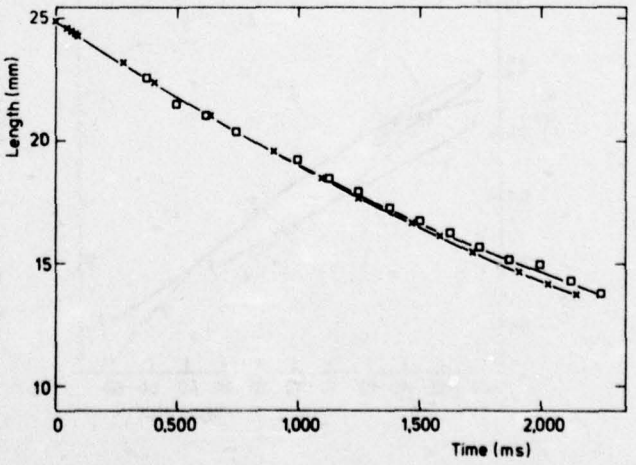

Fig.9 Specimen length versus time by numerical calculation (x) and by calculation from high speed filming (□).

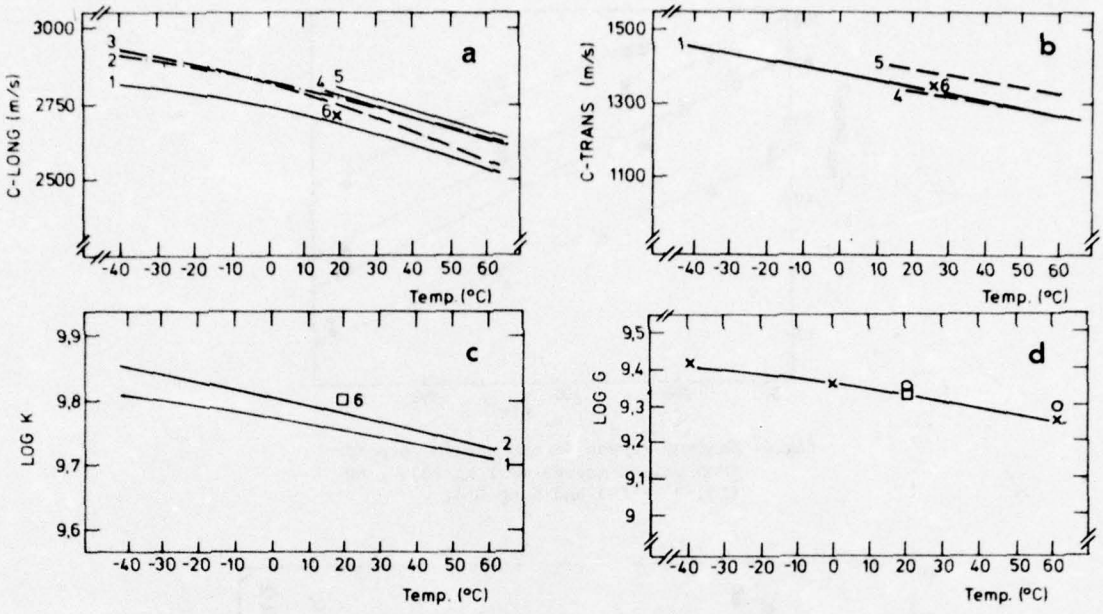

Fig.10 Longitudinal sound velocity (a), transversal sound velocity (b), compression modulus (c) and shear modulus (d) versus temperature for PMMA. 1. H_2O/glycol, 2.Silicone oil, 3.Silicone oil, without reference transducer correction, 4. H_2O, after Kono (Ref.15), 5.After Asay (Ref.16), 6.After Hartmann (Ref.17).
N.B. Figure 10d. Solid line (present work), x (Ref.10), 0 (Ref.15), □ (Ref.17).

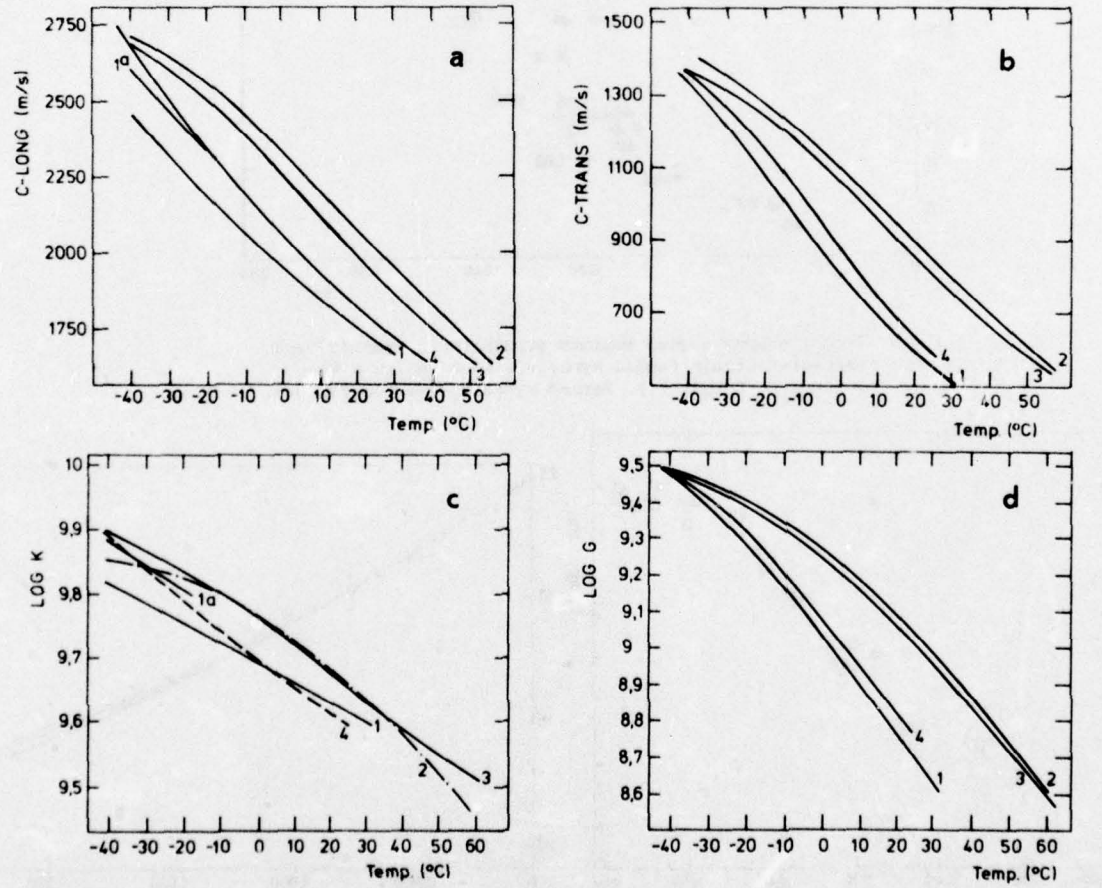

Fig.11 Longitudinal sound velocity (a), transversal sound velocity (b), compression modulus(c) and shear modulus (d) versus temperature for various double base propellants in silicone oil.
1a. JPN in H_2O/glycol, 1. JPN, 2. NK865, 3. OGK, 4. N-4.

METHODES DE MESURE DES BRUITS IMPULSIFS ET EFFETS PHYSIOLOGIQUES

Dr A.Dancer, M.Froböse
membres de l'Institut Franco-Allemand de Recherches (ISL)
68301 Saint-Louis (France)

RESUME

Les armements classiques ou à propulseurs engendrent, au moment du tir, des ondes de pression sous forme de bruits impulsifs complexes, à fronts de montée très raides. Il est nécessaire d'enregistrer ces variations de pression avec le plus d'exactitude possible afin de pouvoir évaluer, à l'aide des grandeurs caractéristiques des profils de pression, leurs effets sur du personnel ou des structures. Des dispositifs de mesure et d'expérimentation répondant à des spécifications sévères s'avèrent indispensables.

L'exposition à des bruits impulsifs entraîne des lésions de l'appareil auditif. Ces lésions peuvent affecter l'oreille moyenne et l'oreille interne. Diverses normes limites d'exposition ont été proposées en fonction de la surpression de crête, de la durée et du nombre d'expositions pendant une période donnée (normes de Pfander, Coles..).

L'application de ces normes pose de nombreux problèmes en ce qui concerne les bruits impulsifs de haut niveau produits par les armes du type lance-roquettes.

I. METHODES DE MESURE DES BRUITS IMPULSIFS

Les difficultés métrologiques rencontrées au cours de l'enregistrement précis d'ondes de choc aériennes à front de compression très raide sont dues, en particulier, aux imperfections que présentent les capteurs de pression mécanoélectriques [1]. Par contre, les éléments de transmission et d'amplification ainsi que les appareils enregistreurs répondent en général aux spécifications requises.

Les transducteurs de pression commercialisés, susceptibles d'être utilisés sur les terrains d'expériences pour l'enregistrement des ondes de choc, présentent des principes de fonctionnement différents. On peut distinguer les capteurs piézoélectriques, les capteurs piézorésistifs et les sondes capacitives. Le choix du transducteur sera déterminé par l'étude envisagée.

Les caractéristiques techniques imposées aux sondes de pression sont les suivantes :

1. dimensions réduites, afin d'éviter toute perturbation gênante du champ de pression ;
2. domaine de mesure suffisamment grand permettant d'enregistrer tous les bruits impulsifs concernés ;
3. sensibilité aussi constante que possible dans tout le domaine de mesure ;
4. large bande de fréquence avec des fréquences de coupure inférieures et supérieures, adaptées à la durée du signal et aux chocs de pression à front raide ;
5. réponse en fréquence linéaire dans tout le domaine de pression ; l'apparition de fréquences de résonance secondaires inférieures à la fréquence de résonance principale est proscrite ;
6. bonne fidélité dans le temps ;
7. faible influence de la température sur la sensibilité ;
8. insensibilité aux forces d'accélération ;
9. phénomènes de dérive et d'hystérésis peu prononcés ;
10. construction résistant aux intempéries pour l'utilisation des sondes en plein air.

Les exigences énumérées sont tellement variées et, en partie, en contradiction les unes avec les autres qu'il n'est guère possible de les satisfaire à tout point de vue. De l'ensemble des sondes disponibles, on peut choisir, en procédant à une optimisation, le type de capteur qui présente les caractéristiques les mieux appropriées aux mesures envisagées.

Parmi les nombreux transducteurs de pression vendus par l'industrie, les quatre modèles présentés sur la figure 1 ont eu, à cause de leurs dimensions réduites, notre préférence et ont permis d'acquérir de nombreuses expériences relatives aux techniques de mesure.

Il s'agit d'un capteur piézoélectrique de diamètre 6,3 mm de la firme KISTLER (Suisse), de deux sondes piézorésistives de diamètre 1,3 mm et 2 mm de la firme KULITE (USA) et d'un microphone capacitif 1/8" de la firme BRÜEL & KJAER (Danemark). Leurs fréquences de résonance se situent, selon le modèle, entre 200 et 750 kHz. La membrane du microphone est fortement amortie, de sorte qu'une fréquence de coupure supérieure de 140 kHz est atteinte.

Dans le cas d'un choc raide, les fréquences de résonance sont excitées et les oscillations résultantes se superposent au signal de mesure. Il s'avère donc indispensable, en vue de l'exploitation des signatures de pression enregistrées, d'éliminer les oscillations dues à la résonance en plaçant un filtre passe-bas dans la chaîne de mesure. Cependant, après filtrage, le temps de montée du signal électrique est plus long que le front de montée du choc de pression, de sorte que l'on note une légère distorsion du

profil de pression enregistré et une erreur d'amplitude plus ou moins prononcée, dont la valeur dépend de la durée et de la forme de l'impulsion de pression.

Les supports des capteurs et leur disposition dans le champ de pression ont également une certaine importance. Leur forme et leur disposition varient suivant que l'on désire enregistrer l'onde de pression en champ libre, non perturbée par la présence de la sonde, ou effectuer des mesures de pression sur les structures.

Pour les mesures en champ libre, nous avons élaboré des sondes-aiguilles de diamètre 2 mm, 4 mm ou 8 mm, présentées sur la figure 2. La membrane des capteurs affleure l'une des extrémités de la sonde tandis que l'autre extrémité est équipée d'un connecteur. Les dimensions des sondes, dictées par les diamètres des capteurs utilisés, ont été maintenues aussi faibles que possible afin d'obtenir des enregistrements quasi-ponctuels et indépendants de l'angle d'incidence de l'onde de choc [2]. En effet, un bruit impulsif n'atteint pas seulement directement la sonde de mesure, mais aussi indirectement, après réflexion sur le sol ou sur d'autres surfaces. La figure 3 présente un tel exemple de bruit d'armes.

Le phénomène sonore global est formé de différentes composantes qui atteignent la membrane du capteur sous des angles d'incidence variables [3]. Elles peuvent s'y réfléchir de façon frontale ou oblique ou passer tangentiellement. De la sorte, elles subissent des transformations d'amplitude plus ou moins accentuées qui seraient négligeables pour une mesure quasi-ponctuelle. Le profil de pression sera d'autant moins faussé que le diamètre de la sonde est faible. Malheureusement, la résistance mécanique de sondes de Ø 2 mm n'est plus parfaite et leur utilisation aux champs de tir est limitée.

Une commission d'experts franco-allemands a élaboré un projet d'uniformisation des techniques de mesure des bruits d'armes et de leur évaluation en vue de rendre comparables les résultats de mesure [4,5]. Elle a admis l'utilisation d'une sonde-aiguille d'un diamètre uniforme de 5,5 mm et d'une longueur de 100 mm. Ce diamètre autorise le montage de tous les capteurs mentionnés, même du capteur piézoélectrique KISTLER, après modification. Ce compromis a été nécessaire du fait que pas tous les groupes de mesure disposent d'un nombre suffisant de capteurs de faible diamètre.

Malheureusement, l'utilisation d'une sonde-aiguille de diamètre 5,5 mm ne permet plus d'effectuer des mesures quasi-ponctuelles, c'est-à-dire indépendantes de l'angle d'incidence de l'onde, dans tout le domaine de pression. La figure 4 présente la courbe de directivité d'une telle sonde pour une surpression de 0,1 bar. L'erreur d'amplitude maximale est obtenue pour une incidence frontale de l'onde, c'est-à-dire $\alpha = 0°$. L'erreur d'amplitude augmente avec la pression, comme le montre la courbe de directivité enregistrée pour une surpression de 0,3 bar (figure 5). L'écart maximal de la pression nominale est encore obtenu pour un angle d'incidence de 0° et s'élève à ≈ 25% ou ≈ 2 dB.

Sur la figure 6 sont présentés les oscillogrammes enregistrés d'une part à l'aide d'une sonde de référence (voie du haut) et, d'autre part, à l'aide de la sonde-aiguille à étudier (voie du bas). Les deux sondes ont été soumises à une onde de pression sphérique issue de la détonation d'une charge explosive sphérique de 35 g, à une distance de 1,80 m, la pression maximale résultante étant de 0,3 bar. La commission a approuvé l'utilisation d'une sonde-aiguille de diamètre 5,5 mm jusqu'à des surpressions comprises entre 0,3 bar et 0,4 bar.

Pour la détermination des diagrammes de directivité, nous avons utilisé une sonde effilée présentée dans la figure 7. Il s'agit d'une sonde effilée circulaire, de diamètre 20 mm. Le capteur piézoélectrique est placé en arrière de la pointe, dans la partie cylindrique, de telle sorte que sa membrane affleure la périphérie de la sonde. L'axe longitudinal de la sonde est orienté sur le centre de détonation afin que l'onde de choc défile sur la membrane du capteur sans y être réfléchie.

Même pour des intensités de pression supérieures à 0,3 bar, ce type de sonde a fourni des enregistrements satisfaisants, tant du point de vue qualitatif que quantitatif. Néanmoins, vu leur encombrement, il s'avère difficile de disposer simultanément plusieurs sondes effilées dans un espace réduit, d'autant plus que si l'on désire éviter toute erreur due à la réflexion de l'onde de pression sur la membrane, il est indispensable d'orienter leur axe longitudinal sur la source sonore.

La pression limite de 0,3 bar à 0,4 bar autorisée pour les sondes-aiguilles présente un certain intérêt si l'on se réfère aux pressions limites admises par l'appareil auditif humain et qui seront discutées après.

Les méthodes de mesure discutées jusqu'à présent se rapportent toutes à l'enregistrement, en champ libre, de l'onde de pression non perturbée. Par contre, lorsqu'on désire enregistrer les profils de pression agissant sur une structure, il paraît opportun de fixer la sonde de pression sur la structure même. A cet effet, nous avons élaboré un récepteur représenté sur la figure 8. Il s'agit d'un récepteur en forme de disque plan-convexe renfermant en son centre le transducteur de pression à membrane affleurante.

II. EFFETS PHYSIOLOGIQUES DES BRUITS IMPULSIFS

Parmi les effets physiologiques des bruits impulsifs, nous n'aborderons que ceux directement liés aux modifications de la sensibilité auditive.

Les bruits impulsifs provoquent des traumatismes au niveau de l'appareil auditif des sujets exposés :

Le traumatisme sonore aigu s'observe chez les sujets exposés à une explosion ou à une séance de tir trop prolongée. Les signes fonctionnels sont très marqués : céphalalgie, acouphènes aigus de grande intensité, sensation d'assourdissement. Les signes cliniques sont plus discrets : tympan normal, peu de modifications à l'examen acoumétrique.

Par contre, l'examen audiométrique montre le plus souvent un scotome auditif au voisinage de la fréquence 4 kHz. Ces perturbations peuvent, en l'absence de nouvelles expositions au bruit, régresser spontanément.

Le traumatisme sonore chronique est d'installation plus insidieuse. On observe tout d'abord (figure 9) une perte de sensibilité de l'ordre de 25 à 30 dB à la fréquence 4 kHz (1er stade), puis un accroissement de ce déficit vers les fréquences élevées (2ème stade), puis un accroissement vers les basses fréquences (3ème stade) et enfin on n'observe plus que des reliquats auditifs aux fréquences élevées alors que les pertes auditives aux basses fréquences augmentent (4ème stade). Le scotome observé au stade 1 n'entraîne pas de gêne sociale du fait qu'il se situe en dehors de la gamme des fréquences conversationnelles ; par contre, une aggravation se développera si le traumatisme sonore est répété.

Voyons maintenant de quelle façon les paramètres physiques des bruits impulsifs (surpression de crête, durée, nombre, intervalle..) influent sur l'importance de la fatigue ou des pertes auditives.

Selon Murray et Reid [6], Ward [7], Kryter [8], la fatigue auditive ou TTS (Temporary Threshold Shift) exprimée en dB croîtrait comme 20 log N (N étant le nombre de bruits impulsifs) ou comme 20 log t (t étant la durée d'exposition à des bruits impulsifs présentés à intervalle constant).

Selon Coles [9] et Ward [7], un doublement de la surpression de crête entraînerait une augmentation de 6 dB du TTS. L'amplitude de la fatigue auditive, exprimée en dB, évoluerait donc comme 20 log Δp. Cependant une étude plus approfondie de l'influence de ce paramètre semble indiquer que la croissance du TTS se ferait selon 40 log Δp.

L'influence de l'intervalle entre l'exposition à deux bruits impulsifs a été étudiée par Ward [7], Smith [10] et Kryter [8]. Selon ces auteurs, l'amplitude du TTS est maximale pour un intervalle de 1 seconde alors que pour des intervalles de durée différente l'amplitude de la fatigue auditive est plus réduite du fait soit du réflexe de protection acoustique (pour les intervalles inférieurs à 1 seconde), soit de l'existence d'une période compensatoire (pour les intervalles supérieurs à 1 seconde).

La récupération de la sensibilité auditive (exprimée en dB) se ferait comme 10 log t (t étant le temps séparant le test audiométrique de la dernière exposition aux bruits impulsifs).

A l'aide de ces relations et à la suite d'observations audiométriques systématiques, de nombreuses normes limites d'exposition aux bruits impulsifs ont été proposées. Parmi celles-ci deux sont couramment utilisées :

a) le diagramme des niveaux limites (figure 10) établi par Pfander à la suite de nombreux tests audiométriques réalisés chez des soldats après participation à des tirs d'entraînement. Ce diagramme a été adopté par le Ministère de la Défense de la République Fédérale d'Allemagne. Il prend en compte la surpression de crête du bruit, sa durée d'action à -10 dB et le nombre d'expositions au bruit par périodes de 8 heures (voir figure 3). Selon Pfander, le respect de ce diagramme permet d'éviter l'apparition de TTS supérieurs à 10 dB à 1000 Hz ou au-dessous, 15 dB à 2000 Hz et 20 dB à 3000 Hz ou au-dessus, 24 heures après l'exposition, chez 95% des sujets ;

b) le diagramme de Coles (figure 11) qui fut adopté en 1968 par le CHABA [Committee on Hearing, Bioacoustics and Biomechanics of the National Academy of Science and National Research Council (USA)] est appliqué dans divers pays anglo-saxons. Coles divise les bruits d'arme en deux types qui correspondent l'un à un bruit d'arme en champ libre (type A), l'autre à un bruit d'arme en ambiance réverbérante (type B). Il appelle durée A la durée de la première impulsion positive dans le cas du bruit produit en champ libre, et durée B la durée à -20 dB du bruit produit en ambiance réverbérante. En fonction de ces durées et de la surpression de crête des bruits, dans le cas d'une exposition quotidienne à 100 bruits d'armes, le respect de ce diagramme permettrait de n'observer, chez 75% des sujets, que des TTS ou des PTS (Permanent Threshold Shift : perte auditive) inférieurs à 10 dB à 1000 Hz ou au-dessous, 15 dB à 2000 Hz et 20 dB à 3000 Hz ou au-dessus. Si l'on désire appliquer ce critère, chez 90% des sujets les surpressions de crête doivent être diminuées de 5 dB et chez 95% des sujets de 10 dB. Lorsque l'incidence des bruits impulsifs est normale à l'oreille exposée, les surpressions de crête doivent, dans le cas d'expositions en ambiance non réverbérante, être diminuées de 5 dB. Des corrections peuvent également être effectuées lorsque le nombre d'expositions quotidiennes est différent de 100. Enfin, le rythme des expositions est supposé compris entre 6 et 30 par minute.

Si l'on compare les diagrammes de Pfander et de Coles (figure 12), dans le cas où l'on n'accepte que des TTS inférieurs à 10 dB à 1000 Hz ou au-dessous, 15 dB à 2000 Hz et 20 dB à 3000 Hz ou au-dessus, chez 95% des sujets on note que l'adoption du diagramme de Coles autoriserait l'exposition à des niveaux de surpression plus élevés et ce d'autant plus que la durée des bruits est plus importante. En effet, si le diagramme de Pfander suit le principe d'isoénergie, (diminution du niveau de surpression de 3 dB pour chaque doublement de la durée), celui de Coles ne diminue que de 2 dB pour chaque multiplication par 2 de cette durée.

On peut également noter que si l'amplitude maximale des TTS tolérés est la même pour chacun de ces auteurs, Coles mesure les TTS juste après la fin de la journée d'exposition aux bruits alors que Pfander les mesure 24 heures après l'exposition. Etant donné ce que l'on sait de la récupération de la fatigue auditive en fonction du temps, la méthode de mesure des TTS selon Coles semble offrir plus de garanties aux sujets puisque les TTS mesurés juste après la fin de la journée d'exposition doivent être de plus forte amplitude que ceux mesurés 24 heures après (toutes choses étant égales par ailleurs).

Bien que Coles pense que son diagramme et celui de Pfander sont assez comparables, on doit cependant noter que les résultats expérimentaux de Coles indiquent une plus large tolérance aux bruits impulsifs alors que les TTS qu'il mesure juste après la fin de la journée d'exposition devraient être supérieurs à ceux observés 24 heures après.

Une norme limite d'exposition aux bruits impulsifs doit offrir les meilleures garanties de sécurité aux tireurs en assurant l'intégrité de leur fonction auditive. Pour cette raison, il semble nécessaire que l'amplitude des TTS mesurés à la suite d'une exposition aux bruits ne dépasse pas 10 dB à 1000 Hz ou au-dessous, 15 dB à 2000 Hz et 20 dB à 3000 Hz ou au-dessus chez 95% des sujets. Les diagrammes de Pfander et de Coles permettent, à notre avis, d'estimer ces risques de façon raisonnable. Le respect de ces normes peut être atteint de deux façons : soit en limitant la surpression de crête et le nombre de bruits auxquels les tireurs sont exposés, soit en imposant le port de dispositifs de protection acoustique. Cette dernière solution nous semble la meilleure, car elle permettrait de maintenir la puissance des armes actuelles ou futures à un niveau qui n'altérerait pas leur efficacité.

BIBLIOGRAPHIE

[1] M.FROBÖSE, G.PARMENTIER, G.MATHIEU, D.SEYDEL (ISL)
Versuchs- und Messanordnungen für Waffenknallregistrierungen. Messungen im Druckfeld eines Infanteriegewehres HK33.
(Dispositifs expérimentaux et métrologiques pour l'enregistrement du bruit des armes. Mesures dans le champ de pression d'un fusil d'infanterie, type HK33.)
1970, RT 14/70.

[2] M.FROBÖSE, G.MATHIEU, E.BURDE (ISL)
Messtechnische Untersuchungen zur 3. Kommissionssitzung über "Vereinheitlichung von Waffenknallmessungen" vom 14.-16. Mai 1974 im Etablissement d'Expériences Techniques de Bourges (ETBS).
(Etudes sur les techniques de mesure effectuées en vue de la 3ème réunion de la commission "Uniformisation des techniques de mesure de bruits d'armes" du 14 au 16 mai 1974 à l'Etablissement d'Expériences Techniques de Bourges (ETBS).)
1974, RT 7/74.

[3] M.FROBÖSE, G.PARMENTIER, G.MATHIEU (ISL)
Knalldruckausbreitung beim Abschuss einer 2-cm-Kanone (20/621). Teil 1.
(Propagation de l'onde de pression produite par le tir d'un canon de 20 mm (20/621). 1ère partie.)
1972, RT 16/72.

[4] En cours de rédaction
Vorschriften und Empfehlungen zur Vereinheitlichung von Waffenknallregistrierungen und ihrer Auswertung.
(Consignes et recommandations relatives à l'uniformisation des enregistrements de bruits d'armes et leur exploitation.)

[5] Rapport ISL en préparation
Bemerkungen und experimentelle Untersuchungen zur Standardisierung der Messmethodik für Knallwellenregistrierungen in Schusswaffennähe.
(Remarques et études expérimentales en vue d'une uniformisation des méthodes de mesure pour l'enregistrement des bruits impulsifs à proximité des armes à feu.)

[6] N.E.MURRAY, G.REID
Experimental observations on the aural effects of gunblast.
Med. J. Aust. 33 (1946) 611.

[7] W.D.WARD, W.SELTERS, A.GLORIG
Exploratory studies on temporal threshold shift from impulses.
J. Acoust. Soc. Am. 33 (1961) 781-793.

[8] K.D.KRYTER, G.GARINTHER
Auditory effects of acoustic impulses from firearms.
Acta Oto-Laryngol. Suppl. 211 (1966).

[9] R.R.A.COLES, G.R.GARINTHER, D.C.HODGE, C.G.RICE
Hazardous exposure to impulse noise.
J. Acoust. Soc. Am. 43 (1968) 336-343.

[10] M.G.SMITH, G.GOLDSTONE
U.S. Army Ordnance, Human Engineering Laboratories, Aberdeen Proving Ground, Maryland.
A pilot study of temporary threshold shift resulting from exposure to high intensity impulse noise.
1961, Rept. TM-19-61.

Capteurs de pression pour l'enregistrement d'ondes de choc aériennes

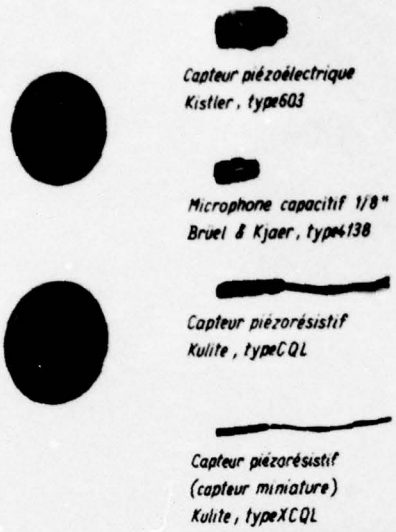

Fig.1

Sondes-aiguilles pour l'enregistrement d'ondes de choc aériennes

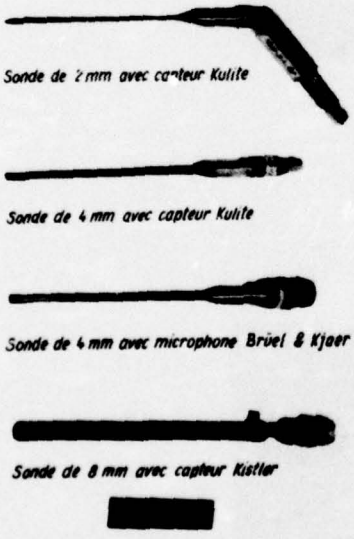

Fig.2

Pression en fonction du temps d'un bruit d'arme (canon 2 cm calibre)

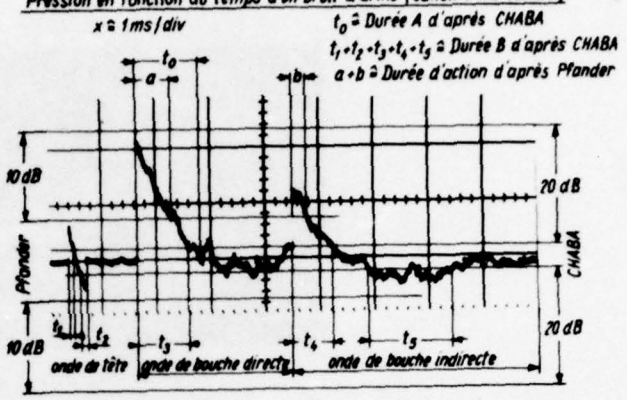

Fig.3

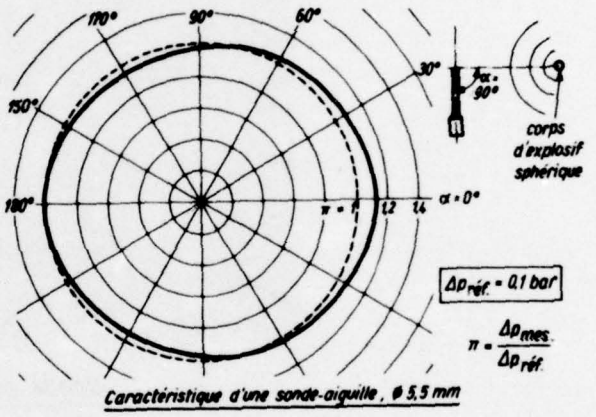

Caractéristique d'une sonde-aiguille, ∅ 5,5 mm

Fig.4

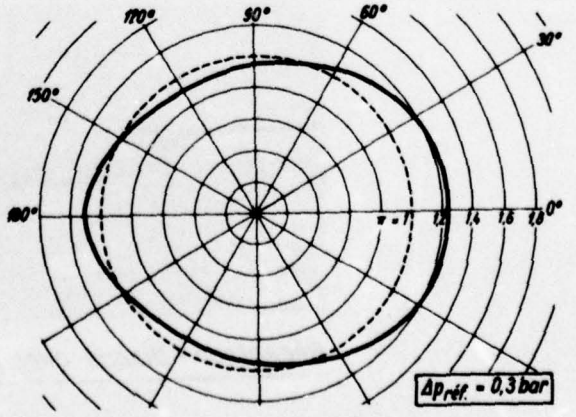

Fig.5

Sonde effilée de référence ; ϕ 20 mm
x ≙ 1ms/div. α = 30°

Sonde-aiguille ; ϕ 5,5 mm

Fig.6

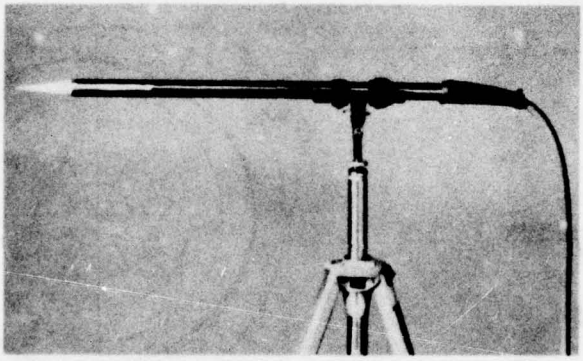

Sonde effilée

Fig.7

Récepteur - disque avec couvercle de protection

Fig.8

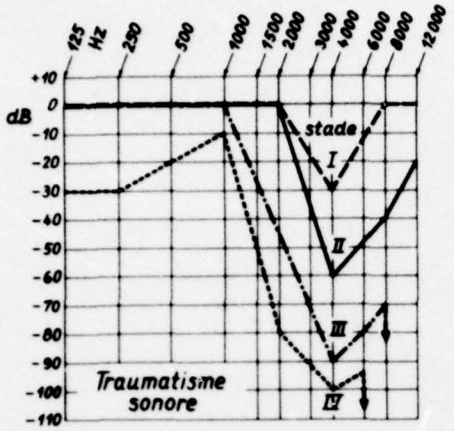

Fig.9

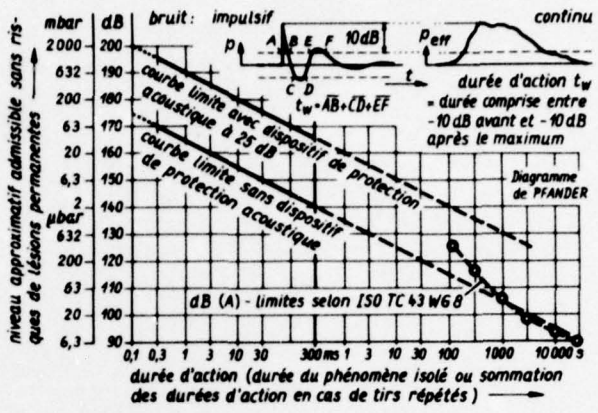

Fig.10

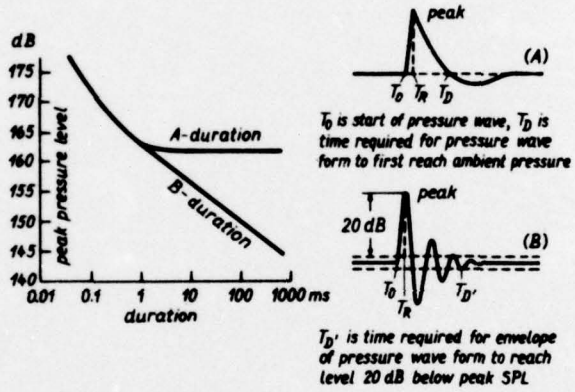

Fig.11
Diagramme de Coles

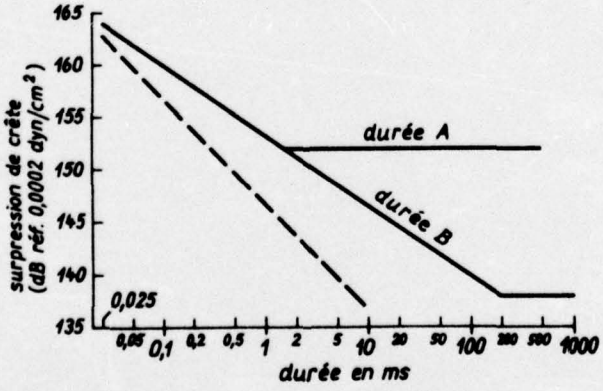

Fig.12

——— Critère d'exposition aux bruits d'armes (Coles : CHABA 1968) (TTS inférieurs à 10 dB à 1000 Hz ou au-dessous, 15 dB à 2000 Hz et 20 dB à 3000 Hz ou au-dessus chez 95% des sujets)

— — — Critère de Pfander pour 100 expositions à un même bruit d'arme pendant une période de 8 heures

THE BLAST PRESSURE MILIEU ENVIRONING SOME RECOILLESS RIFLES/RECOILLESS LAUNCHERS

by

Svein O Engenes
Norwegian Defence Research Establishment
P O Box 25, N-2007 Kjeller,Norway

SUMMARY

High blast pressures can force restrictions on the flexibility of the use of a recoilless rifle/recoilless launcher. The restrictions may be introduced for tactical reasons, or they may be introduced to ensure the user safe operation.
In order to get a generalized enlightening of the pressure milieu surrounding some antitank hand weapons, a series of pressure measurements were taken in various environments. The pressure records furnished characteristics such as pressure level, pulse duration, and spectral content for each individual weapon at specific locations, and thus permitted general comparisons.
The pressure measurements were compared with a set of medical criteria to define safe zones and safe use of the individual weapon in various environments.
The results indicate that if necessary precautions are taken, restrictions which would otherwise reduce a weapon's potential usefullness by considerable amounts, can be liberated.

1. INTRODUCTION

Several controversial factors are connected with recoilless weapon systems. Good precision and a short flight time are factors which require high muzzle velocities. High muzzle velocities are equivalent to high blast pressures. To reduce damage hazards from blast pressures on the user and nearby personnel; to reduce the visible contour of flame, smoke, and dust and thus the possibility of detection; to lessen the strain on the gunner and thus the number of shots necessary for training purpose, and to increase overall weapon flexibility, the blast pressure should be endeavoured kept to a minimum. A thorough knowledge of the importance of such factors should be available when deciding a weapon's tactical directions.
General considerations and some crude pressure measurements have been the governing factors in working out the directions for use for most recoilless weapons in the Norwegian Army. To ensure safe use, strict limitations have been enforced for each weapon with respect to individual grouping and launch environment. Firing a recoilless weapon from any enclosure was prohibited because of unknown but anticipated high pressures.
With the aim of lifting some of the restrictions, the Norwegian Defence Research Establishment in cooperation with the Norwegian School of Infantry, initiated work to enlighten the pressure milieu environing some recoilless rifles (RCR)/recoilless launchers (RCL) in various weapon sites. Most of the work was consentrated on developing a bunker from which the 84 mm RCR Carl Gustaf could be fired and on mapping the blast pressure level behind a number of recoilless weapon systems.
Recent lethality studies (1) show that unprotected anti-armour squads are very vulnerable to indirect fire. The survivability increases significantly with the degree of protection. Since the prime commission of the Norwegian Brigade is to defend, time to prepare protected weapon sites will often be at hand.
In order that the recoilless weapon squads also can take advantage of such protection, it was decided to try design an adequate bunker from which a recoilless weapon could be safely fired. Since the 84 mm RCR Carl Gustaf (CG) still is the back-bone of our antitank force this weapon was the one the bunker use was specified for.
The organization, balance, and relative positioning of the RCR- and RCL-squads in the combat zone has great influence on the effectiveness of an antitank force. To improve the flexibility with regards to positioning the weapons, the safety zone because of pressure damage risks behind the weapons should be kept a minimum. To update the data for existing safety zones the actual blast pressures behind the following weapons were measured:

- 57 mm RCR
- 66 mm RCL (LAW)
- 75 mm RCR
- 84 mm RCR (CARL GUSTAF)
- 88 mm RCL
- 106 mm RCR
- 127 mm RCL (TOW

General comparisons of the blast pictures and the spectral content in the pressure signals were made at selected points for the various weapons.

2. TEST OBJECTIVES

The general objective of the work was to identify the pressure picture surrounding various recoilless weapons with the aim of easing the restrictions on weapon use because of pressure hazards. The following specific test program evolved:

1. Design and build a bunker onto the base of the existing open 84 mm RCR Carl Gustaf site, from which the weapon can be fired safely
2. Establish the pressure load on the 84 mm RCR Carl Gustaf crew when firing the weapon from the open position and from the bunker. For the same position and weapon, establish how changes in site construction will influence the pressure load on the crew.
3. Identify the free field pressure picture behind the following weapons when they are fired from an open position:

    57 mm RCR
    66 mm RCL (LAW)
    75 mm RCR
    84 mm RCR (CARL GUSTAF)
    88 mm RCL
    106 mm RCR
    127 mm RCL (TOW)

From the numerous pressure measurements available the spectral content in some selected signals were calculated to identify differences between the various weapons at specific measuring points.

3. INSTRUMENTATION

The pressure sensors used to monitor the pressure loads on personnel in the open site and in the bunker were piezo-electric transducers (Atlantic Research Corp , Type LC-65) with a rise time of about 7 us.
The sensors used to map the free field pressure picture behind the different weapons were pencil type piezo-electric transducers (Atlantic Research Corp, Type LC 33) with a rise time of about 10 us.
The pressure signals were recorded on a 14 x Sangamo recorder, with a cut-off frequency of 10 kHz.
The spectra were calculated using digital procedures.

4. BLAST PRESSURE MEASUREMENTS

Blast pressures were measured in an open 84 mm RCR CG weapon site, in a CG bunker, and in the free field gas stream behind the CG and other recoilless weapons. In tests where one wanted to measure the pressure load on the users, the pressure sensors were mounted on life-sized dummies. In the free field blast measurements the side on pressure was measured by pencil-type pressure cells.

4.1 Measurements of the blast pressure on the 84 mm RCR Carl Gustaf Crew in the open weapon site

The open CG weapon site can roughly be described as an open trench with an underground shelter. Figure 4.1 shows a horizontal view and a side view of the site. The 70 x 70 cm^2 square to the right is the loader's position. The weapon is placed on top of the platform. The gunner's position is to the left of the platform. During preparatory artillery fires the personnel can bring the weapon into the fragment-proof cover room. Dummies were placed at the positions of the crew in the measurements. The pressure signals were monitored at the positions of the right and the left ear and at the back head on both gunner and loader by inserting pressure cells into the doll's heads which were made of metal.
The pressure was measured for a total of 16 rounds fired from the open site. The first 6 rounds were fired to get a general picture of the pressure on the personnel. The target was placed at a distance of 500 m which corresponds to a weapon elevation of about 5^{o}. The last 10 rounds were fired to investigate the effect of obstructions in the path of the rear exit flow of the CG on the pressure signal. A 4x4 m^2 plank was placed at distances from 2 m to 5 m behind the weapon and at varying inclinations.

4.2 Measurement of the blast pressure on the 84 mm RCR Carl Gustaf crew in the Carl Gustaf bunker

The open 84 mm RCR Carl Gustaf site was used as the base for the Carl Gustaf bunker. Onto the base, it was built a fragmentproof enclosure with an embrasure and a rear opening for exit gases and an entrance was added. Figure 4.2 shows the horizontal view of the bunker and figure 4.3 the side view. The idea behind the bunker was to permit the CG crew to shoot or observe while the attacking tanks are supported by artillery.
A total of 23 shots were fired from the bunker. The first 14 shots were fired to determine the general pressure load on the crew when weapon elevation was changed from $+5^{o}$ to -14^{o} and azimuth from $+31.5^{o}$ to -30^{o}. The next 9 shots were fired to study the effect of bunker-alternations on the pressure. As in the case of the open site, dummies replaced the crew and the measuring points were at the ears and the backheads.

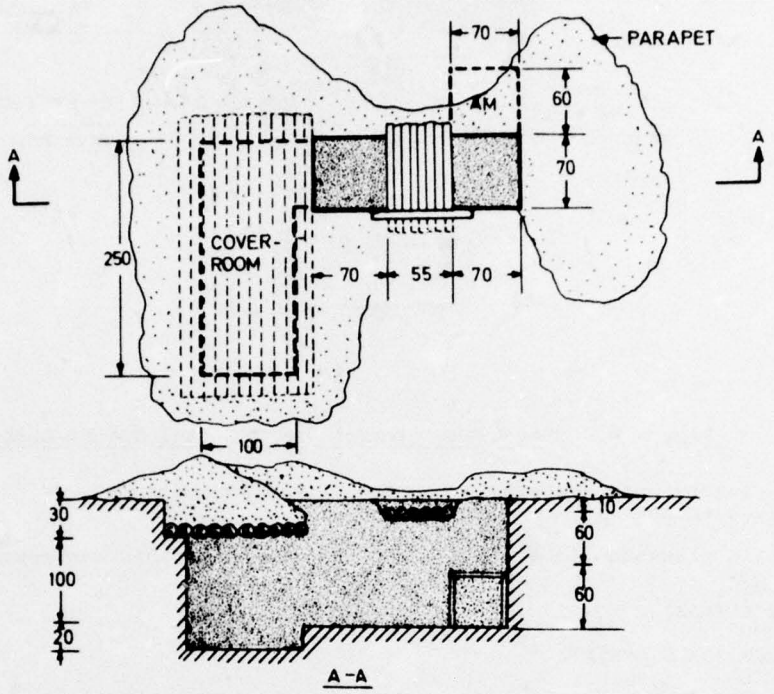

Figure 4.1 The open Carl Gustaf weapon site

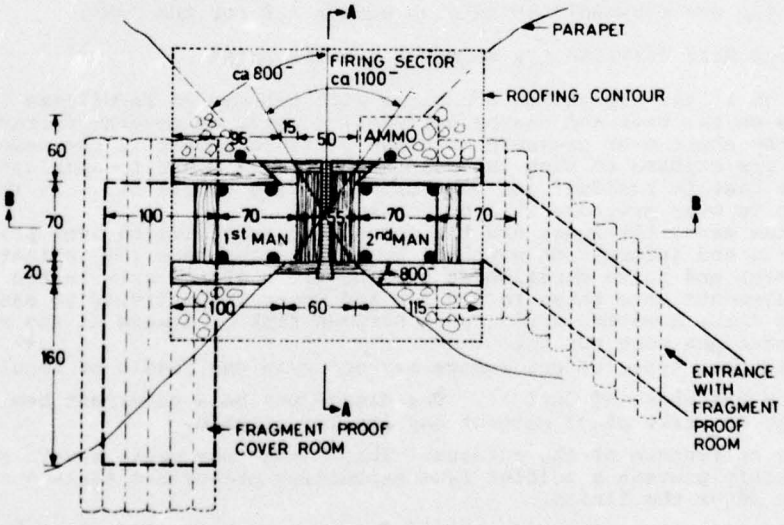

Figure 4.2 Plan view of the 84 mm RCR Carl Gustaf bunker

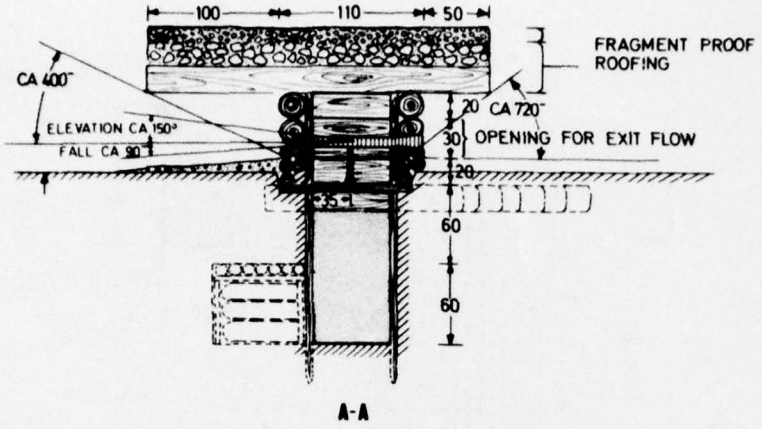

Figure 4.3 Side view of the 84mm RCR Carl Gustaf bunker

4.3 Blast pressure measurements in the free field behind some recoilless weapons

The free field pressure picture behind the following weapons was measured:

57 mm RCR
66 mm RCL (LAW)
75 mm RCR
84 mm RCR (CARL GUSTAF)
88 mm RCL
106 mm RCR
127 mm RCL (TOW)

The ground on which the measurements were taken was hard and covered by a thin layer of fine-grained sand. The target for each weapon was placed at a distance equal to the weapon's normal engagement distance. The rear muzzle of each weapon was placed at the origin of a Cartesian coordinate system. The pressure cells were placed radially backwards from origo at angles varying from 0^{o} to 90^{o}. All pressure cells (pencil type which measure the side on pressure) were pointed toward the blast source. The cells were mounted on sticks, 25 cm above ground level.
Four rounds were fired from each weapon except for the TOW. Only two rockets were available for this weapon at the time of the test. With 14 measuring stations a total of 56 pressure records were obtained to identify the pressure picture in half of the area (symmetry was assumed) behind each weapon (28 for the TOW).

5. EAR DAMAGE RISK CRITERIA FOR PRESSURE IMPULSE NOISE

The effect of lethal mechanisms connected with the use of recoilless launchers/recoilless rifles on the user and nearby personnel depends on several factors. One major factor is the sheer over pressure or blast pressure people in the weapon's close vicinity inevitably are exposed to when the weapon is fired. Other incapasitating factors are such as the heat in residual gas explosions, flying debris etc. In this text only the hazards due to over pressure will be considered.
Second to the ears, the lungs are the organ most sensitive to over pressure. Data from earlier tests and information supplied by weapon producers (2) indicate that the pressure level and pulse duration at the locations of the crew in the various sites where measurements were taken is too low and short respectively to cause damage to the lungs. The ears, however, could run a serious risk of damage at the same location if proper precautions were not taken.
The following two types of ear damage may occur as the result of impulse noise:

. Leakage on the organ of Cortis'. The damage may be a permanent hearing loss. The damage can take place without any feeling of pain.

. Damage to or rupture of the eardrum. This damage may cause severe pain and can thus possibly prevent a soldier from expediting prescribed tasks during and some time after the firing.

As a general rule, no ear damage should due to weapon impulse noise be tolerated in peace time. In war time one has to make sure the pressure on the ear is kept below the threshold of pain (often when ear drum rupture occurs).
To control hearing loss hazards, several factors have to be considered. The most important ones are:

. Peak pressure level
. Duration of over pressure
. Number of rounds fired per unit of time
. Timelag between each round fired

. The spectral content in the pressure signal

The pressure on the ear is determined by the weapon system, the environment, and the type of earprotection used. Depending on type and construction, earprotection can reduce the pressure level by appreciable amounts. A typical ear clock will reduce the pressure level about 25 dB, earplugs from 5 dB up to 25 dB depending on how they are inserted, and glass quilt about 25 dB.
A number of different agencies have, based on various working schemes and requirements, formulated general criteria for ear damage risk due to impulse noise (3,4). Examples are shown in figure 5.1 Pressure in dB is the dependent variable while the duration of the pressure signal in seconds is plotted along the abscissa. The dotted line which is taken from US Military Standard 1474 is the criterion for the 95th percentile protection when muffs or plugs are used. The number of exposures permitted per 24 hours are 5 or less. The duration is defined as the sum of the time intervals when the pressure exceeds 10% of the peak pressure. The solid lines which stem from a criterion defined by Pfander (4) are based on slightly different definitions. The upper curve presupposes an ear protection reducing the noise level 25 dB at 1000 Hz. The lower solid curve is specified for an unprotected ear. For durations of less than 0.3 seconds, Pfander's criterion is based on a single exposure. For durations larger than 0.3 seconds the total time is obtained by multiplying the single-shot duration by the number of exposures in an 8 hour period. The single-shot duration is defined as the sum of the time intervals where the absolute pressure value is higher than 10 dB below maximum pressure.

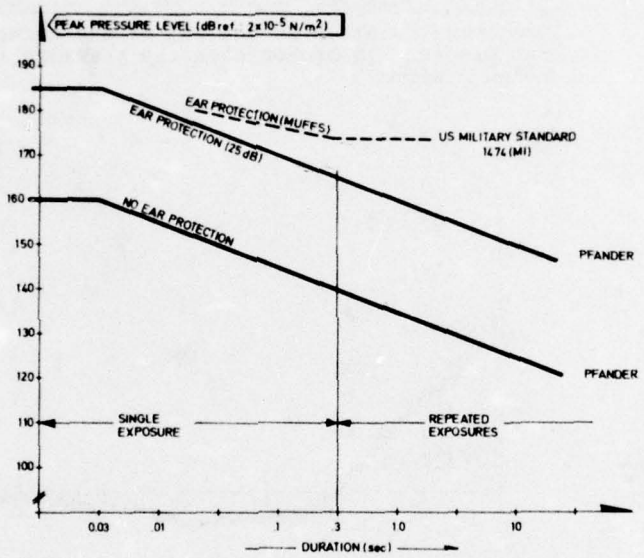

Figure 5.1 Ear damage risk criteria for blast pressure impulse noise

6. RESULTS

6.1 General

Two typical pressure-time samples are shown in figure 6.1 and 6.2. The pressure signal shown in figure 6.1 was measured inside the bunker at the gunner's right ear. The short duration pressure spikes are the results of reflected pressurewaves from the ground and the walls. The duration defined by Pfander, is the sum of the intervals where the pressure is higher than the levels indicated by the broken lines, parallel to the time axis. The total duration is less than a millisecond. Figure 6.2 shows the free field pressure-time signal 6 metres behind the rear nozzle of the 84 mm RCR Carl Gustaf. The duration, again as defined by Pfander, is approx. 2.5 milliseconds.

6.2 Blast pressures on the Carl Gustaf crew in the open site and in the bunker

The average blast pressures on the gunner and the loader in the open Carl Gustaf site and in the bunker are shown in table 6.1. In both sites the weapon elevation was 5^{o} and the azimuth 0^{o}. In the open site the average pressure is higher on the loader than on the gunner (the gunner and the loader are both facing the target, the gunner's head is closer to the weapon than the loader's). In the bunker the average pressure load on the gunner is higher than on any of the crew members in the open site.

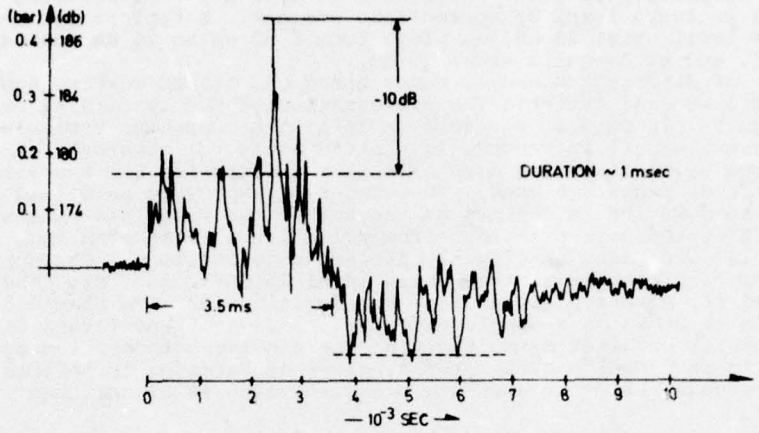

Figure 6.1 Typical blast pressure-time record measured at the gunner's right ear in the 84mm RCR Carl Gustaf bunker

The total duration is the sum of the durations where the pressure is higher than the pressure level 10 dB below maximum.

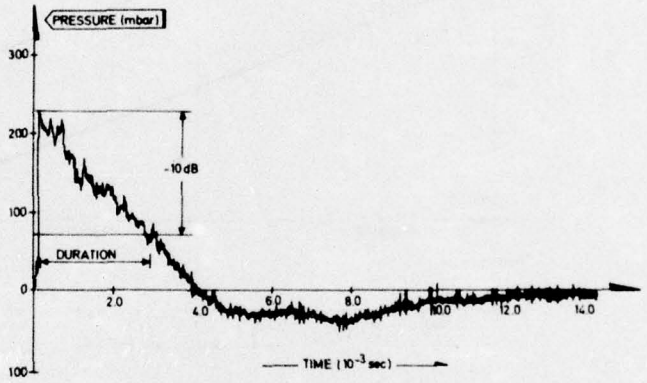

Figure 6.1 Typical side on free field blast pressure record measured behind a recoilless weapon

The total duration is the sum of the durations where the pressure is higher than the pressure level 10 dB below maximum. The pressure is measured 6 m straight behind the 84 mm RCR Carl Gustaf and 25 cm above ground

The loader, however, experiences a lower pressure in the bunker than in the open site. This is due to the shielding offered by the rear bunker wall.
Table 6.2 gives the maximum pressures measured on the crews in the two sites. Again it is noticed that the pressure is highest on the gunner in the Carl Gustaf bunker and on the loader in the open site. The durations of the overpressures (Pfander), range from about 0.2 milliseconds to about 10 milliseconds. The durations are longer in the bunker than in the open site. In figure 6.3 the pressure results from table 6.1 and 6.2 are shown in relation to Pfander's damage criterion.
Standard ear clocks, which on the average reduce the pressure level about 25 dB are unable to meet this protection criterion. In addition, the physical form of these ear clocks make them unsuitable for use in conjunction with the Carl Gustaf due to the narrow space between the barrel and the sight. Therefore, better ear protection is an absolute necessity, even in the open site, if one aims to protect the Carl Gustaf operators from ear damage.

Site		Gunner		Loader	
		Left ear	Right ear	Left ear	Right ear
Open site	Pressure	180 mbar (179.1 dB)	340 mbar (184.6 dB)	360 mbar (185.1 dB)	210 mbar (180.4 dB)
	Duration	3.2 msec	2.4 msec	1.2 msec	2.0 msec
Bunker	Pressure	250 mbar (181.9 dB)	460 mbar (187.2 dB)	340 mbar (184.6 dB)	170 mbar (178.6 dB)
	Duration	2.2 msec	2.6 msec	3.9 msec	3.0 msec

Table 6.1 Average blast pressures and durations (as defined by Pfander) on Carl Gustaf operators in the open site and in the bunker

Site		Gunner		Loader	
		Left ear	Right ear	Left ear	Right ear
Open site	Pressure	190 mbar (179.6 dB)	370 mbar (185.3 dB)	460 mbar (187.2 dB)	250 mbar (181.9 dB)
	Duration	3.0 msec	2.0 msec	0.7 msec	1.3 msec
Bunker	Pressure	330 mbar (184.4 dB)	600 mbar (189.5 dB)	440 mbar (186.8 dB)	230 mbar (181.2 dB)
	Duration	1.0 msec	0.7 msec	0.3 msec	1.8 msec

Table 6.2 Maximum blast pressures and durations (as defined by Pfander) on Carl Gustaf operators in the open site and the bunker

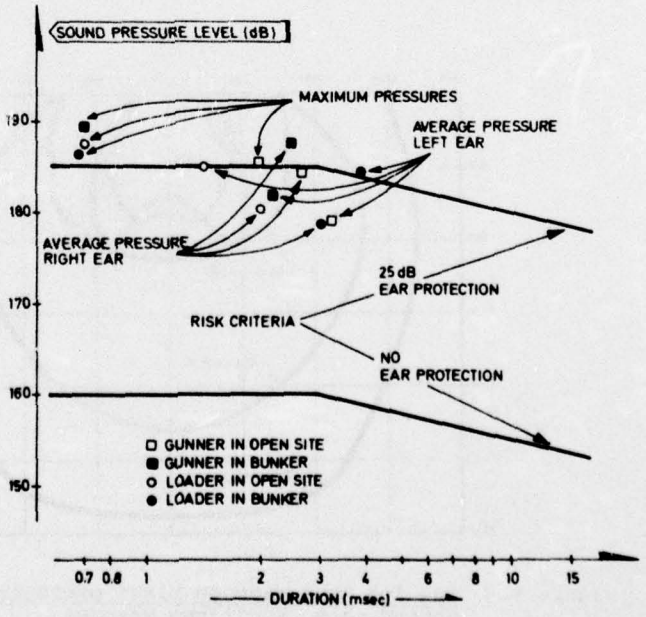

Figure 6.3 Maximum and average blast pressures measured on the gunner and on the loader in the open 84 mm Carl Gustaf site and in the Carl Gustaf bunker, seen in relation to Pfander's ear damage risk criterion

6.3 Effect of variations in bunker dimensions on the pressure load on the crew

The general conclusions to be drawn from the firings to investigate how changes in bunker dimensions will affect the pressure level on the crew, can be summarized as follows:

- Roof's height relative to ground is not critical as long as the roof is high enough above ground to permit the operators standing erect
- Roof size is not critical (± 15 cm)
- Depth of the site (in firing direction) becomes critical when the depth is large enough to permit the rear exit muzzle to swing inside the bunker
- Clothing the inside of the site with mineral wool may decrease the average pressure on the loader with about 60% and on the gunner with about 20%.

6.4 Obstructions in the path of the rear gas flow of the 84 mm RCR Carl Gustaf

The firings from the open site with a 4m x 4m plank behind the weapon to simulate situations where obstructions come in the flow path of the rear exit gases of the Carl Gustaf, gave no clear results. The rigidity of the plank and the plank support did in an ambigious way affect the pressure signals. However, using Pfander's risk criterion and assuming an earprotection sufficient to ensure safe operation in the bunker, one could from the test conclude that firing the Carl Gustaf in an otherwise open terrain should not be permitted with major obstructions closer than 5 metres behind the weapon.

6.5 Results of free field blast pressure measurements behind some recoilless weapons

According to Pfander, a pressure signal with a duration of about 10 milliseconds and a peak pressure of about 180 dB (200 mbar), is the limit to what the ear protected with clocks should be exposed to. It is reasonable to assume that the pressure on the ear is closer to the face on (static) type than to the side on (dynamic) type. The relation between the two pressure forms are given by

$$P_f = 2\ Ps\ \frac{102.9+4Ps}{102.9+Ps}$$

where P_f is the face on pressure in psi and Ps in the side on pressure in psi. The side on pressure of value 100 mbar corresponds to a 200 mbar (180 dB) face on pressure. The measured side on 100 mbar pressure isobars (behind the tested weapons) are drawn in figure 6.4. The isobars give a good indication on where the safety limits due to pressure hazards lie for the various weapons. The TOW values are based on half the number of measurements (two firings) that were available for the other weapons (four firings).

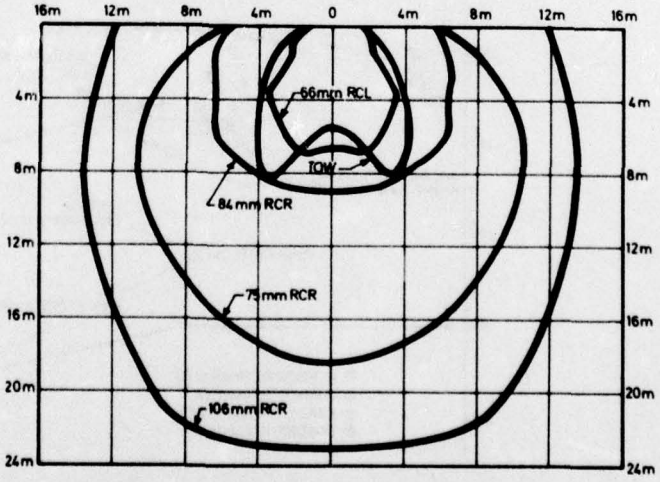

Figure 6.4 The 100 mbar side on blast pressure isobars behind some recoilless weapons

Figures 6.5 to 6.11 show some face on pressure isobars for the following weapons: the 57 mm RCR, the 66 mm RCL (LAW), the 75 mm RCR, the 84 mm RCR (CG), the 88 mm RCL, the 106 mm RCR, and the 127 mm RCL (TOW).

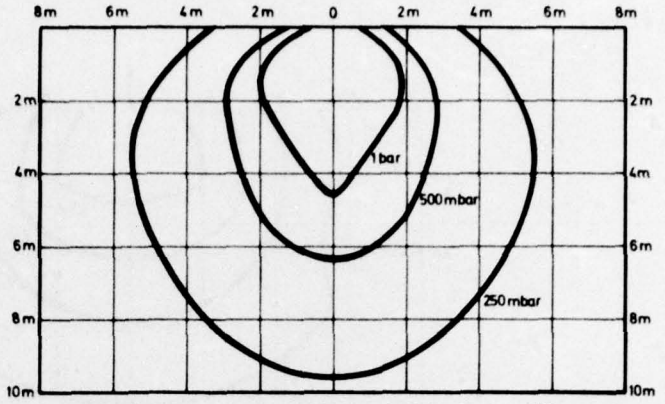

Figure 6.5 Face on blast pressure isobars behind the 57mm RCR

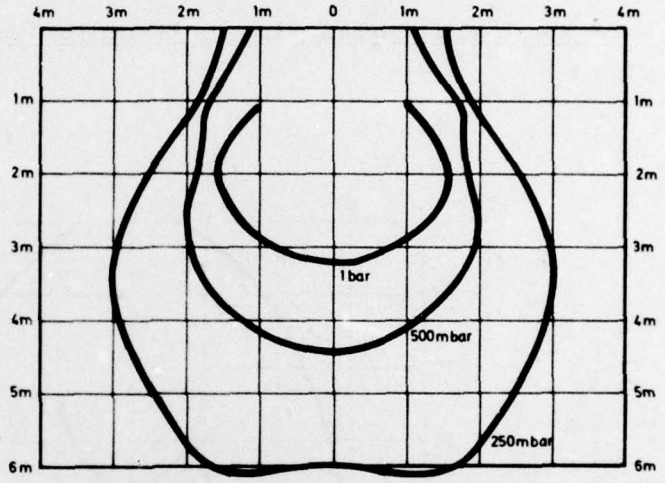

Figure 6.6 Face on blast pressure isobars behind the 66mm RCL, LAW

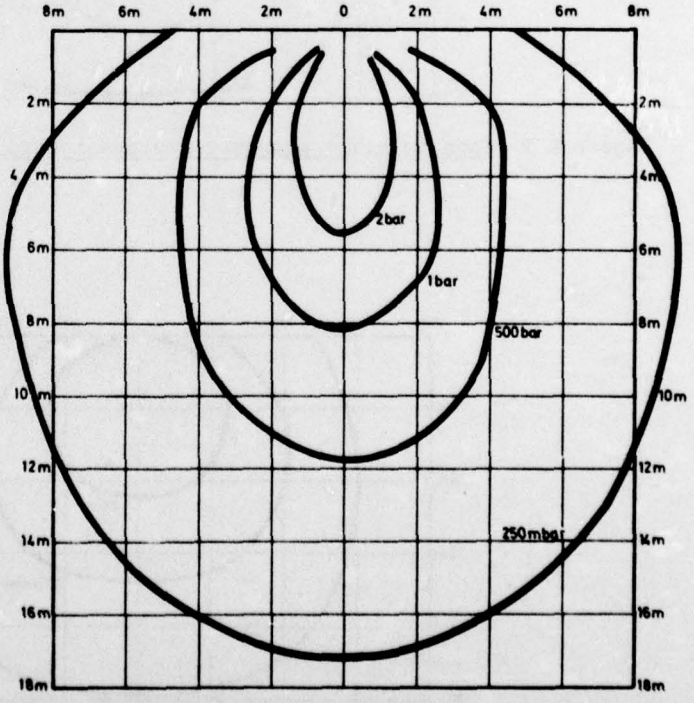

Figure 6.7 Face on blast pressure isobars behind the 75 mm RCR

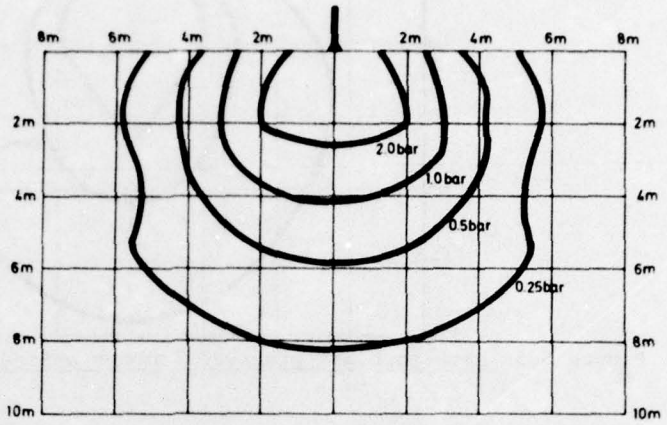

Figure 6.8 Face on blast pressure isobars behind the 84mm RCR, Carl Gustaf

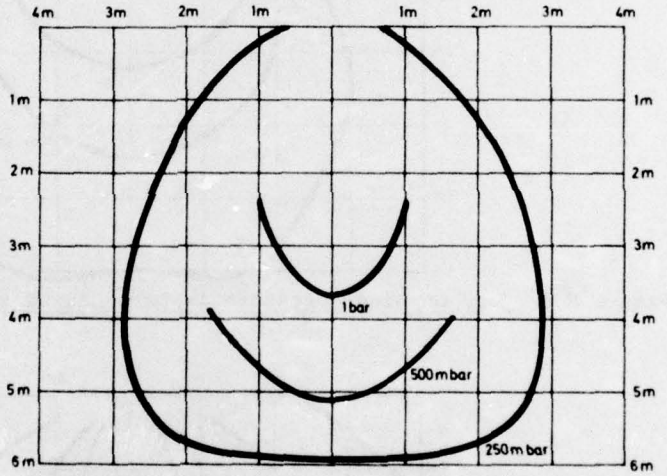

Figure 6.9 Face on blast pressure isobars behind the 88mm RCL

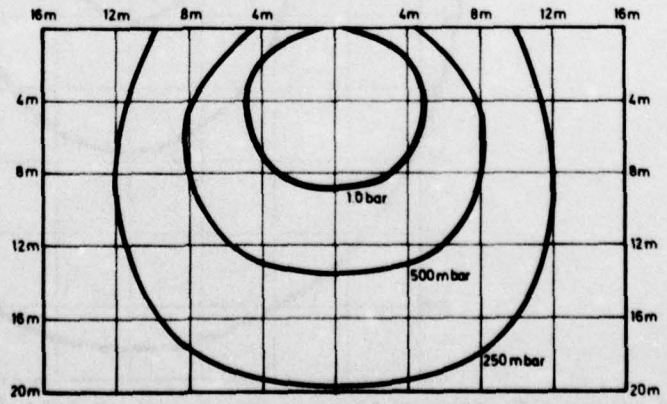

Figure 6.10 Face on blast pressure isobars behind the 106mm RCR

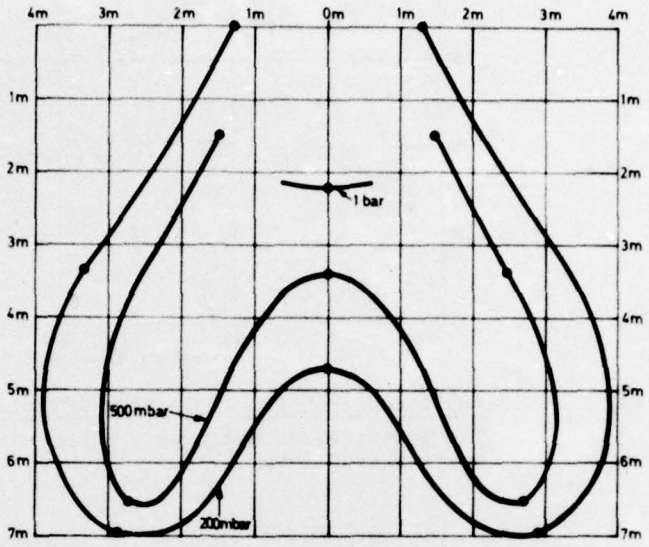

Figure 6.11 Face on blast pressure isobars behind the 127mm RCL, TOW

6.6 The spectral content of various weapon signals

Examples on the Fourier transform of digitalized pressure signals for the LAW, the CG, and the 106 mm RCR, are shown in figures 6.12 to 6.14.
Pressure level in dB is the dependent variable. Frequence is the independent variable. The unfortunate high base frequency of about 75 Hz is due to there being only a small computer available at the time of the digitalization. This, however, does not change the fact that most of the "energy" for each weapon is in the frequency band from about 75 Hz to 1000 Hz. A modified Cooley-Tukey algorithm is used to calculate the spectra (5). The pressure signals are measured from 4 to 6 metres behind each weapon and 25 cm above ground level.

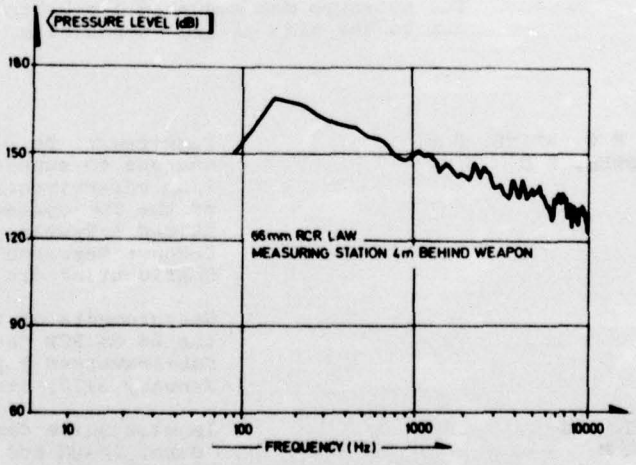

Figure 6.12 Amplitude spectrum in a 66 mm RCL blast pressure signal
The pressure was measured 4 m behind the weapon, 15° off to the side of the weapon axis, and 25 cm above ground level.

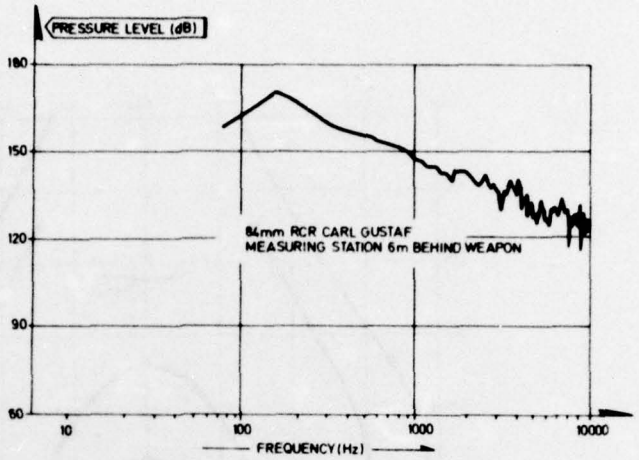

Figure 6.13 Amplitude spectrum in an 84mm RCR blast pressure signal

The pressure was measured 6 m behind the weapon and 25 cm above ground level

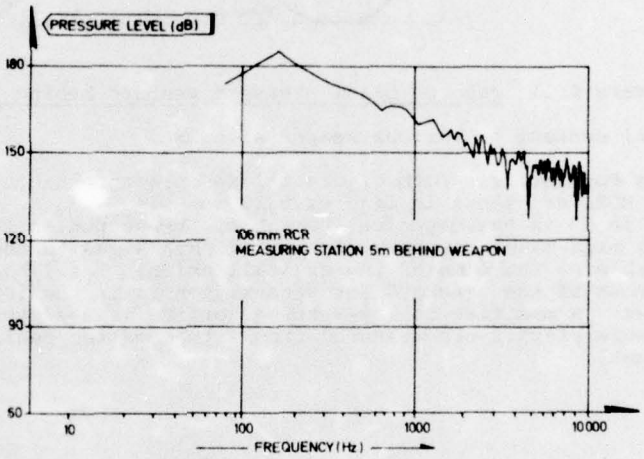

Figure 6.14 Amplitude spectrum in a 106mm RCR blast pressure signal

The pressure was measured 5 m behind the weapon, 22.5° off to the side of the weapon axis, and 25 cm above ground level

REFERENCES

(1) WESSEL, E G, REINE, E R, and ENGENES, S O — Requirement for long range anti-armour weapons to support an infantry battalion, - An effectiveness study of three versions of the TOW-system and a semi-active laser guided A/T-weapon, Notat S-429, Norwegian Defence Research Establishment (1976), Confidential (in Norwegian)

(2) — Measurements of the pressure around the 84 mm RCR Carl Gustaf, Förenade Fabriksverken Rapport FT 145-81:302, January 1972, (in Swedish)

(3) RICE, C G, and MARTIN, A M — Impulse noise damage risk criteria, Journ. Sound and Vibration (1973) 28(3), 359-367

(4) BONGARTZ, H — Der Waffenknall und das Gehör, Wehrtechnik, 12/73

(5) GODFREY, M D, BINGHAM, C, and TUKEY, J W — Modern technique of power spectrum estimation, IEEE Trans. on Audio and Electroacoustics (June 1967), 56-66

Reducing Exposure of Gunner and Environment Caused by Anti-tank Hand Weapons through the Application of the ARMBRUST Principle.

Dipl. Ing E. Harraeus
MESSERSCHMITT-BÖLKOW-BLOHM GMBH
Unternehmensbereich Apparate, AE043
Postfach 80 11 49

8000 München 80

Conventional hand weapons involve considerable exposure of the gunner to reports, toxic smoke, fire, etc. Enclosed area firing is practically impossible. Due to the signature, the gunner can easily be detected and thus destroyed, a second shot usually out of the question. The ARMBRUST principle

- permits firing without ear protection
- achieves low weapon signature (2nd shot)
- allows of enclosed area firing
- permits firing with a concrete wall up to 0.80 m behind the gunner
- entails no recoil
- provides high system precision accuracy

This briefing is not concerned primarily with the actual MBB development of the ARMBRUST 300 anti-tank hand weapon, but rather intends describing general aspects underlying the decision for such a development.

It is a known fact that the gunner of a conventional anti-tank hand weapon based on the rocket motor, on guns with a rear end nozzle, or on combinations of these, is subjected to considerable exposure. In the case of open area firing this is mainly exposure to reports. With enclosed area firing, necessary today in urban combat situations, this exposure is increased due to wall reflexion, as well as toxic gases, smoke and heat, which should not be neglected.

The high signature, again mainly due to smoke, flash and fire of a conventional weapon, is extremely unfavourable for the gunner. Therefore the gunner can easily be detected, this meaning his own certain destruction in view of the enemy of today. A second shot would have allowed him to detect any errors such as range or speed estimation errors, which considerably affect the hit probability.

PROBABILITY FOR ONE HIT WITH TWO SHOTS HAVING DIFFERENT SINGLE HIT PROBABILITIES

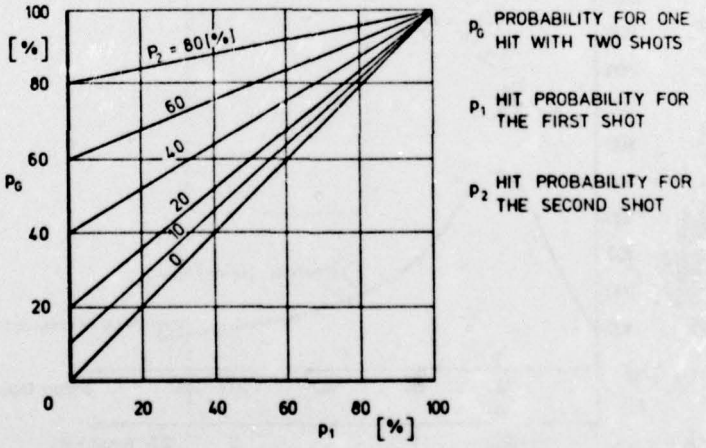

Small rooms offer the gunner the best hiding-place, especially in urban areas. This camouflage is practically impossible to utilise with conventional weapons. Should the gunner nevertheless dare to fire, a second shot would be out of the question.

The recoil represents a further exposure for the gunner which, however, can also largely be avoided using conventional firing principles.

The above main disadvantages of conventional anti-tank hand weapons can be almost completely eliminated using the ARMBRUST principle.

We have seen that nearly all disadvantages inherent in conventional anti-tank hand weapons are due to the fact that propellant gas is ejected on firing. This was the point of departure for our considerations.

The ARMBRUST principle solves this assignment in the following manner.

ARMBRUST OPERATION

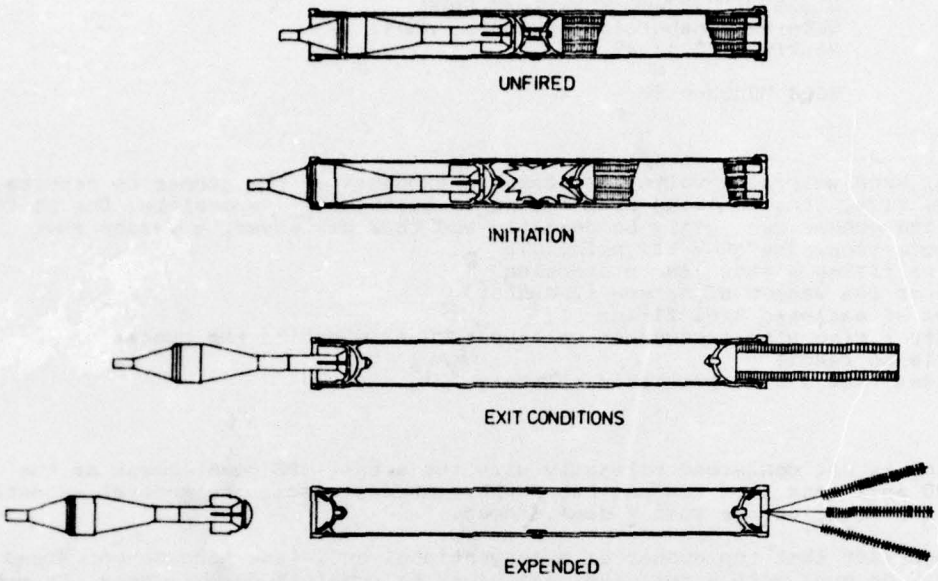

The projectile (propelled or not by a sustainer motor) is located in a tube at the front, a countermass for recoilless operation, to be described later, at the rear.

On ignition of the propellant charge in the middle and after the bolt ruptures, the projectile as well as the countermass are shifted by one piston each in opposite directions. The pressure-time characteristic in the tube corresponds to that of a gun and can be influenced by the combustion process of the propellant.

The propellant charge may consist of any suitable single-base or double-base standard propellant.

ARMBRUST INTERNAL PRESSURE

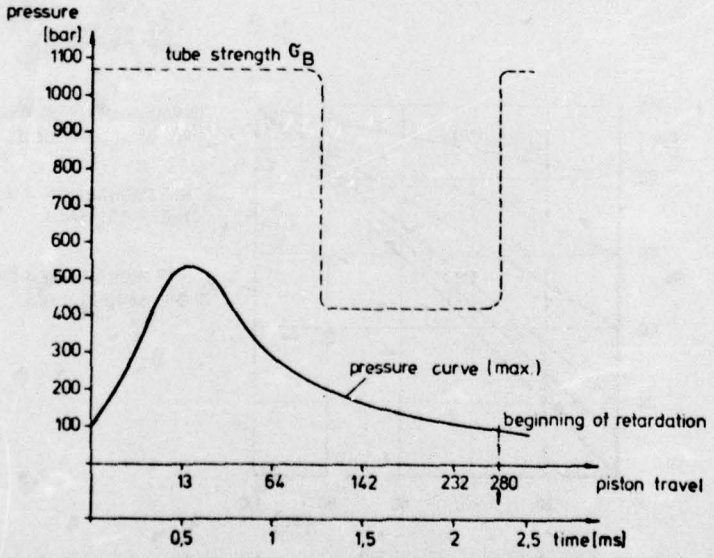

When the two pistons reach the end of the tube they are stopped simultaneously by a suitable brake and sealed thereby. The generated gas remains in the tube. Naturally the design takes into consideration the fact that the combustion process of the propellant powder is at an end, otherwise the pressure would increase again.

The countermass must be such that it disintegrates as soon as possible in order to minimize the rear end hazard zone. In addition, the countermass may not rebound on striking a concrete wall even before complete disintegration ARMBRUST provides a solution which has proved itself fully in hundreds of tests.

The countermass is made of thousands of thin punched plastic leaflets which are then layered in several piles. When the piles are exposed to the air flow they are slanted. The air flow causes the light leaflets, due to their large surface area, to fall rapidly to the ground.

COUNTERMASS DISINTEGRATION

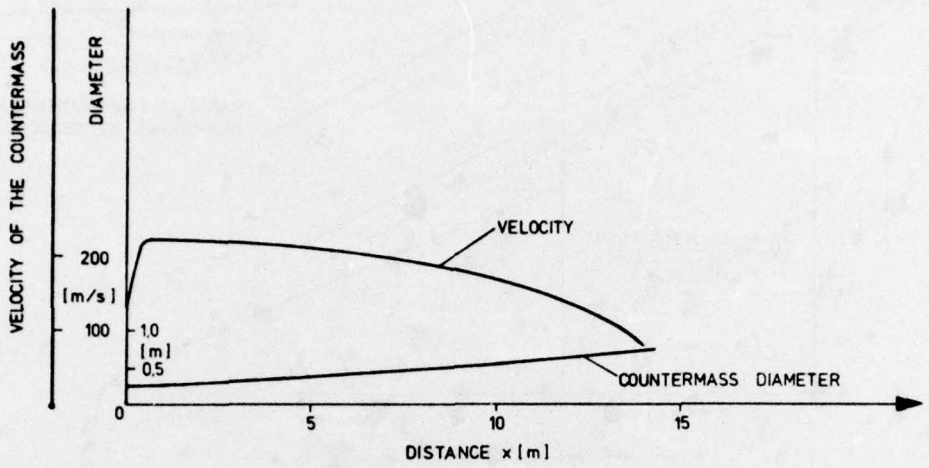

On striking a wall behind the gunner the leaflets split but do not rebound. They flow like a stream of water down the wall to the ground.

A non-reflecting, transparent material was chosen taking on the colour of the respective background and which can only be seen briefly against the horizon. This can only be observed more accurately with the aid of high-speed cameras.

In order to minimize the silhouette of the gunner with the weapon itself (and so reduce the possibility of detection) the ARMBRUST concept was expended by a laterally-mounted reflex sight (along the lines of a camera). This ensures that the gunner is not betrayed by his own silhouette.

SILHOUETTE OF AN ARMBRUST GUNNER

It could be demonstrated that the principle presented here achives the required precision due to the low firing deviations and high muzzle velocities. In this context, however, it is merely intended to describe the special advantages provided by the ARMBRUST principle, and only to a very limited extent by other hand weapons.

Exposure to reports

Since the ARMBRUST is such that no gas leaves the tube, the report is mainly due to sound conducted through solids. The tube is made to vibrate when the pressure increases and the brake is stopped. The report is comparable to a hard knock on a steel tube mixed with other noises.

Investigations are currently being conducted on the different physiological effects of various reports. The following diagram is generally taken as the limiting curve.

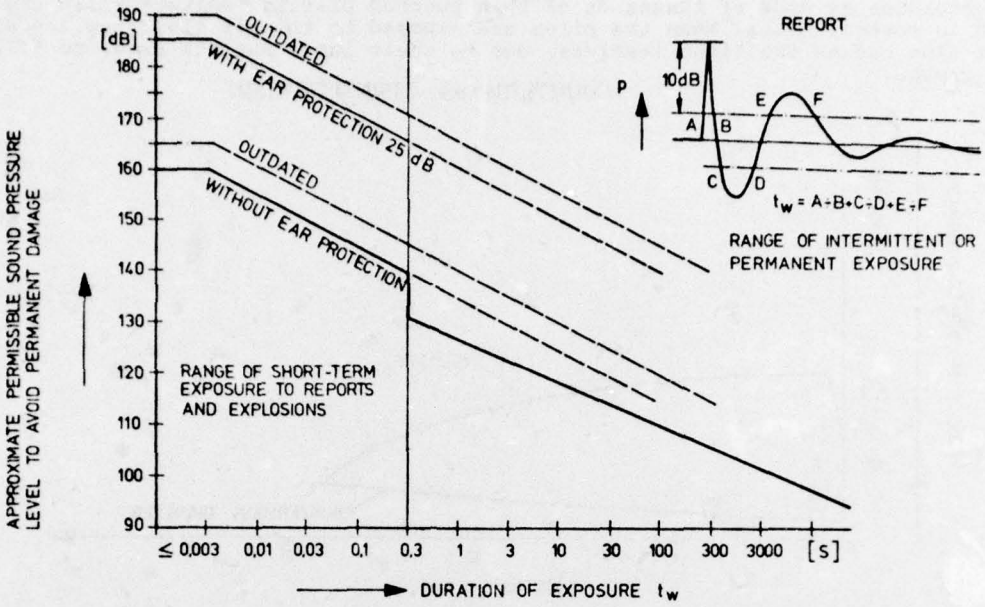

AMENDED PROVISIONAL DIAGRAM (1972)

The diagram is based on the considerations that not only the initial peak values but the accumulated peaks over a certain time are decisive (especially true of enclosed areas). No quantitative evaluation of possible psychical impacts, in particular the gunner's fear of the loud report whilst aiming and of resultant aiming errors are available. However, it can be assumed that a "quiet" weapon would greatly reduce gunner errors.

Despite the doubts arising in view of the different and unknown measuring methods, the following, however, can be stated:

Firing conventional hand weapons without ear protection is a health hazard, and in the case of heavy weapons would entail permanent damage even with ear protection.

REPORT OF ANTI-TANK HAND WEAPONS

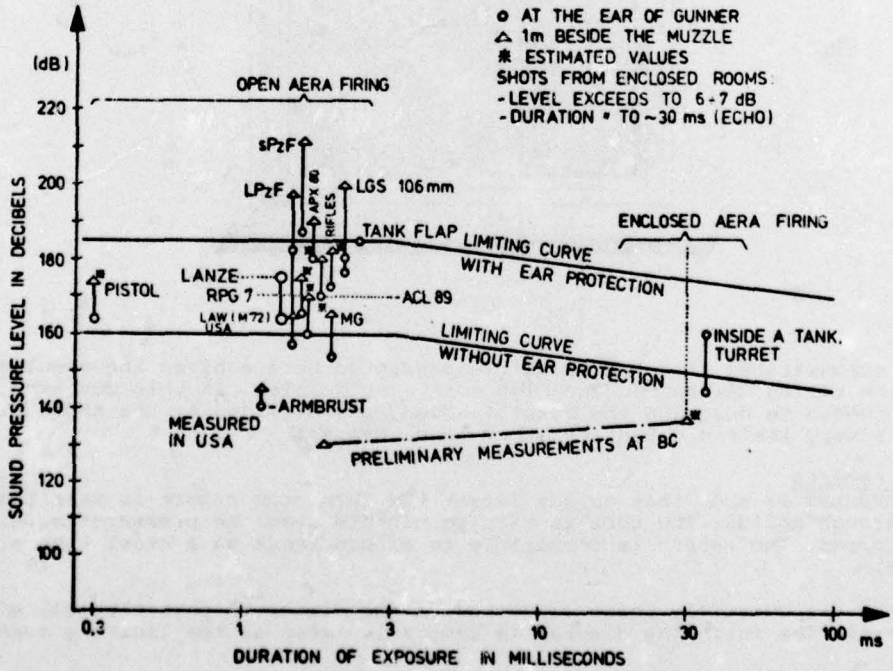

The following must always be borne in mind for values given in decibels:

i.e. 10 dB more means a tripling of the sound pressure and ten times the intensity.
20 dB more means ten times the sound pressure and a hundred times the intensity.

INCREASE OF SOUND PRESSURE AND SOUND INTENSITY
BY INCREASING THE DECIBEL VALUE [dB]

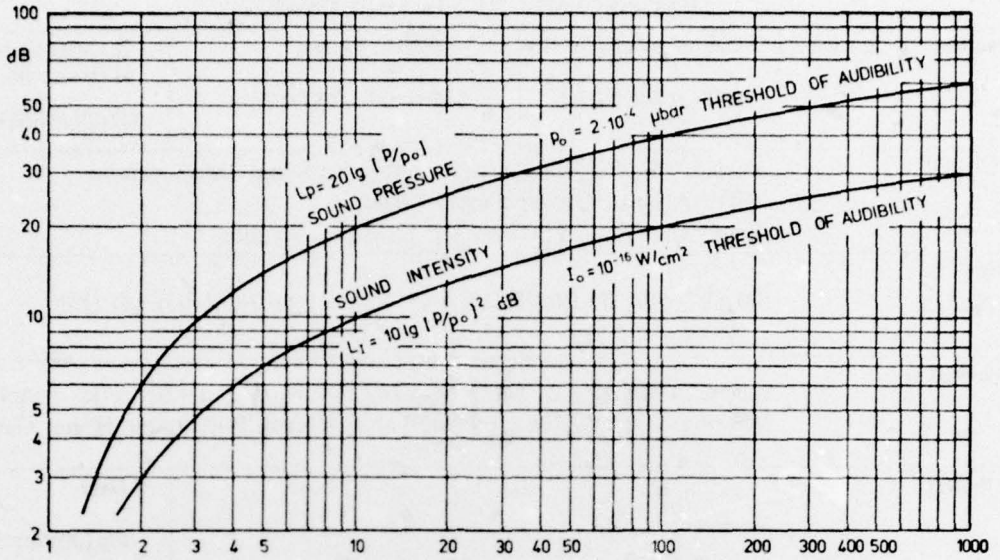

Fire, flash and smoke
No statement can be made as to exposure of the gunner or of the environment to the above, since no gas is released.

Launch tube under pressure
The tube under pressure after firing represents no danger to the gunner, provided that the ductility of the material is such that no blow-up occurs even when the tube is perforated. It could be demonstrated, using a flow-turned steel tube, that a tube perforated directly after firing does not burst.

Heating up of the tube
Since not much energy (= propellant) is required for firing, the tube itself does not heat up to a large extent. Even using thin-walled tubes (1 mm) 150°C were never exceeded. Since the actual weapon has a plastic stock there is no danger for the gunner.

The above-described ARMBRUST principle can be adapted to the most varied weapon sizes and categories. Theoretical studies have demonstrated that not only ARMBRUST 300 (termination of development with firing from shoulder planned for this year) can be realised on this basis, but a whole weapon family, too.

REPORT DOCUMENTATION PAGE			
1. Recipient's Reference	**2. Originator's Reference** AGARD-CP-194	**3. Further Reference** ISBN 92-835-0174-8	**4. Security Classification of Document** UNCLASSIFIED
5. Originator	Advisory Group for Aerospace Research and Development North Atlantic Treaty Organization 7 rue Ancelle, 92200 Neuilly sur Seine, France		
6. Title	SMALL SOLID PROPELLANT ROCKETS FOR FIELD USE		
7. Presented at	the 47th Meeting of the AGARD Propulsion and Energetics Panel Meeting held at DFVLR Porz-Wahn, 5 Köln 90, Linder Höhe, Germany		
8. Author(s) Various			**9. Date** September 1976
10. Author's Address Various			**11. Pages** 156
12. Distribution Statement	This document is distributed in accordance with AGARD policies and regulations, which are outlined on the Outside Back Covers of all AGARD publications.		

13. Keywords/Descriptors

Solid propellant rockets	Solid propellant rocket engines	Specifications
Thrust vector control	Missile propulsion	Environmental tests
weapon systems	Solid propellants	

14. Abstract

These Proceedings consist of 25 papers, including the discussion after each paper, and a Technical Evaluation Report of the Specialists' Meeting held at the 47th Propulsion and Energetics Panel Meeting in DFVLR, Porz-Wahn, near Cologne, Germany, 17-19 May 1976. The papers from seven nations were divided into five sessions: Requirements and Systems Specifications (3), Development of Small Rocket Motors (6), Thrust Vectoring and Control (3), High Performance Solid Propellants (7), and Qualification, Testing and Environmental Effects (6). Eleven papers and the Technical Evaluation Report are not included in these unclassified proceedings, but are published in a classified supplement.

AGARD Conference Proceedings No.194 Advisory Group for Aerospace Research and Development, NATO SMALL SOLID PROPELLANT ROCKETS FOR FIELD USE Published September 1976 156 pages These Proceedings consist of 25 papers, including the discussion after each paper, and a Technical Evaluation Report of the Specialists' Meeting held at the 47th Propulsion and Energetics Panel Meeting in DFVLR, Porz-Wahn, near Cologne, Germany, 17-19 May 1976. The papers from seven nations were divided into five sessions: Requirements and Systems Specifications (3), Development of Small Rocket Motors (6), Thrust P.T.O.	AGARD-CP-194 Solid propellant rockets Thrust vector control weapon systems Solid propellant rocket engines Missile propulsion Solid propellants Specifications Environmental tests	AGARD Conference Proceedings No.194 Advisory Group for Aerospace Research and Development, NATO SMALL SOLID PROPELLANT ROCKETS FOR FIELD USE Published September 1976 156 pages These Proceedings consist of 25 papers, including the discussion after each paper, and a Technical Evaluation Report of the Specialists' Meeting held at the 47th Propulsion and Energetics Panel Meeting in DFVLR, Porz-Wahn, near Cologne, Germany, 17-19 May 1976. The papers from seven nations were divided into five sessions: Requirements and Systems Specifications (3), Development of Small Rocket Motors (6), Thrust P.T.O.	AGARD-CP-194 Solid propellant rockets Thrust vector control weapon systems Solid propellant rocket engines Missile propulsion Solid propellants Specifications Environmental tests
AGARD Conference Proceedings No.194 Advisory Group for Aerospace Research and Development, NATO SMALL SOLID PROPELLANT ROCKETS FOR FIELD USE Published September 1976 156 pages These proceedings consist of 25 papers, including the discussion after each paper, and a Technical Evaluation Report of the Specialists' Meeting held at the 47th Propulsion and Energetics Panel Meeting in DFVLR, Porz-Wahn, near Cologne, Germany, 17-19 May 1976. The papers from seven nations were divided into five sessions: Requirements and Systems Specifications (3), Development of Small Rocket Motors (6), Thrust P.T.O.	AGARD-CP-194 Solid propellant rockets Thrust vector control weapon systems Solid propellant rocket engines Missile propulsion Solid propellants Specifications Environmental tests	AGARD Conference Proceedings No.194 Advisory Group for Aerospace Research and Development, NATO SMALL SOLID PROPELLANT ROCKETS FOR FIELD USE Published September 1976 156 pages These Proceedings consist of 25 papers, including the discussion after each paper, and a Technical Evaluation Report of the Specialists' Meeting held at the 47th Propulsion and Energetics Panel Meeting in DFVLR, Porz-Wahn, near Cologne, Germany, 17-19 May 1976. The papers from seven nations were divided into five sessions: Requirements and Systems Specifications (3), Development of Small Rocket Motors (6), Thrust P.T.O.	AGARD-CP-194 Solid propellant rockets Thrust vector control weapon systems Solid propellant rocket engines Missile propulsion Solid propellants Specifications Environmental tests

Vectoring and Control (3), High Performance Solid Propellants (7), and Qualification, Testing and Environmental Effects (6). Eleven papers and the Technical Evaluation Report are not included in these unclassified proceedings, but are published in a classified supplement. ISBN 92-835-0174-8	Vectoring and Control (3), High Performance Solid Propellants (7), and Qualification, Testing and Environmental Effects (6). Eleven papers and the Technical Evaluation Report are not included in these unclassified proceedings, but are published in a classified supplement. ISBN 92-835-0174-8
Vectoring and Control (3), High Performance Solid Propellants (7), and Qualification, Testing and Environmental Effects (6). Eleven papers and the Technical Evaluation Report are not included in these unclassified proceedings, but are published in a classified supplement. ISBN 92-835-0174-8	Vectoring and Control (3), High Performance Solid Propellants (7), and Qualification, Testing and Environmental Effects (6). Eleven papers and the Technical Evaluation Report are not included in these unclassified proceedings, but are published in a classified supplement. ISBN 92-835-0174-8

AGARD

NATO OTAN

7 RUE ANCELLE · 92200 NEUILLY-SUR-SEINE

FRANCE

Telephone 745.08.10 · Telex 610176

DISTRIBUTION OF UNCLASSIFIED AGARD PUBLICATIONS

AGARD does NOT hold stocks of AGARD publications at the above address for general distribution. Initial distribution of AGARD publications is made to AGARD Member Nations through the following National Distribution Centres. Further copies are sometimes available from these Centres, but if not may be purchased in Microfiche or Photocopy form from the Purchase Agencies listed below.

NATIONAL DISTRIBUTION CENTRES

BELGIUM
Coordonnateur AGARD – VSL
Etat-Major de la Force Aérienne
Caserne Prince Baudouin
Place Dailly, 1030 Bruxelles

CANADA
Defence Scientific Information Service
Department of National Defence
Ottawa, Ontario K1A OZ2

DENMARK
Danish Defence Research Board
Østerbrogades Kaserne
Copenhagen Ø

FRANCE
O.N.E.R.A. (Direction)
29 Avenue de la Division Leclerc
92 Châtillon sous Bagneux

GERMANY
Zentralstelle für Luft- und Raumfahrt-
dokumentation und -information
D-8 München 86
Postfach 860880

GREECE
Hellenic Armed Forces Command
D Branch, Athens

ICELAND
Director of Aviation
c/o Flugrad
Reykjavik

ITALY
Aeronautica Militare
Ufficio del Delegato Nazionale all'AGARD
3, Piazzale Adenauer
Roma/EUR

LUXEMBOURG
See Belgium

NETHERLANDS
Netherlands Delegation to AGARD
National Aerospace Laboratory, NLR
P.O. Box 126
Delft

NORWAY
Norwegian Defence Research Establishment
Main Library
P.O. Box 25
N-2007 Kjeller

PORTUGAL
Direccao do Servico de Material
da Forca Aerea
Rua de Escola Politecnica 42
Lisboa
Attn: AGARD National Delegate

TURKEY
Department of Research and Development (ARGE)
Ministry of National Defence, Ankara

UNITED KINGDOM
Defence Research Information Centre
Station Square House
St. Mary Cray
Orpington, Kent BR5 3RE

UNITED STATES
National Aeronautics and Space Administration (NASA),
Langley Field, Virginia 23365
Attn: Report Distribution and Storage Unit

THE UNITED STATES NATIONAL DISTRIBUTION CENTRE (NASA) DOES NOT HOLD STOCKS OF AGARD PUBLICATIONS, AND APPLICATIONS FOR COPIES SHOULD BE MADE DIRECT TO THE NATIONAL TECHNICAL INFORMATION SERVICE (NTIS) AT THE ADDRESS BELOW.

PURCHASE AGENCIES

Microfiche or Photocopy

National Technical
Information Service (NTIS)
5285 Port Royal Road
Springfield
Virginia 22151, USA

Microfiche

Space Documentation Service
European Space Agency
114, Avenue Charles de Gaulle
92200 Neuilly sur Seine, France

Microfiche

Technology Reports
Centre (DTI)
Station Square House
St. Mary Cray
Orpington, Kent BR5 3RF
England

Requests for microfiche or photocopies of AGARD documents should include the AGARD serial number, title, author or editor, and publication date. Requests to NTIS should include the NASA accession report number. Full bibliographical references and abstracts of AGARD publications are given in the following journals:

Scientific and Technical Aerospace Reports (STAR),
published by NASA Scientific and Technical
Information Facility
Post Office Box 8757
Baltimore/Washington International Airport
Maryland 21240, USA

Government Reports Announcements (GRA),
published by the National Technical
Information Services, Springfield
Virginia 22151, USA

Printed by Technical Editing and Reproduction Ltd
Harford House, 7–9 Charlotte St, London W1P 1HD

ISBN 92-835-0174-8